



**DEVELOPMENT OF CSMM-BASED SHELL ELEMENT FOR  
REINFORCED CONCRETE STRUCTURES**

A Dissertation

Presented to

the Faculty of the Department of Civil and Environmental Engineering

University of Houston

In Partial Fulfillment

of the Requirements for the Degree

Doctor of Philosophy

in Civil Engineering

by

Hieu Cong Luu

May 2016

**DEVELOPMENT OF CSMM-BASED SHELL ELEMENT FOR  
REINFORCED CONCRETE STRUCTURES**

---

Hieu Cong Luu

Approved:

---

Chair of the Committee  
Yi-Lung Mo, Professor,  
Civil and Environmental Engineering

Committee Members:

---

Thomas T. C. Hsu, Moores Professor,  
Civil and Environmental Engineering

---

Roberto Ballarini,  
Thomas and Laura Hsu Professor,  
Department Chairman,  
Civil and Environmental Engineering

---

Mohamad Mansour, Adjunct Professor,  
Civil and Environmental Engineering

---

Arghadeep Laskar, Assistant Professor,  
Civil Engineering  
Indian Institute of Technology Bombay

---

Suresh K. Khator, Associate Dean,  
Cullen College of Engineering

---

Roberto Ballarini,  
Thomas and Laura Hsu Professor,  
Department Chairman,  
Civil and Environmental Engineering

## ACKNOWLEDGMENTS

I would like to express my sincerest gratitude to my supervisors, Professor Y.L. Mo and Professor Thomas T.C. Hsu, for their continuing support and guidance throughout this research. I always wanted to learn more from both professors and am impressed with their knowledge, professionalism, and friendly approach to their students.

I would like to express my special thanks to Dr. M. Ballarini, Dr. M. Mansour, and Dr. A. Laskar for serving on the dissertation committee. Their friendly guidance, provoking suggestions, and insightful comments are greatly appreciated.

I also am grateful for the support of the National Center for Research on Earthquake Engineering (NCREE) in Taipei, Taiwan. As part of this research, the experimental study of nuclear containment tests was a joint effort between the NCREE and the University of Houston. I would like to thank all technician staffs in NCREE, Dr. Chiun-Lin Wu, Yu-Chih Chen, Chang-Ching Chang, Hu-Jhong Lu, Kung-Juin Wang, Hsuan-Chih Yang, and Yuan-Sen Yang for their strong support and for conducting the tests.

The computer program developed as part of this research is based on the OpenSees software framework released by the Pacific Earthquake Engineering Research Center. I greatly appreciate the generous consultations on the OpenSees framework by Dr. Frank McKenna and many other researchers. Also, I would like to thank Professor Gregory L. Fenves, Professor Filip C. Filippou, Dr. Frank McKenna, and many other researchers for their generous contributions to the OpenSees framework.

I am grateful to many people for the truly inspiring, challenging, and enjoyable years I

spent at the University of Houston. Sincere thanks are given to fellow graduate students Emad Labib, Sinjaya Tan, Yiqun Yan, Yuping Liu, Masoud Dehghani, Mehdi Zomorodian, Guang Yang, Reza Mousavi, FNU Witarto, Jamshaid Sawab, Zhibao Cheng, Feng Qin, and lab supervisor Gerald McTigret for their help.

Finally, I would like to thank my parents and my sister. Without their love, patience, and support, I could not have completed this work.

**DEVELOPMENT OF CSMM-BASED SHELL ELEMENT FOR  
REINFORCED CONCRETE STRUCTURES**

An Abstract  
of a  
Dissertation  
Presented to  
the Faculty of the Department of Civil and Environmental Engineering  
University of Houston

In Partial Fulfillment  
of the Requirements for the Degree  
Doctor of Philosophy  
in Civil Engineering

by  
Hieu Cong Luu

May 2016

## **ABSTRACT**

Reinforced concrete (RC) shell structures have been widely used in a variety of modern engineering applications. It is found from the earthquake reconnaissance that the RC shell structures, such as nuclear containments, cooling towers, roof domes, shear walls, are the key elements to resist earthquake disturbances. This research presents the development of a finite element analysis (FEA) program to predict the inelastic behavior of RC shell structures. In the program, a new shell element, so-called CSMM-based shell element, was developed based on the formulation of the degenerated shell theory with layered approach and taking into account the Cyclic Softened Membrane Model developed at the University of Houston. An analysis procedure was developed to perform nonlinear analyses of RC shell structures using the developed CSMM-based shell element. To develop the FEA program, the developed shell element and the proposed analysis procedure were implemented into a finite element program development framework, OpenSees, which was developed at University of California, Berkeley. Several large-scale structural tests were used to validate the developed FEA program, including panels subjected to pure shear or combination of shear and bending, a three-dimensional (3D) RC shear wall, a cylindrical RC tank, and circular and rectangular RC hollow bridge columns. More importantly, the versatile application of the developed finite element analysis program SCS-3D was further investigated by the modeling of two 1/13-scaled nuclear containment vessel specimens and a two-story unsymmetrical RC building subjected to reserved cyclic loadings. Both test programs were undertaken as part of an international collaboration projects between the

National Center for Research on Earthquake Engineering (NCREE) in Taipei, Taiwan, and the University of Houston (UH), Houston, Texas. The experimental work was performed at NCREE, and the specimen design and study of the experimental results were performed at UH.

# TABLE OF CONTENTS

<b>ACKNOWLEDGMENTS</b> .....	<b>iv</b>
<b>ABSTRACT</b> .....	<b>vii</b>
<b>TABLE OF CONTENTS</b> .....	<b>ix</b>
<b>LIST OF FIGURES</b> .....	<b>xvi</b>
<b>LIST OF TABLES</b> .....	<b>xxx</b>
<b>1 INTRODUCTION</b> .....	<b>1</b>
1.1 Overview.....	1
1.2 Research Background .....	5
1.3 Objectives of Research .....	9
1.4 Outlines of Dissertation .....	10
<b>2 LITERATURE REVIEW</b> .....	<b>13</b>
2.1 Background of Shell Elements.....	13
2.1.1 Types of Shell Elements.....	13
2.1.2 Thin Shell and Thick Shell.....	15
2.1.3 Degenerated Curved Shell Elements .....	16
2.2 Previous Work on Simulation of RC Shell-type Structures .....	18
2.2.1 Hand et al. (1972) .....	18
2.2.2 Cervera et al. (1987) .....	19
2.2.3 Scordelis and Chan (1987).....	21
2.2.4 Hu and Schnobrich (1991).....	22

2.2.5 Adebar and Colins (1994) .....	23
2.2.6 Polak and Vecchio (1994) .....	23
2.2.7 Kim et al. (2002) .....	24
2.2.8 Zhang et al. (2007) .....	25
2.2.9 Xiang et al. (2012) .....	26
2.3 Research on Constitutive Model for RC .....	26
2.4 Previous Analytical Models Developed by the Research Group at UH .....	27
2.5 Cyclic Softened Membrane Model (CSMM) .....	30
2.5.1 Coordinate Systems .....	30
2.5.2 Equilibrium Equations .....	31
2.5.3 Compatibility Equations .....	32
2.5.4 Relationship between Biaxial Strains and Uniaxial Strains.....	33
2.5.5 Constitutive Model of Concrete in Tension and Compression .....	34
2.5.6 Constitutive Model of Concrete in Shear.....	37
2.5.7 Constitutive Model of Embedded Reinforcement .....	37
2.6 OpenSees Framework .....	39
2.7 Previous FEA by Research Group at UH.....	42
<b>3 CSMM-BASED SHELL ELEMENT .....</b>	<b>47</b>
3.1 Introduction.....	47
3.2 Element Formulation .....	47
3.2.1 Element Assumption .....	49
3.2.2 Coordinate Systems .....	50
3.2.3 Geometry.....	52

3.2.4 Displacements .....	52
3.2.5 Strains .....	53
3.2.6 Shape Function and Jacobian Matrix.....	55
3.2.7 Constitutive Equation.....	56
3.2.8 Element Stiffness Matrix and Internal Force Vector.....	57
3.2.9 Stress Resultant.....	58
3.2.10 Numerical Integration and Layer Approach .....	59
3.3 Constitutive Model.....	61
3.3.1 Stress and Strain Relationship in Each Layer .....	61
3.3.2 Material Matrix for In-plane Behavior .....	62
3.3.3 Material Matrix for Out-of-plane Behavior .....	71
3.4 Solution Algorithm.....	71
3.4.1 Load Control Scheme .....	72
3.4.2 Displacement Control Scheme.....	74
3.5 Analysis Procedure.....	76
3.6 Nonlinear Finite Element Program SCS-3D.....	80
3.6.1 Implementation .....	80
3.6.2 Program Commands.....	82
3.6.3 Graphical User Interface Module for Post-processing.....	83
<b>4 VALIDATIONS .....</b>	<b>88</b>
4.1 Introduction.....	88
4.2 Simulation of RC Panels Tested by Pang (1991).....	88
4.2.1 Test Description .....	88

4.2.2 Analytical Model.....	90
4.2.3 Comparison of Analytical Results with Experimental Results .....	91
4.3 Simulation of RC Panels Tested by Mansour (2001).....	92
4.3.1 Test Description .....	92
4.3.2 Analytical Model.....	93
4.3.3 Comparison of Analytical Results with Experimental Results .....	94
4.4 Simulation of RC Panels Tested by Polak (1992).....	96
4.4.1 Test Description .....	96
4.4.2 Analytical Model.....	98
4.4.3 Comparison of Analytical Results with Experimental Results .....	102
4.5 Simulation of a RC Cylindrical Tank.....	104
4.5.1 Test Description .....	104
4.5.2 Analytical Model.....	107
4.5.3 Comparison of Analytical Results with Experimental Results .....	108
4.6 Simulation of a 3D RC Shear Wall .....	109
4.6.1 Test Description .....	109
4.6.2 Analytical Model.....	113
4.6.3 Comparison of Analytical Results with Experimental Results .....	114
4.7 Analysis of RC Hollow Bridge Piers .....	115
4.7.1 Test Description .....	115
4.7.2 CSMM for Confined Concrete.....	119
4.7.3 Analytical Model.....	122
4.7.4 Comparison of Analytical Results with Experimental Results .....	126

## **5 EXPERIMENT AND SIMULATION OF RC NUCLEAR CONTAINMENT**

<b>VESSEL .....</b>	<b>132</b>
5.1 Introduction.....	132
5.2 Experimental Program .....	136
5.2.1 Specimen Design .....	136
5.2.2 Specimen Description .....	139
5.2.3 Material .....	146
5.2.4 Manufacturing.....	148
5.2.5 Instrumentations.....	158
5.2.6 Test Setup.....	162
5.2.7 Loading Protocol.....	166
5.3 Experimental Results .....	167
5.3.1 Cracking Patterns of Concrete .....	167
5.3.2 Load-Displacement Characteristic.....	169
5.3.3 Behaviors of Steel Bars.....	173
5.3.4 Failure Modes .....	181
5.4 Analytical Model.....	183
5.4.1 Finite Element Mesh.....	183
5.4.2 Analytical Algorithm.....	185
5.4.3 Sensitivity Analysis.....	185
5.5 Comparison of Analytical Results with Experimental Outcomes.....	188
5.5.1 Analytical Load-displacement Relationships.....	188
5.5.2 Behaviors of Concrete and Steel Bars at the First Cracking.....	193

5.5.3 Behaviors of Concrete and Steel Bars at First Yielding of Steel Bars .....	200
5.5.4 Behaviors of Concrete and Steel Bars at the Peak Load.....	206
5.6 Further Analytical Studies.....	213
5.6.1 Improving Sliding Shear Failure Prediction of Specimen No. 1 .....	213
5.6.2 Improving the Prediction for the Descending Branch of Specimen No. 2 ....	218
<b>6 SIMULATION OF A TWO-STORY UNSYMMETRICAL REINFORCED</b>	
<b>CONCRETE BUILDING.....</b>	<b>220</b>
6.1 Introduction.....	220
6.2 Test Description .....	220
6.2.1 Specimen.....	220
6.2.2 Material Properties.....	227
6.2.3 Test setup and Instruments.....	229
6.2.4 Loading Procedure .....	230
6.2.5 Experimental Results .....	233
6.3 Description of Analytical Model.....	235
6.3.1 Modeling Slabs .....	235
6.3.2 Modeling Beams and Columns.....	236
6.3.3 Modeling Shear Walls.....	241
6.3.4 Modeling Shear-governed Columns .....	242
6.3.5 Applying Load .....	244
6.3.6 Solution algorithm .....	245
6.4 Effects of Modeling Assumption on the Analytical Results .....	245
6.4.1 Effect of RC Walls .....	245

6.4.2 Effect of Shear-governed Columns.....	249
6.4.3 Effect of Buckling Columns .....	251
6.5 Comparison of Analytical Result with Experimental Outcome.....	252
<b>7 SUMMARY AND CONCLUSIONS.....</b>	<b>254</b>
7.1 Summary.....	254
7.2 Conclusions.....	256
7.3 Recommendations for future research .....	259
<b>REFERENCES.....</b>	<b>261</b>
<b>APPENDIX A INPUT FILE OF RCCV NO.1 SPECIMEN.....</b>	<b>272</b>
<b>APPENDIX B INPUT FILE OF RCCV NO.2 SPECIMEN .....</b>	<b>281</b>
<b>APPENDIX C INPUT FILE OF 2-STORY BUILDING SPECIMEN.....</b>	<b>290</b>

## LIST OF FIGURES

Figure 1.1 Ancient shell structures: (a) Pantheon of ancient Rome; (b) Hagia Sophia in Istanbul, Turkey; (c) St Paul’s Cathedral in London, England; and (d) Taj Mahal in Agra, India .....	2
Figure 1.2 Modern RC shell structures: (a) Sydney Opera House in Sydney, Australia; (b) JFK Airport in New York .....	2
Figure 1.3 Modern RC shell structures in a nuclear power plant .....	3
Figure 1.4 Examples of RC Shell Structures .....	3
Figure 1.5 Universal Panel Tester (1987 to present).....	8
Figure 2.1 A classical curved shell element (Javaherian et al., 1980) .....	14
Figure 2.2 A flat shell element (Cook, 2002).....	14
Figure 2.3 A degenerated shell element (Cook, 2002).....	15
Figure 2.4 Types of degenerated shell element.....	17
Figure 2.5 20-DOF shell element with layer section (Hand et al., 1972).....	19
Figure 2.6 Twenty-node isoparametric solid element with reinforcement .....	20
Figure 2.7 Curved RC shell element with edge beam .....	21
Figure 2.8 Layered model.....	22
Figure 2.9 A typical reinforced concrete panel (Hsu & Mo, 2010) .....	31
Figure 2.10 Stress states of the 2D panel.....	32
Figure 2.11 Cyclic stress-strain relationship of smeared concrete.....	35
Figure 2.12 Cyclic stress-strain relationship of steel bar .....	38

Figure 2.13 Principal objects in OpenSees framework (Fenves, 2001).....	41
Figure 2.14 SCS program for RC (Zhong, 2005) .....	43
Figure 2.15 SCS program for PC (Laskar, 2009) .....	43
Figure 2.16 Detailing of shear walls (Gao, 1999).....	44
Figure 2.17 FEM modeling of 2D shear walls (Mo, Zhong, & Hsu, 2008) .....	45
Figure 2.18 Validation of SCS with 2D RC wall (SW13) .....	46
Figure 2.19 Validation of SCS with 2D RC wall (SW4) .....	46
Figure 3.1 Eight-node degenerated curved shell element.....	48
Figure 3.2 Mindlin theory assumption for the shell element .....	49
Figure 3.3 The 8-node Serendipity degenerated shell element.....	51
Figure 3.4 (a) Typical node $i$ , and thickness-direction vector $V_{3i}$ (b) Orthogonal vectors at node $i$ and nodal DOF.....	53
Figure 3.5 The stress resultants in the shell element (Cook, 2002) .....	58
Figure 3.6 The concept of layered approach.....	59
Figure 3.7 Gauss point positions.....	60
Figure 3.8 Local coordinate systems in each layer .....	63
Figure 3.9 Envelope stress-strain curve of concrete in compression.....	66
Figure 3.10 Envelope stress-strain curve of concrete in tension .....	66
Figure 3.11 Cyclic stress-strain curve of uniaxial material model for concrete .....	67
Figure 3.12 Envelope stress-strain curve of for steel.....	69
Figure 3.13 Cyclic stress-strain curve of uniaxial material model for steel .....	69
Figure 3.14 Load control scheme using the full Newton-Raphson method .....	73
Figure 3.15 Load control scheme using the modified Newton-Raphson method.....	73

Figure 3.16 Load control scheme using the initial stiffness method .....	74
Figure 3.17 Analysis procedure for the CSMM-based shell element with iteration.....	78
Figure 3.18 Analysis procedure for the CSMM-based shell element without iteration....	79
Figure 3.19 Implementation of element and material classes of SCS-3D program.....	82
Figure 3.20 Programming graphical model with Eyeshot .....	85
Figure 3.21 User interface of SCS-3D program .....	86
Figure 3.22 Post-processing function of SCS-3D program .....	86
Figure 3.23 Files of analytical results .....	87
Figure 4.1 Dimensions of panels A2, A3, and A4 (Pang & Hsu, 1995) .....	89
Figure 4.2 Finite element mesh used for panels A2, A3, and A4.....	90
Figure 4.3 Cross section mesh of the shell element used for Pang's panels.....	91
Figure 4.4 Comparison between experimental and analytical shear stress versus shear strain for panels A2, A3, and A4.....	92
Figure 4.5 Dimensions of panel CA3 (Mansour, 2001).....	94
Figure 4.6 Dimensions of panels CE4 (Mansour, 2001).....	95
Figure 4.7 Comparison between experimental and analytical shear stress versus shear strain for panel CA3.....	96
Figure 4.8 Comparison between experimental and analytical shear stress versus shear strain for panel CE4 .....	96
Figure 4.9 Dimensions of panels SM1, SM2, and SM3 (Polak, 1992).....	98
Figure 4.10 Dimensions of panel SM4 (Polak, 1992) .....	99
Figure 4.11 Finite element mesh used for panel SM1 .....	100
Figure 4.12 Finite element mesh used for panel SM2 .....	100

Figure 4.13 Finite element mesh used for panel SM3 .....	101
Figure 4.14 Finite element mesh used for panel SM4 .....	101
Figure 4.15 Cross section mesh of the shell element used for Polak’s panels.....	102
Figure 4.16 Comparison between experimental and analytical moment versus curvature for panel SM1 .....	103
Figure 4.17 Comparison between experimental and analytical moment versus curvature for panel SM2 .....	103
Figure 4.18 Comparison between experimental and analytical moment versus curvature for panel SM3 .....	104
Figure 4.19 Comparison between experimental and analytical moment versus curvature for panel SM4 .....	104
Figure 4.20 Dimensions and reinforcement details of RC cylindrical tank.....	106
Figure 4.21 Test setup of RC cylindrical tank .....	107
Figure 4.22 Finite element mesh used for RC cylindrical tank .....	108
Figure 4.23 Cross-section mesh of the shell element used for RC cylindrical tank .....	109
Figure 4.24 Comparison between experimental and analytical load versus displacement for RC cylindrical tank .....	110
Figure 4.25 Elevation view of 3D shear wall .....	112
Figure 4.26 Dimensions and reinforcement details of 3D shear wall.....	112
Figure 4.27 Test setup of the 3D shear wall.....	113
Figure 4.28 Finite element mesh used for RC cylindrical tank .....	114
Figure 4.29 Cross section mesh of the shell element used for RC cylindrical tank .....	114
Figure 4.30 Comparison between experimental and analytical load versus displacement for	

3D RC shear wall .....	116
Figure 4.31 Test setup of RC hollow columns.....	118
Figure 4.32 Cross sections of RC hollow bridge piers .....	119
Figure 4.33 Finite element mesh of the RC hollow piers using 2D model (Zhong, 2005) .....	121
Figure 4.34 The proposed softened compressive stress-strain relationship for confined concrete.....	123
Figure 4.35 Finite element mesh used for RC hollow rectangular piers .....	125
Figure 4.36 Finite element mesh used for RC hollow circular piers .....	125
Figure 4.37 Cross section mesh of the shell element used for RC hollow piers (Unconfined) .....	126
Figure 4.38 Cross section mesh of the shell element used for RC hollow piers (Confined) .....	126
Figure 4.39 Comparison between confined model and unconfined model for flexural- governed column (Column PS1-C).....	128
Figure 4.40 Comparison between confined model and unconfined model for flexural-shear- governed column (Column PI2-C).....	128
Figure 4.41 Comparison between experimental and analytical load versus displacement for column PS1 .....	130
Figure 4.42 Comparison between experimental and analytical load versus displacement for column PI1 .....	130
Figure 4.43 Comparison between experimental and analytical load versus displacement for column PI2 .....	131

Figure 4.44 Comparison between experimental and analytical load versus displacement for column PS1-C .....	131
Figure 4.45 Comparison between experimental and analytical load versus displacement for column PI1-C .....	132
Figure 4.46 Comparison between experimental and analytical load versus displacement for column PI2-C .....	132
Figure 5.1 Stress states and resulting cracks in containment.....	134
Figure 5.2 Elevation view of the Lungmen Nuclear Power Plan (NPP) .....	137
Figure 5.3 RC containment vessel of Lungmen NPP: (a) Elevation view (b) Plan view	138
Figure 5.4 Cross-section detail of Lungmen RCCV .....	139
Figure 5.5 Dimensions of the RCCV specimens: (a) Elevation view (b) Plan view .....	142
Figure 5.6 Reinforcement details of the RCCV specimens .....	143
Figure 5.7 Reinforcement details of the RCCV specimens .....	144
Figure 5.8 Reinforcement details of the top and bottom slabs .....	145
Figure 5.9 Welding connection of the circumferential bars.....	146
Figure 5.10 Details of the end-bolt connection of the vertical bars.....	146
Figure 5.11 Slump flow test of concrete .....	148
Figure 5.12 Slump flow diameter of concrete .....	148
Figure 5.13 Formwork of the RCCV specimens .....	150
Figure 5.14 Formwork of the top slab .....	150
Figure 5.15 Applying oil to the formwork before casting .....	151
Figure 5.16 Removing the formwork.....	151
Figure 5.17 The specimen outside the laboratory after removing the formworks.....	152

Figure 5.18 The RCCV specimen inside the laboratory before testing .....	152
Figure 5.19 Reinforcement detail of Specimen No. 1 .....	153
Figure 5.20 Reinforcement detail of Specimen No. 2 .....	154
Figure 5.21 Typical reinforcement detail inside the bottom slab.....	155
Figure 5.22 Typical reinforcement detail inside the top slab .....	155
Figure 5.23 Pumping concrete from the truck inside the laboratory .....	156
Figure 5.24 Casting the top slab inside the laboratory.....	157
Figure 5.25 Moving the specimen into the lab by truck .....	158
Figure 5.26 Lifting the specimen toward the testing location by crane.....	158
Figure 5.27 The testing location .....	159
Figure 5.28 Strain gauges were attached to the steel bars .....	160
Figure 5.29 Plastic pipes protected the strain gauge cables.....	160
Figure 5.30 Instruments outside of the specimen .....	161
Figure 5.31 Instruments inside the specimen.....	161
Figure 5.32 Arrangement of the strain gauges for Specimen No. 1.....	162
Figure 5.33 Arrangement of the strain gauges for Specimen No. 2.....	162
Figure 5.34 Three-dimensional view of the test setup.....	164
Figure 5.35 Side view of the test setup (East-West) .....	165
Figure 5.36 Horizontal actuators (Total capacity: 8000 kN) .....	165
Figure 5.37 Overview of the test set up .....	166
Figure 5.38 Horizontal displacement control scheme (Inelastic test).....	167
Figure 5.39 Typical cracking patterns of the RCCV specimens (north-east view).....	169
Figure 5.40 Typical cracking patterns of the RCCV specimens (north-west view).....	169

Figure 5.41 Horizontal load versus displacement curve of Specimen No. 1 .....	170
Figure 5.42 Horizontal load versus the displacement curve of Specimen No. 2.....	171
Figure 5.43 Strains of the vertical steel bars in Specimen No. 1 (at the stage of the first yielding of the vertical steel bars in the positive direction).....	175
Figure 5.44 Strains of the vertical steel bars in Specimen No. 1 (at the stage of the first yielding of the vertical steel bars in the negative direction).....	176
Figure 5.45 Strains of the vertical steel bars in Specimen No. 2 (at the stage of the first yielding of the vertical steel bars in the negative direction).....	176
Figure 5.46 Strains of the vertical steel bars in Specimen No. 2 (at the stage of the first yielding of the vertical steel bars in the negative direction).....	177
Figure 5.47 Strains of the circumferential steel bars in Specimen No. 1 (at the stage of the first yielding of the circumferential steel bars in the positive direction).....	177
Figure 5.48 Strains of the circumferential steel bars in Specimen No. 1 (at the stage of the first yielding of the circumferential steel bars in the positive direction).....	178
Figure 5.49 Strains of the circumferential steel bars in Specimen No. 2 (at the stage of the first yielding of the circumferential steel bars in the negative direction).....	178
Figure 5.50 Strains of the circumferential steel bars in Specimen No. 2 (at the stage of the first yielding of the circumferential steel bars in the negative direction).....	179
Figure 5.51 Strains of the vertical steel bars in Specimen No. 1 (at the stage of the peak load in the positive direction) .....	180
Figure 5.52 Strains of the vertical steel bars in Specimen No. 2 (at the stage of the peak load in the positive direction) .....	181
Figure 5.53 Strains of the circumferential steel bars in Specimen No. 1 (at the stage of the	

peak load in the positive direction).....	181
Figure 5.54 Strains of the circumferential steel bars in Specimen No. 2 (at the stage of the peak load in the positive direction).....	182
Figure 5.55 Failure due to sliding shear of Specimen No. 1 .....	183
Figure 5.56 Failure due to web shear of Specimen No. 2.....	183
Figure 5.57 Finite element mesh along the thickness of the RCCV specimens .....	184
Figure 5.58 Finite element mesh of the RCCV specimens.....	185
Figure 5.59 Finite element meshes of the RCCV specimens for sensitivity analysis.....	187
Figure 5.60 Comparison of results of different mesh sizes.....	188
Figure 5.61 Comparison of results on different numbers of layer .....	188
Figure 5.62 Analytical load versus displacement curve of Specimen No. 1.....	190
Figure 5.63 Analytical load versus displacement curve of Specimen No. 2.....	191
Figure 5.64 Analytical load versus horizontal displacement curve of RCCV Specimen No. 1.....	192
Figure 5.65 Analytical load versus horizontal displacement curve of RCCV Specimen No. 2.....	192
Figure 5.66 Analytical cracking orientation of Specimen No. 1 and Specimen No. 2 in the positive and negative directions (at the drift of 0.375%).....	195
Figure 5.67 Analytical stresses of concrete in Specimen No. 1 and Specimen No. 2 in case of positive loading direction (elastic) .....	196
Figure 5.68 Analytical stresses of concrete in Specimen No. 1 and Specimen No. 2 in case of negative loading direction (elastic).....	197
Figure 5.69 Analytical strains of concrete in Specimen No. 1 (at the stage of the first	

cracking of concrete).....	198
Figure 5.70 Analytical stresses of concrete in Specimen No. 1 (at the stage of the first cracking of concrete).....	198
Figure 5.71 Analytical strains of steel bars in Specimen No. 1 (at the stage of the first cracking of concrete).....	198
Figure 5.72 Analytical stresses of steel bars in Specimen No. 1 (at the stage of the first cracking of concrete).....	199
Figure 5.73 Analytical strains of concrete in Specimen No. 2 (at the stage of the first cracking of concrete).....	200
Figure 5.74 Analytical stresses of concrete in Specimen No. 2 (at the stage of the first cracking of concrete).....	200
Figure 5.75 Analytical strains of steel bars in Specimen No. 2 (at the stage of the first cracking of concrete).....	200
Figure 5.76 Analytical stresses of steel bars in Specimen No. 2 (at the stage of the first cracking of concrete).....	201
Figure 5.77 Analytical strains of steel bars in Specimen No. 1 (at the stage of first yield of the vertical steel bars in the positive direction) .....	202
Figure 5.78 Analytical stresses of steel bars in Specimen No. 1 (at the stage of first yield of the vertical steel bars in the positive direction) .....	202
Figure 5.79 Analytical strains of concrete Specimen No. 1 (at the stage of first yield of steel bars in the positive direction).....	203
Figure 5.80 Analytical stresses of concrete Specimen No. 1 (at the stage of first yield of steel bars in the positive direction) .....	203

Figure 5.81 Analytical strains of steel bars in Specimen No. 2 (at the stage of first yield of the circumferential steel bars in the positive direction) .....	205
Figure 5.82 Analytical stresses of steel bars in Specimen No. 2 (at the stage of first yield of the circumferential steel bars in the positive direction).....	205
Figure 5.83 Analytical strains of concrete Specimen No. 2 (at the stage of first yield of steel bars in the positive direction).....	206
Figure 5.84 Analytical stresses of concrete Specimen No. 2 (at the stage of first yield of steel bars in the positive direction) .....	206
Figure 5.85 Analytical strains of steel bars in Specimen No. 1 (at the stage of the peak load in the positive direction) .....	208
Figure 5.86 Analytical stresses of steel bars in Specimen No. 1 (at the stage of the peak load in the positive direction) .....	208
Figure 5.87 Analytical strains of concrete in Specimen No. 1 (at the stage of the peak load in the positive direction) .....	209
Figure 5.88 Analytical stresses of concrete in Specimen No. 1 (at the stage of the peak load in the positive direction) .....	209
Figure 5.89 Stress-strain curve of concrete at the point CT in Specimen No. 1 (at the stage of the peak load in the positive direction).....	210
Figure 5.90 Stress-strain curve of concrete at the point CM in Specimen No. 1 (at the stage of the peak load in the positive direction).....	211
Figure 5.91 Analytical strains of steel bars in Specimen No. 2 (at the stage of the peak load in the positive direction) .....	212
Figure 5.92 Analytical stresses of steel bars in Specimen No. 2 (at the stage of the peak	

load in the positive direction) .....	212
Figure 5.93 Analytical strains of concrete in Specimen No. 2 (at the stage of the peak load in the positive direction) .....	213
Figure 5.94 Analytical stresses of concrete in Specimen No. 2 (at the stage of the peak load in the positive direction) .....	213
Figure 5.95 Stress-strain curve of concrete at the point S2 in Specimen No. 2 (at the stage of the peak load in the positive direction).....	214
Figure 5.96 Sliding shear failure mechanism .....	215
Figure 5.97 Analytical algorithm with sliding shear checking .....	216
Figure 5.98 Analytical load versus horizontal drift ratio curve of RCCV Specimen No. 1 .....	217
Figure 5.99 Stress-strain curve of steel bars at the point ST in Specimen No. 1 (at the stage of maximum load in the negative direction - Point 5) .....	218
Figure 5.100 Stress-strain curve of concrete at the point S2 in Specimen No. 2 (at the stage of sliding shear failure - Point 6) .....	218
Figure 5.101 Stress-strain curve of concrete.....	220
Figure 5.102 Parametric study on the load-displacement curve of Specimen No. 2.....	220
Figure 6.1 Three-dimensional view of the two-story unsymmetrical RC building specimen .....	222
Figure 6.2 Dimension of the two-story unsymmetrical RC building specimen in (a) Elevation view (b) Plan view .....	224
Figure 6.3 Dimensions and detailings of the columns.....	225
Figure 6.4 Dimensions and detailings of the beams and the slabs.....	225

Figure 6.5 Dimensions and detailings of Wall A and Wall B.....	226
Figure 6.6 Dimensions and detailings of Wall C .....	227
Figure 6.7 Dimensions and detailings of the RC blocks.....	228
Figure 6.8 Notations of the actuators .....	231
Figure 6.9 Test setup of the two-story unsymmetrical RC building specimen .....	232
Figure 6.10 Loading protocol .....	233
Figure 6.11 The experimental base shear versus roof displacement relationship.....	234
Figure 6.12 Failure sequences of the two-story unsymmetrical RC building specimen	235
Figure 6.13 NonlinearBeamColumn element .....	237
Figure 6.14 Discretization of fiber sections of the beams and the columns .....	238
Figure 6.15 Concrete01 model for concrete (OpenSees, 2013).....	239
Figure 6.16 Modified Kent and Park Model for confined concrete.....	239
Figure 6.17 Steel01 model for concrete (OpenSees, 2013) .....	240
Figure 6.18 Hysteretic model for steel (OpenSees, 2013) .....	241
Figure 6.19 Low-cycle fatigue stress-strain curve of steel .....	242
Figure 6.20 Finite element mesh of shear walls .....	243
Figure 6.21 Finite element mesh of column C1-2F and column C2-2F .....	244
Figure 6.22 Conceptual deformation of the specimen .....	245
Figure 6.23 Force distribution of the specimen .....	245
Figure 6.24 Finite element mesh of the building specimen (Model 1: Frame only) .....	247
Figure 6.25 Finite element mesh of the building specimen (Model 2: Frame + Elastic Wall) .....	247
Figure 6.26 Finite element mesh of the building specimen (Model 3: Frame + CSMM Wall)	

.....	248
Figure 6.27 Effect of RC walls on the base shear versus second-tory displacement relationship.....	249
Figure 6.28 Finite element mesh of the building specimen (Model 4: Frame + CSMM Wall + Shear-governed column).....	251
Figure 6.29 Effect of the shear-governed column on the base shear versus the roof displacement relationship.....	251
Figure 6.30 Finite element mesh of the building specimen (Model 5: frame + CSMM wall + shear-governed & buckled column).....	252
Figure 6.31 Effect of buckling columns on the base shear versus roof displacement relationship.....	253
Figure 6.32 Effect of RC walls on the base shear versus roof displacement relationship.....	254

## LIST OF TABLES

Table 3.1 Developed Modules in OpenSees .....	61
Table 3.2 Element and Material Classes of SCS-3D Program.....	81
Table 4.1 Loading and Material Properties of Pang’s Panels .....	89
Table 4.2 Loading and Material Properties of Mansour’s Panels .....	94
Table 4.3 Loading and Material Properties of Polak’s Panels .....	98
Table 4.4 Dimension and Material Properties of the RC Cylindrical Tank .....	106
Table 4.5 Dimension and Material Properties of the 3D Shear Wall .....	111
Table 4.6 Loading and Material Properties of RC Hollow Rectangular Piers.....	117
Table 4.7 Loading and Material Properties of RC Hollow Circular Piers .....	117
Table 5.1 Dimensions and Material Properties of RCCV Specimens.....	141
Table 5.2 Demonstration of Critical Points on the Load Versus Displacement Curves..	172
Table 5.3 Ductility of the Test Specimen .....	173
Table 5.4 Ductility of the Test Specimen from the Analytical Results .....	191
Table 6.1 Result of Compressive Strength Tests of Concrete.....	229
Table 6.2 Results of Tensile Tests of Reinforcement .....	229
Table 6.3 Control Modes and Equations of Actuators .....	233

# CHAPTER 1

## INTRODUCTION

### 1.1 Overview

Shell structures have been in existence for many centuries. In ancient history, when most of the structures were made of stone or brick, people found that they could build a large span by designing structures with domed or arched shapes. The dome structures, such as roofs of temples, cathedrals, monuments, and the arch structures in ancient stone bridges are the earliest examples of the shell application in structural forms. Many notable historical examples of shell structures (Figure 1.1) include the Pantheon of ancient Rome, built around 2,000 years ago; the Hagia Sophia of Constantinople (now Istanbul), approximately 1,500 years old; St Paul's Cathedral in London, built approximately 300 years ago; and the Taj Mahal in India, built in the seventeenth century (Zingoni, 1997). Although the use of shell structures started centuries ago, the use of reinforced concrete (RC) shell structures began since the nineteenth century. Due to the high strength-to-weight ratio and the efficient load-carrying capacity, the RC shell structures have been used widely in a variety of modern engineering applications such as pressure vessels, water tanks, cooling towers, arch dams, roof domes, and containers (Ugural, 2009). RC shell structures can serve as roofs on large span structures such as the Sydney Opera House in Sydney, Australia (Figure 1.2a) and the TWA Flight Center at JFK Airport in New York City (Figure 1.2b). RC shell structures have many applications in the nuclear industry. A thin-walled hyperbolic concrete cooling tower and a cylindrical RC containment are RC shell structures in a nuclear power plant, as shown in Figure 1.3.

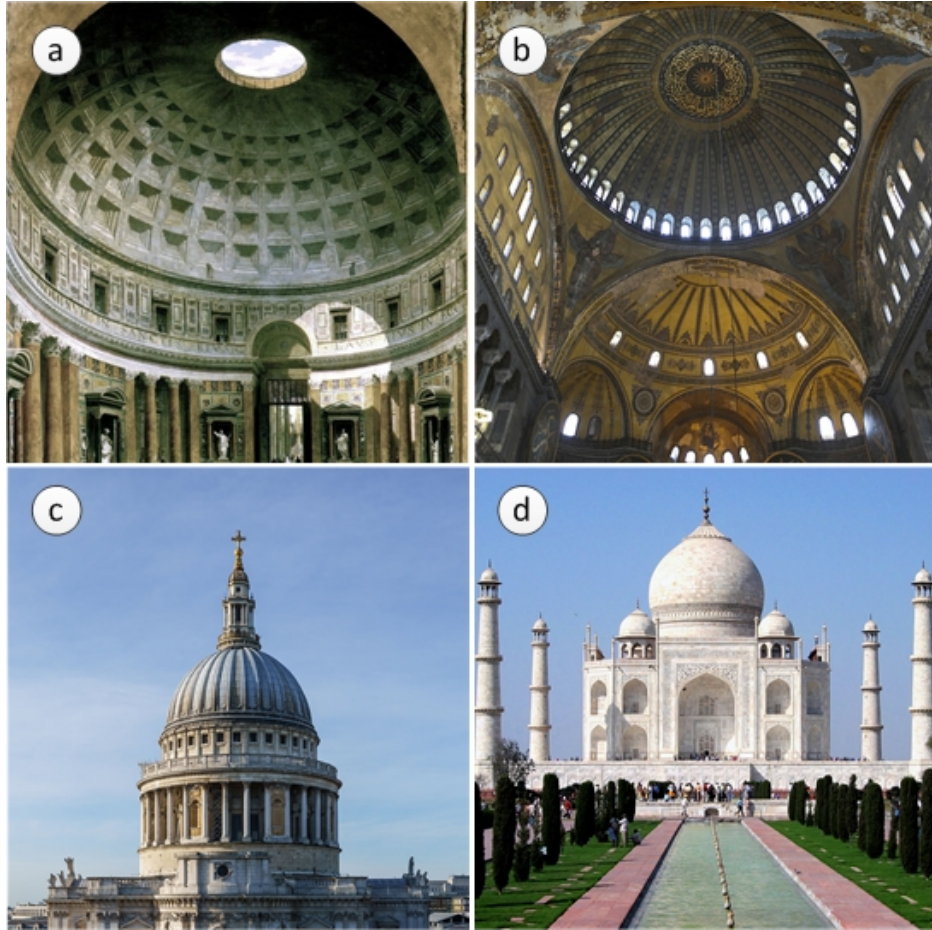


**Figure 1.1 Ancient shell structures: (a) Pantheon of ancient Rome ; (b) Hagia Sophia in Istanbul, Turkey; (c) St Paul's Cathedral in London, England; and (d) Taj Mahal in Agra, India**

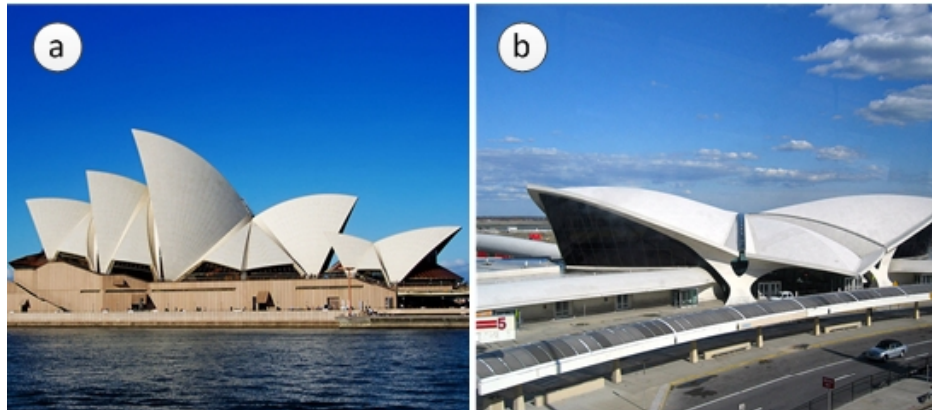


**Figure 1.2 Modern RC shell structures: (a) Sydney Opera House in Sydney, Australia; (b) JFK Airport in New York**

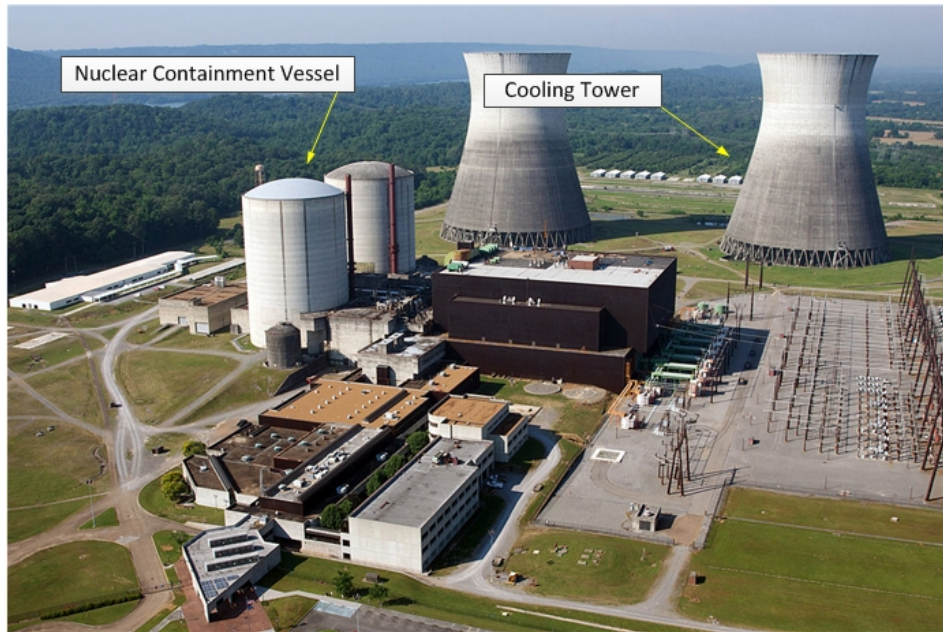


Figure 1.3 Modern RC shell structures in a nuclear power plant

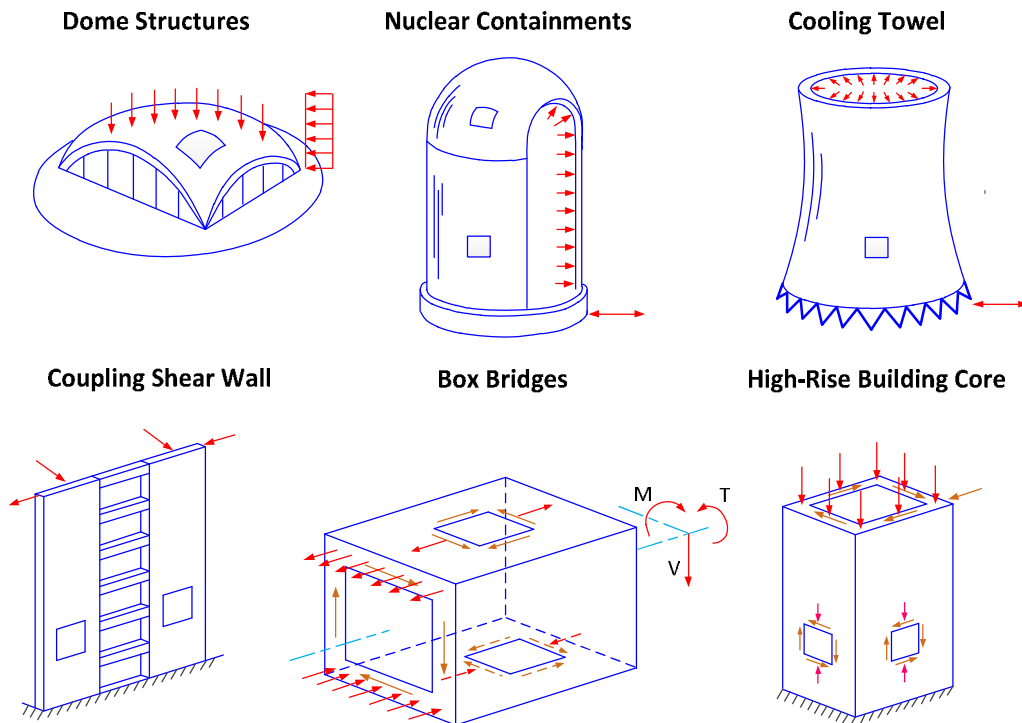


Figure 1.4 Examples of RC Shell Structures

Shell structures can have curved or flat configurations, in which their thickness is much smaller than other dimensions, as shown in Figure 1.4. The classical analysis of the shell structures includes two applied theories: the membrane theory and the bending theory. Similar to plates, the shell structures can carry lateral loads by developing two bending moments and a twisting moment. The shell structures also can carry compressive and tensile loads in their plane by developing membrane actions (Cook, 2002).

Compared to other types of shell structures, the structural behavior of RC shell structures is difficult to predict, especially when they are subjected to earthquake loading. The seismic response of RC shell structures is highly inelastic, which is caused by the highly nonlinear behavior of materials including the nonlinear constitutive relationships for both the reinforcement and concrete under reversed cyclic actions. However, from the structural point of view, a whole RC shell structure can be visualized as assemblies of many RC elements. This concept makes the analysis of this complex structure become easier in which the finite element analysis combined with the proper constitutive models for concrete and reinforcing steel serves as a powerful tool. The key to rational analysis of the RC structure is to understand the behavior of one element isolated from the structure. Once a rational model is developed to predict the behavior of one element, this rational model can be incorporated into a finite element program to predict the behavior of the whole structure under different kinds of loading.

Since the 1960s, finite element analysis program has been a popular analytical tool for the analysis of RC structures. With the recent advancements with the modern computer and the capability of the powerful computational techniques such as finite element, the inelastic behavior of RC shell structures can be stimulated under different kinds of

loading. A nonlinear finite element analysis of the RC shell structures can be achieved by the iterative solution algorithm until the solution is obtained with an acceptable tolerance. In most of nonlinear finite element programs, the analysis involves the classic procedures: (1) create finite element models such as nodes, elements, loads, and defining boundaries; (2) establish element stiffness matrix and assemble global stiffness matrix; (3) solve nonlinear equations using the iterative solution algorithm; and (4) record the results of analysis such as stress, strain, force, and displacement.

To explore the complex behavior of RC shell structures using the finite element method, the major objective of this research is to develop a finite element program based on the Cyclic Softening Membrane Model (CSMM) proposed by a research group at the University of Houston. This program is to accurately predict the inelastic behavior of the RC shell structures under seismic loadings. The research is conducted using the model-based simulation approach, which includes total four steps: modeling, implementation, validation, and application.

## **1.2 Research Background**

Since the 1970s, many researchers have proposed the analytical model to predict the behavior of RC shell structures using the finite element method, for example, Ahmad, Irons, and Zienkiewicz (1970), Hand, Pecknold, and Schnobrich (1972); Cervera, Hinton, and Hassan (1987); Hinton and Owen (1984); Scordelis and Chan (1987); Hu and Schnobrich (1991); Adebar and Collins (1994); Polak and Vecchio (1994); Yamamoto and Vecchio (2001); Kim, Lee, and Shin (2002); Song, Shim, Byun, and Maekawa (2002); Maekawa, Okamura, and Pimanmas (2003); Zhang, Bradford, and Gilbert (2007);

Lee (2011); and Xiang, Mo, and Hsu (2012). The main approach used by most researchers was to develop a reinforced concrete shell element by combining a rational constitutive model of reinforced concrete material into finite element formulations of a general shell element with layered approach. In the analysis of RC shell structures using finite element method, the main problems faced by most researchers are the expensive computational time due to the complicated material models and the difficulties encountered in the stability and accuracy of the solutions. Some material models for reinforced concrete material, such as fracture mechanics or detail crack localizations, were successfully verified at the element level but faced numerical problem when applying to the structure level that requires a large number of elements. Therefore, the selection of appropriate material models, which provides adequate accuracy with reasonable computational time, plays an important role in the success of the analysis of the RC shell structures using finite element method.

In recent years, the smeared-crack concept has been used widely in the analysis of RC structures. This concept allows internally cracked reinforced concrete composite to be treated as a simple, continuous material, rather than a complicated, discontinuous composite. The advantage of this simplification is that mechanics-based analysis can be applied to predict the behavior of the RC shell structures regardless of cracking. To implement this simplification, the material constitutive models must be based on the smeared (averaged) stress and strain relationship of the internally cracked RC elements. Since the 1980s, researchers have conducted studies on the constitutive material of reinforced concrete based on the smeared-crack concept; however, only a few research groups could carry out an experimental study of shell elements with special testing

equipment. Two famous systems for testing RC shell elements are the Shear Rig developed by Vecchio and Collins (1981a) at the University of Toronto and the Universal Panel Tester developed by Hsu, Belarbi, and Xiaobo (1995) at the University of Houston. Using the experimental results of the panel tests, many constitutive models for RC have been proposed. The models are the Compression-Field Theory and Modified Compression Field Theory by (Vecchio & Collins, 1981b, 1982); Disturbed Stress Field Theory by Vecchio (2000); Rotating-Angle Softened Truss Model (RA-STM) (Belarbi & Hsu, 1995; Pang & Hsu, 1995); Fixed-Angle Softened Truss Model (FA-STM) (Pang & Hsu, 1996a), the Softened Membrane Model (SMM) (Hsu & Zhu, 2002), and the Cyclic Softened Membrane Model (CSMM) (Mansour & Hsu, 2005). Among these constitutive models, the CSMM is the most versatile and accurate and is capable of rationally predicting the cyclic shear behavior of reinforced concrete membrane elements including the stiffness, ultimate strength, descending branch, ductility, and energy dissipation capacity.

Many commercial finite element programs are available for nonlinear analysis of shell structures, i.e. ABAQUS, ANSYS, SAP2000, etc. However, not many of them have good constitutive models for reinforced concrete, especially models that can account for shear failure. Consequently, they are not appropriate to be used to simulate the shear behavior of RC shell structures. Additionally, these commercial programs usually are not open source and impose limitations to users in developing their material constitutive models. In recent years, the Pacific Earthquake Engineering Research (PEER) Center in the University of California, Berkeley developed OpenSees, which is an open/free finite element framework using object-oriented languages (C++). OpenSees stands for Open

System for Earthquake Engineering Simulation (Fenves, 2001; OpenSees, 2013). OpenSees is an object-oriented framework for simulation applications in earthquake engineering using finite element methods. Key features of OpenSees include the interchangeability of components and the ability to integrate existing libraries and new components into the framework without the need to change the existing code. These features make it convenient to implement new classes of elements, materials, and other components. Many advanced finite element techniques that are suitable for the nonlinear finite element analysis have been implemented into OpenSees.

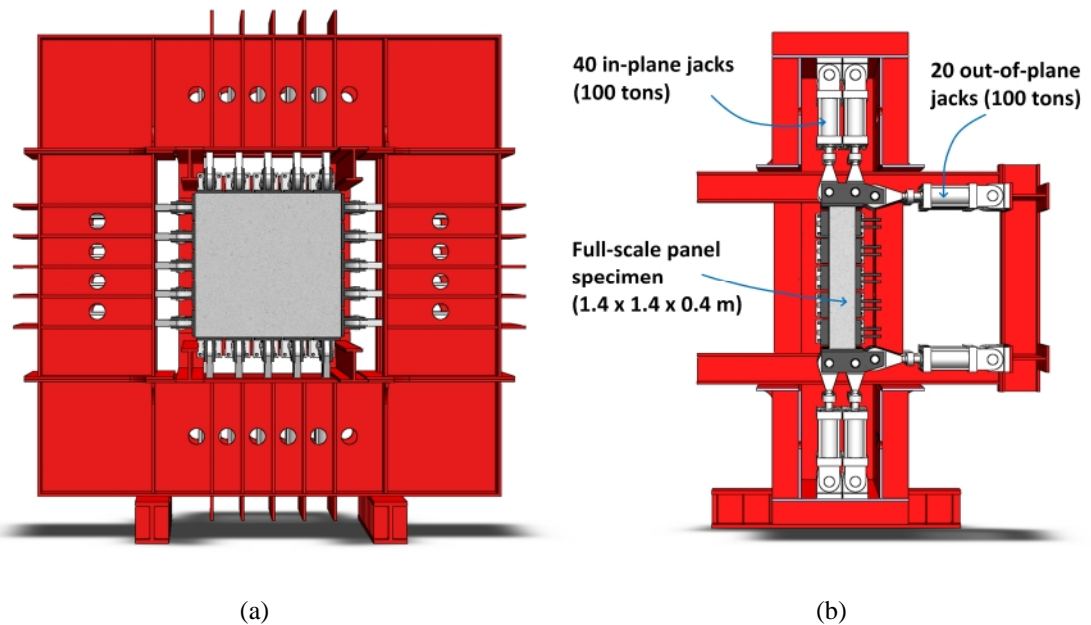


**Figure 1.5 Universal Panel Tester (1987 to present)**  
**(a) Front view; (b) Cross section.**

Over the past decades, researchers at the University of Houston have made significant contributions to the finite element analysis of reinforced concrete elements and members subjected to shear. Using the OpenSees framework, they developed a two-dimensional (2D) reinforced concrete element, the RCPlaneStress Quadrilateral element, which is based on the CSMM. The UH researchers implemented the element into the Simulation

of Concrete Structures (SCS), which is a nonlinear finite element computer program. SCS showed a significant capability of simulating the behavior of RC structures such as shear walls, bridges columns subjected to static, reversed cyclic, and dynamic loading.

Although, the SCS program with RCPlaneStress Quadrilateral element based on the CSMM is capable of accurately predicting behavior of concrete structures, it, however, cannot be used to model RC shell structures. Because the RC shell structures are three-dimensional (3D), problems with complex loading conditions while the RCPlaneStress Quadrilateral element can only be valid for 2D problems. Therefore, a new shell element based on CSMM needs to be developed, and this is a key step to verify the capacity of the CSMM for predicting 3D RC shell structures and to better understand the seismic behavior of the structures.

### **1.3 Objectives of Research**

The major objectives of this research are as follows:

- Develop a new shell element (named CSMMShellS8) based on the formulation of the degenerated shell theory with layered approach and taking into account the Cyclic Softened Membrane Model.
- Create a new finite element program (SCS-3D) with the developed shell element based on OpenSees framework to predict the nonlinear behavior of RC structures.
- Validate the developed finite element program SCS-3D with several large-scale tests of RC shell structures subjected to reserved cyclic loadings.
- This research is undertaken as part of an international collaboration project between the National Center for Research on Earthquake Engineering (NCREE)

and the University of Houston to investigate the inelastic behavior of RC nuclear containment vessels and two-story unsymmetrical RC building structures. The tests were performed at NCREE, and the design of the specimens and the study of the experimental results were performed at UH.

#### **1.4 Outlines of Dissertation**

To attain the objectives, several goals were accomplished through this research and will be addressed in this dissertation. A brief description of each chapter follows:

In Chapter 1, the overview, the applications of shell structures and the background in simulation of RC shell structures are briefly discussed. The objectives and outlines of the research are provided.

In Chapter 2, the literature review of the research is conducted. First, the background of the shell elements is presented. The previous work on simulation of RC shell structures using finite element analysis and the research on constitutive models for reinforced concrete are reviewed. The cyclic softening membrane model, which serves as the fundamental core of this research, is briefly discussed. The chapter ends by presenting the object-oriented finite element framework, OpenSees (Fenves, 2001), and summarizing the finite element analysis on 2D RC structures previously studied by research groups at UH.

In Chapter 3, the development of the CSMM-based shell element for nonlinear finite element analysis for RC shell structures is proposed. First, the FE formulation of an 8-node degenerated curved shell element with layer approach selected from the literature is summarized. Second, the FE formulation of the CSMM is extended from 2D to 3D so

that it can be implemented with the adopted curved shell element to form the CSMM-based shell element. The development of a finite element program SCS-3D based on the OpenSees framework is presented. Finally, the analysis procedures of the finite element program are described.

In Chapter 4, several correlation studies are reported that verify the accuracy of the CSMM-based curved shell element developed in the study. The structures selected for validations include a panel tested under pure shear (Mansour & Hsu, 2005a; Pang & Hsu, 1996b), panels tested under pure bending and combination of shear and bending (Polak & Vecchio, 1994), a 3D RC cylindrical tank (Maekawa et al., 2003), RC shear wall (Palermo & Vecchio, 2002), and six RC rectangular and circular hollow bridge piers (Yeh & Mo, 1999; Yeh, Mo, & Yang, 2001). The analytical results compared well with the experimental data.

In Chapter 5, tests and simulations are presented of two 1/13-scaled reinforced concrete nuclear containment vessel specimens subjected to reserved cyclic loadings. The tests were undertaken as part of an international collaboration project between National Center for Research on Earthquake Engineering (NCREE) and the University of Houston (UH). The tests were performed at NCREE, while the design of the specimens and the study of the experimental results were performed at UH. First, the test program is described including the test specimens, the test procedures, and the loading method. Then, the experimental behaviors of the specimens are investigated. Next, a nonlinear analyses of the nuclear containment vessel specimen are conducted by the finite element program SCS-3D using the proposed CSMM-based shell element, and the analytical results are compared with the test data.

In Chapter 6, tests and simulation are presented of a two-story reinforced concrete building specimen subjected to bi-directional reserved cyclic loadings. The specimen was designed and tested in 2005 by an international collaborated research collaboration between the UH and NCREE (Tseng, Hwang, Mo, Yeh, & Lee, 2009). However at that time, the response of the test specimen was not predicted due to lack of appropriate numerical tools. In this research, the test program is fully reinvestigated. Also, an analytical study of the two-story RC building specimen is conducted by the finite element program SCS-3D using the proposed CSMM-based shell element combined with the available beam-column element, which is available in OpenSees. Finally, the analytical results are compared with the test data.

Chapter 7 provides a summary of the work and presents suggestions for future research.

# **CHAPTER 2**

## **LITERATURE REVIEW**

### **2.1 Background of Shell Elements**

Shells are curved structures, whose thickness is much smaller than other dimensions. Examples of shell structures are pressure vessels, water tanks, cooling towers, arch dams, airplane wings, pipes, the exterior of rockets, missiles, automobile tires, incandescent lamps, cap, roof domes, factory or car sheds, and varieties of containers (Ugural, 2009). The analysis of a shell structure includes two applied theories: the membrane theory and the bending theory (Cook, 2002). Similar to plates, a shell structure can carry lateral loads by developing two bending moments and a twisting moment. A shell structure can also carry compressive and tensile loads in the plane of the shell by developing membrane actions.

#### **2.1.1 Types of Shell Elements**

Three types of shell elements exist: classical curved shell element, flat shell element, and degenerated shell element. A classical curved shell element is based on the classical shell theory. A well-known element of this shell type is the semi-Loof element derived by Irons (1976), as shown in Figure 2.1. The two types of nodes for this element are the corner and mid-side nodes and Loof nodes. Loof nodes are located at the Gauss points along the element side. The element has three global translational degree of freedoms at each of the corner and midside nodes and two rotational degree of freedoms at each Loof node (Javaherian, Dowling, & Lyons, 1980). As derived based on based on the classical

shell theory, this element has high accuracy. However, the element is not frequently used because it is complex and difficult to implement in a finite element program.

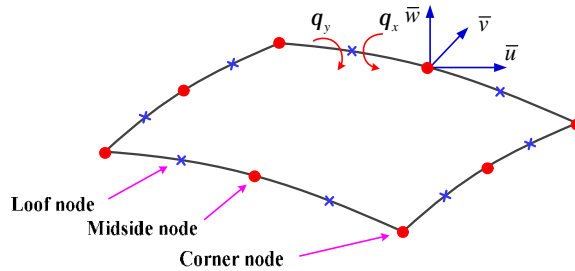


**Figure 2.1 A classical curved shell element (Javaherian et al., 1980)**

A flat element is based on a simple combination of a membrane element (plane stress) and a plate element (bending), as shown in Figure 2.2. This element has a lower accuracy than the other elements. When using this element for curved shell structures, in order to capture accurate behavior, a finer mesh is required. Furthermore, using a flat shell element usually results in a phenomenon that does not occur in the real continuously curved structure, the discontinuity bending moment (Hinton & Owen, 1984). Despite the shortcomings, the flat shell element has been widely used due to its simplicity of its formulation compared to the other elements. This element is easier to couple with edge beam and rib members and is more efficient in the case of non-curved structures.

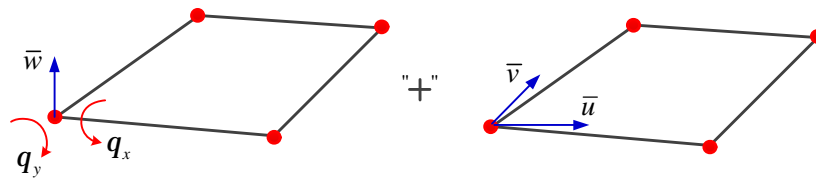


**Figure 2.2 A flat shell element (Cook, 2002)**

A degenerated shell element is derived from 3D equations of continuum mechanics, as shown in Figure 2.3 (Cook, 2002). The element includes sophisticated formulations,

which enable the modeling curvilinear shape of shell structures. The element has advantages that cannot be gained by the flat shell element, i.e. smaller number of elements can provide improved accuracy. The word degenerated indicates that the 3D stress and strain conditions are degenerated to the shell behavior. Many degenerated curved shell elements have been developed successfully for the nonlinear analysis of reinforced concrete shell structures (Hinton & Owen, 1984; Maekawa, Okamura, & Pimanmas, 2003; Polak & Vecchio, 1993). This element is more accurate than the flat shell element and less complicated than the classical curved shell element; therefore, a degenerated curved element is appropriate to use in a finite element program to predict the behavior of general shell structures.

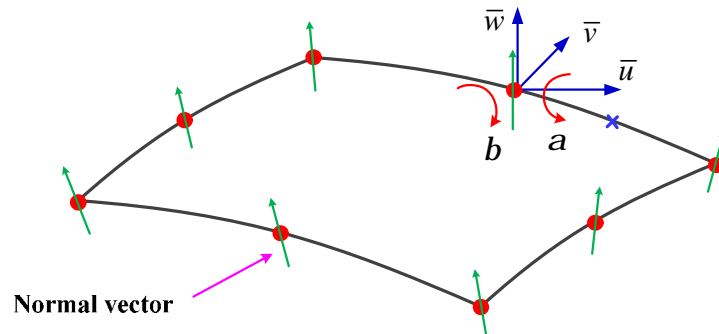


Figure 2.3 A degenerated shell element (Cook, 2002)

### 2.1.2 Thin Shell and Thick Shell

The classification of thin shell and thick shell is based on the significance of transverse shear deformations, which is similar to plate elements. In a thin shell element, the thickness is thin enough so that it can be assumed that the transverse shear deformations can be neglected (Zienkiewicz & Taylor, 2005). This shell element is usually derived based on the Kirchhoff theory and is classified as a C1 element, for which the first derivatives of deflection need to be continuous function. Many Kirchhoff

elements had been proposed to meet this requirement, for example, elements using higher-order shape function or elements based on mixed and hybrid formulation (Polak, 1992). For both plates and shells, Kirchhoff theory provides good results with span/radius-to-thickness ratio ( $a/d$ ) greater than 20 (Reddy, 2004). In a thick shell element, the transverse shear deformations exist throughout the element. This shell element is usually derived based on the Mindlin theory and is classified as a C0 element, in which one shape function can be assumed for displacements and rotations to satisfy the continuity condition. The Mindlin theory also can be applied to the thin shell element; however, shear locking usually occurs when the thickness is thin. To overcome shear locking, reduced or selective integration techniques often are used to calculate the stiffness matrix of the Mindlin element (Cook, 2002).

### **2.1.3 Degenerated Curved Shell Elements**

#### **2.1.3.1 Serendipity Element**

The Serendipity shell element has a total of eight nodes with five degrees of freedom (DOF) at each node, three translational DOFs, and two rotational DOFs, as shown in Figure 2.4a. Ahmad, Irons, and Zienkiewicz (1970) originally introduced the element for the linear analysis of thick and thin shells. The idea of creating this element arose from the difficulty of solving the ill-conditioned equations that occurred in the 3D solid element when the dimension in the thickness direction was small. The Serendipity shape function is applied to all DOFs. The element showed excellent performance when applied to the cases of moderate thick shell structures by using normal integration rule (3 x 3). However, the element became stiff when applied to the case of shells with a small thickness. This problem was regarded as a shear-locking phenomenon. To solve this

problem, a reduced integration technique was proposed in which the reduced integration rule (2 x 2) was used instead of the normal integration rule (3 x 3). This technique showed significant improvement on the results (Zienkiewicz, Taylor, & Too, 1971).

### 2.1.3.2 Lagrangian Element

The Lagrangian shell element has a total of nine nodes with five DOFs at each node, three translational DOFs, and two rotational DOFs. The Lagrangian shell element is similar to the Serendipity element except with an additional node at the middle of the element (Figure 2.4b). Thus, the Lagrangian shape function is applied to all DOFs instead of only the Serendipity shape function. This element exhibits good performance when applied to the cases of both thin and thick shell structures. When using reduced integration, the Lagrangian does not have the locking phenomenon, as does the Serendipity element. However, another problem of the Lagrangian is that it has spurious mechanisms, i.e. zero energy mode due to insufficiency of rank of the stiffness matrix (Hinton & Owen, 1984).

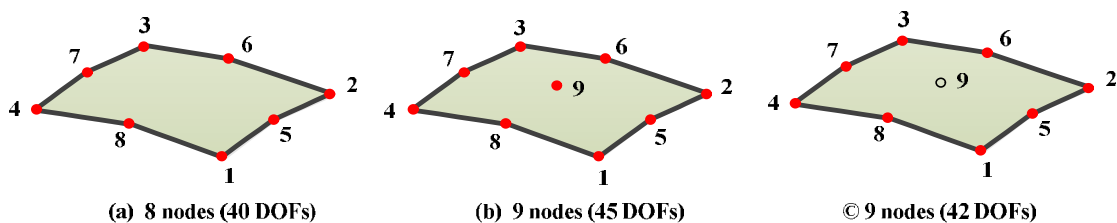


Figure 2.4 Types of degenerated shell element

### 2.1.3.3 Heterosis Element

The Heterosis element has a total of nine nodes, in which eight nodes have five DOFs and the middle node has only two rotational DOFs, as shown in Figure 2.4c. The Serendipity shape function is applied for all translational DOFs, and the Lagrangian shape function is applied for all rotational DOFs. Using this element with selective

integration completely overcomes the drawbacks of the two previous elements that are the locking phenomenon and spurious mechanisms (Hinton & Owen, 1984). However, the implementation of this element is quite complex when compared to the two previous elements because it needs to define the different number of DOFs at each node.

## **2.2 Previous Work on Simulation of RC Shell-type Structures**

Since the 1970s, many researchers have proposed the analytical model to predict the behavior of RC shell structures using the finite element method, for example, Hand, Pecknold, and Schnobrich (1972); Cervera, Hinton, and Hassan (1987); Hinton and Owen (1984); Scordelis and Chan (1987); Hu and Schnobrich (1991); Adebar and Collins (1994); Polak and Vecchio (1994); Yamamoto and Vecchio (2001); Kim, Lee, and Shin (2002); Song, Shim, Byun, and Maekawa (2002); Maekawa et al. (2003); Zhang, Bradford, and Gilbert (2007); and Xiang, Mo, and Hsu (2012). The main approach used by most researchers was to develop a reinforced concrete shell element by combining a rational constitutive model of reinforced concrete material into finite element formulations of a general shell element with layered approach. Details of the research on the simulation of RC shell structures using the finite element method conducted by some researchers are reviewed in the following sections.

### **2.2.1 Hand et al. (1972)**

Hand et al. (1972) conducted an early study of nonlinear finite element analysis of reinforced concrete plates and shells with layer approach. In this study, the authors derived a 20 degree-of-freedom shell element formulation for a shallow shell (Figure 2.5). Here, the word shadow represents that the shell is a medium thick or thin shell, and the dominant load-carrying mechanism is either bending or membrane action or a

combination of the two. For the materials used in the model, the steel reinforcement was assumed to be elastic plastic. The bilinear elastic, perfectly plastic model was used for concrete in compression; the elastic-brittle model with a limited tensile strength was used for concrete in tension. Furthermore, the yielding criterion proposed by Kupfer, Hilsdorf, and Rusch (1969) was applied to the concrete model. In addition, the torsional and shear stiffness of crack concrete that represents aggregate interlock and dowel action was accounted for by a shear retention factor. The study results showed that the layered approach (Figure 2.5), which allows the material properties to vary through the element depth, permits a coupling phenomenon between in-plane and transverse bending behaviors. The author found that the layered approach was more economical than a true-dimensional approach and provided as good or better results than a modified stiffness approach. This technique can also produce a whole load-deflection curve of a reinforced concrete plate or shell.

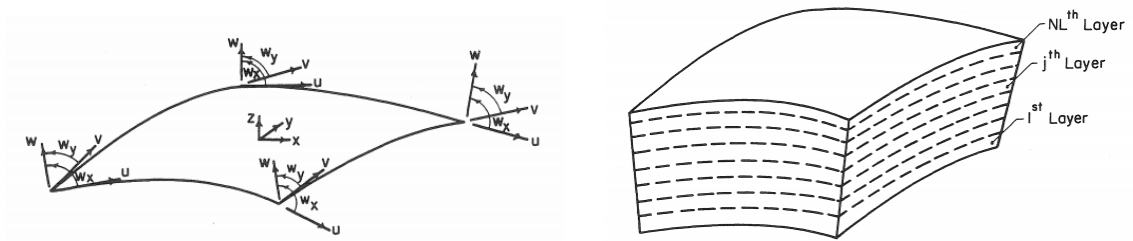


**Figure 2.5 20-DOF shell element with layer section (Hand et al., 1972)**

### **2.2.2 Cervera et al. (1987)**

Cervera et al. (1987) proposed to use a standard 3D computational model, a 20-node isoparametric element, as shown in Figure 2.6. Each set of reinforcing bars was assumed to be a 2D membrane layer of equivalent thickness and perfect bond between the reinforcement and the surrounding concrete. For modeling of uncracked concrete, the

authors employed a linear elasticity approach for elastic strains and a work-hardening plasticity approach for plastic strains. For modeling of cracked concrete, a smeared crack model was adopted in this work. The smeared crack model consists of a cracking criterion, a tension-stiffening rule, and a model for shear transfer. The authors proposed a 3D tensile failure envelope model to accommodate the triaxial response of cracked concrete.

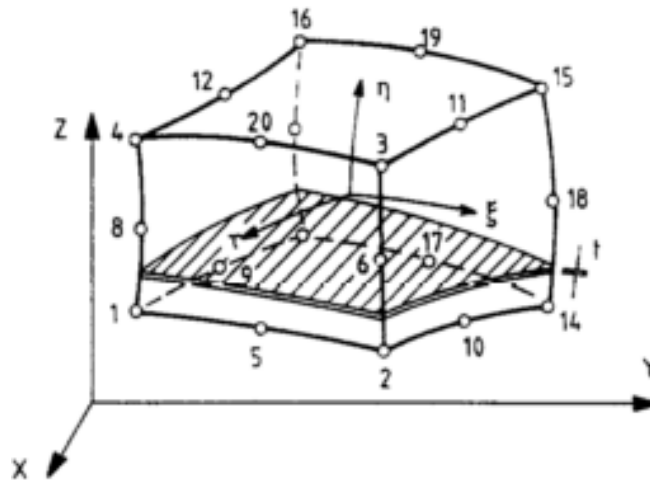


**Figure 2.6 Twenty-node isoparametric solid element with reinforcement**

For validation of the modeling technique, a series of panels tested by Collins and Vecchio (1982), a series of two slab-column specimens tested by Sunidja, Foutch, and Gamble (1982), and two deep beams tested by Ramakrishan and Anathanarayana (1968) were studied. Although good agreement between the analytical and experimental results were obtained in this research, many studies from the literature showed that using the 3D solid element is not a good option for shell structures because using a 3D solid element for shell structures usually leads to numerical problem due to large stiffness coefficients from strains in the shell thickness direction (Zienkiewicz & Taylor, 2005).

### 2.2.3 Scordelis and Chan (1987)

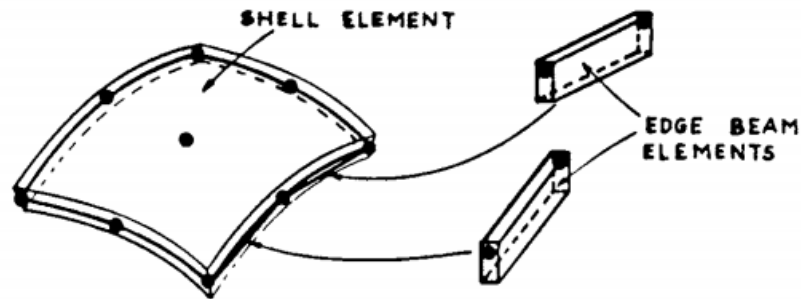


Figure 2.7 Curved RC shell element with edge beam

Scordelis and Chan (1987) conducted a research on nonlinear behavior of reinforced concrete shell structures with edge beams, as shown in Figure 2.7. The analysis includes effects of nonlinear material, nonlinear geometry, and the time-dependent effect of creep and shrinkage. For the shell element, an improved layer composite 9-node Lagrangian shell element was developed. For the material nonlinearities, the tension stiffening, the nonlinear response of concrete in compression and the yielding of reinforcement were considered. A biaxial orthotropic material with biaxial effect represented the nonlinear behavior of concrete. Shear resistance of concrete is assumed to be carried by shear interlock between cracks, represented by a shear retention factor  $B$ , where  $0 < B < 1$ . The steel reinforcement was assumed to be in a uniaxial stress state and is modeled as a bilinear material with strain hardening. The model was validated with 11 cylindrical reinforced concrete shells, simply supported at two ends, tested by Bouma et al. (1983). The researchers discovered that as each of the nonlinear factors was considered, a significant difference occurred in the calculated ultimate load.

#### 2.2.4 Hu and Schnobrich (1991)

Hu and Schnobrich (1991) proposed a new model for nonlinear finite element analysis of reinforced concrete plates and shells under monotonic loading. The model includes 9-node Lagrangian shell element with full and reduced integration. A new set of equations based on plasticity concept with yield surfaces and strain hardening was proposed to accommodate the nonlinear behavior of concrete in compression. For concrete in tension, the elastic brittle fracture model was used. Reinforcing steel was simulated as an equivalent uniaxial layered material located at the depth of the centerline of the bars and smeared out horizontally over the region of bar effect, as shown in Figure 2.8. The stress-strain curve of reinforcing steel was simulated by an idealized bilinear curve in both compression and tension. Using the 9-node Lagrangian shell element with reduced integration produced spurious energy modes. To overcome this problem, the authors proposed the techniques of using fully integrated elements alternately with reduced integrated elements. This zero energy modes could be suppressed by using an overlaid technique. In this technique, every nonlinear reduced integrated 9-node element was overlaid with an elastic 8-node element whose modulus of elasticity was of 10 to 3 times than that used for the nonlinear element.

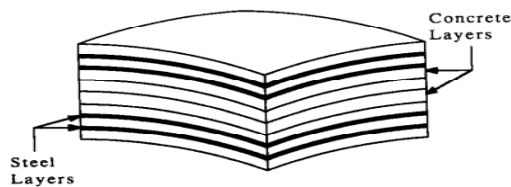


Figure 2.8 Layered model

### **2.2.5 Adebar and Collins (1994)**

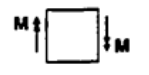
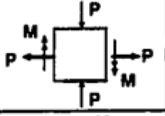
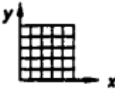
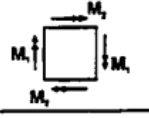
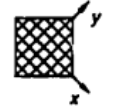
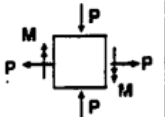
Adebar and Collins (1994) tested nine large-scale experiments under a combination of the membrane shear and the transverse shear. The experimental program focused on two factors: the directions of in-plane shear reinforcement and the principal membrane stress relative to that of the principal transverse (out-of-plane) shear stresses. From the test results, they observed that the out-of-plane shear capacity of the panels depended on the orientation of the in-plane reinforcement. In other words, membrane shear had an effect on the transverse shear response of concrete shell element. The interaction diagram between the applied transverse (out-of-plane) shear stress and the in-plane shear strength was first developed. Afterward, a program SHELL474 was developed to predict the behavior of the test specimens and the interaction curve. The program was based on the extension of the modified compression field theory from biaxial shear behavior to triaxial shear behavior.

### **2.2.6 Polak and Vecchio (1994)**

Polak and Vecchio (1994) developed a theoretical formulation for reinforced concrete shell elements and implemented in APECS, the finite element program. The authors thought that the degenerated shell element were the best among the shell element types that had been used to predict the behavior of shells with various shapes and various loading types applying on the shells. The constitutive laws for reinforced concrete adopted in the model were based on the Modified Compression Field Theory, which assumes that the directions of principal stresses and strains were coincident. The developed shell element was validated by the experimental result of four identical full-scale panels subjected to complex loading combinations. In-plane forces were observed

to be lowering the out-of-plane flexural strength of the tested shells. Agreement was obtained between the experimental and analytical response of the investigated structures under the conditions of in-plane load, bending, out-of-plane load, and load combinations.

Table 2.1 Parameters of Panel Tests by Polak (1992)

Name	Concrete $f'_c$ (MPa)	Reinforcement (same top & bottom)	X - Reinforcement		Y - Reinforcement		Loading	Loading Ratio
			$\rho_x$ per layer of steel	$f_y$	$\rho_y$ per layer of steel	$f_y$		
SM1	47		1.25%	425 MPa	0.42%	430 MPa		
SM2	62		1.25%	425 MPa	0.42%	430 MPa		$\frac{M}{P} = 0.25 \text{ m}$
SM3	56		1.25%	425 MPa	0.42%	430 MPa		$\frac{M_x}{M_y} = 3.2$
SM4	64		1.32%	425 MPa	0.44%	430 MPa		$\frac{M}{P} = 0.25 \text{ m}$

### 2.2.7 Kim et al. (2002)

Kim et al. (2002) implemented a new model in the FEAP program, which Taylor (2000) developed, to predict the nonlinear behavior of reinforced concrete shells. The model was composed of a 4-node quadrilateral flat-shell element with drilling rotational stiffness and layer approach. A set of constitutive models for reinforced concrete was proposed including tensile, compressive, and shear models of crack concrete. The constitutive models described the loading, unloading, and reloading paths. For the cracked concrete, the authors used separated constitutive laws in different directions. In the direction normal to the cracking plane, the authors used the model proposed by Shima, Chou, and Okamura (1987). The model related the stresses in concrete as the sum of the stresses from bond action, with the reinforcing bars and with the contact surface at

the crack plane. In the direction of the cracking plane, the authors used a modified elastoplastic fracture model developed by Okamura, Maekawa, and Izumo (1987). In the model, the degradation in compressive stiffness was illustrated by modifying the fracture parameter in terms of the strain perpendicular to the cracking plane. In the shear direction at the cracking plane, the authors also used the shear transfer model. The model was based on the Contact Surface Density Function developed by Li and Maekawa (1988), which takes into account the effect the shear stress transfer due to the aggregate interlock at the cracking surface. The proposed model had sufficient accuracy when compared with experimental specimens.

#### **2.2.8 Zhang et al. (2007)**

Zhang et al. (2007) developed a simple 4-node, 24-DOF layered quadrilateral flat plate/shell element for predicting the behavior of reinforced concrete slabs and cylindrical shell structures. The element was based on Kirchhoff's thin plate assumption that ignored the transverse shear deformations. The nonlinear finite element formulation considered both geometrical nonlinearity and material nonlinearity. The geometrical nonlinearity was applied to the large-displacement problem. The material nonlinearity took into account concrete cracking, tension stiffening, and biaxial compression of concrete as well as the yielding of steel reinforcement. For the material properties, the stress-strain curves for both concrete and steel reinforcement were assumed to be elastic perfectly plastic. The limit strain of 0.0035 was used to determine the crushing point of concrete. The model proposed by Cedolin and Dei Poli (1977) was used to simulate the shear behavior of cracked concrete that assumed the crack shear modulus function of the tensile strain. The two test specimens validated the proposed element. The first specimen

was flat reinforced concrete flat slabs tested by Macneal and Harder (1988). The second one was a shallow parabolic reinforced concrete arch tested by Wang, Bradford, and Gilbert (2005). The results demonstrated good correlations with the tests.

### **2.2.9 Xiang et al. (2012)**

Xiang et al. (2012) made an initial effort to develop a softened shell model based on CSMM and implemented into OpenSees. CSMM was applied to the in-plane component of the material stiffness matrix of a 4-node flat element. The model was shown to have good capacity of predicting in-plane behavior of shear walls, which are flat structures. No curved structures were used to validate the model. This element was not yet capable of predicting accurately the bending behavior of shell structures because it did not consider concrete layer and reinforcement layer separately. The gap in the study will be fulfilled by this research, in which a more accurate curved shell element will be developed and better improvement in the layered approach will be considered.

## **2.3 Research on Constitutive Model for RC**

To predict the behavior of RC shell structure, understanding the material behavior is important. Many researchers have developed different types of analytical models of reinforced concrete such as truss models, orthotropic models, nonlinear elastic models, plastic models, micro models, etc. The orthotropic model stands out both in accuracy and in efficiency as compared to the other models. Since the 1980s, orthotropic models have been developed to predict the shear behavior of reinforced concrete elements by many researchers, for example, Vecchio and Collins (1981a) (1982); Balakrishnan and Murray (1988a) (1988b) (1988c); Crisfield and Wills (1989); Izumo, Shin, Maekawa, and Okamura (1992); Shin, Maekawa, and Okamura (1992); Belarbi and Hsu (1995); Pang

and Hsu (1995) (1996b); Sittipunt and Wood (1995); Hsu and Zhang (1997); Ayoub and Filippou (1998); Kaufmann and Marti (1998); Vecchio (2000) (2001); Ile and Reynouard (2000); Belletti, Cerioni, and Iori (2001); Hsu and Zhu (2002); Kwon and Spacone (2002); Palermo and Vecchio (2003); Mansour and Hsu (2005a) (2005b).

Over the past 20 years, research groups at UH have carried out extensive experimental and analytical studies on the behavior of reinforced concrete. A series of four analytical models were established to predict the nonlinear shear behavior of reinforced concrete membrane elements. The models are the RA-STM by Hsu (1993), Belarbi and Hsu (1995), and Pang and Hsu (1995); the FA-STM by Pang and Hsu (1996b) and Hsu and Zhang (1997); the SMM by Hsu and Zhu (2002); and the CSMM by Mansour and Hsu (2005a) (2005b). All four models are rational because they satisfy Navier's three principles of mechanics of materials: the stress equilibrium, the strain compatibility, and the constitutive relationships of materials. Among these constitutive models, the Cyclic Softened Membrane Model (CSMM) is the most versatile and accurate. CSMM is capable of rationally predicting the cyclic shear behavior of reinforced concrete membrane elements including the stiffness, ultimate strength, descending branch, ductility, and energy dissipation. In this research, the CSMM is employed and implemented into the finite element analysis program to predict the behavior of reinforced concrete structures.

## **2.4 Previous Analytical Models Developed by the Research Group at UH**

Four analytical models have been developed in the past for predicting the nonlinear shear behavior of reinforced concrete membrane elements. These models are the Rotating-Angle Softened Truss Model (RA-STM) (Belarbi & Hsu, 1995; Pang & Hsu,

1995), Fixed-Angle Softened Truss Model (FA-STM) (Pang & Hsu, 1996a), the Softened Membrane Model (SMM) (Hsu & Zhu, 2002), and the Cyclic Softened Membrane Model (CSMM) (Mansour & Hsu, 2005). They all satisfy Navier's three principles of mechanics of materials and, thus, are rational.

The first model was the Rotating-Angle Softened Truss Model (RA-STM) (Belarbi & Hsu, 1995; Pang & Hsu, 1995), which assumed the cracks to be oriented along the principal tensile strain direction. Compared with the model developed earlier in Toronto, Compression Field Theory (CFT) (Vecchio & Collins, 1981b), the RA-STM had two improvements: (1) The tensile stress of concrete was taken into account so that the deformations could be correctly predicted, and (2) The average stress-strain curve of the steel bars embedded in concrete was derived on the smeared crack level so that it could be correctly used in the equilibrium and compatibility equations, which are based on continuous materials.

The second model was the Fixed-Angle Softened Truss Model (FA-STM) (Hsu & Zhang, 1997; Pang & Hsu, 1996b), which assumed the cracks to be oriented along the applied principal tensile stress direction. A complicated constitutive relationship of concrete in shear was used to account for the shear stresses in the concrete struts along the cracks. Although more complex than the RA-STM, the FA-STM was capable of predicting the concrete contribution ( $V_c$ ). Zhu, Hsu, and Lee (2001) derived a rational shear modulus and produced a new solution algorithm of FA-STM that was as simple as when compared to that of the RA-STM.

The third model was the Softened Membrane Model (SMM) developed by (Hsu and Zhu (2002)) to predict the shear behavior of reinforced concrete membrane elements. The

SMM model could predict the post-peak branches of the shear stress versus shear strain curves by considering the Poisson effect of cracked concrete which was characterized by Hsu/Zhu ratios (Zhu & Hsu, 2002). Similar to FA-STM, SMM model assumes that the cracks are oriented in the direction perpendicular to the applied principal tensile stress. This would result in concrete contribution ( $V_C$ ). Zhu et al. (2001) simplified the SMM model by developing a simple and rational shear modulus instead of the empirical constitutive relationships of concrete in shear.

The fourth model was the Cyclic Softened Membrane Model (CSMM), which Mansour and Hsu (2005b) developed to predict the reversed cyclic response of RC membrane elements, including the unloading and reloading stress-strain curves. The CSMM is an extension of SMM that incorporates the cyclic constitutive laws of concrete and steel bars in membrane elements (Mansour, Lee, & Hsu, 2001). CSMM is a smeared crack model in which the cracked reinforced concrete is treated as a continuous material. To relate the stresses and strains in equilibrium and compatibility equations, the material laws for concrete and steel should be developed based on smeared stresses and strains. The smeared models of concrete and mild steel bars have been established for monotonic and cyclic loading at the University of Houston (Belarbi & Hsu, 1994, 1995; Mansour & Hsu, 2005a, 2005b). The constitutive laws in the CSMM were found to accurately predict the hysteretic loops, the shear stiffness, the shear ductility, and the energy dissipation capacities of RC panels under cyclic shear.

These models are advantageous because they determine the overall behavior of the reinforced concrete elements without dealing with variables such as crack width and spacing and interface bond slip. The smeared crack models account for these variable

indirectly in the formulation of the smeared stress-strain curve for embedded steel bars. These models consider the effect of the Poisson ratio using Hsu/Zhu ratios. The Hsu/Zhu ratios are considered the same for both steel and concrete because SMM and CSMM treats cracked reinforced concrete as a continuous material. SMM and CSMM assume that the cracks in the reinforced concrete element are oriented in the direction of the applied principal compressive stress of the element and not the principal compressive stress of the concrete.

## 2.5 Cyclic Softened Membrane Model (CSMM)

### 2.5.1 Coordinate Systems

The in-plane element considered in this model and shown in Figure 2.9 is reinforced by two layers of orthogonal steel grids oriented at a given angle to the principal stress direction. Two reference Cartesian coordinates are used in the formulation. The first reference Cartesian  $\mathbf{l}$ - $t$  coordinate system represents the longitudinal and transverse steel bar directions. The second reference Cartesian 1-2 coordinate system represents the direction of the principal stresses. For the computational purposes, it is assumed that the steel bars are uniformly distributed in the  $\mathbf{l}$ - and  $t$ - directions and that the membrane element is of uniform thickness. The principal applied stresses acting on the four boundary edges of the element are assumed to be uniformly distributed.

Stresses and strains of different coordinate systems can be related to each other by using the transformation matrix  $[T(\mathbf{a})]$  given in Eq. (2.1)

$$[T(\mathbf{a})] = \begin{bmatrix} c^2 & s^2 & 2sc \\ s^2 & c^2 & -2sc \\ -sc & sc & c^2 - s^2 \end{bmatrix}. \quad (2.1)$$

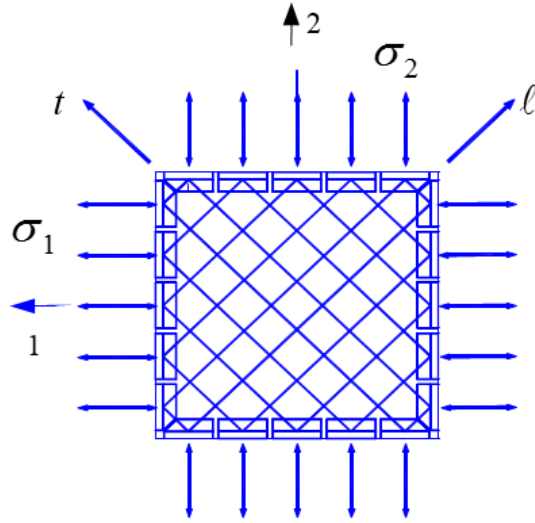


Figure 2.9 A typical reinforced concrete panel (Hsu & Mo, 2010)

### 2.5.2 Equilibrium Equations

The stress states of the element are shown in Figure 2.10. The stresses of the element are assumed to be a combination of two components: concrete and embedded reinforcement. The equilibrium equations, which relate the applied stresses of the element  $(s_x, s_y, t_{xy})$  to the internal principal stresses of concrete  $(s_1^c, s_2^c, t_{12}^c)$ , embedded reinforcement stresses ( $f_1$  and  $f_t$ ) are expressed as

$$s_1 = s_2^c \cos^2 a_2 + s_1^c \sin^2 a_2 + t_{12}^c 2 \sin a_2 \cos a_2 + r_1 f_1, \quad (2.2)$$

$$s_t = s_2^c \sin^2 a_2 + s_1^c \cos^2 a_2 - t_{12}^c 2 \sin a_2 \cos a_2 + r_t f_t, \text{ and} \quad (2.3)$$

$$t_{1t} = (s_2^c - s_1^c) \sin a_2 \cos a_2 + t_{12}^c (\sin^2 a_2 - \cos^2 a_2), \quad (2.4)$$

where  $r_1$  and  $r_t$  are the ratios of rebar in  $i^{\text{th}}$  direction, and  $a_2$  is the fixed angle that is defined from the  $\mathbf{1}$ - $t$  coordinate to the 1-2 coordinate.

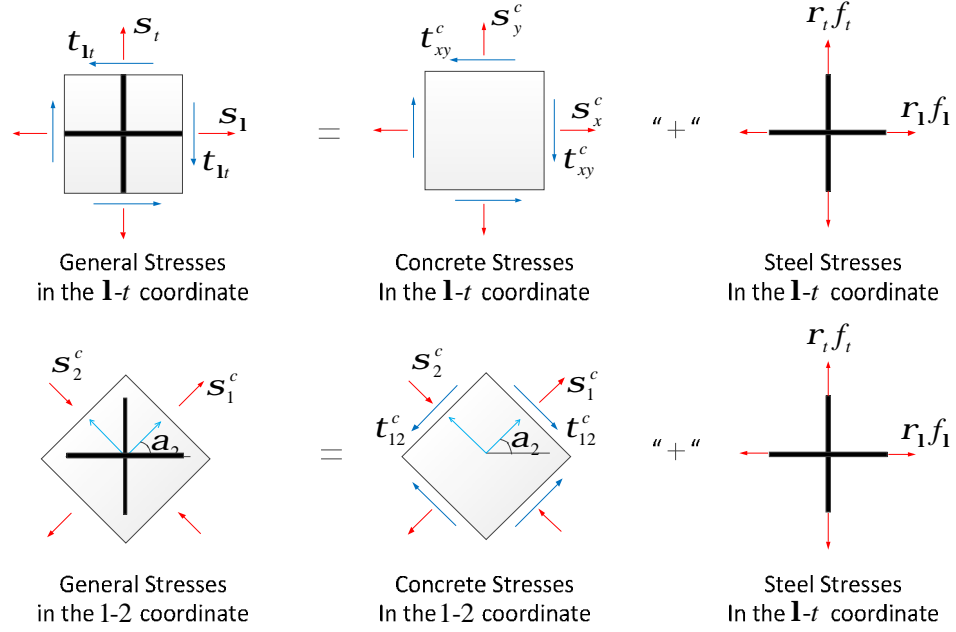


Figure 2.10 Stress states of the 2D panel

In terms of matrix form, Eq. (2.2) through Eq. (2.4) can also be written as

$$\begin{Bmatrix} s_1 \\ s_t \\ t_{1t} \end{Bmatrix} = [T(-a_2)] \begin{Bmatrix} s_1^c \\ s_2^c \\ t_{12}^c \end{Bmatrix} + [T(0^\circ)] \begin{Bmatrix} r_1 f_1 \\ 0 \\ 0 \end{Bmatrix} + [T(-90^\circ)] \begin{Bmatrix} r_t f_t \\ 0 \\ 0 \end{Bmatrix}, \quad (2.5)$$

where  $[T(-a_2)]$  is the transformation matrix from the 1-2 coordinate to the  $\mathbf{1-t}$  coordinate.

### 2.5.3 Compatibility Equations

The compatibility equations, which represent the relationships between the steel strains ( $e_1$ ,  $e_t$  and  $g_{1t}$ ) in the  $\mathbf{1-t}$  coordinate of the reinforcement and the concrete strains ( $e_1$ ,  $e_2$  and  $g_{12}$ ) in the 1-2 coordinate of the principal applied stresses, are defined by the following compatibility equations:

$$e_1 = e_2 \cos^2 a_2 + e_t \sin^2 a_2 + \frac{g_{12}}{2} 2 \sin a_2 \cos a_2, \quad (2.6)$$

$$e_t = e_2 \sin^2 a_2 + e_1 \cos^2 a_2 - \frac{g_{12}}{2} 2 \sin a_2 \cos a_2, \text{ and} \quad (2.7)$$

$$\frac{g_{1r}}{2} = (e_2 - e_1) \sin a_2 \cos a_2 + \frac{g_{12}}{2} (\sin^2 a_2 - \cos^2 a_2). \quad (2.8)$$

In terms of the matrix form, Eq. (2.6) through Eq. (2.8) also can be written as

$$\begin{Bmatrix} e_1 \\ e_r \\ \frac{1}{2}g_{1r} \end{Bmatrix} = [T(-a_2)] \begin{Bmatrix} e_1 \\ e_2 \\ \frac{1}{2}g_{12} \end{Bmatrix}, \quad (2.9)$$

where  $e_1$ ,  $e_2$ ,  $e_1$ , and  $e_r$  are the biaxial strains, taking into account the Hsu/Zhu ratios of cracked reinforced concrete (Zhu and Hsu, 2002).

#### 2.5.4 Relationship between Biaxial Strains and Uniaxial Strains

To solve the problems in the 2D equilibrium and compatibility equations, the biaxial strains need to be converted to uniaxial strains so that the uniaxial constitutive material models tested in laboratory can be used. For cracked concrete, the uniaxial strains ( $\bar{e}_1, \bar{e}_2, \bar{e}_1$ , and  $\bar{e}_r$ ) are related to the biaxial strains ( $e_1, e_2$ , and  $g_{12}$ ) by using a set of four equations has been derived (Hsu and Zhu, 2002) as shown in Eq. (2.10) through Eq. (2.13). Once the uniaxial strains,  $\bar{e}_1, \bar{e}_2, \bar{e}_1$ , and  $\bar{e}_r$  are determined, the stresses  $s_1^c, s_2^c, t_{12}^c, f_1$ , and  $f_r$  in Eq. (2.5) can be calculated using the uniaxial constitutive relationships under cyclic loading by the following equations:

$$\bar{e}_1 = \frac{1}{1-n_{12}n_{21}} e_1 + \frac{n_{12}}{1-n_{12}n_{21}} e_2, \quad (2.10)$$

$$\bar{e}_2 = \frac{n_{21}}{1-n_{12}n_{21}} e_1 + \frac{1}{1-n_{12}n_{21}} e_2, \quad (2.11)$$

$$\bar{e}_1 = \bar{e}_2 \cos^2 a_2 + \bar{e}_1 \sin^2 a_2 + \frac{g_{12}}{2} 2 \sin a_2 \cos a_2, \text{ and} \quad (2.12)$$

$$\bar{e}_r = \bar{e}_2 \sin^2 a_2 + \bar{e}_1 \cos^2 a_2 - \frac{g_{12}}{2} 2 \sin a_2 \cos a_2. \quad (2.13)$$

In terms of the matrix form, Eq. (2.10) and Eq. (2.11) can also be written as

$$\begin{Bmatrix} \bar{e}_1 \\ \bar{e}_2 \\ 0.5g_{12} \end{Bmatrix} = [V_c] \begin{Bmatrix} e_1 \\ e_2 \\ 0.5g_{12} \end{Bmatrix}, \quad (2.14)$$

where  $[V_c]$  is defined as

$$[V_c] = \begin{bmatrix} (1 - \nu_{12}\nu_{21})^{-1} & \nu_{12}(1 - \nu_{12}\nu_{21})^{-1} & 0 \\ \nu_{21}(1 - \nu_{12}\nu_{21})^{-1} & (1 - \nu_{12}\nu_{21})^{-1} & 0 \\ 0 & 0 & 1 \end{bmatrix}. \quad (2.15)$$

In Eq. (2.15),  $\nu_{12}$  is the ratio of the resulting tensile strain increment in the principal 1-direction to the source compressive strain increment in the principal 2-direction, and  $\nu_{21}$  is the ratio of the resulting compressive strain increment in the principal 2-direction to the source tensile strain increment in the principal 1-direction. For the monotonic loading case, Zhu and Hsu (2002) found that the first ratio  $\nu_{12}$  increased with the increase of steel strain and became a constant 1.9 after yielding, and the second ratio was zero throughout the loading history. The following equation was suggested for the  $\nu_{12}$ :

$$\nu_{12} = 0.2 + 850e_{sf}, \quad e_{sf} \leq 0.002, \quad (2.16)$$

or 
$$\nu_{12} = 1.9, \quad e_{sf} > 0.002, \quad (2.17)$$

where  $e_{sf}$  is the strain of steel which yields first. For the reserve cyclic loading case, Mansour and Hsu (2005) concluded that the upper limit of the first ratio  $\nu_{12}$  need should be 1.0 to consider effect of opening and closing of cracks.

### 2.5.5 Constitutive Model of Concrete in Tension and Compression

The cyclic uniaxial constitutive relationships of cracked concrete in compression and tension are summarized in Figure 2.11. In the graph, the vertical axis represents the cyclic stress, with positive tensile stress above the origin and negative compressive stress below

the origin. The horizontal axis represents the cyclic uniaxial strain, with positive tensile strain to the right of origin and negative compressive strain to the left of origin. The tensile envelope stress–strain curves T1 and T2 are in the upper right quadrant. The compression envelope stress–strain curves C1 and C2 are in the lower left quadrant

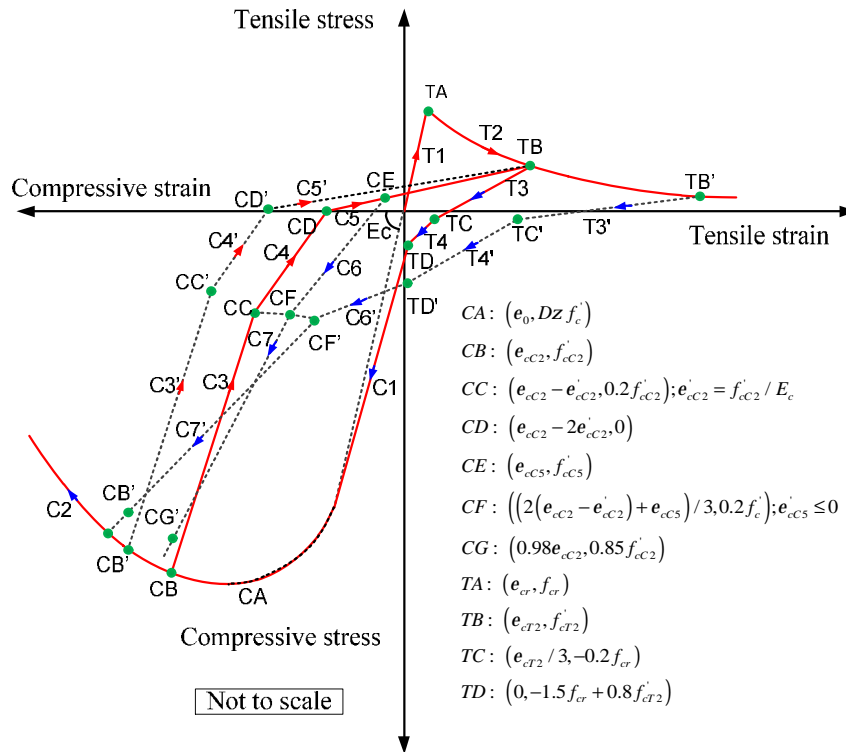


Figure 2.11 Cyclic stress-strain relationship of smeared concrete

These envelope curves for the cyclic stress-strain curves of concrete closely resemble the monotonic stress-strain curves of concrete developed by Belarbi and Hsu (1994, 1995) and by Hsu and Zhang (1996). The full curve of cyclic uniaxial constitutive relationships of concrete with embedded reinforcement were proposed by Mansour and Hsu (2005b). The characteristics of these concrete constitutive laws include: (1) the softening effect on the concrete in compression due to the tensile strain in the

perpendicular direction; (2) the softening effect on the concrete in compression under reversed cyclic loading; (3) the opening and closing of cracks, which are taken into account in the unloading and reloading stages. The unloading and reloading curves are represented by the series of straight lines C3-C7 in the compressive strain regions, and T3, T4 in the tensile strain region. Each straight line connects two points with their coordinates specified in the lower right quadrant. The equations of this model are summarized as follows:

Concrete in compression

$$s^c = Dz f'_c \left[ 2 \left( \frac{\bar{e}}{ze_0} \right) - \left( \frac{\bar{e}}{ze_0} \right)^2 \right], \quad 0 \leq |\bar{e}| \leq |ze_0|, \quad (2.18)$$

$$s^c = Dz f'_c \left[ 1 - \left( \frac{\bar{e}/e_0 - 1}{4/z - 1} \right)^2 \right], \quad |\bar{e}| > |ze_0|, \quad (2.19)$$

$$z = \left( \frac{5.8}{\sqrt{f'_c}(\text{MPa})} \right) \left( \frac{1}{\sqrt{1 + 400\bar{e}_T}} \right) \left( 1 - \frac{|b|}{24^\circ} \right) \leq 0.9, \quad (2.20)$$

$$b = \frac{1}{2} \tan^{-1} \left[ \frac{g_{12}}{e_2 - e_1} \right], \text{ and} \quad (2.21)$$

$$D = 1 - 0.4 \frac{e'_c}{e_0} \leq 1.0. \quad (2.22)$$

Concrete in tension

$$s^c = E_c \bar{e}, \quad \text{for } 0 \leq \bar{e} < e_{cr}, \text{ with } e_{cr} = 0.00008 \text{ mm/mm}, \quad (2.23)$$

$$s^c = f_{cr} \left( \frac{e_{cr}}{\bar{e}} \right)^{0.4}, \quad \text{for } \bar{e} > e_{cr}, \text{ with } f_{cr} = 0.31 \sqrt{f'_c}(\text{MPa}). \quad (2.24)$$

Unloading and reloading

$$s^c = s_i^c + E_{cc} (\bar{e}_i - \bar{e}), \text{ and} \quad (2.25)$$

$$E_{cc} = \frac{S_i^c - S_{i+1}^c}{\bar{e}_i - \bar{e}_{i+1}}. \quad (2.26)$$

### 2.5.6 Constitutive Model of Concrete in Shear

Zhu, Hsu, and Lee (2001) present the rational equation relating the shear stress of concrete ( $t_{12}^c$ ) and the shear strain ( $g_{12}$ ) in the 1-2 coordinate system as follow:

$$t_{12}^c = \frac{S_1^c - S_2^c}{2(e_1 - e_2)} g_{12}, \quad (2.27)$$

where  $S_1^c$  and  $S_2^c$  are the smeared (average) concrete stresses and  $e_1$  and  $e_2$  are the biaxial smeared strains in the 1- and 2-directions of the principal applied stresses, respectively.

### 2.5.7 Constitutive Model of Embedded Reinforcement

The uniaxial cyclic constitutive relationships of reinforcing steel bars embedded in concrete in compression and tension (Mansour & Hsu, 2005b) are summarized in Figure 2.12. The solid curves represent the smeared stress–strain curves of steel bars; the dotted curves are the monotonic stress–strain relationship of a bare bar. In the smeared stress–strain curves, stages 1T, 2T, 1C, and 2C are the envelope curves, and stages 3 and 4 are the unloading and reloading curves.

In Figure 2.12, the smeared yield stress of the embedded mild steel bars is lower than the yield stress of bare steel bars. The hardening ratio of the steel bars after yielding is calculated from the steel ratio, steel strength, and concrete strength. The unloading and reloading stress-strain curves of embedded steel bars take into account the Bauschinger effect. The equations of this model are summarized as follows:

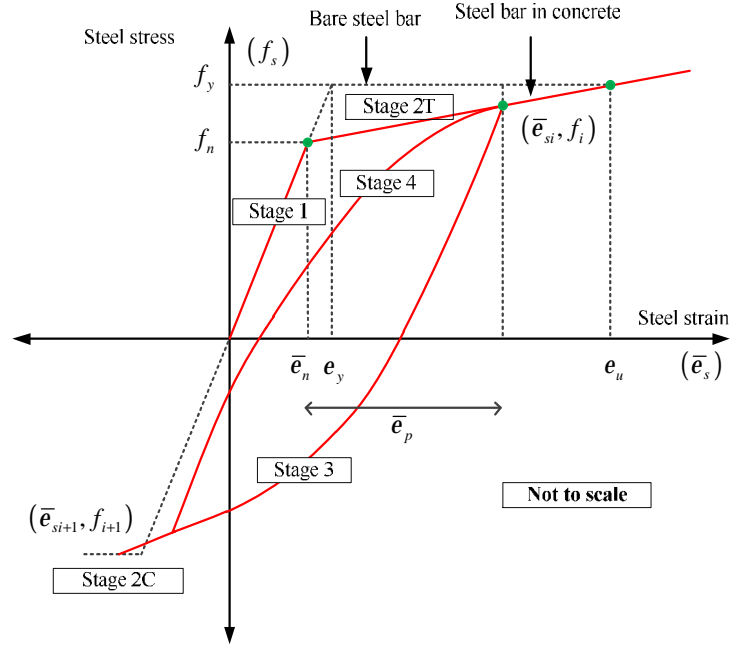


Figure 2.12 Cyclic stress-strain relationship of steel bar

Steel in tension

$$f_s = E_s \bar{e}_s, \quad \text{with } (\bar{e}_s \leq \bar{e}_n), \quad (2.28)$$

$$f_s = f_y \left[ (0.91 - 2B) + \left( 0.02 + 0.25B \frac{\bar{e}_s}{e_y} \right) \right], \quad \text{with } (\bar{e}_s > \bar{e}_n), \quad (2.29)$$

$$B = \frac{1}{r} \left( \frac{f_{cr}}{f_y} \right)^{1.5} \quad \text{with } r \geq 0.5\%, \quad \text{and} \quad (2.30)$$

$$\bar{e}_n = e_y (0.93 - 2B). \quad (2.31)$$

Steel in compression

$$f_s = E_s \bar{e}_s, \quad \text{with } (\bar{e}_s > -\bar{e}_n), \quad \text{and} \quad (2.32)$$

$$f_s = -f_y, \quad \text{with } (\bar{e}_s < -\bar{e}_n). \quad (2.33)$$

Unloading and reloading

$$\bar{e}_s - \bar{e}_{si} = \frac{f_s - f_i}{E_s} \left[ 1 + A^{-R} \left| \frac{f_s - f_i}{f_y} \right|^{R-1} \right], \quad \text{and} \quad (2.34)$$

$$A=1.9k_p^{-0.1}, R=10k_p^{-0.2}, \text{ and } k_p = \frac{\bar{e}_p}{e_n}. \quad (2.35)$$

When a steel bar embedded in concrete starts to yield at the cracks, the stresses in the steel bars between the cracks will be less than the yield stress at the cracks because part of the tensile force is resisted by the concrete. Using the smeared crack concept, the steel stresses are then averaged along the steel bar traversing several cracks. The resulting smeared (average) steel stress at first yield will be less than the local yield stress of a bare bar at the cracks. As shown in Figure 2.12, stage 2T, the smeared stress of the steel bar at initial yielding,  $f_n$ , is lower than the yield stress of the bare steel bars,  $f_y$ .

Hsu (1993) and Belarbi and Hsu (1994, 1995) showed that the difference between  $f_n$  and  $f_y$  depended on the parameter B, where  $B = (1/r)(f_{cr}/f_y)^{1.5}$ . Parameter B was derived to be a function of the three variables  $r$ ,  $f_{cr}$ , and  $f_y$ , which are related to the variables of crack width, crack spacing, and interface bond slip. For example, a decrease of steel ratio  $r$  will cause a decrease in the smeared yield stress  $f_n$  of mild steel bars and at the same time will cause a visual increase of crack widths and crack spacings. Parameter B is valid within the practical range of  $r$  from 0.25% to 5.24%, and  $f_c'$  up to 100 MPa as reported by Hsu and Zhu (2002).

## 2.6 OpenSees Framework

Many available commercial finite element programs are available for the nonlinear analysis of shell structures, i.e. ABAQUS, ANSYS, ADINA, etc. However, not many of them have good constitutive models for reinforced concrete, especially models that can

account for shear failure. These commercial programs usually are not open-source and, thus, put limitations on users in developing their material constitutive models. In recent years, the Pacific Earthquake Engineering Research (PEER) Center in the University of California, Berkeley developed an open/free finite element framework using object-oriented languages (C++), OpenSees (Open System for Earthquake Engineering Simulation) (OpenSees, 2013). OpenSees is an object-oriented framework for simulation applications in earthquake engineering using finite element methods. Key features of OpenSees include the interchangeability of components and the ability to integrate existing libraries and new components into the framework without the need to change the existing code. These features make it convenient to implement new classes of elements, materials, and other components. Many advanced finite element techniques that are suitable for the nonlinear finite element analysis have been implemented into OpenSees.

Under the OpenSees framework, each finite element analysis consists of four main types of objects: ModelBuilder object, Domain object, Analysis object, and Recorder object, as shown in the Figure 2.13. The ModelBuilder object constructs the nodes and masses on the nodes, creates the elements and materials of the elements, defines the loads acting on the nodes and the elements, and defines the constraints acting on the nodes. The ModelBuilder is responsible for building the objects in the model such as Node, Mass, Material, Element, LoadPattern, Constraint, etc. and adding them to the domain. After the ModelBuilder object creates the objects, they are stored in the Domain object. The Domain object also provides access of Analysis and Recorder objects to the objects in the Domain and holds the state of the model during the analysis procedure.

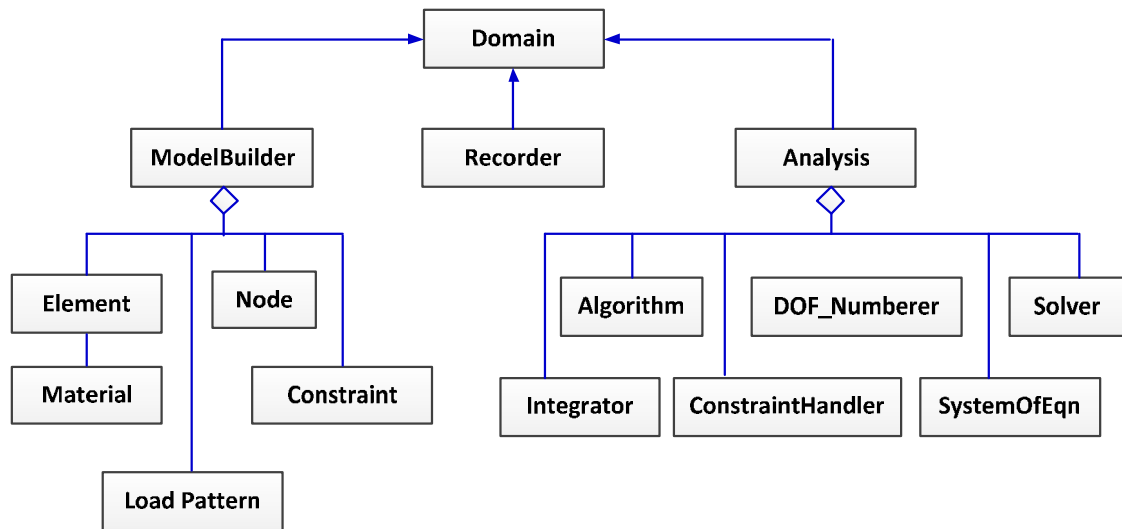


**Figure 2.13 Principal objects in OpenSees framework (Fenves, 2001)**

The analysis object performs the static or dynamic analysis on the model. The Analysis object includes objects such as the ConstraintHandler, Numberer, AnalysisModel, SolutionAlgorithm, Integrator, and SystemOfEquation. These objects define how the analysis is performed. The ConstraintHandler object defines the relationships between the degrees of freedom (DOF) of the nodes and determines the constraint equation in the analysis. The Numberer object is used to construct the DOF\_Numberer object, which determines the mapping between equation numbers and degrees-of-freedom. The AnalysisModel object comprises many FE\_Element objects and DOF\_Group objects. The SolutionAlgorithm object defines the solution algorithm that is used to solve the nonlinear equation. Currently, the SolutionAlgorithm objects in OpenSees include many methods such as the Linear, Newton-Raphson, Modified Newton-Raphson, Newton-Raphson with line search, Newton-Raphson with acceleration, and other algorithms. The Integrator object determines the predictive step and corrective step during the time  $(t+dt)$  in the analysis and specifies the tangent matrix and residual vector at any iteration. The type of Integrator is different for static analysis and dynamic

analysis. The Integrator objects for static analysis include load control, displacement control and arc-length control. The Integrator objects for dynamic analysis include the Newmark method, Wilson- $\theta$  method, Hilbert-Hughes-Taylor method, and other methods. The SystemOfEquation objects store and solve the system of equations in the analysis. The Recorder object monitors the state of domain components during an analysis, and write the state to a file or to a database.

Under this framework, if a new type of element or new material is to be introduced, a new corresponding class of objects can be added to the OpenSees according to the designated specification of the framework without changing the existing code. This is because the interface, which is defined in the core components (abstract classes), is minimal to make adding new component classes easier but large enough to ensure that everything is required can be accommodated (Fenves, 2005).

## **2.7 Previous FEA by Research Group at UH**

Over the past decades, researchers at the University of Houston have made significant contributions on the finite element analysis of RC elements and members subjected to shear. Using the OpenSees framework, the Cyclic Softened Membrane Model was implemented, and Zhong (2005) developed a nonlinear finite element computer program, the Simulation of Concrete Structures (SCS). A 2D reinforced concrete plane stress material module, the RCPlaneStress, and three uniaxial material modules of concrete and steel, ConcreteZ01, ConcreteZ02, and SteelZ01, were first implemented into SCS program, as shown in Figure 2.14. SCS became a powerful FE tool to simulate the behavior of reinforced concrete elements/members/structures subjected to static, reversed cyclic, and dynamic loading.

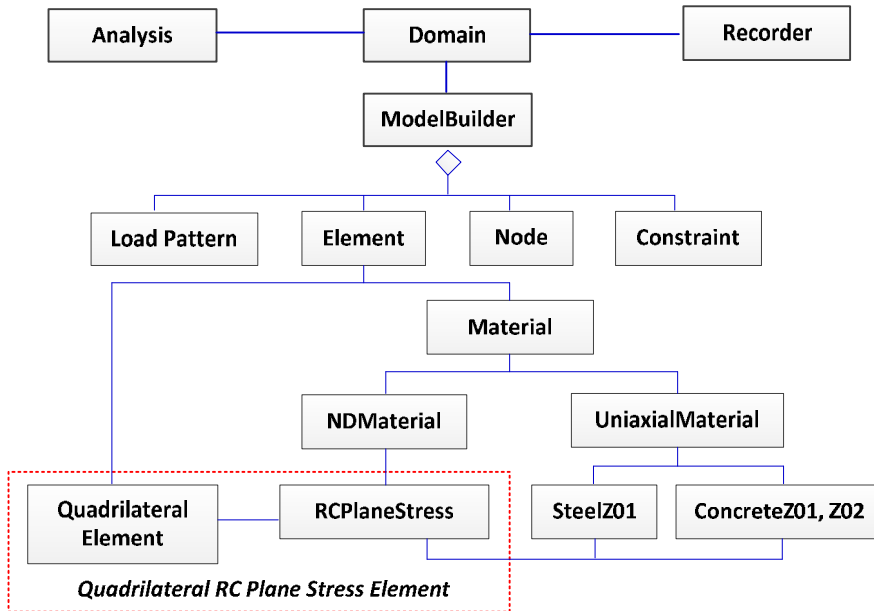


Figure 2.14 SCS program for RC (Zhong, 2005)

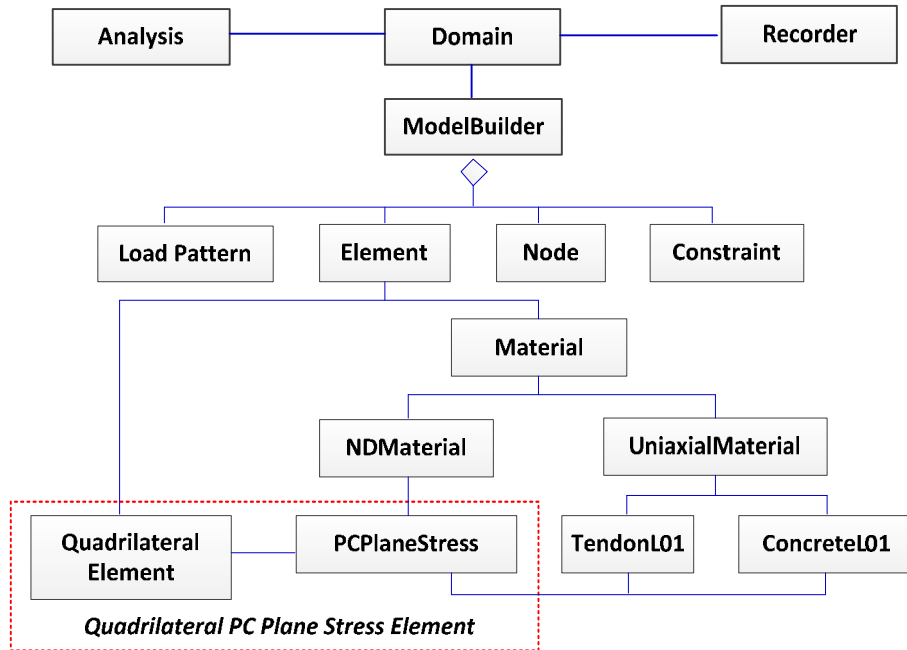


Figure 2.15 SCS program for PC (Laskar, 2009)

Laskar (2009) continued to implement a 2D prestressed concrete plane stress material module based on the CSMM-PC into the SCS program, as shown in Figure 2.15 (Wang,

2006). These were the PCPlaneStress and two uniaxial material modules of concrete and steel, the ConcreteL01 and the TendonL01. Since then, the SCS program has become a powerful, most advanced, analytical tool in simulating many prestressed concrete elements/members/structures subjected to static, reversed cyclic, and dynamic loading (Laskar, 2009; Laskar et al., 2010; Tadepalli et al., 2011; Labib et al., 2013).

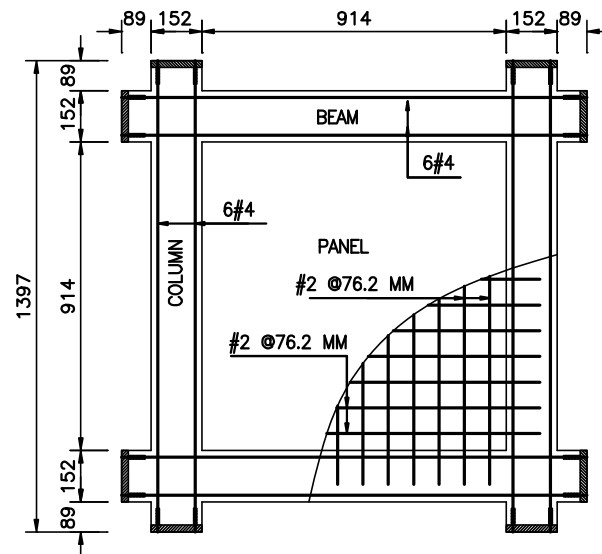


Figure 2.16 Detailing of shear walls (Gao, 1999)

An example of the simulation of RC structures using SCS program is shown in Figure 2.16 through Figure 2.19. Gao (1999) tested the two framed shear walls to evaluate the seismic performance of the shear walls under a constant axial load and reserved cyclic loading. The wall dimensions are 914.4 mm by 914.4 mm with a thickness of 76.2 mm. The cross section of the boundary columns is 152.4 mm square. The dimension and the reinforcement details of the specimens are illustrated in Figure 2.16. The bottom left and right corners of each specimen were supported by a hinge and a roller, respectively. The concrete strengths used in the two specimens are similar. Specimen SW13 has less

reinforcement ratio and lower axial load ratio than Specimen SW4. As observed from the test results, Specimen SW13 has ductile behavior and Specimen SW4 has brittle behavior.

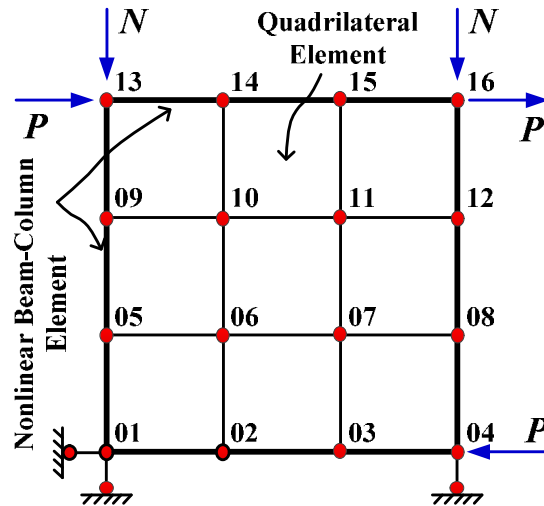
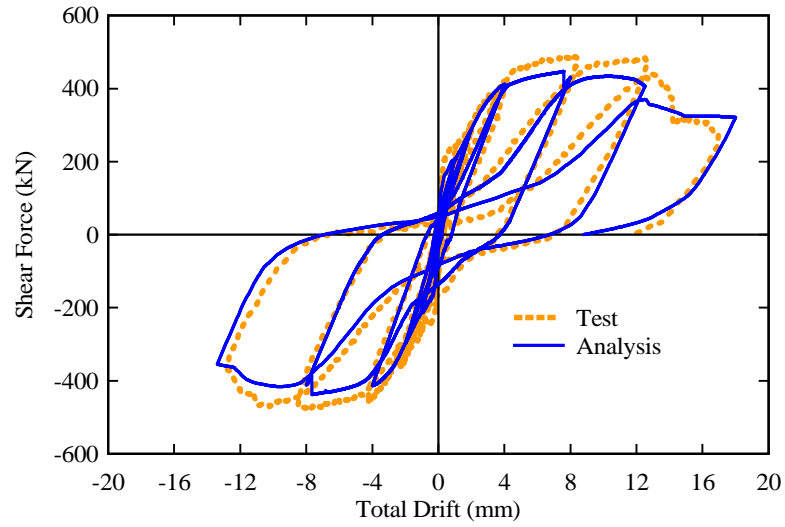


Figure 2.17 FEM modeling of 2D shear walls (Mo, Zhong, & Hsu, 2008)

Finite element analyses were conducted on the shear walls named SW4 and SW13 using the SCS program. The two specimens were modeled by the finite element mesh, as illustrated in Figure 2.17. The wall panels are simulated by RCPlaneStress quadrilateral elements, mentioned previously. The boundary columns and beams are simulated with NonlinearBeamColumn elements, which are available elements in OpenSees. The axial loads acting on the columns were applied as vertical nodal forces that remain constant in the analysis.

The comparison of the analytical result with test data of the shear force-drift relationship of the structures is illustrated in Figure 2.18 and Figure 2.19. The analytical result is shown to provide a good correlation with experimental data. The primary backbone curve, the initial stiffness, the yield point, the peak strength, the descending

branch, and the failure characteristics of the analytical results match closely with the experimental data.



**Figure 2.18 Validation of SCS with 2D RC wall (SW13)**

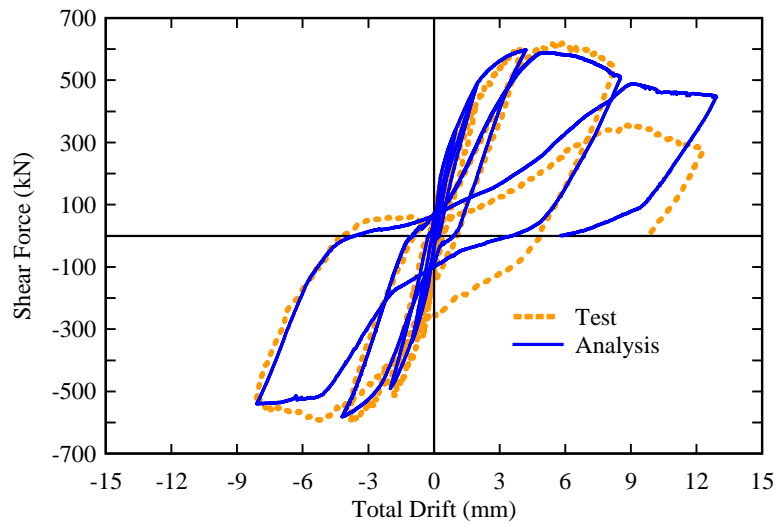


**Figure 2.19 Validation of SCS with 2D RC wall (SW4)**

# **CHAPTER 3**

## **CSMM-BASED SHELL ELEMENT**

### **3.1 Introduction**

This chapter presents the development of a finite element (FE) program to predict the nonlinear behavior of RC shell-type structures. In the FE program, a new shell element, so-called CSMM-based shell element, was developed by utilizing the formulation of the degenerated shell theory with layered approach (Cook, 2002; Hinton & Owen, 1984) , and taking into account the Cyclic Softened Membrane Model (Hsu & Mo, 2010). An analysis procedure was developed to perform nonlinear analyses of RC shell structures using the developed CSMM-based shell element. To develop the FEA program, the developed shell element and the proposed analysis procedure were implemented into a finite element program development framework, OpenSees, which was developed at University of California, Berkeley. Additionally, a visualization module was created for the post-processing of the finite element results.

### **3.2 Element Formulation**

As reviewed in Chapter 2, there are three types of shell elements: classical curved shell element, degenerated shell element, and flat shell element. The degenerated shell element with layered approach has been recognized as one of the most promising methods for analysis of RC curved shell structures since the 1970s (Ahmad, Irons, & Zienkiewicz, 1970; Bathe & Bolourchi, 1980; Cook, 2002; Hinton & Owen, 1984). By using the degenerated shell element with layered approach, the behavior of RC both curved and flat shell members can be captured directly from cyclic stress-strain relationships of the

materials and no phenomenological rule is needed (Hu & Schnobrich, 1991; Hughes & Liu, 1981). The element is based on Reissner-Mindlin theory, which only requires  $C_0$  continuity and can model the behavior of reinforced concrete shells with significant transverse shear deformation. The elements are derived from the equations of 3D continuum mechanics by reducing their dimensions in the thickness direction (Cook, 2002; Polak, 1998). The three types of the degenerated shell element are the 8-node Serendipity, 9-node Lagrangian, and 9-node Hysterisis elements. The 8-node Serendipity shell element is adopted for finite element analysis of reinforced concrete structures to implement into the FE program in this study because of its simplicity and accuracy when compared to the other shell elements. The formulation of the shell element is summarized in the following section.

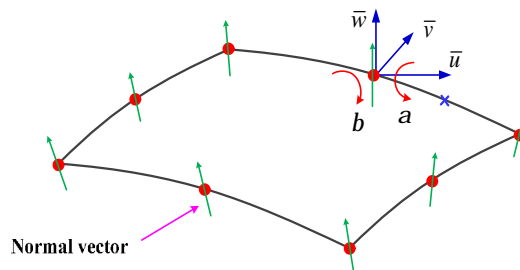


**Figure 3.1 Eight-node degenerated curved shell element**

Ahmad et al. (1970) originally introduced this element for the linear analysis of curved thick and thin shell structures. Since then, many researches have widely used this element for the nonlinear analysis of thick and thin shells (Bathe & Bolourchi, 1980; Hughes & Liu, 1981). The idea of creating this element evolved from the difficulty of solving the ill-conditioned equations that occurred in the 3D solid element when the dimension in the thickness direction was small. The 8-node Serendipity shell element has a total eight nodes with five DOFs at each node, three translational DOFs, and two rotational DOFs, as shown

in Figure 3.1. The Serendipity shape function is applied to all DOFs. The element showed excellent performances when applied to the cases of moderate thick shell structures by using the full integration rule (3 x 3). However, the element became stiff when applied to shell structures that had a small thickness. This problem is referred to as the locking phenomenon. The reduced integration technique proposed by Zienkiewicz, Taylor, and Too (1971) can be used to improvement the performance of the element.

### 3.2.1 Element Assumption

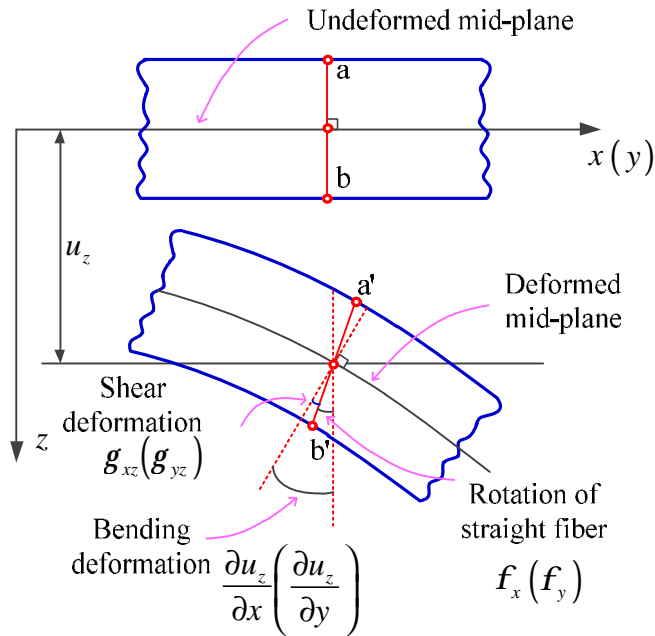


Figure 3.2 Mindlin theory assumption for the shell element

The derivation of the element is based on three assumptions. First, the stress normal to the mid-surface,  $S_z$ , is small when compared to the other stress components and may be negligible. The assumption implies that there is no deformation along the thickness of the element. The second assumption is that, after the element deformed, a straight fiber of the element, which was previously perpendicular to the undeformed middle surface, needs to remain straight but does not need to be perpendicular to the deformed middle surface. This

assumption is the same as the Mindlin theory assumption for plates. It means that the transverse shear strains  $g_{xz}$  and  $g_{yz}$  exist and are uniformly distributed in the thickness direction of the shell element, as shown in Figure 3.2. The third assumption is that the out-of-plane shear behavior is assumed to be independent of the in-plane behavior. This assumption allows CSMM to be implemented to the stiffness matrix of the shell element as a plane stress material.

### 3.2.2 Coordinate Systems

Four coordinate systems are used in the finite element formulation of the degenerated shell element. These coordinate systems include the global coordinate system  $(X, Y, Z)$ , the nodal coordinate system  $(V_{1i}, V_{2i}, V_{3i})$ , the curvilinear coordinate system  $(x, h, z)$ , and the local coordinate system  $(x, y, z)$ , as shown in Figure 3.3.

The global coordinate system or Cartesian coordinate system  $(X, Y, Z)$  is used to define global geometry, nodal coordinates, and nodal displacements of shell structures. The global stiffness matrices and applied force vectors are also determined based on this coordinate system.

The nodal coordinate system is specified by three vectors  $V_{1i}$ ,  $V_{2i}$ , and  $V_{3i}$  defined at the node  $i$  of the shell element. Vector  $V_{3i}$  is referred to as the normal vector and is perpendicular to the middle surface of the shell element. Vectors  $V_{1i}$  and  $V_{2i}$  are the tangent vectors and are perpendicular to vector  $V_{3i}$  and used to define directions of rotational DOFs at each node. While the users need to input vector  $V_{3i}$ , vectors  $V_{1i}$  and  $V_{2i}$  can be calculated based on the vector  $V_{3i}$  by using the following method: assume that the  $i$ ,  $j$ , and  $k$  are unit vectors corresponding to the  $X$ -axis,  $Y$ -axis, and  $Z$ -axis of the global coordinate system, respectively. The vector  $V_{1i}$  can be taken as the result of the cross product  $i \times V_{3i}$ . Because

the vector  $V_{2i}$  is perpendicular to both  $V_{1i}$  and  $V_{3i}$ , it results in  $V_{2i} = V_{1i} \times V_{3i}$ . In the finite element formulation, the unit vectors  $u_{1i}$ ,  $u_{2i}$ , and  $u_{3i}$  correspond to vectors  $V_{1i}$ ,  $V_{2i}$ , and  $V_{3i}$  are used more often. The cosine expressions of the nodal coordinate vectors are:

$$u_{1i} = \frac{V_{1i}}{|V_{1i}|} = \begin{Bmatrix} l_{1i} \\ m_{1i} \\ n_{1i} \end{Bmatrix}, \quad u_{2i} = \frac{V_{2i}}{|V_{2i}|} = \begin{Bmatrix} l_{2i} \\ m_{2i} \\ n_{2i} \end{Bmatrix}, \quad \text{and} \quad u_{3i} = \frac{V_{3i}}{|V_{3i}|} = \begin{Bmatrix} l_{3i} \\ m_{3i} \\ n_{3i} \end{Bmatrix}, \quad (3.1)$$

where  $(l_{1i}, m_{1i}, n_{1i})$ ,  $(l_{2i}, m_{2i}, n_{2i})$  and  $(l_{3i}, m_{3i}, n_{3i})$  are direction cosines of vectors  $u_{1i}$ ,  $u_{2i}$ , and  $u_{3i}$  corresponding to the global coordinate system, respectively.

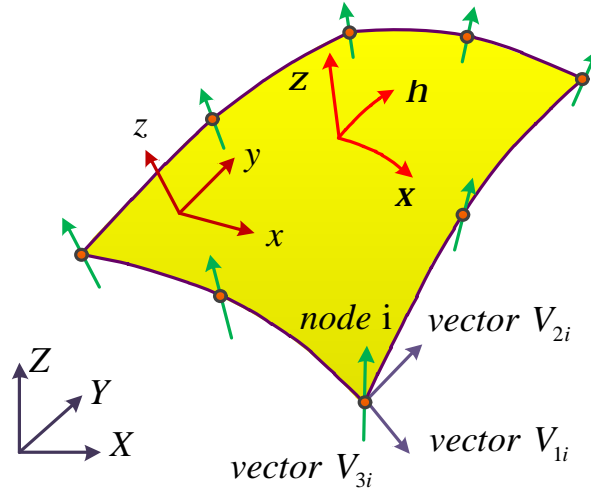


Figure 3.3 The 8-node Serendipity degenerated shell element

The shell element uses the isoparametric concept, in which one idealized element should be used to represent all the elements that have the same type. Integrations are performed on the idealized element. The results are converted to the original element by the Jacobian matrix. The idealized element is defined based on a normalized coordinate system, also known as the curvilinear coordinate system. In this system,  $x$  and  $h$  are two curvilinear coordinate in the middle plane and  $z$  is a linear coordinate in the thickness direction of

the shell element. It is assumed that  $x$ ,  $h$ , and  $z$  vary between -1 and +1 on the respective face of the shell element.

This local coordinate system  $(x, y, z)$  is defined at a sampling point (Gauss point) to represent local stresses and strains in each element. The stiffness matrix of each element usually is evaluated based on a local coordinate system and transformed to the global coordinate system. The unit vectors  $u_1, u_2, u_3$  corresponding to the  $x, y, z$  axis are established by shape function interpolation from the nodal vectors at all nodes of the shell element by the following equations:

$$u_1 = \sum N_i(x, h) \cdot u_{1i}, \quad u_2 = \sum N_i(x, h) \cdot u_{2i}, \quad \text{and} \quad u_3 = \sum N_i(x, h) \cdot u_{3i}, \quad (3.2)$$

where  $N_i$  is the shape function evaluated at the sampling point  $i$  (Cook, 2002).

### 3.2.3 Geometry

The global coordinate of an arbitrary point inside the shell element is determined by the global coordinates and the normal vectors are defined at each node of the element through the following equation:

$$\begin{Bmatrix} X \\ Y \\ Z \end{Bmatrix} = \sum N_i \begin{Bmatrix} X_i \\ Y_i \\ Z_i \end{Bmatrix} + \sum N_i z \frac{t_i}{2} \begin{Bmatrix} l_{3i} \\ m_{3i} \\ n_{3i} \end{Bmatrix}, \quad (3.3)$$

where  $t_i$  is the thickness at node  $i$  of the shell element, and  $l_{3i}$ ,  $m_{3i}$ , and  $n_{3i}$  are the direction cosines of the vector  $V_{3i}$  corresponding to the global coordinate system.

### 3.2.4 Displacements

The displacements of an arbitrary point inside the shell element are computed by the interpolation of the displacements and rotations of all nodes of the element using shape

functions. The displacements correspond to the global coordinate system and are expressed by the following equation:

$$\begin{Bmatrix} u_x \\ u_y \\ u_z \end{Bmatrix} = \sum N_i(x, h) \left( \begin{Bmatrix} u_{xi} \\ u_{yi} \\ u_{zi} \end{Bmatrix} + z \frac{t_i}{2} \begin{bmatrix} -l_{2i} & l_{1i} \\ -m_{2i} & m_{1i} \\ -n_{2i} & n_{1i} \end{bmatrix} \begin{Bmatrix} a_i \\ b_i \end{Bmatrix} \right), \quad (3.4)$$

where  $u_{xi}$ ,  $u_{yi}$ , and  $u_{zi}$  are the global displacements, and  $a_i$ , and  $b_i$  are rotations with respect to the nodal coordinates at the node  $i$  of the shell element, respectively, as shown in Figure 3.4. In terms of matrix forms, Eq. (3.4) can be written as

$$\left\{ u_{x,h,z} \right\}_{3 \times 1} = [N(x, h, z)]_{3 \times 40} \left\{ U^e \right\}_{40 \times 1}, \quad (3.5)$$

where  $\{U^e\}$  is the displacement vector of the shell element  $\{U^e\} = \{U_1^e \ U_2^e \ \dots \ U_n^e\}$  where  $\{U_i^e\} = \{u_{xi}, u_{yi}, u_{zi}, a_i, b_i\}$  is the displacement vector at each node of the shell element,  $n$  is the total number of nodes.

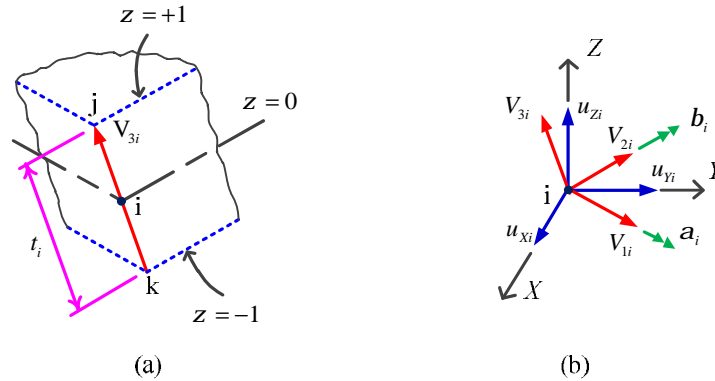


**Figure 3.4 (a) Typical node  $i$ , and thickness-direction vector  $V_{3i}$   
(b) Orthogonal vectors at node  $i$  and nodal DOF**

### 3.2.5 Strains

For a small displacement problem, the strains are taken as the first-order derivative of displacements. The strain-displacement relationship is expressed by the following equation

$$\begin{Bmatrix} \mathbf{e}_X \\ \mathbf{e}_Y \\ \mathbf{e}_Z \\ \mathbf{g}_{XY} \\ \mathbf{g}_{YZ} \\ \mathbf{g}_{XZ} \end{Bmatrix} = \begin{bmatrix} 1 & 0 & 0 & 0 & 0 & 0 & 0 & 0 & 0 \\ 0 & 0 & 0 & 0 & 1 & 0 & 0 & 0 & 0 \\ 0 & 0 & 0 & 0 & 0 & 0 & 0 & 0 & 1 \\ 0 & 1 & 0 & 1 & 0 & 0 & 0 & 0 & 0 \\ 0 & 0 & 0 & 0 & 0 & 1 & 0 & 1 & 0 \\ 0 & 0 & 1 & 0 & 0 & 0 & 1 & 0 & 0 \end{bmatrix} \begin{Bmatrix} \mathbf{u}_{X,X} \\ \mathbf{u}_{X,Y} \\ \mathbf{u}_{X,Z} \\ \mathbf{u}_{Y,X} \\ \mathbf{u}_{Y,Y} \\ \mathbf{u}_{Y,Z} \\ \mathbf{u}_{Z,X} \\ \mathbf{u}_{Z,Y} \\ \mathbf{u}_{Z,Z} \end{Bmatrix}. \quad (3.6)$$

In terms of matrix forms, Eq. (3.6) can be written as follow:

$$\left\{ \mathbf{e} \Big|_{X,Y,Z} \right\}_{6 \times 1} = [\mathbf{H}]_{6 \times 9} \left\{ \partial u \Big|_{X,Y,Z} \right\}_{9 \times 1}. \quad (3.7)$$

The displacements need to be transformed from the global coordinate system to the curvilinear coordinate system by the following equation:

$$\begin{Bmatrix} \mathbf{u}_{X,X} \\ \mathbf{u}_{X,Y} \\ \mathbf{u}_{X,Z} \\ \mathbf{u}_{Y,X} \\ \mathbf{u}_{Y,Y} \\ \mathbf{u}_{Y,Z} \\ \mathbf{u}_{Z,X} \\ \mathbf{u}_{Z,Y} \\ \mathbf{u}_{Z,Z} \end{Bmatrix} = \begin{bmatrix} \mathbf{J}^{-1} & \mathbf{0} & \mathbf{0} \\ \mathbf{0} & \mathbf{J}^{-1} & \mathbf{0} \\ \mathbf{0} & \mathbf{0} & \mathbf{J}^{-1} \end{bmatrix} \begin{Bmatrix} \mathbf{u}_{x,x} \\ \mathbf{u}_{x,h} \\ \mathbf{u}_{x,z} \\ \mathbf{u}_{h,x} \\ \mathbf{u}_{h,h} \\ \mathbf{u}_{h,z} \\ \mathbf{u}_{z,x} \\ \mathbf{u}_{z,h} \\ \mathbf{u}_{z,z} \end{Bmatrix}. \quad (3.8)$$

In terms of matrix forms, Eq. (3.8) can be written as

$$\left\{ \partial u \Big|_{X,Y,Z} \right\}_{9 \times 1} = [\mathbf{J}_0]_{9 \times 9}^{-1} \left\{ \partial u \Big|_{x,h,z} \right\}_{9 \times 1}, \quad (3.9)$$

where  $[\mathbf{J}_0]^{-1}$  is the inverse of the 3 by 3 Jacobian matrix  $[\mathbf{J}]$ . Strains in (3.6) are referred to the global coordinate system  $(X, Y, Z)$ . All six strains are included because the shell mid-surface may have any orientation with respect to the global coordinate directions.

From (3.4) we obtain

$$\begin{Bmatrix} u_{x,x} \\ u_{x,h} \\ u_{x,z} \\ u_{h,x} \\ u_{h,h} \\ u_{h,z} \\ u_{z,x} \\ u_{z,h} \\ u_{z,z} \end{Bmatrix} = \sum \begin{bmatrix} N_{i,x} & 0 & 0 & -0.5zt_i N_{i,x} l_{2i} & 0.5zt_i N_{i,x} l_{1i} \\ N_{i,h} & 0 & 0 & -0.5zt_i N_{i,h} l_{2i} & 0.5zt_i N_{i,h} l_{1i} \\ 0 & 0 & 0 & -0.5t_i N_{i,z} l_{2i} & 0.5t_i N_{i,z} l_{1i} \\ 0 & N_{i,x} & 0 & -0.5zt_i N_{i,x} m_{2i} & 0.5zt_i N_{i,x} m_{1i} \\ 0 & N_{i,h} & 0 & -0.5zt_i N_{i,h} m_{2i} & 0.5zt_i N_{i,h} m_{1i} \\ 0 & 0 & 0 & -0.5t_i N_{i,z} m_{2i} & 0.5t_i N_{i,z} m_{1i} \\ 0 & 0 & N_{i,x} & -0.5zt_i N_{i,x} n_{2i} & 0.5zt_i N_{i,x} n_{1i} \\ 0 & 0 & N_{i,h} & -0.5zt_i N_{i,h} n_{2i} & 0.5zt_i N_{i,h} n_{1i} \\ 0 & 0 & 0 & -0.5t_i N_{i,z} n_{2i} & 0.5t_i N_{i,z} n_{1i} \end{bmatrix} \begin{Bmatrix} u_i \\ v_i \\ w_i \\ a_i \\ b_i \end{Bmatrix}. \quad (3.10)$$

In terms of matrix forms, Eq. (3.10) can be written as

$$\left\{ \partial u \Big|_{x,h,z} \right\}_{9 \times 1} = \left[ \partial N(x,h,z) \right]_{9 \times 40} \left\{ U^e \right\}_{40 \times 1}. \quad (3.11)$$

Combining Eq. (3.7), Eq. (3.9), and Eq. (3.11) yields

$$\left\{ e \Big|_{x,y,z} \right\}_{6 \times 1} = [H]_{6 \times 9} [J_0]_{9 \times 9}^{-1} \left[ \partial N(x,h,z) \right]_{9 \times 40} \left\{ U^e \right\}_{40 \times 1}. \quad (3.12)$$

The complete strain-displacement matrix  $[B]$  is determined by the following equation:

$$[B]_{6 \times 40} = [H]_{6 \times 9} [J_0]_{9 \times 9}^{-1} \left[ \partial N(x,h,z) \right]_{9 \times 40}. \quad (3.13)$$

### 3.2.6 Shape Function and Jacobian Matrix

The shape function  $N_i(x,h)$  used in the above equations is the 2D shape function. For the 8-node degenerated shell element, the shape function is the Serendipity shape function, which is defined as follows:

$$N_1(x,h) = -\frac{1}{4}(1-x)(1-h)(1+x+h), \quad (3.14)$$

$$N_2(x,h) = -\frac{1}{4}(1+x)(1-h)(1-x+h), \quad (3.15)$$

$$N_3(x,h) = -\frac{1}{4}(1+x)(1+h)(1-x-h), \quad (3.16)$$

$$N_4(\mathbf{x}, \mathbf{h}) = -\frac{1}{4}(1-\mathbf{x})(1+\mathbf{h})(1+\mathbf{x}-\mathbf{h}), \quad (3.17)$$

$$N_5(\mathbf{x}, \mathbf{h}) = \frac{1}{2}(1-\mathbf{x})(1-\mathbf{h})(1+\mathbf{x}), \quad (3.18)$$

$$N_6(\mathbf{x}, \mathbf{h}) = \frac{1}{2}(1+\mathbf{x})(1-\mathbf{h})(1-\mathbf{h}), \quad (3.19)$$

$$N_7(\mathbf{x}, \mathbf{h}) = \frac{1}{2}(1+\mathbf{x})(1+\mathbf{h})(1-\mathbf{x}), \text{ and} \quad (3.20)$$

$$N_8(\mathbf{x}, \mathbf{h}) = \frac{1}{2}(1-\mathbf{x})(1+\mathbf{h})(1-\mathbf{h}). \quad (3.21)$$

The Jacobian matrix used in Eq. (3.8) is defined as

$$[J] = \begin{bmatrix} X_{,x} & Y_{,x} & Z_{,x} \\ X_{,h} & Y_{,h} & Z_{,h} \\ X_{,z} & Y_{,z} & Z_{,z} \end{bmatrix}. \quad (3.22)$$

From Eq. (3.3) we obtain

$$[J] = \begin{bmatrix} \sum N_{i,x}(X_i + zt_i l_{3i}/2) & \sum N_{i,x}(Y_i + zt_i m_{3i}/2) & \sum N_{i,x}(Z_i + zt_i n_{3i}/2) \\ \sum N_{i,h}(X_i + zt_i l_{3i}/2) & \sum N_{i,h}(Y_i + zt_i m_{3i}/2) & \sum N_{i,h}(Z_i + zt_i n_{3i}/2) \\ \sum N_i(t_i l_{3i}/2) & \sum N_i(t_i m_{3i}/2) & \sum N_i(t_i n_{3i}/2) \end{bmatrix}. \quad (3.23)$$

### 3.2.7 Constitutive Equation

For an isotropic material, the stress-strain relation can be expressed by the following equation:

$$\begin{Bmatrix} \mathbf{s}_x \\ \mathbf{s}_y \\ \mathbf{t}_{xy} \\ \mathbf{s}_z \\ \mathbf{t}_{xz} \\ \mathbf{t}_{yz} \end{Bmatrix} = \begin{bmatrix} E & \nu E & 0 & 0 & 0 & 0 \\ \nu E & E & 0 & 0 & 0 & 0 \\ 0 & 0 & 0 & 0 & 0 & 0 \\ 0 & 0 & 0 & G_0 & 0 & 0 \\ 0 & 0 & 0 & 0 & k_s G_0 & 0 \\ 0 & 0 & 0 & 0 & 0 & k_s G_0 \end{bmatrix} \begin{Bmatrix} \mathbf{e}_x \\ \mathbf{e}_y \\ \mathbf{g}_{xy} \\ \mathbf{e}_z \\ \mathbf{g}_{xz} \\ \mathbf{g}_{yz} \end{Bmatrix}, \quad (3.24)$$

where  $E = E_0 / (1 - n^2)$ ;  $G_0 = 0.5E_0 / (1 + n)$ ;  $E_0$  is elastic modulus;  $n$  is the Poisson ratio of the material;  $k_s$  is the shear correction factor, taken as 5/6 (Crisfield, 1991). All

coefficients in the third column and the third row of the material matrix are set to be zeros to ensure the normal stress  $\mathbf{s}_z = \mathbf{0}$ , which satisfies the second assumption of the shell element. Eq. (3.24) can also be written as

$$\{\mathbf{s}_{xyz}\} = [\mathbf{D}_{xyz}] \{\mathbf{e}_{xyz}\}, \quad (3.25)$$

where  $[\mathbf{D}_{xyz}]$  is the local material matrix, and  $\{\mathbf{s}_{xyz}\}$  and  $\{\mathbf{e}_{xyz}\}$  are stresses and strains in the local coordinate system, respectively. The global material matrix is related to the local material matrix by the following transformation equation:

$$[\mathbf{D}_{XYZ}] = [\mathbf{T}_e]^T [\mathbf{D}_{xyz}] [\mathbf{T}_e], \quad (3.26)$$

where  $[\mathbf{T}_e]$  is the transformation matrix given by

$$[\mathbf{T}_e] = \begin{bmatrix} l_1^2 & m_1^2 & n_1^2 & l_1 m_1 & m_1 n_1 & n_1 l_1 \\ l_2^2 & m_2^2 & n_2^2 & l_2 m_2 & m_2 n_2 & n_2 l_2 \\ l_3^2 & m_3^2 & n_3^2 & l_3 m_3 & m_3 n_3 & n_3 l_3 \\ 2l_1 l_2 & 2m_1 m_2 & 2n_1 n_2 & l_1 m_2 + l_2 m_1 & m_1 n_2 + m_2 n_1 & n_1 l_2 + n_2 l_1 \\ 2l_2 l_3 & 2m_2 m_3 & 2n_2 n_3 & l_2 m_3 + l_3 m_2 & m_2 n_3 + m_3 n_2 & n_2 l_3 + n_3 l_2 \\ 2l_3 l_1 & 2m_3 m_1 & 2n_3 n_1 & l_3 m_1 + l_1 m_3 & m_3 n_1 + m_1 n_3 & n_1 l_2 + n_3 l_1 \end{bmatrix}, \quad (3.27)$$

where  $(l_1, m_1, n_1)$ ,  $(l_2, m_2, n_2)$  and  $(l_3, m_3, n_3)$  are direction cosines of vectors  $x$ ,  $y$  and  $z$  corresponding to the global coordinate system at each sampling point (Cook, 2002).

### 3.2.8 Element Stiffness Matrix and Internal Force Vector

The element stiffness matrix and the element internal force vector are expressed in the following equations:

$$[\mathbf{k}^e]_{40 \times 40} = \int_{-1}^1 \int_{-1}^1 \int_{-1}^1 [\mathbf{B}]^T [\mathbf{D}] [\mathbf{B}] \det[\mathbf{J}] \, dx \, dh \, dz, \quad (3.28)$$

$$\{\mathbf{f}^e\}_{40 \times 1} = \int_{-1}^1 \int_{-1}^1 \int_{-1}^1 [\mathbf{B}]^T \{\mathbf{S}\} \det[\mathbf{J}] \, dx \, dh \, dz, \quad (3.29)$$

where [B] is the strain-displacement matrix, determined by Eq. (3.13),  $\det[J]$  is the determinant of Jacobian matrix.

### 3.2.9 Stress Resultant

The stress resultants are evaluated based on stresses along the cross section of the shell element. The sign convention for the stress resultants is illustrated in Figure 3.5. The equations to determine the stress resultants are expressed as follows:

For in-plane shear behavior

$$N_x = \frac{t}{2} \int_{-1}^{+1} s_x dz, \quad N_y = \frac{t}{2} \int_{-1}^{+1} s_y dz, \quad \text{and} \quad N_{xy} = \frac{t}{2} \int_{-1}^{+1} t_{xy} dz. \quad (3.30)$$

For out-of-plane bending behavior

$$M_x = -\frac{t^2}{4} \int_{-1}^{+1} s_x z dz, \quad M_y = -\frac{t^2}{4} \int_{-1}^{+1} s_y z dz, \quad \text{and} \quad M_{xy} = -\frac{t^2}{4} \int_{-1}^{+1} t_{xy} z dz. \quad (3.31)$$

For out-of-plane shear behavior

$$Q_x = \frac{t}{2} \int_{-1}^{+1} t_{xz} dz, \quad \text{and} \quad Q_y = \frac{t}{2} \int_{-1}^{+1} t_{yz} dz. \quad (3.32)$$

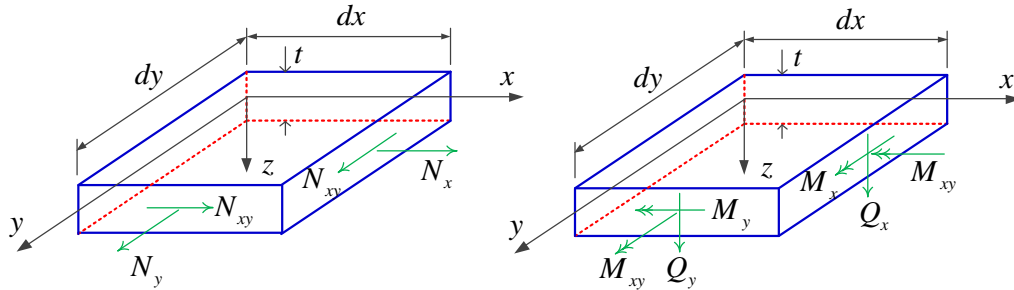


Figure 3.5 The stress resultants in the shell element (Cook, 2002)

### 3.2.10 Numerical Integration and Layer Approach

Numerical integration can be used to evaluate the element stiffness matrix, the internal force vector, and the stress resultants in Eq. (3.26) through Eq. (3.31) (Hinton & Owen, 1984). For the stress resultant, the numerical integration can be performed along the thickness direction by using the layered approach, as shown in Figure 3.6. The layered approach is computationally expensive; however, it is more accurate for nonlinear material such as reinforced concrete in which the material properties (and stress) are discontinuous functions of  $Z$ . As shown in Figure 3.2, along the thickness of the element, the strains are linear functions of  $Z$  and the stresses are nonlinear functions of  $Z$ .

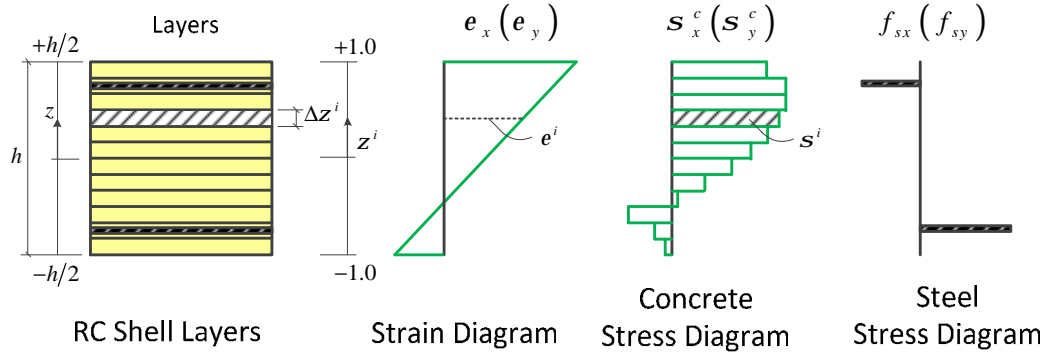


Figure 3.6 The concept of layered approach

The equations to evaluate the stress resultants based on the layered approach are expressed in the following equations:

For in-plane shear behavior

$$N_x = \frac{t}{2} \sum_{i=1}^n s_x^i \Delta z^i, \quad N_y = \frac{t}{2} \sum_{i=1}^n s_y^i \Delta z^i, \quad N_{xy} = \frac{t}{2} \sum_{i=1}^n t_{xy}^i \Delta z^i. \quad (3.33)$$

For out-of-plane bending behavior

$$M_x = -\frac{t^2}{4} \sum_{i=1}^n s_x^i z^i \Delta z^i, \quad M_y = -\frac{t^2}{4} \sum_{i=1}^n s_y^i z^i \Delta z^i, \quad M_{xy} = -\frac{t^2}{4} \sum_{i=1}^n t_{xy}^i z^i \Delta z^i. \quad (3.34)$$

For out-of-plane shear behavior

$$Q_x = \frac{t}{2} \sum_{i=1}^n t_{xz}^i \Delta z^i, \quad Q_y = \frac{t}{2} \sum_{i=1}^n t_{yz}^i \Delta z^i, \quad (3.35)$$

where  $n$  is the number of layers.

The integration to evaluate the element stiffness matrix and the internal force vector can be divided into two processes. The first process is to perform the integration along the thickness direction by using the layered approach. The constitutive material matrix  $[D]$ , the strain-displacement matrix  $[B]$ , and the Jacobian matrix  $[J]$  vary through thickness direction and are functions of  $(x, h, z)$ . The second process is to perform the integration on the middle surface of the element by using Gaussian quadrature rules. The normal full integration rule that consists of  $3 \times 3$  Gauss points can be applied, as shown in Figure 3.7.

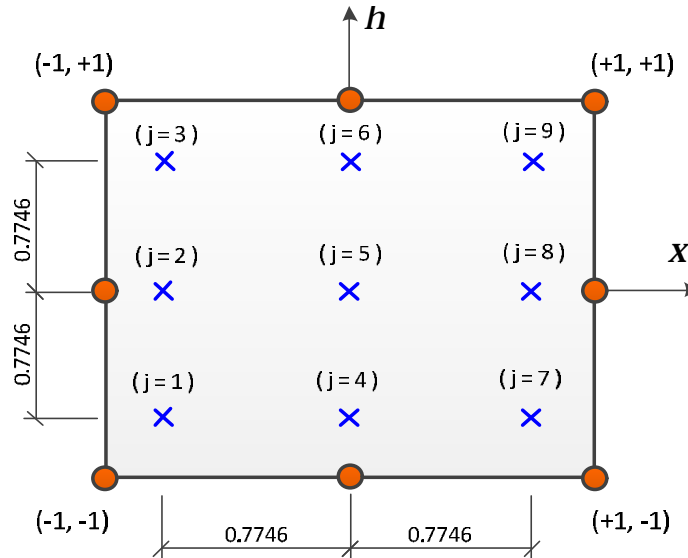


Figure 3.7 Gauss point positions

The equations to evaluate the element stiffness matrix and the internal force vector based on the Gaussian quadrature rules and the layered approach are expressed in the following equations:

$$[\mathbf{k}^e] = \sum_{j=1}^{nG} \sum_{i=1}^n w_j \Delta z^i [\mathbf{B}(x_j, h_j, z_i)]^T [\mathbf{D}] [\mathbf{B}(x_j, h_j, z_i)] \det[\mathbf{J}(x_j, h_j, z_i)], \text{ and} \quad (3.36)$$

$$\{\mathbf{f}^e\} = \sum_{j=1}^{nG} \sum_{i=1}^n w_j \Delta z^i [\mathbf{B}(x_j, h_j, z_i)]^T \{\mathbf{S}\} \det[\mathbf{J}(x_j, h_j, z_i)], \quad (3.37)$$

where nG is the number of Gauss points,  $w_j$  is the weight function. The values of  $x_j, h_j$  and  $w_j$  are given in Table 3.1.

**Table 3.1 Developed Modules in OpenSees**

Point Number	Shape Function	$w_j$	$x_j$	$h_j$
1	N <sub>1</sub>	25/81	-0.7746	-0.7746
2	N <sub>2</sub>	40/81	-0.7746	0.0
3	N <sub>3</sub>	25/81	-0.7746	0.7746
4	N <sub>4</sub>	40/81	0.0	-0.7746
5	N <sub>5</sub>	64/81	0.0	0.0
6	N <sub>6</sub>	40/81	0.0	0.7746
7	N <sub>7</sub>	25/81	0.7746	-0.7746
8	N <sub>8</sub>	40/81	0.7746	0.0
9	N <sub>9</sub>	25/81	0.7746	0.7746

### 3.3 Constitutive Model

#### 3.3.1 Stress and Strain Relationship in Each Layer

In the layered approach, the section of the shell element is divided into several layers throughout the thickness. The strains at each layer are assumed to be uniform and interpolated by the shape function from the displacements at nodes of the element. For each layer of the shell element, the material matrix is a 6 x 6 matrix and corresponds to six independent strains ( $\mathbf{e}_x, \mathbf{e}_y, \mathbf{e}_z, \mathbf{g}_{xy}, \mathbf{g}_{yz}, \mathbf{g}_{xz}$ ) given in the local coordinate system ( $x, y, z$ ), including the in-plane and the out-of-plane strains. The relationship between stresses and strains in each layer for both steel and concrete is expressed as

$$\begin{Bmatrix} \mathbf{s}_x \\ \mathbf{s}_y \\ t_{xy} \\ \mathbf{s}_z \\ t_{xz} \\ t_{yz} \end{Bmatrix} = \begin{bmatrix} & & 0 & 0 & 0 \\ & [\bar{\mathbf{D}}_{in}] & 0 & 0 & 0 \\ & & 0 & 0 & 0 \\ 0 & 0 & 0 & 0 & 0 \\ 0 & 0 & 0 & 0 & [\bar{\mathbf{D}}_{out}] \\ 0 & 0 & 0 & 0 & \end{bmatrix} \begin{Bmatrix} \mathbf{e}_x \\ \mathbf{e}_y \\ \mathbf{g}_{xy} \\ \mathbf{e}_z \\ \mathbf{g}_{xz} \\ \mathbf{g}_{yz} \end{Bmatrix}, \quad (3.38)$$

where  $[\bar{\mathbf{D}}_{in}]$  and  $[\bar{\mathbf{D}}_{out}]$  are in-plane and out-of-plane tangential material matrices, respectively.

Because the strain in the direction perpendicular to the mid-surface of the shell element  $\mathbf{e}_z$  is considered, the coefficients in the third column and the third row of the material matrix are assumed to be zero to ensure the normal stress  $\mathbf{s}_z$  equals to zero. Based on the assumptions of the element, the in-plane and out-of-plane responses are calculated independently. Each layer is assumed to be in a state-of-plane stress. Hence, Eq. (3.47) is assumed to be the combination of the following equations:

$$\begin{Bmatrix} \mathbf{s}_x \\ \mathbf{s}_y \\ t_{xy} \end{Bmatrix} = \begin{bmatrix} & \\ & \bar{\mathbf{D}}_{in} \\ & \end{bmatrix} \begin{Bmatrix} \mathbf{e}_x \\ \mathbf{e}_y \\ \mathbf{g}_{xy} \end{Bmatrix} \text{ for in-plane behavior, and} \quad (3.39)$$

$$\begin{Bmatrix} t_{xz} \\ t_{yz} \end{Bmatrix} = \begin{bmatrix} & \\ & \bar{\mathbf{D}}_{out} \end{bmatrix} \begin{Bmatrix} \mathbf{g}_{xz} \\ \mathbf{g}_{yz} \end{Bmatrix} \text{ for out-of-plane behavior.} \quad (3.40)$$

### 3.3.2 Material Matrix for In-plane Behavior

#### 3.3.2.1 Coordinate Systems

Three Cartesian coordinates,  $x$ - $y$ , 1-2, and  $x_{si}$ - $y_{si}$ , are defined for each layer of the reinforced concrete shell elements, as demonstrated in Figure 3.8. Coordinate  $x$ - $y$  defines the local coordinate. Coordinate 1-2 represents the principal stress directions of the applied stresses that have an angle  $\mathbf{q}_1$  with respect to the  $x$ -axis. Steel bars can be oriented in

different directions in the rebar layer. Coordinate  $x_{si}-y_{si}$  indicates the direction of the  $i^{\text{th}}$  group of rebars, where the  $i^{\text{th}}$  group of rebars are located in the direction of axis  $x_{si}$  with an angle  $q_{si}$  to the  $x$ -axis.

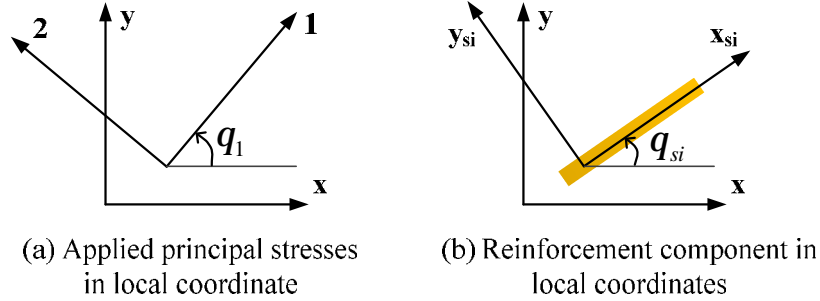


Figure 3.8 Local coordinate systems in each layer

### 3.3.2.2 Strain and Stress Transformations

Stresses and strains of different coordinate systems can be related to each other by using the transformation matrix  $[T_e(a)]$  expressed as

$$[T_e(a)] = \begin{bmatrix} c^2 & s^2 & sc \\ s^2 & c^2 & -sc \\ -2sc & 2sc & c^2 - s^2 \end{bmatrix}, \quad (3.41)$$

where  $c = \cos(a)$ ,  $s = \sin(a)$ , and the angle  $a$  is the angle between the two coordinates.

For concrete layer, the transformation of strains and stresses between the  $x$ - $y$  coordinate and the 1-2 coordinate using the transformation matrix are expressed as

$$\begin{Bmatrix} e_1 \\ e_2 \\ g_{12} \end{Bmatrix} = [T_e(q_1)] \begin{Bmatrix} e_x \\ e_y \\ g_{xy} \end{Bmatrix}, \text{ and} \quad (3.42)$$

$$\begin{Bmatrix} s_x \\ s_y \\ t_{xy} \end{Bmatrix} = [T_e(q_1)]^{-T} \begin{Bmatrix} s_1^c \\ s_2^c \\ t_{12}^c \end{Bmatrix}. \quad (3.43)$$

For the steel layer, the transformation of strains and stress between the 1-2 coordinate and the  $x_{si}$ - $y_{si}$  coordinate using the transformation matrix are expressed as

$$\begin{Bmatrix} e_{si} \\ e_{si'} \\ 0 \end{Bmatrix} = [T_e(q_{si} - q_1)] \begin{Bmatrix} e_1 \\ e_2 \\ g_{12} \end{Bmatrix}, \text{ and} \quad (3.44)$$

$$\begin{Bmatrix} s_x \\ s_y \\ t_{xy} \end{Bmatrix} = \sum [T_e(q_{si})]^{-T} \begin{Bmatrix} f_{si} \\ 0 \\ 0 \end{Bmatrix}, \quad (3.45)$$

where the steel strains ( $e_{si}$ ) and concrete strains ( $e_1, e_2$ ) in Eq. (3.42) and Eq. (3.44) are biaxial strains, which need to be converted to uniaxial strains so that the constitutive material models of concrete and steel can be applied.

### 3.3.2.3 Biaxial and Uniaxial Strain Relationship

The relationship between biaxial strains and uniaxial strains has been derived using the Hsu/Zhu ratios ( $v_{12}, v_{21}$ ) (Hsu and Zhu, 2002), which was introduced in Chapter 2. Using the Hsu/Zhu ratios ( $v_{12}, v_{21}$ ), the biaxial strains of concrete ( $e_1, e_2$ ) are converted into the uniaxial strains of concrete ( $\bar{e}_1, \bar{e}_2$ ), which are then transformed into the uniaxial strain of steel ( $\bar{e}_{si}$ ) by the following equations:

$$\begin{Bmatrix} \bar{e}_1 \\ \bar{e}_2 \\ g_{12} \end{Bmatrix} = [V] \cdot \begin{Bmatrix} e_1 \\ e_2 \\ g_{12} \end{Bmatrix}, \quad (3.46)$$

$$\begin{Bmatrix} \bar{e}_{si} \\ 0 \\ 0 \end{Bmatrix} = [V] \begin{Bmatrix} e_{si} \\ e_{si'} \\ 0 \end{Bmatrix}, \text{ and} \quad (3.47)$$

$$[V] = \begin{bmatrix} \frac{1}{1-n_{12}n_{21}} & \frac{n_{12}}{1-n_{12}n_{21}} & 0 \\ \frac{n_{21}}{1-n_{12}n_{21}} & \frac{1}{1-n_{12}n_{21}} & 0 \\ 0 & 0 & 1 \end{bmatrix}. \quad (3.48)$$

The uniaxial strains of concrete ( $\bar{e}_1, \bar{e}_2$ ) and steel ( $\bar{e}_{si}$ ) are obtained by Eq. (3.46) and Eq. (3.47), respectively. The stresses of concrete ( $s_1^c, s_2^c, t_{12}^c$ ) and steel ( $f_{si}$ ) in Eq. (3.43) and Eq. (3.45) can be determined from the uniaxial strains based on the uniaxial constitutive relationships of the materials given in the next sections.

### 3.3.2.4 Uniaxial Model for Concrete

The cyclic uniaxial constitutive relationships of concrete with embedded reinforcement were based on the CSMM described in Chapter 2. The characteristics of these concrete constitutive laws include: (1) the softening effect on the concrete in compression due to the tensile strain in the perpendicular direction; (2) the softening effect on the concrete in compression under reversed cyclic loading; and (3) the opening and closing of cracks, which are taken into account in the unloading and reloading stages.

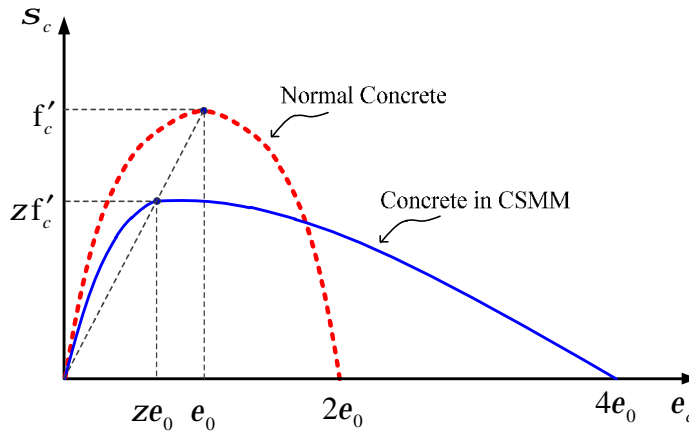
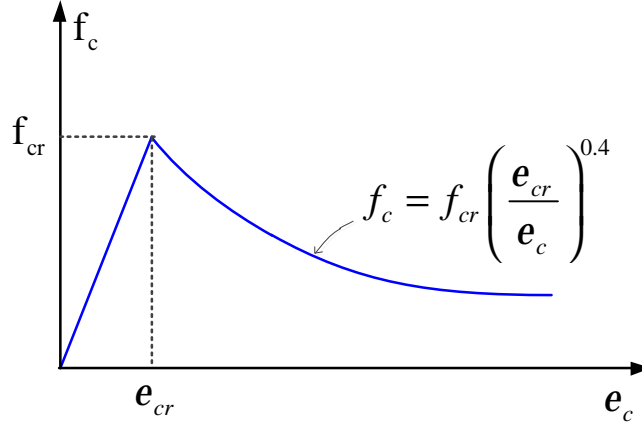


Figure 3.9 Envelope stress-strain curve of concrete in compression



**Figure 3.10 Envelope stress-strain curve of concrete in tension**

The envelopes of the cyclic stress-strain curve of concrete in tension and compression are shown in Figure 3.9 and Figure 3.10. The equations defining the envelope curves are described as follows:

The equations for concrete in compression are

$$s^c = Dz f'_c \left[ 2 \left( \frac{\bar{e}}{ze_0} \right) - \left( \frac{\bar{e}}{ze_0} \right)^2 \right], \quad 0 \leq |\bar{e}| \leq |ze_0|, \quad (3.49)$$

$$s^c = Dz f'_c \left[ 1 - \left( \frac{\bar{e}/e_0 - 1}{4/z - 1} \right)^2 \right], \quad |\bar{e}| > |ze_0|, \quad (3.50)$$

$$z = \left( \frac{5.8}{\sqrt{f'_c(\text{MPa})}} \right) \left( \frac{1}{\sqrt{1 + 400\bar{e}_T}} \right) \left( 1 - \frac{|b|}{24^\circ} \right) \leq 0.9, \quad (3.51)$$

$$b = \frac{1}{2} \tan^{-1} \left[ \frac{g_{12}}{e_2 - e_1} \right], \text{ and} \quad (3.52)$$

$$D = 1 - 0.4 \frac{e'_c}{e_0} \leq 1.0. \quad (3.53)$$

The equations for concrete in tension are:

$$s^c = E_c \bar{e}, \quad 0 \leq \bar{e} < e_{cr}, \text{ with } e_{cr} = 0.00008 \text{ mm/mm, and} \quad (3.54)$$

$$s^c = f_{cr} \left( \frac{e_{cr}}{\bar{e}} \right)^{0.4}, \quad \bar{e} > e_{cr}, \quad \text{with } f_{cr} = 0.31\sqrt{f'_c(\text{MPa})}. \quad (3.55)$$

The unloading and reloading curves of the cyclic stress-strain curve of concrete used for the finite element model, however, are simplifications of the model proposed by Mansour and Hsu (2002), as shown in Figure 3.11. Several unloading and reloading paths with different slopes from the compressive envelope were simplified as two straight lines. Slopes of the straight lines are  $E_{co}$  and  $0.8E_{co}$  for the ascending and descending branches, respectively.

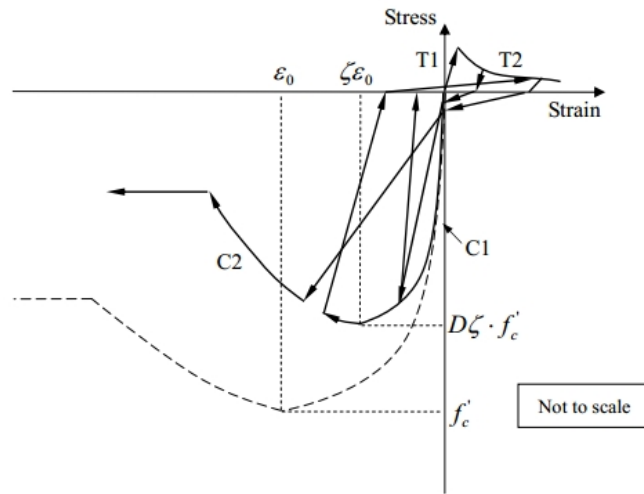


**Figure 3.11 Cyclic stress-strain curve of uniaxial material model for concrete**

The model proposed by Mansour and Hsu (2005b) is more accurate than the simplified model. However, regarding the numerical simulation, reducing the number of equations can increase the efficiency of the simulation.

### 3.3.2.5 Uniaxial Model for Steel

The cyclic uniaxial constitutive relationships of the embedded steel bars were based on the CSMM described in Chapter 2. The envelope of the cyclic stress-strain curve of the steel in tension is shown in Figure 3.12. The smeared yield stress of embedded mild steel

bars is lower than the yield stress of bare steel bars, and the hardening ratio of the steel bars after yielding is calculated from the steel ratio, steel strength, and concrete strength. For compression, the envelope of the cyclic stress-strain curve of the steel is assumed to be elastic and perfectly plastic.

The equations defining the envelope curves are described as follows:

The equation for steel in tension

$$f_s = E_s \bar{e}_s, \quad (\bar{e}_s \leq \bar{e}_n), \quad (3.56)$$

$$f_s = f_y \left[ (0.91 - 2B) + \left( 0.02 + 0.25B \frac{\bar{e}_s}{e_y} \right) \right], \quad (\bar{e}_s > \bar{e}_n), \quad (3.57)$$

$$B = \frac{1}{r} \left( \frac{f_{cr}}{f_y} \right)^{1.5} \text{ with } r \geq 0.5\%, \quad (3.58)$$

$$\bar{e}_n = e_y (0.93 - 2B). \quad (3.59)$$

The equation for steel in compression

$$f_s = E_s \bar{e}_s, \quad \text{with } (\bar{e}_s > -\bar{e}_n), \text{ and} \quad (3.60)$$

$$f_s = -f_y, \quad \text{with } (\bar{e}_s < -\bar{e}_n). \quad (3.61)$$

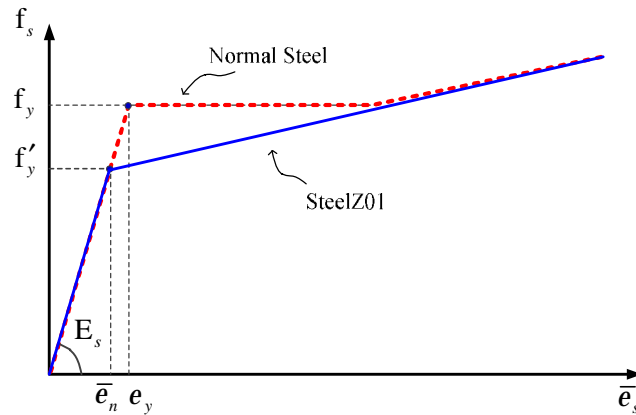


Figure 3.12 Envelope stress-strain curve of for steel

The unloading and reloading curves of the cyclic stress-strain curve of the steel used in the finite element model, however, are based on the simplified model proposed by Jeng (2002), as shown in Figure 3.13. In the model, the original unloading and reloading curves, which represent the Bauschinger effect (Mansour, 2001), are replaced by multi-linear straight-line with two turning points  $(\epsilon_{m1}, f_{m1})$  and  $(\epsilon_{m2}, f_{m2})$ . By doing so, the iteration required to determine stress from strain is bypassed, and convergence is easily achieved.

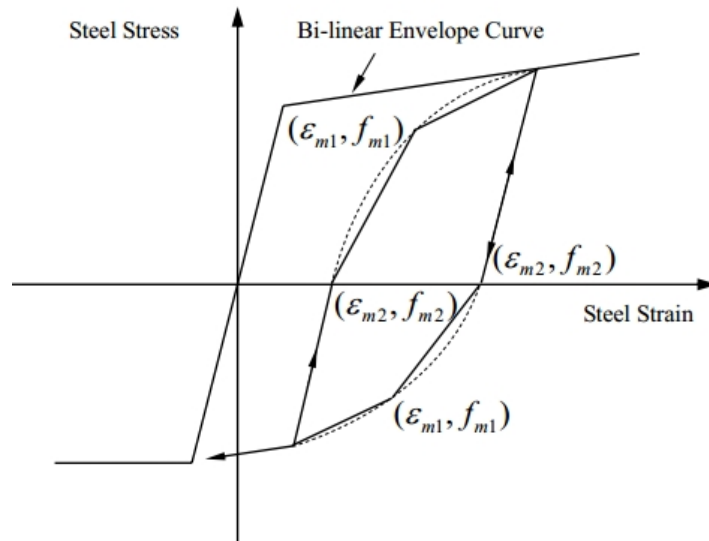


Figure 3.13 Cyclic stress-strain curve of uniaxial material model for steel

### 3.3.2.6 Material Constitutive Matrix

The in-plane tangent material constitutive matrix  $[\bar{D}_{in}]$  for a reinforced concrete element is formulated as

For a concrete layer

$$[\bar{D}_{in}] = [T(q_1)]^T [\bar{D}_c] [V] [T(q_1)]. \quad (3.62)$$

For an embedded reinforcement layer

$$[\bar{D}_{in}] = \sum_i [T(q_{si})]^T [\bar{D}_{si}] [T(q_{si} - q_1)] [V] [T(q_1)], \quad (3.63)$$

where  $[\bar{D}_c]$  and  $[\bar{D}_{si}]$  are the uniaxial tangential stiffness matrix of concrete and embedded reinforcement, respectively. The derivations of  $[\bar{D}_c]$  and  $[\bar{D}_{si}]$  are similar to the RC membrane element (Zhong, 2005).

The uniaxial constitutive matrix of concrete  $[\bar{D}_c]$  is given by

$$[\bar{D}_c] = \begin{bmatrix} \bar{E}_1^c & \partial s_1^c / \partial \bar{e}_2 & 0 \\ \partial s_2^c / \partial \bar{e}_1 & \bar{E}_2^c & 0 \\ 0 & 0 & G_{12}^c \end{bmatrix}, \quad (3.64)$$

where  $\bar{E}_1^c$  and  $\bar{E}_2^c$  are the tangential uniaxial moduli of concrete in the 1 and 2 directions, respectively, evaluated at a certain stress/strain state. The off-diagonal terms  $\partial s_1^c / \partial \bar{e}_2$  and  $\partial s_2^c / \partial \bar{e}_1$  are obtained by using the uniaxial constitutive relationships and take into account the state of the concrete stresses and uniaxial strains in the 1-2 directions, which are not zero because the stress and strain of the concrete in compression is softened by the orthogonal tensile strains.  $G_{12}^c$  is the shear modulus of concrete, taken as  $(s_2^c - s_1^c) / 2(e_2 - e_1)$ .

The uniaxial stiffness matrix of steel bars  $[\bar{D}_{si}]$  is evaluated as

$$[\bar{D}_{si}] = \begin{bmatrix} r_{si} \bar{E}_{si} & 0 & 0 \\ 0 & 0 & 0 \\ 0 & 0 & 0 \end{bmatrix}, \quad (3.65)$$

where  $\bar{E}_{si}$  is the uniaxial tangential modulus for the reinforcement embedded in concrete, which is determined for a particular stress/strain state.

### 3.3.3 Material Matrix for Out-of-plane Behavior

In this shell element, the out-of-plane action is taken only by concrete. For simplicity, the relationship between the out-of-plane shear stresses and the out-of-plane shear strains is assumed to be linear. The out-of-plane shear stiffness matrix including the constant coefficient is expressed as

$$\left[ \overline{D}_{out} \right] = k_s \begin{bmatrix} \overline{G}_{xz} & 0 \\ 0 & \overline{G}_{yz} \end{bmatrix}, \quad (3.66)$$

where  $\overline{G}_{xz} = \overline{G}_{yz} = \overline{G}_c = 0.5 \overline{E}_c / (1+n)$ ,  $\overline{E}_c$  is the tangential modulus of concrete, taken as  $3875 \sqrt{f'_c} \text{ (MPa)}$  (Hsu & Mo, 2010);  $n$  is the Poisson ratio of concrete, taken as 0.2; and  $k_s$  is the shear correction factor, taken as 5/6 (Maekawa, Okamura, & Pimanmas, 2003).

### 3.4 Solution Algorithm

Finite element analyses are often performed by using an incremental procedure. For nonlinear problems, the incremental procedure will lead to a buildup of error. An iterative procedure using a certain solution algorithm should be used to correct the build-up errors. Therefore, a combination of the incremental approach and iterative procedure is used as the basis for most of the nonlinear finite element analyses. In the analysis procedure, the integrator determines the next predictive step during the analysis procedure and specifies the tangent matrix and residual vector at any iteration. In this study, the commonly used integrators for static analyses such as load control, displacement control is introduced, and the analysis procedure of each integrator is described. The algorithm determines the sequence of steps taken to solve the nonlinear equations during the iterative procedures.

### 3.4.1 Load Control Scheme

In load control scheme, the total load is divided into small load increments. Each load step is applied in turn, and iterations are performed until convergence is achieved at the structural level. Then the next load step is processed. The three solution algorithms for solving nonlinear equations are the initial stiffness method, modified Newton-Raphson method, and the full Newton-Raphson method. The most common solution algorithm is full Newton-Raphson method, as shown in Figure 3.14. In each iteration within a load step, the stiffness matrix is refined iteratively until a convergence criterion is achieved. The stiffness matrix is computed from the last iterative solution during the iterative procedure until convergence is achieved. The initial stiffness method uses an initial stiffness matrix throughout the iterative procedure, as shown in Figure 3.16. The modified Newton-Raphson procedure also is used in the solution algorithms, as shown in Figure 3.15. Different from the full Newton-Raphson method, the stiffness matrix from the last converged equilibrium was used during the iterative procedure until convergence was achieved.

The full Newton-Raphson method converges more rapidly, and the progress will converge in fewer iterations. However, this method requires that the tangent stiffness matrix is evaluated at each iteration, which can be significant for large structures. In contrast to the full Newton-Raphson method, the initial stiffness matrix is calculated at the beginning of the load step, and the stiffness matrix remains the same throughout the procedure. A large number of iterations are required to achieve convergence. The modified Newton-Raphson method shows the balance between the computation and iteration numbers. Many algorithms were developed by improving the Newton-Type methods with

the acceleration technology such as the KrylovNewton method (Carlson & Miller, 1998). The KrylovNewton method is a modified Newton-Raphson method with Krylov subspace acceleration, which greatly decreases the number of iterations in the solution.

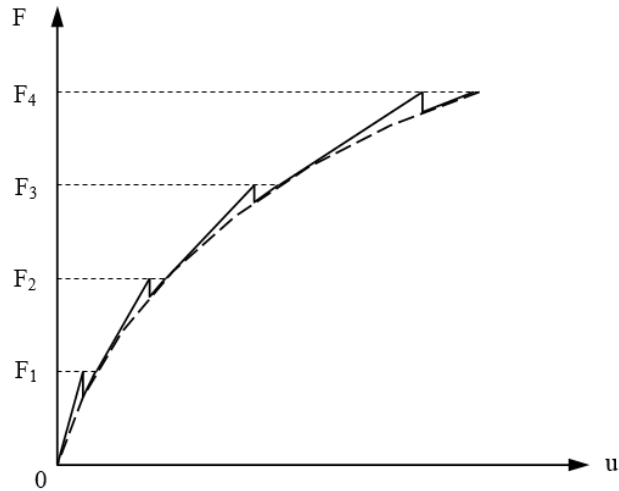


**Figure 3.14** Load control scheme using the full Newton-Raphson method

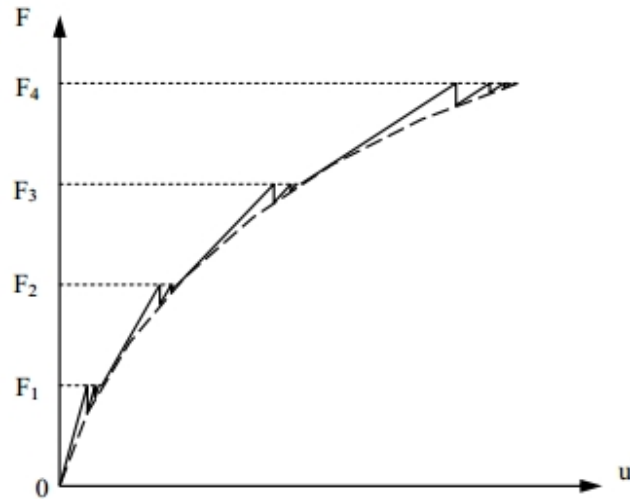


**Figure 3.15** Load control scheme using the modified Newton-Raphson method

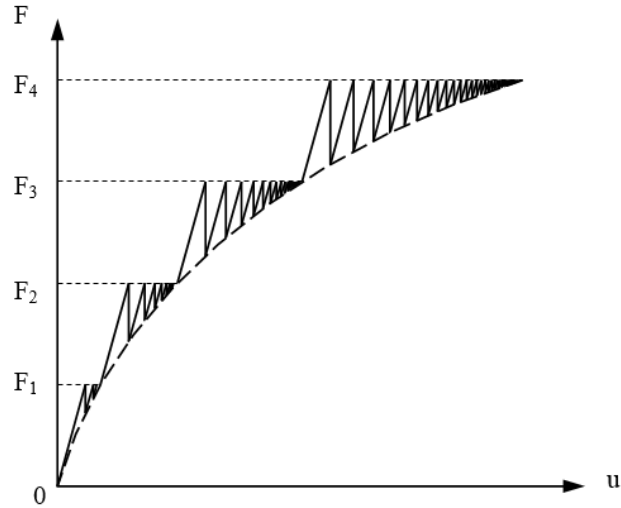


**Figure 3.16 Load control scheme using the initial stiffness method**

The load control scheme can be effective to get solutions for the nonlinear finite element problems until the load reaches its maximum value. However, this method cannot be used to indicate the behavior of the structure at a local limit such as the temporary drop of force due to the initial concrete cracking. More importantly, this method is incapable of obtaining the ultimate strength of the structure and of tracing the behavior of the structure in the post-peak region. Under the load control, the tangent stiffness matrix becomes nearly singular at the peak point of the load-displacement curve. Ayoub (1995) and Ayoub and Filippou (1998) pointed out that the failure of the solution to converge is not an indication that the structure has reached its collapse but rather a failure of the solution convergence.

### **3.4.2 Displacement Control Scheme**

Many researchers (Batoz & Dhat, 1979; Haisler, Stricklin, & Key, 1977; Zienkiewicz, 1971) have proposed the displacement control scheme to overcome the limits of the load control method. Using the displacement control, especially with arc-length scheme, it is possible to obtain the behavior of the structure beyond the crack point and the maximum

point and to determine the entire response including ascending and descending branches. The arc-length method was developed to overcome the local and global limit points in the nonlinear analysis, which treated the load factor as a variable. Riks (1972) originally proposed the arc-length method, which Crisfield (1981) improved. In the following, a displacement control with an arc-length scheme originally proposed by Batoz and Dhat (1979) is presented.

The displacement increments are decomposed into two parts:

$$\Delta \mathbf{u} = \Delta \mathbf{u}_u + I \Delta \mathbf{u}_r, \quad (3.67)$$

where  $\Delta \mathbf{u}_u$  = displacement increments induced by the unbalanced load;  $\Delta \mathbf{u}_r$  = displacement increments induced by a reference load,  $I$  = the load factor, a coefficient to be determined.

Now, define a vector operator as

$$\Gamma_n = \{0 \quad \dots \quad 1 \quad \dots \quad 0\}^T, \quad (3.68)$$

where only the  $n$ -th component is 1, and the other components are all zero.

The first-order approximation of  $\Delta \mathbf{u}_u$  and  $\Delta \mathbf{u}_r$  can be obtained by solving the linearized system of equations:

$$\Delta u_u = K_t^{-1} \Delta P_u, \text{ and} \quad (3.69)$$

$$\Delta u_r = K_t^{-1} \Delta P_r, \quad (3.70)$$

where  $K_t$  = stiffness matrix,  $\Delta P_u$  = the unbalanced external load,  $\Delta P_r = p_r \Gamma_n$ , and  $p_r$  = the magnitude of the reference load.

The  $n$ -th component of the displacement increments can be denoted by

$$\Gamma_n \cdot \Delta u = \Gamma_n \cdot \Delta u_u + I \Gamma_n \cdot \Delta u_r . \quad (3.71)$$

For a prescribed increment of displacement  $d$  is imposed on the  $n$ -th degree of freedom, Eq. (3.71) can be expressed as

$$\Gamma_n \cdot \Delta u = \Gamma_n \cdot \Delta u_u + I \Gamma_n \cdot \Delta u_r = d . \quad (3.72)$$

The iterative procedure to achieve the  $d$  is expressed as follows:

(1) For the first iteration from Eq. (3.72) we can obtain

$$I = \frac{d - \Gamma_n \cdot \Delta u_u}{\Gamma_n \cdot \Delta u_r} . \quad (3.73)$$

(2) For the remainder of the iterations, the displacement of the  $n$ -th DOF must be kept constant, that is,

$$\Gamma_n \cdot \Delta u = \Gamma_n \cdot \Delta u_u + \Delta I \cdot \Gamma_n \cdot \Delta u_r = 0 . \quad (3.74)$$

So

$$\Delta I = -\frac{\Gamma_n \cdot \Delta u_u}{\Gamma_n \cdot \Delta u_r} , \text{ and} \quad (3.75)$$

$$I = I + \Delta I , \quad (3.76)$$

where the  $\Delta I$  is the increment of the magnitude of the reference load factor.

(3) After the convergence is achieved, the actual load  $P$  for the predescribed displacement increment  $d$  can be obtained:

$$P = I \cdot P_r . \quad (3.77)$$

This displacement control scheme can be incorporated with both full and modified Newton-Raphson solution algorithms.

### 3.5 Analysis Procedure

An analysis procedure was developed to perform nonlinear analyses of RC shell structures using the developed CSMM-based shell element. A flow chart for the analysis

solutions under load increment using the Newton-Raphson method are described in Figure 3.18. Throughout the procedures, the material matrix  $[\bar{D}]$  is determined first, and the local stiffness matrix  $[k^e]$  and the local resisting force increment vector  $\{\Delta f\}$  are calculated. Then, the global stiffness matrix  $[K]$  and global resisting force increment vector  $\{\Delta F\}$  are assembled. In each iteration, the local material matrix  $[\bar{D}]$ , the local stiffness matrix  $[k^e]$ , and the global stiffness matrix  $[K]$  are iteratively refined until a convergence criterion is achieved.

There are two analysis procedures for establishing the constitutive material matrix at each layer of the CSMM-based shell element. In CSMM, the principal stress direction  $q_1$  is an unknown value that needs to be determined before the local material matrix  $[\bar{D}_{layer}]$  at each layer is established. In the first analysis procedures, shown in the grey block in Figure 3.17, the principal stress direction  $q_1$  is determined based on an iteration method. Theoretically, this procedure provides more accurate results; however, it has a very expensive computational time and is not efficient when applying in the case of the shell element, which has many layers as well as dealing with large structures with large numbers of elements. In this study, a modified analysis procedure without using the iteration method is proposed by assuming that the principal stress direction  $q_1$  can be evaluated at the cracking loading step and be maintained during the analysis, as shown in Figure 3.18. Before cracking, it can be assumed that the principal stress is coincided with the principal strain; therefore the angle  $q_1$  can be computed from the local in-plane cracking strains as well. Once the principal stress direction  $q_1$  is defined, the local material matrix  $[\bar{D}_{layer}]$  can be obtained at each layer of the shell element. The procedure for the calculation of the

global element stiffness and global resisting force of the shell elements is outlined by the outer white block in Figure 3.18.

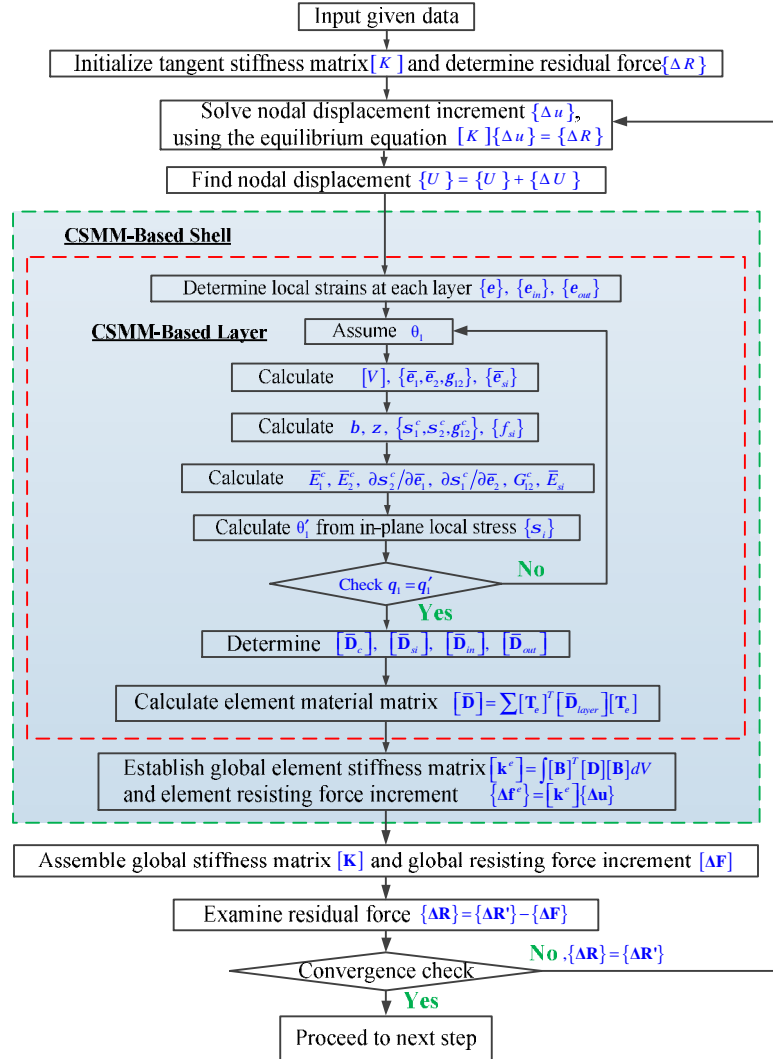


Figure 3.17 Analysis procedure for the CSMM-based shell element with iteration

This flow chart shows the simple analysis procedure of RC shell structures using load increment. The procedure can be incorporated with other static integrators such as displacement control for different kinds of nonlinear finite element analysis. The solution algorithm in the flow chart uses the Newton-Raphson method. The constitutive material matrix  $[\bar{D}]$ , the element tangent stiffness matrix  $[k]$ , and the global stiffness matrix  $[K]$

are calculated in each iteration. The Newton-type methods with acceleration technology such as KrylovNewton method (Carlson and Miller 1998) also can be used.

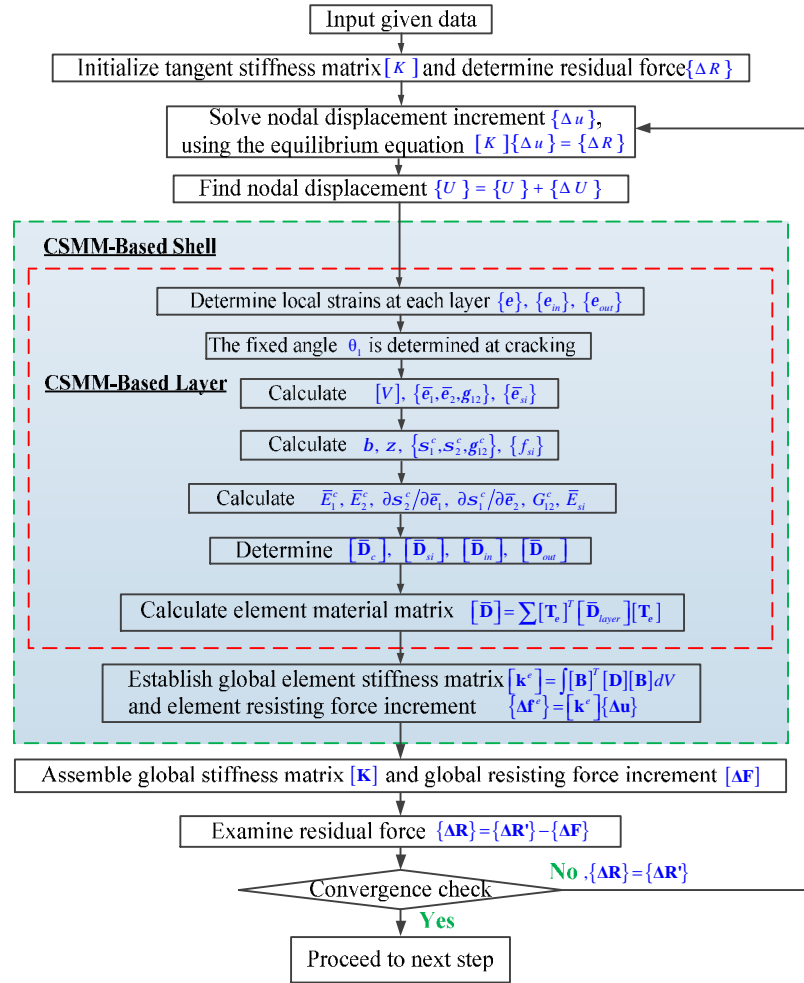


Figure 3.18 Analysis procedure for the CSMM-based shell element without iteration

Convergence criterion is required to determine if convergence has been achieved at the end of an iteration step. The criterion can be based on the accuracy of the unbalance nodal force, displacement increment, and energy increment. The general convergence criteria are force criterion, displacement criterion, and energy criterion. The criteria based on the normalized relative values are expressed as follows:

$$\text{For force criterion} \quad \frac{\sqrt{\sum R_i^T R_i}}{\sqrt{\sum R_0^T R_0}} < TOL, \quad (3.78)$$

$$\text{For displacement criterion} \quad \frac{\sqrt{\sum (\Delta U_i)^2}}{\sqrt{\sum (\Delta U_0)^2}} < TOL, \text{ and} \quad (3.79)$$

$$\text{For energy criterion} \quad \frac{\sqrt{\sum \Delta U_i^T R_i}}{\sqrt{\Delta U_0^T R_0}} < TOL, \quad (3.80)$$

where  $\Delta U$  is the nodal displacement increment;  $R$  is the unbalanced nodal force; subscription “ $i$ ” represents the  $i$ th iteration; subscription “0” represents the first iteration; and  $TOL$  is the specified tolerance, which will be dependent on the accuracy required and the problem type.

## 3.6 Nonlinear Finite Element Program SCS-3D

### 3.6.1 Implementation

In this study, new classes that represent the proposed element and material are implemented into the OpenSees framework to create a finite element program named SCS-3D (Simulation of Reinforced Concrete Structures in Three Dimension). This program can perform nonlinear finite element analysis of reinforced concrete shell structures under static, reversed cyclic, and dynamic loading. Chapter 4 validates the program by comparing the predictions to the tests of panels, framed shear walls, and bridge columns. In Chapter 5 and Chapter 6, the program was used to predict the behavior of a RC nuclear containment vessel and a RC two-story building under reversed cyclic and seismic loading. The details of the finite element program SCS-3D program are presented in this section.

Table 3.2 presents all of the classes employed for the CSMM-based shell element in this study. Two UniaxialMaterial modules for concrete (ConcreteZ01) and steel (SteelZ01)

were created previously based on the uniaxial constitutive relationship of concrete and steel in CSMM (Zhong, 2005). In this study, the proposed 8-node CSMM-based shell element, so-called CSMMShellS8, was implemented into OpenSees. The element has six degree of freedoms (DOFs) at each node, in which, three DOFs represent the displacements, two DOFs represent rotations, and one DOF is drilling degree for freedom derived based on drilling theory. The NDMaterial module, so-called CSMMLayer, was created to incorporate the formulation of the tangential material matrix for concrete and steel into each layer of the developed shell element.

**Table 3.2 Element and Material Classes of SCS-3D Program**

Module	Type	Remark
ConcreteZ01	UniaxialMaterial	Uniaxial constitutive model for concrete
SteelZ01	UniaxialMaterial	Uniaxial constitutive model for steel
CSMMLayer	NDMaterial	3D material model for each layer of CSMM-based shell element
CSMMShellS8	Element	8-node CSMM-based shell element

The implementation of the developed modules into OpenSees is shown in Figure 3.19. The ModelBuilder and Recorder objects are omitted in this figure. The CSMMLayer is implemented with the CSMMShellS8 element to represent the CSMM-based shell element. The CSMMLayer is related with the two UniaxialMaterial modules, SteelZ01 and ConcreteZ01, to determine the material constitutive matrix and calculate the stress of the elements at each layer. The program commands of the element and the materials are provided in the next section.

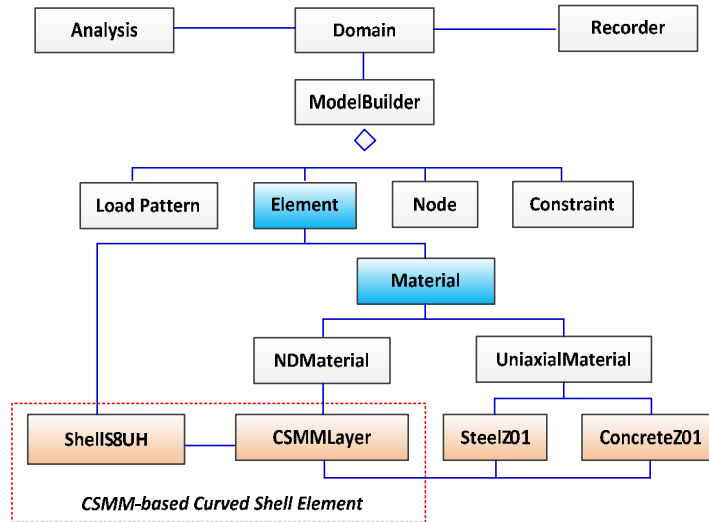


Figure 3.19 Implementation of element and material classes of SCS-3D program in OpenSees framework

## 3.6.2 Program Commands

### 3.6.2.1 ConcreteZ01

The input parameters for ConcreteZ01 are described as follows:

```
uniaxialMaterial ConcreteZ01 $mtag $fc $sec0
```

where \$mtag = unique integer tag identifying concrete material; \$fc = compressive strength of concrete; and \$sec0 = concrete strain at maximum strength. Note that both \$fc and \$sec0 should be in negative value.

### 3.6.2.2 SteelZ01

The input parameters for SteelZ01 are described as follows:

```
uniaxialMaterial SteelZ01 $mtag $fy $Es $fc $roust
```

where \$mtag = unique integer tag identifying steel material; \$fy = yield stress of steel; \$Es = initial elastic tangent of steel; \$fc = compressive strength of concrete; and \$roust = percentage of steel.

### 3.6.2.3 CSMMLayer

The input parameters for CSMMLayer are described as follows:

<b>nDMaterial</b>	<b>CSMMLayer</b>	\$mtag	\$rho	\$s1	\$s2	\$c1	\$c2	\$anfas1	\$anfas2
\$rous1	\$rous2	\$fc	\$fy	\$Es	\$ec0	\$Gc	\$type		

where \$mtag = unique integer tag identifying layer; \$rho = density of material; \$s1 = integer tag identifying the first uniaxial in-plane steel; \$s2 = integer tag identifying the second uniaxial in-plane steel; \$c1 = integer tag identifying uniaxial concrete in the first principal direction; \$c2 = integer tag identifying uniaxial concrete in the second principal direction; \$anfas1 = orientation angle identifying the direction of the first uniaxial in-plane steel material w.r.t. the local axes; \$anfas2 = orientation angle identifying the direction of the second uniaxial in-plane steel with respect to the local axes; \$rous1 = percentage of the first uniaxial in-plane steel; \$rous2 = percentage of the second uniaxial in-plane steel; ; \$fc = compressive strength of concrete; \$fy = yield stress of steel; \$Es = initial elastic tangent of steel; \$ec0 = concrete strain at maximum strength; \$Gc = out-of-plane shear modulus of concrete; and \$type = type of layer.

### 3.6.2.4 CSMMShellS8

The input parameters for CSMMShellS8 are described as follows:

<b>element</b>	<b>CSMMShellS8</b>	\$etag	\$node1	\$node2	\$node3	\$node4	\$node5
		\$node6	\$node7	\$node8	\$nlayer	\$t0	\$a0
						\$stag	\$ctag

where \$etag = unique integer tag identifying the shell element; \$node1. \$node8 = eight nodes defining element boundary; \$t0 = total thickness of the shell element; \$a0 = concrete cover; \$stag = integer tag identifying the steel layer; and \$ctag = integer tag identifying the concrete layer.

### 3.6.3 Graphical User Interface Module for Post-processing

The graphical post-processing of analytical results is one the most important steps in finite element analysis. It helps to investigate the behavior of the analyzed structures in a

more efficient way. Nowadays most of the general commercial FE software that has gone through long-term revision and evolution has had sophisticated GUI. The OpenSees framework is the domain-specific FE programs that are developed from and shared among the research communities. OpenSees is powerful in terms of finite element computational technologies. However, it does not design to support graphical post-processing. There are few research groups developed some graphical interface software for OpenSees, for example, OpenSeesNavigator or OpenSeesPL. These software programs have limited function or are not open-source so that other researchers are allowed to implement their developed element. Because this research is aimed at developing a complete set of FE software, effort is also made to develop a graphical user interface (GUI) module.

In this study, in addition to the implementation of the proposed element and material models, a GUI module is also developed for the finite element program SCS-3D. The user interface function of SCS-3D is developed based on a graphical framework, Eyeshot, using Visual Basic .Net. Eyeshot is a 3D graphics control component for .NET Framework developed by devDept Software company in Italy, is written in managed C#, and provides integration with Visual Studio .NET IDE. This allows programmers to use Visual Studio .NET to leverage their current programming language (C# or Visual Basic .NET) when programming with Eyeshot, as shown in Figure 3.20. The product is based on a per-developer licensing scheme and is royalty-free to distribute ([www.devdept.com](http://www.devdept.com)). The user interface module is described in this section.

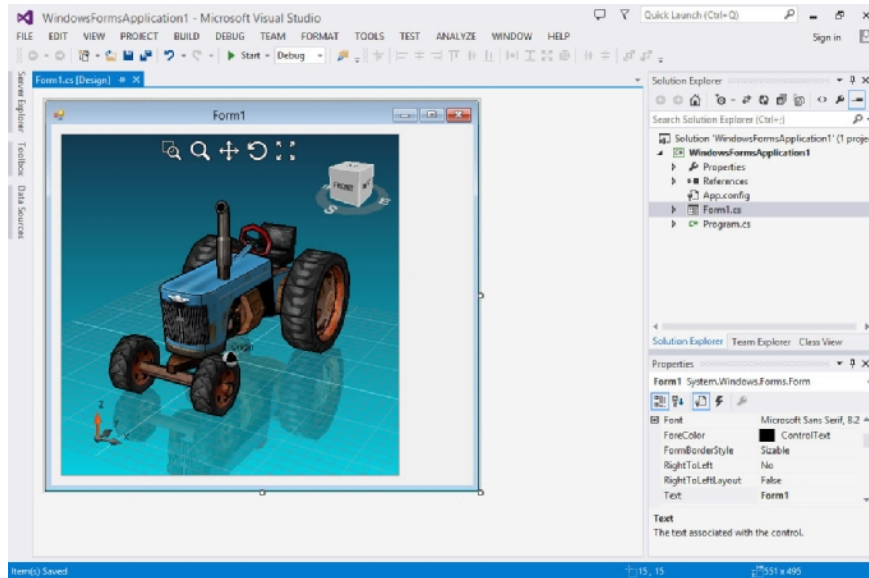


**Figure 3.20 Programming graphical model with Eyeshot framework using VisualBasic.Net**

The developed GUI software is built as an MDI (multiple document interface) application under Microsoft Windows system on PCs using Visual Basic .Net programming language. The full-screened main window of the software serves as the background workspace, as shown in Figure 3.21. The full-screen main window consists of two child windows. The left window is used for the inputting command to build the mode, and the right window is used for showing the visualization of the result. Pull-down menus, short-cut buttons for command editing and post-processing, and status and message bars, appear with the main workspace on the main window.

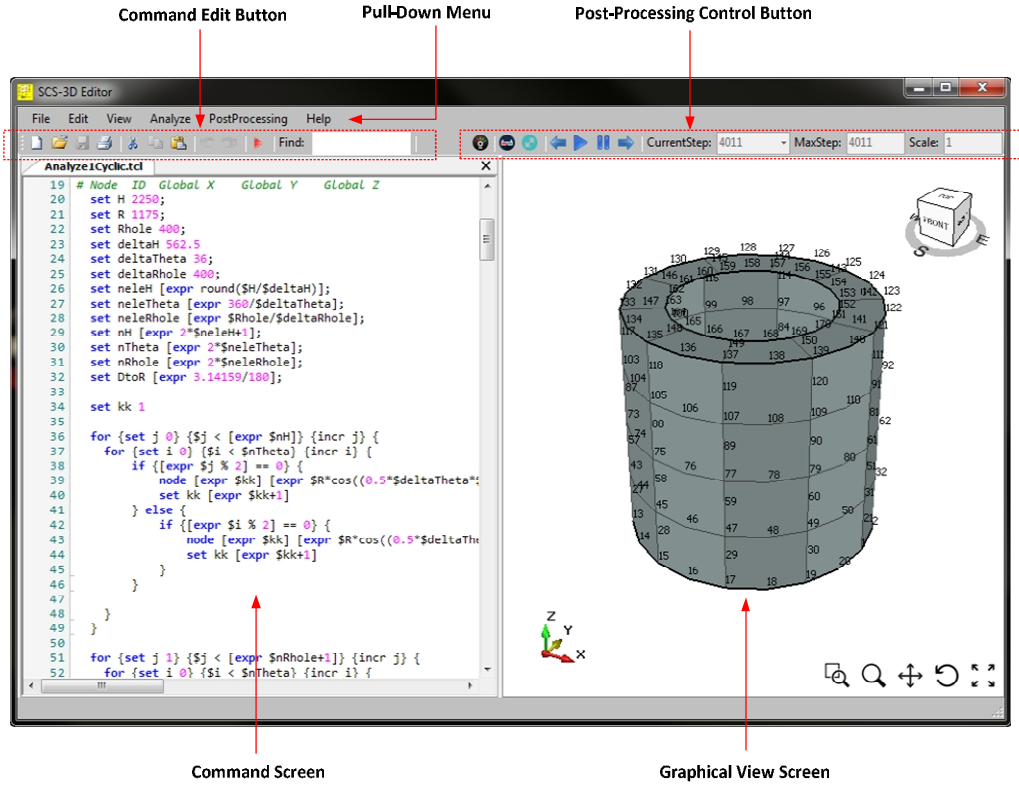


Figure 3.21 User interface of SCS-3D program

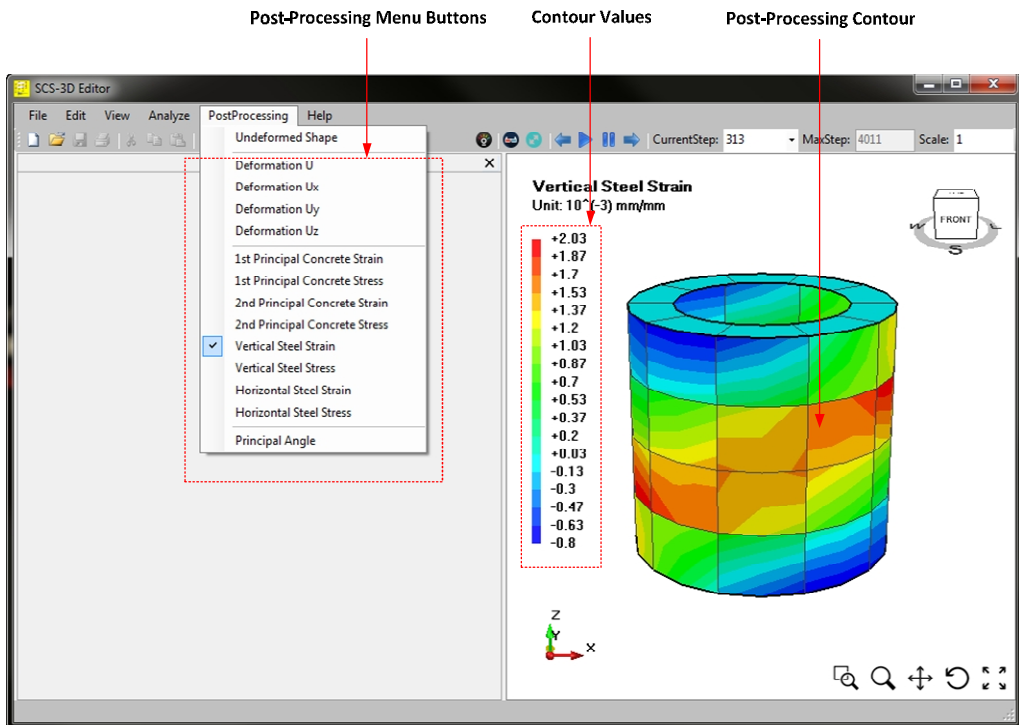
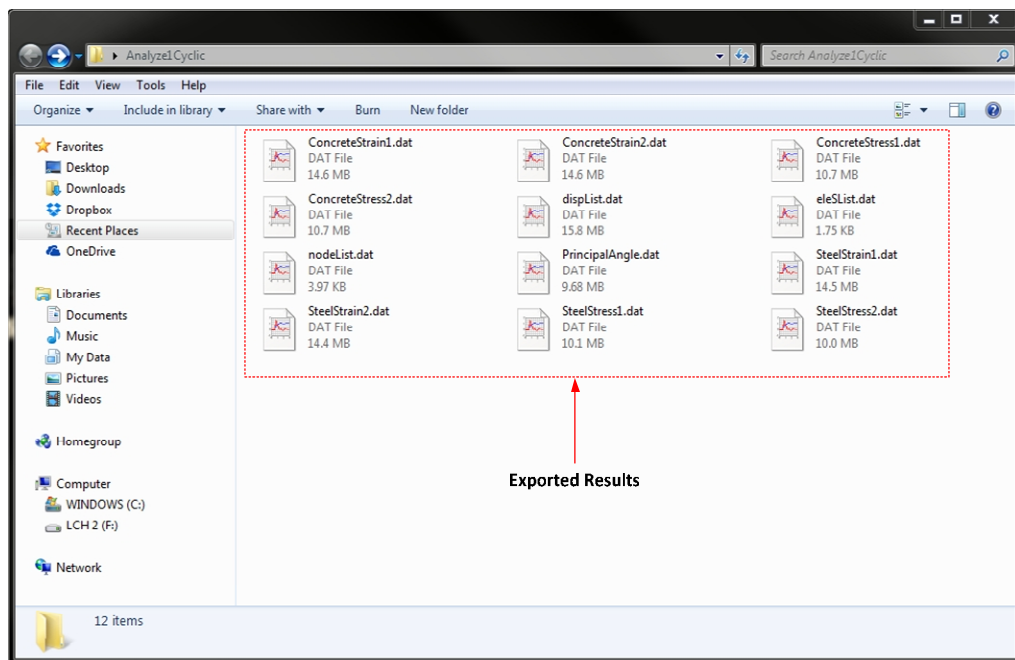


Figure 3.22 Post-processing function of SCS-3D program

The program currently can perform post-processing for the developed shell element, which allow users to be able to see the total displacement, the displacement in each of the global x-, y- or z- direction. Additionally, the stresses and strains of concrete and reinforcement at each layer can also be plotted. In Figure 3.22, a contour diagram is shown with a measurement bar to allow the users to observe of the interested parameter at any location in the model. To use the post-processing function, the users need to select the folder that contains all the exported data files, as shown in Figure 3.23.



**Figure 3.23 Files of analytical results**

# CHAPTER 4

## VALIDATIONS

### 4.1 Introduction

This chapter describes the several correlation studies that were conducted to verify the accuracy of the CSMM-based shell element developed in the study. The structures selected for validations included a panel tested under pure shear (Mansour & Hsu, 2005a; Pang & Hsu, 1996), panels tested under pure bending and a combination of shear and bending (Polak & Vecchio, 1994), a 3D RC cylindrical tank (Maekawa, Okamura, & Pimanmas, 2003), RC shear wall (Palermo & Vecchio, 2002), and six RC rectangular and circular hollow bridge piers (Yeh & Mo, 1999; Yeh, Mo, & Yang, 2001). All structures were tested until failure happened under either monotonic or reverse cyclic loading. The failure modes of the selected structures involved both flexural and shear failures.

### 4.2 Simulation of RC Panels Tested by Pang (1991)

#### 4.2.1 Test Description

The three panels Pang (1991) tested were selected to validate the capacity of the developed CSMM-based shell element in predicting the structural behavior of the RC panels under monotonic pure shear. The selected panels, named A2, A3, and A4, had the same dimensions of 1397 x 1397 x 178 mm, as shown in Figure 4.1. The percentages of reinforcement in panels A2, A3, and A4 were 1.19%, 1.79%, and 2.98%, respectively, in each orthogonal direction. The material properties of the specimens are presented in Table 4.1, in which, the panels A3 and A4 had similar compressive strengths of 42 MPa

while the compressive strength for panel A2 was 41 MPa. The yielding stresses of steel bars were 463 MPa, 447 MPa, and 470 MPa for panels A2, A3, and A4, respectively.

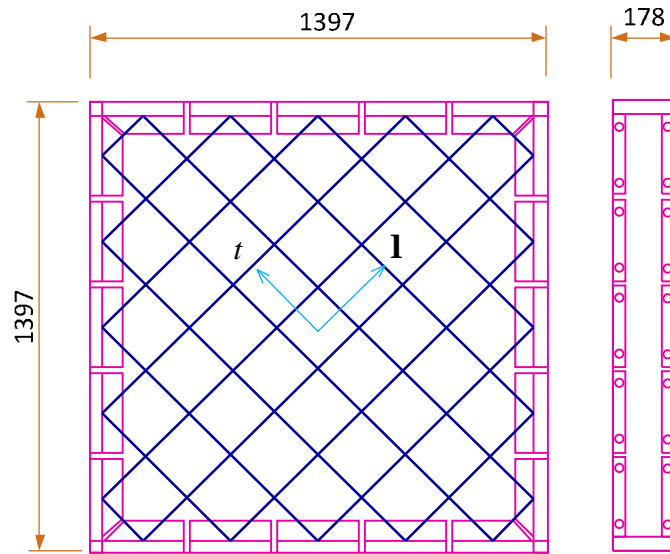


Figure 4.1 Dimensions of panels A2, A3, and A4 (Pang & Hsu, 1995)

Table 4.1 Loading and Material Properties of Pang's Panels

Specimen Name	Loading Scheme	$f'_c$ (MPa)	Reinforcement in <b>I</b> -direction		Reinforcement in <i>t</i> -direction	
			$f_y$ (MPa)	$r_1$ (%)	$f_y$ (MPa)	$r_t$ (%)
A2		41	463	1.19	463	1.19
A3		42	447	1.79	447	1.79
A4		42	470	2.98	470	2.98

#### 4.2.2 Analytical Model

The finite element analyses were carried out to simulate the behavior of the panel using the CSMM-based shell element developed in this study, the CSMMShellS8. Figure 4.2 shows the finite element mesh used for each panel. Because material properties and stress are uniformly distributed within each panel, only one CSMMShellS8 element was needed to model the behavior of the panel. Five layers of concrete and two layers of steel were assigned for each element using the CSMMLayer material module, as illustrated in Figure 4.3. To simulate the pure shear condition, constraints and applied loads were assigned so that the element was subjected to uniform tensile stress in the horizontal direction and uniform compressive stress in the vertical direction simultaneously.

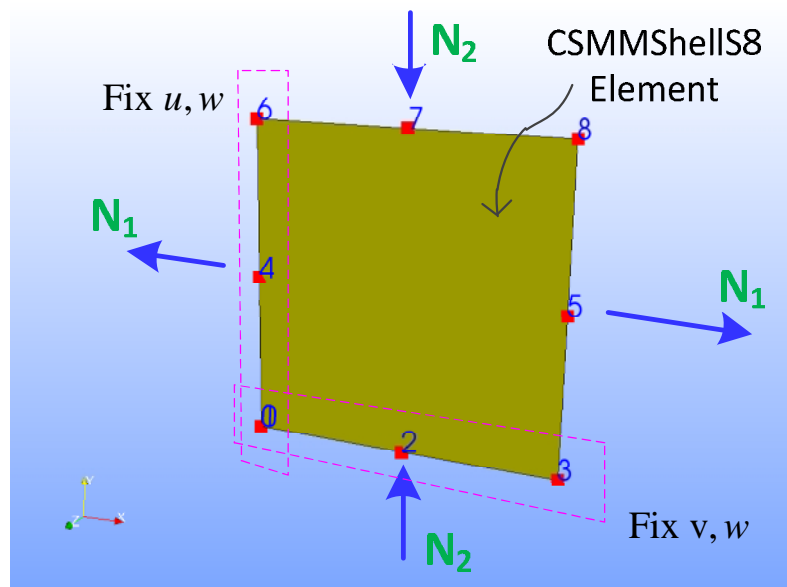
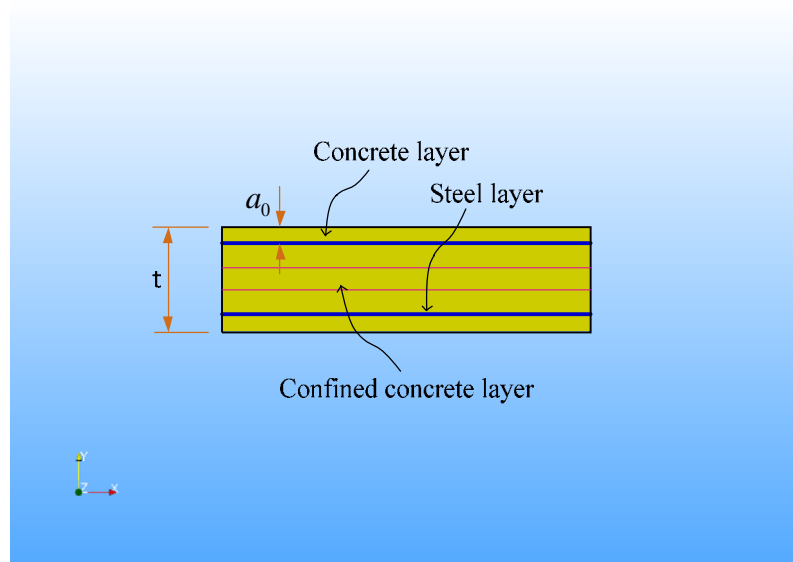


Figure 4.2 Finite element mesh used for panels A2, A3, and A4

The analyses were performed by a predetermined displacement control scheme. The common displacement increment used in the analyses was 0.01 mm. The KrylovNewton

method was used as the solution algorithm. The nodal displacement and corresponding horizontal forces were recorded at each converged displacement step, and the stress and strain of the elements were monitored.



**Figure 4.3** Cross section mesh of the shell element used for Pang's panels

#### **4.2.3 Comparison of Analytical Results with Experimental Results**

The analytical shear stresses versus the shear strains of the three panels obtained from the analytical model were compared with the experimental results, as shown in Figure 4.4. The analytical results and the experimental results are illustrated by solid curve and dotted curve, respectively.

The analytical result shows a good correlation with experimental data. The panels were chosen from a test group to verify the effect of the amount of reinforcement on the shear stress-strain relationship of RC panel under the monotonic pure shear. Figure 4.4 shows that the increase of the amount of reinforcement causes the rising of the shear

strength and the reducing of the shear ductility. This effect was captured well by the analytical model. Not only the shear strength but also the shear ductility of the panels were estimated. Furthermore, the ascending branch of the shear stress and strain curve was predicted, which reflected the failure mode caused by the crushing of the diagonal concrete.

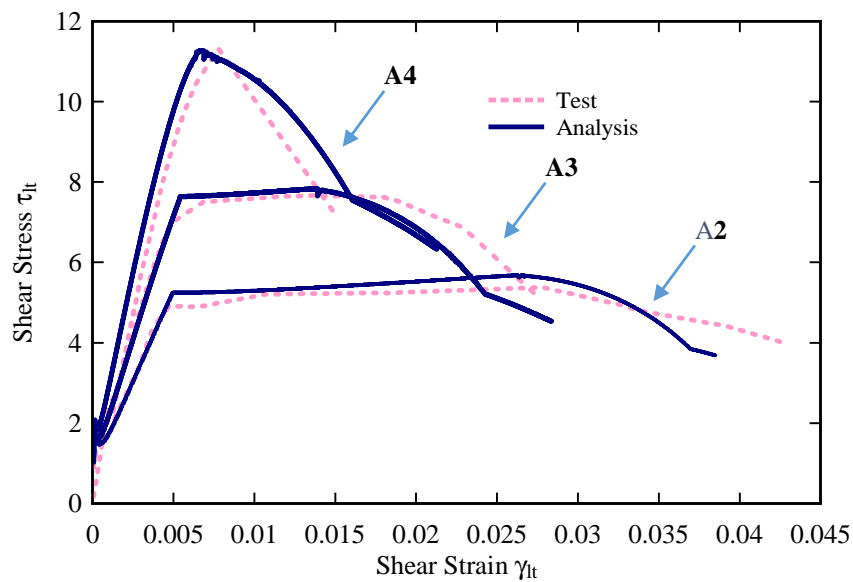


Figure 4.4 Comparison between experimental and analytical shear stress versus shear strain for panels A2, A3, and A4

### 4.3 Simulation of RC Panels Tested by Mansour (2001)

#### 4.3.1 Test Description

The developed CSMM-based shell element can be used to predict the cyclic shear behavior of reinforced concrete structure because CSMM is a cyclic constitutive model. Two RC panels tested by Mansour were chosen to verify this capacity of the developed shell element. The two panels, CA3 and CE4, had the same dimensions of 1397 x 1397 x

178 mm, as shown in Figure 4.5 and Figure 4.6. However, the orientations of steel in the panels were different. Panel CA3 was reinforced by steel bars of 45° angles, and panel CE4 was reinforced by steel bars of 0° angles. The angles were the difference between the steel orientation and the principal tensile stress. Material properties of the specimens are given in Table 4.2, in which, the compressive concrete strengths used for panels A3 and A4 were 46 MPa and 48 MPa, respectively. The percentage of reinforcement in panels CA3 and CE4 were 1.7% and 1.9%, respectively, in each direction. The yielding stresses of steel bars were 425.4 MPa and 453.4 MPa for panel CA3 and panel CE4, respectively.

#### 4.3.2 Analytical Model

The finite element analyses were conducted to simulate the behavior of the panel using the CSMM-based shell element. The finite element models of the two panels were similar to the monotonic pure shear panels (Figure 4.2), except that the monotonic loading was replaced by the reserved cyclic loading.

**Table 4.2 Loading and Material Properties of Mansour's Panels**

Specimen Name	Loading Scheme	$f'_c$ (MPa)	Reinforcement in $\mathbf{l}$ -direction		Reinforcement in $t$ -direction	
			$f_y$ (MPa)	$r_1$ (%)	$f_y$ (MPa)	$r_t$ (%)
CA3		46	425.4	1.7	425.4	1.7
CE3		48	453.4	1.9	453.4	1.9

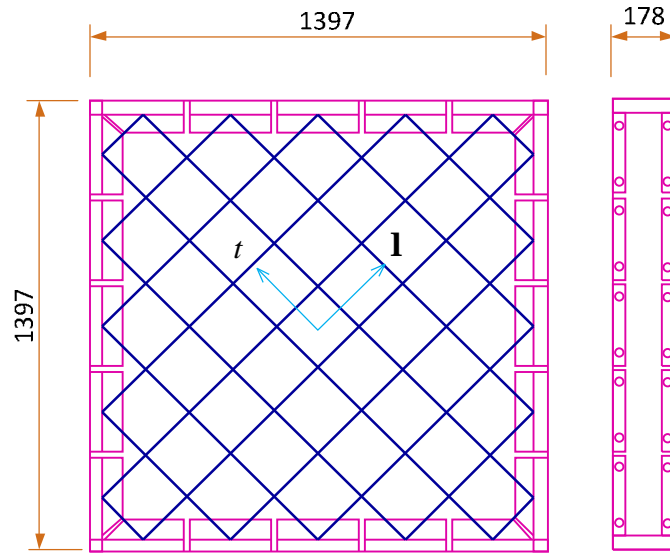


**Figure 4.5 Dimensions of panel CA3 (Mansour, 2001)**

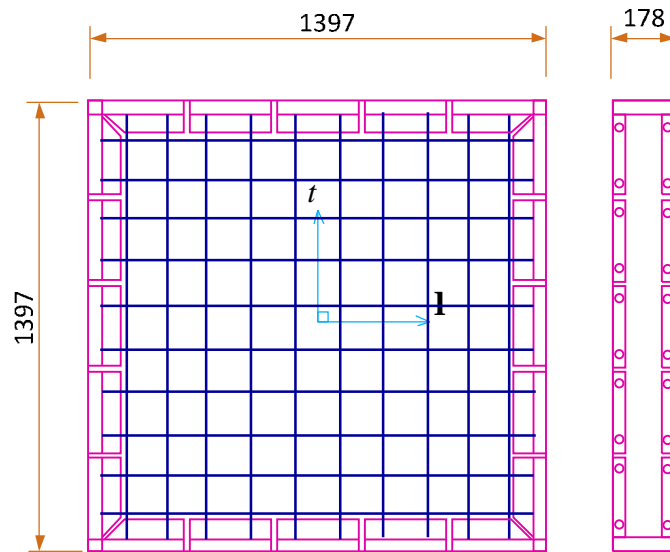


**Figure 4.6 Dimensions of panels CE4 (Mansour, 2001)**

### **4.3.3 Comparison of Analytical Results with Experimental Results**

The analytical shear stresses versus shear strains of the two panels obtained from the analytical model are compared with the experimental result, as shown in Figure 4.7 and

Figure 4.8. The analytical result and the experimental result are illustrated by a solid curve and a dotted curve, respectively. The analytical results are shown to have a good agreement with the experimental data. Overall, the backbone envelopes as well as the unloading and reloading paths of the shear stress and shear strain curve are predicted well by the model. One important characteristic obtained from experimental results of the two panels, which is simulated by the model, is the pinching effect. As shown in the figures, the panel CA3 displayed a highly pinched shape in the hysteretic loops of the shear stress versus shear strain curve; in contrast, the hysteretic loops of the panel CE4 were robust and well-rounded with no trace of pinched shape.

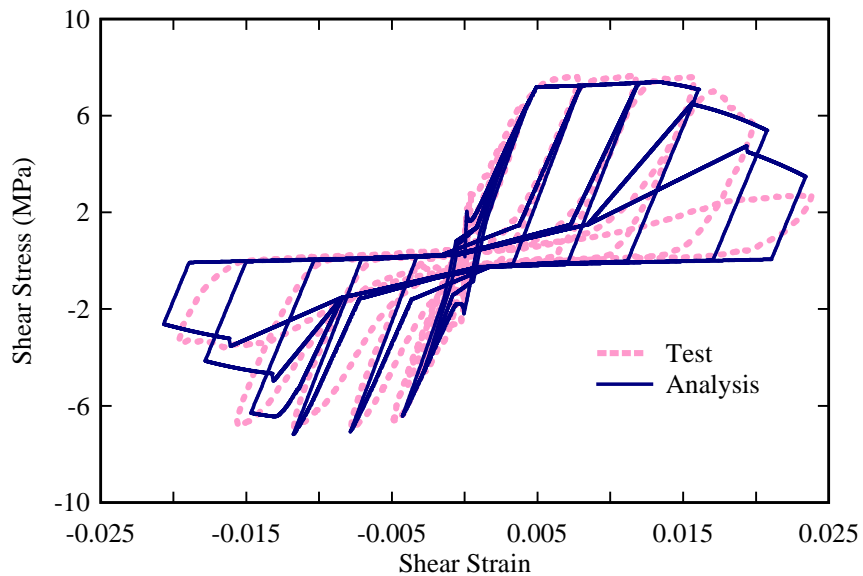


**Figure 4.7 Comparison between experimental and analytical shear stress versus shear strain for panel CA3**

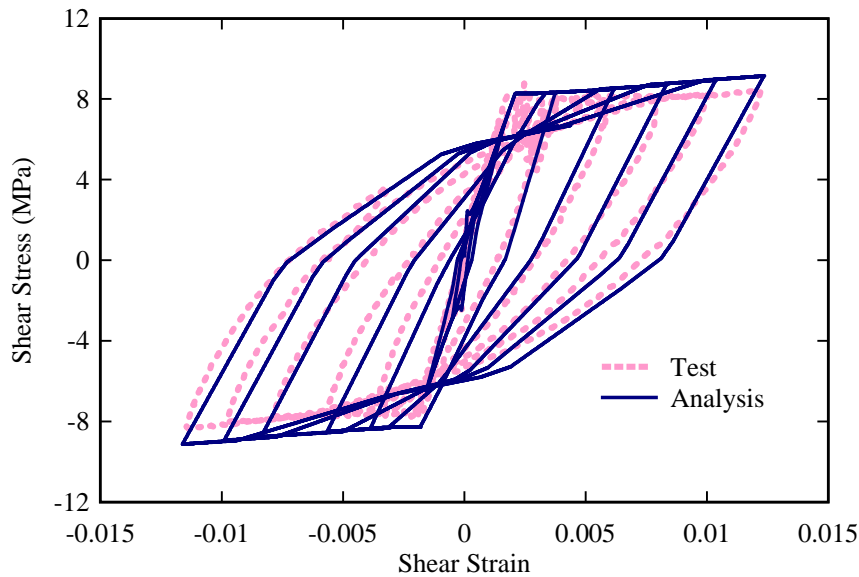


**Figure 4.8 Comparison between experimental and analytical shear stress versus shear strain for panel CE4**

## **4.4 Simulation of RC Panels Tested by Polak (1992)**

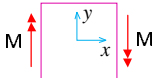
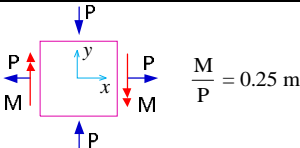
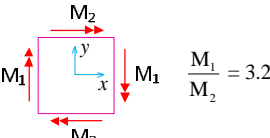
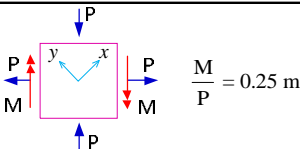
### **4.4.1 Test Description**

The proposed shell element was continued to be verified by four panels subjected to a combination of out-of-plane bending moment and in-plan shear. The tests were performed by Polak (1992) at the University of Toronto, Canada. All four panels had the same dimension of 1625 x 1625 x 316 mm. However, the orientations of steel in the panels were different. Panels SM1, SM2, and SM3 were reinforced by steel bars of  $0^\circ$  angles, and panel SM4 was reinforced by steel bars of  $45^\circ$  angles, as shown in Figure 4.9 and Figure 4.10. The angles were the difference between the steel orientation and the principal tensile stress. Material properties and loading schemes of the specimens are given in Table 4.3. Each panel used different compressive concrete strength; however, the properties of reinforcement were similar. All four panels were reinforced with 1.25% steel per layer and 0.42% steel per layer in the x-direction and y-direction, respectively.

The yielding strength of steel bars in the x- direction and y-direction were 425 MPa and 430 MPa, respectively.

As shown in Table 4.3, four different loading schemes were used in the experimental program. Panels SM1 and SM3 were subjected to pure uniform out-of-plane bending moment, in which one-way moment was applied to SM1 along the horizontal direction and two-way moments were applied to panel SM2 in both horizontal and vertical direction with the moment ratio of 3.2. Panels SM2 and SM4 were subjected to a combination of uniform out-of-plane moment and uniform in-plane shear.

**Table 4.3 Loading and Material Properties of Polak's Panels**

Specimen Name	Loading Scheme	$f'_c$ (MPa)	Reinforcement in x-direction		Reinforcement in y-direction	
			$f_y$ (MPa)	$r_x^*$ (%)	$f_y$ (MPa)	$r_y^*$ (%)
SM1		47	425	1.25	430	0.42
SM2		62	425	1.25	430	0.42
SM3		56	425	1.25	430	0.42
SM4		64	425	1.25	430	0.42

Note \* Percentage of reinforcement of each layer at top and bottom of the panel

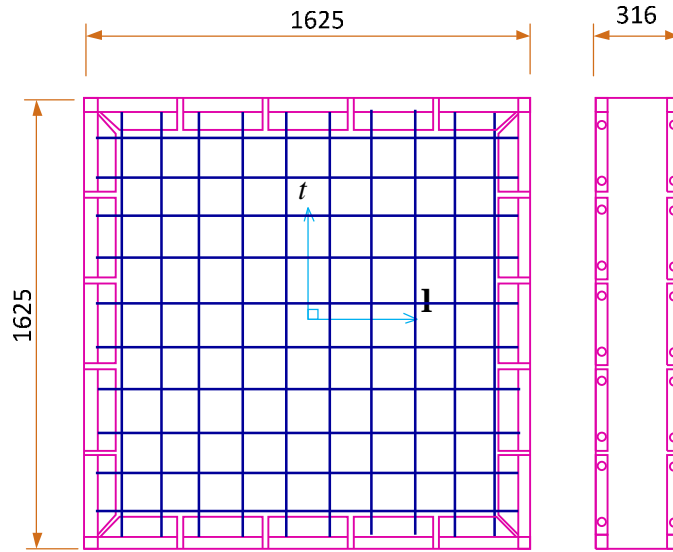


Figure 4.9 Dimensions of panels SM1, SM2, and SM3 (Polak, 1992)

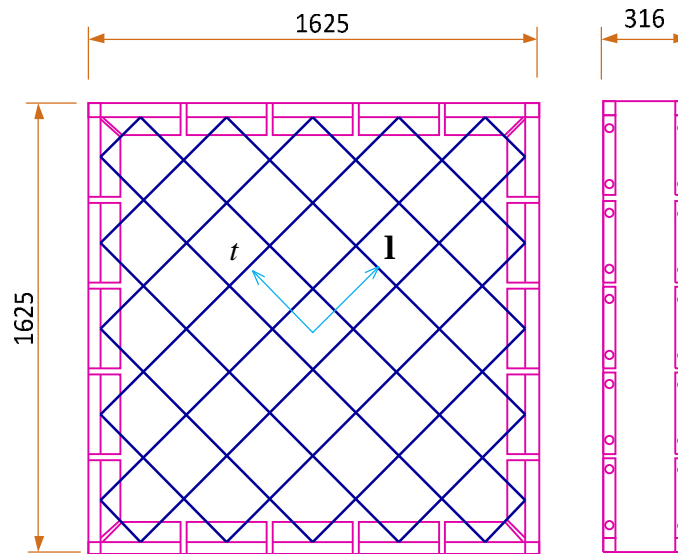
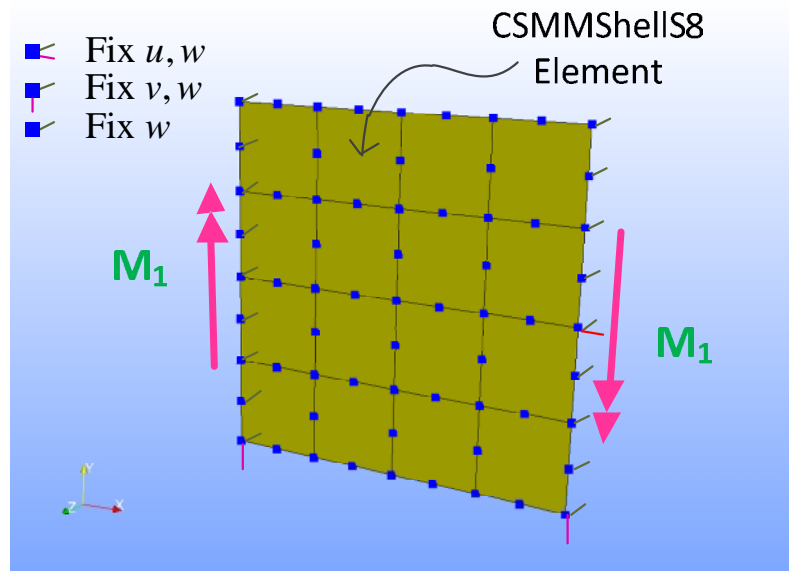


Figure 4.10 Dimensions of panel SM4 (Polak, 1992)

#### 4.4.2 Analytical Model

The finite element meshes of the four panels are illustrated in Figure 4.11 through Figure 4.14. In the model, a total of 16 CSMMShellS8 elements were utilized for each

panel. Because the model was expected to simulate bending behavior, many concrete layers should be used to capture the variation of stress along the cross-section of the element. Ten layers of concrete and two layers of steel were assigned for each element using the CSMMLayer material module. The figures also showed the constraints and loads applied to each element. To simulate the out-of-plane bending condition, uniform moments were applied along the edges of each element. To simulate the in-plane shear condition, constraints and loads were assigned so that the element was subjected to uniform tensile stress in the horizontal direction and uniform compressive stress in the vertical direction simultaneously.



**Figure 4.11** Finite element mesh used for panel SM1

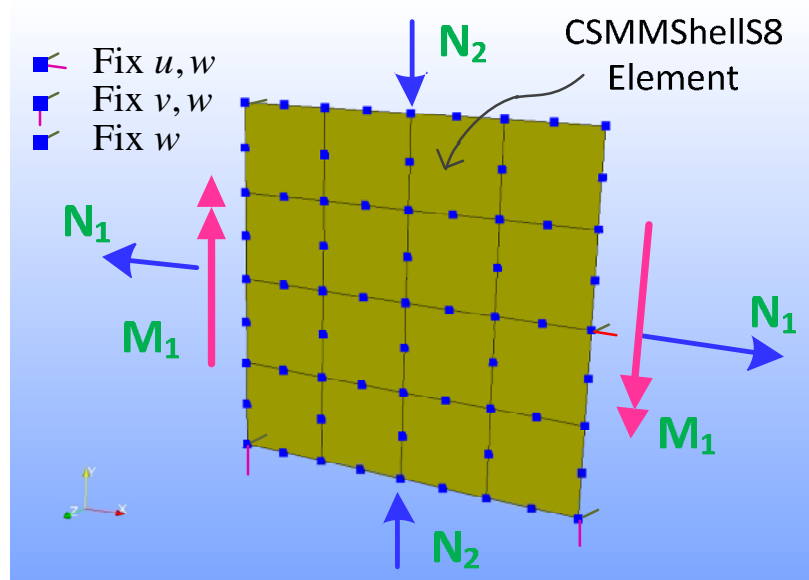


Figure 4.12 Finite element mesh used for panel SM2

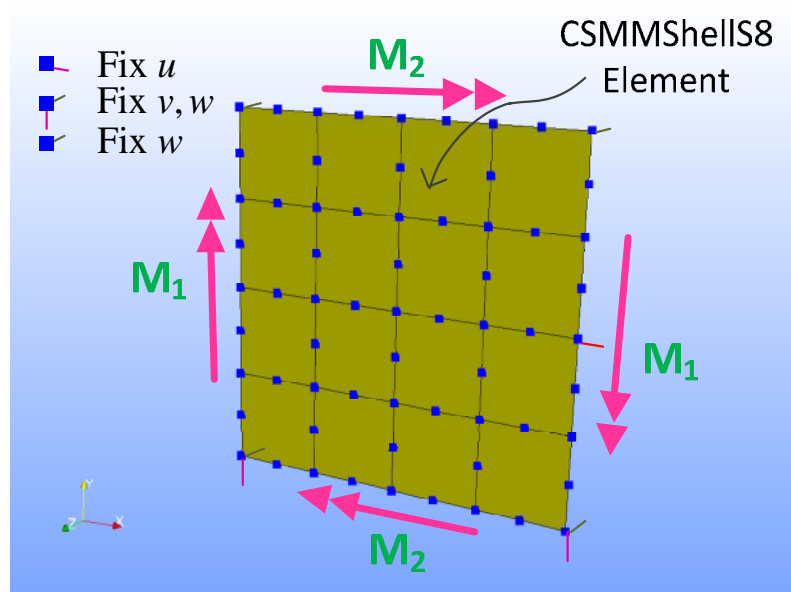


Figure 4.13 Finite element mesh used for panel SM3

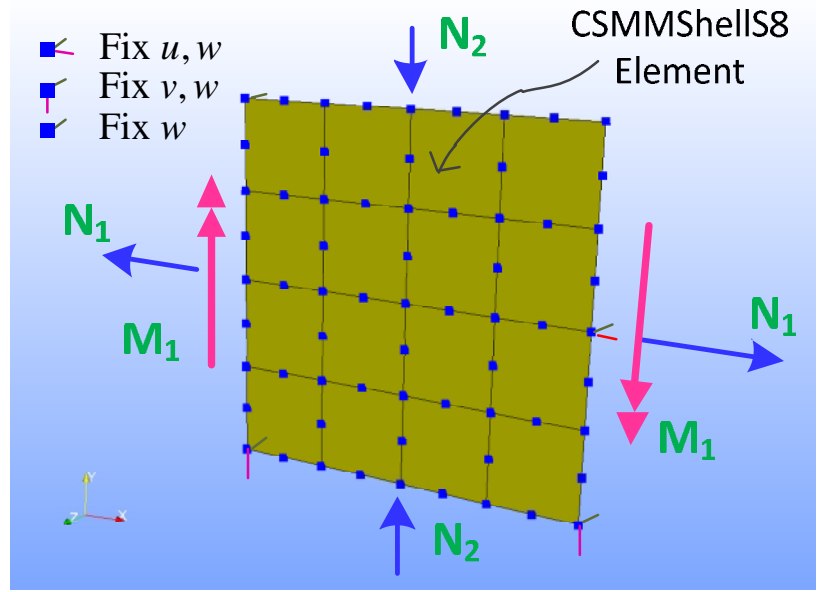


Figure 4.14 Finite element mesh used for panel SM4

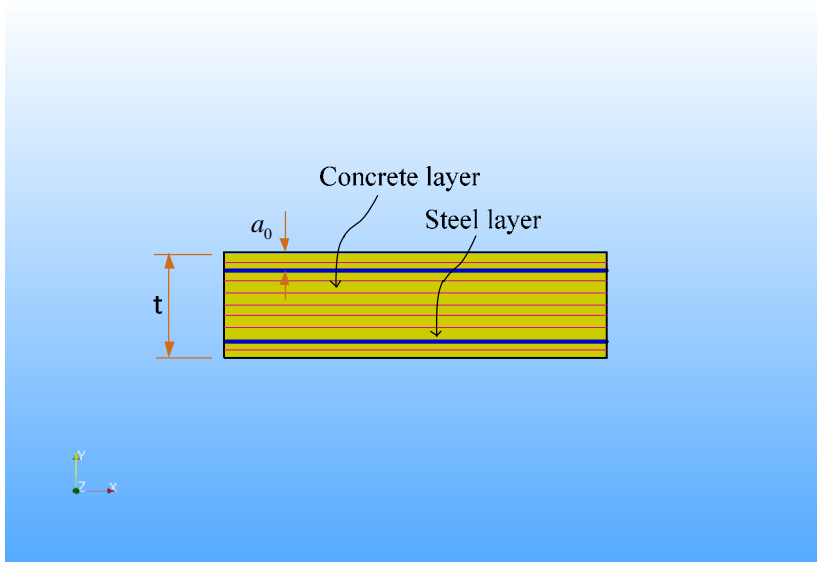


Figure 4.15 Cross section mesh of the shell element used for Polak's panels

The analyses were performed by a predetermined displacement control scheme. The common displacement increment used in the analyses was 0.01 mm. The KrylovNewton method was used as the solution algorithm. The nodal displacement, nodal rotation and corresponding moment were recorded at each converged displacement step. The curvature of the element was determined based on nodal rotations to compare with the experimental data.

#### 4.4.3 Comparison of Analytical Results with Experimental Results

The analytical moments versus curvatures of the four panels obtained from the analytical model were compared with the experimental result, as shown in Figure 4.16 to Figure 4.19. The analytical result and the experimental result were illustrated by solid curve and dotted curve, respectively. In general, the analytical results are shown to have a good agreement with the experimental data. The initial stiffness, the yielding point, and the ultimate moment were predicted well by the model.

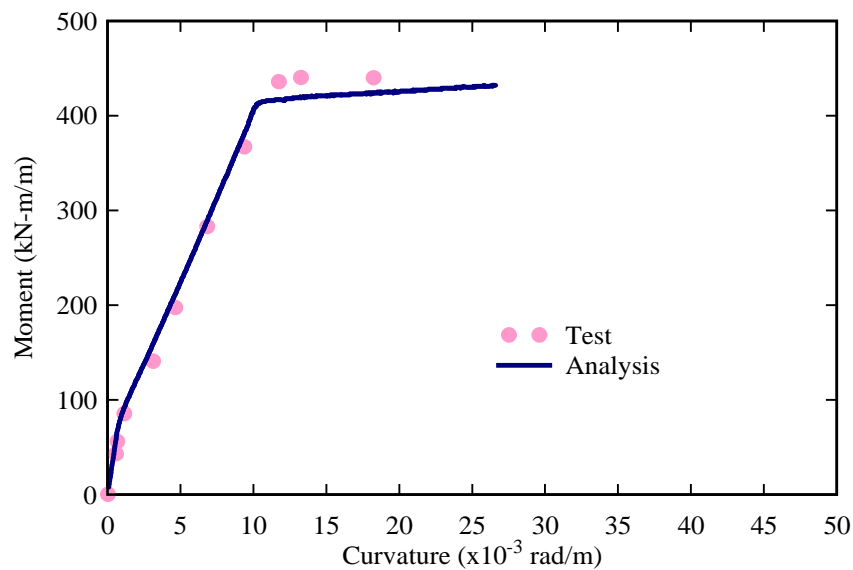
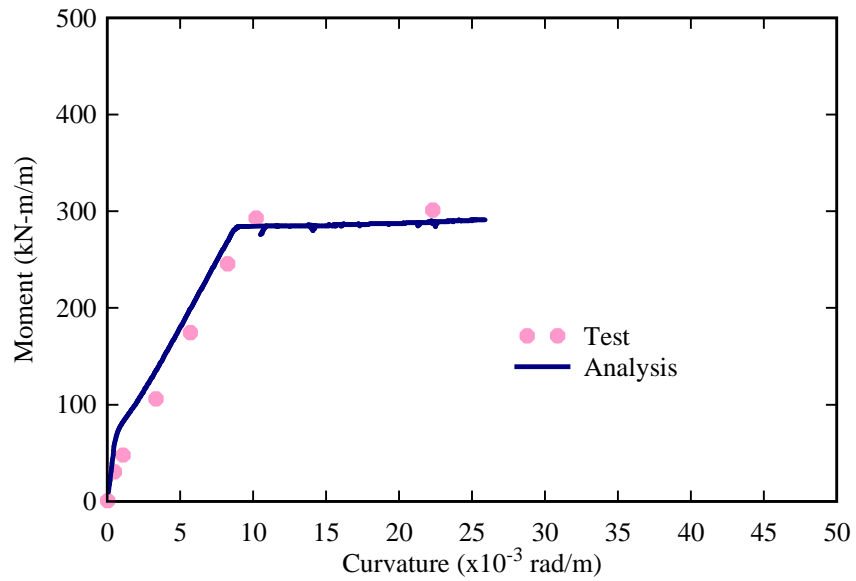
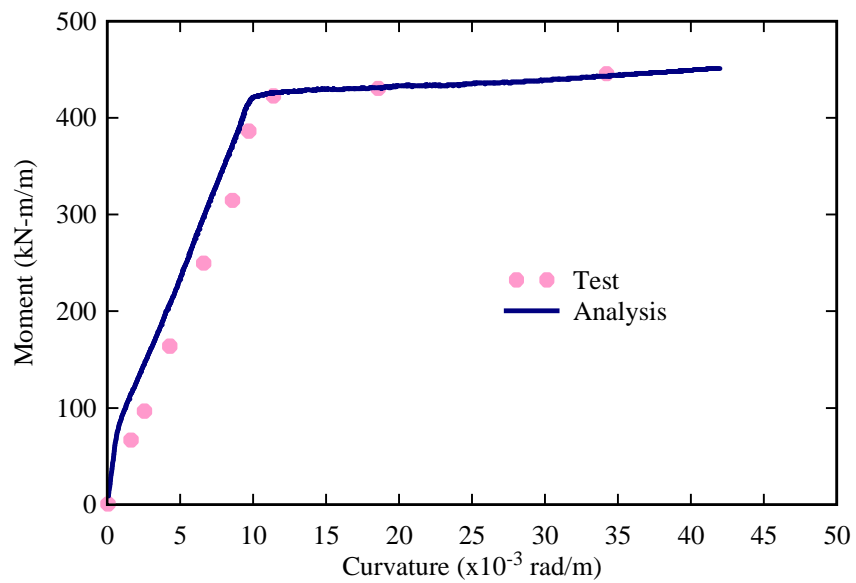


Figure 4.16 Comparison between experimental and analytical moment versus curvature for panel SM1



**Figure 4.17 Comparison between experimental and analytical moment versus curvature for panel SM2**



**Figure 4.18 Comparison between experimental and analytical moment versus curvature for panel SM3**

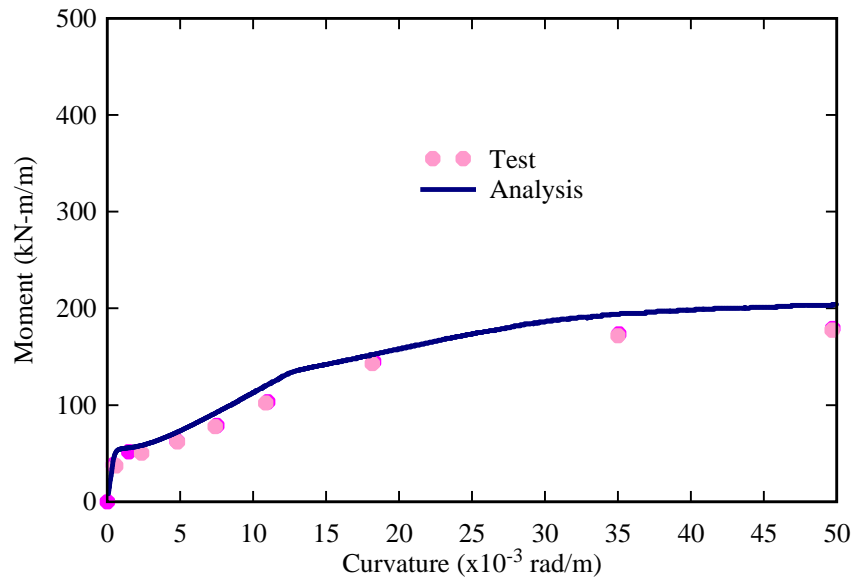


**Figure 4.19 Comparison between experimental and analytical moment versus curvature for panel SM4**

## 4.5 Simulation of a RC Cylindrical Tank

### 4.5.1 Test Description

The reduced-scale reinforced concrete (RC) tank specimen tested by Harada, Onituka, Adachi, and Matsuo (2001) (Figure 4.20) was selected to validate the capacity of the developed CSMM-based shell element in predicting the structural behavior of cylindrical RC structures under the reserved cyclic loading. The tank had a dimension of 2.0 m net height and 1.8 m radius (centerline dimension). The outer and inner diameters of the tank were 3.1 m and 2.9 m, respectively. The thickness of the tank was 0.1 m, as shown in Figure 4.20. The specimen was reinforced with 0.8% reinforcement ratios equally in both vertical and circumferential directions. Detail of dimensions and material properties of the specimen are summarized in Table 4.4. The average compressive strength of concrete used for the specimen was 28 MPa. The nominal yielding strength of vertical and

circumferential reinforcement was 384 MPa and 410 MPa, respectively. Figure 4.21 demonstrates the test setup of the specimen. The specimen was fixed at the bottom by steel rods that connected the specimen with a rigid plate foundation. The cyclic load was applied by three actuators, one with the capacity of 3000 kN and the others with the capacity of 500 kN each. No axial load was applied to the specimen. The cyclic load was transferred through a steel ring located on the top of the specimen. Bolt connections fixed the steel ring along the perimeter of the specimen. This test configuration allowed the loads to be uniformly distributed to the specimen (Maekawa et al., 2003)

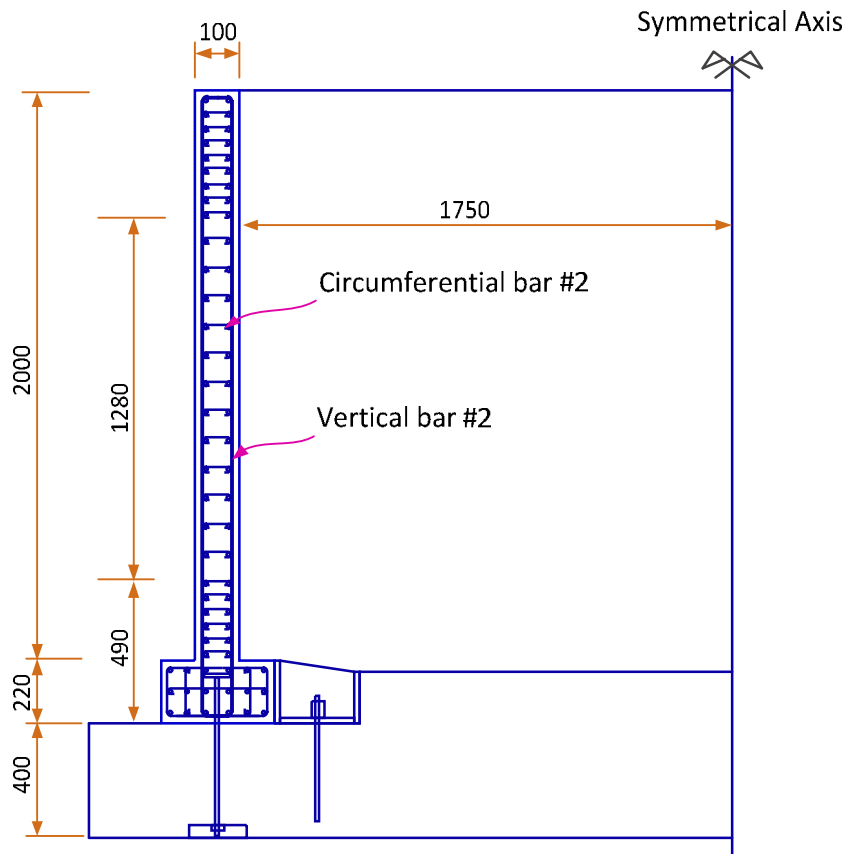
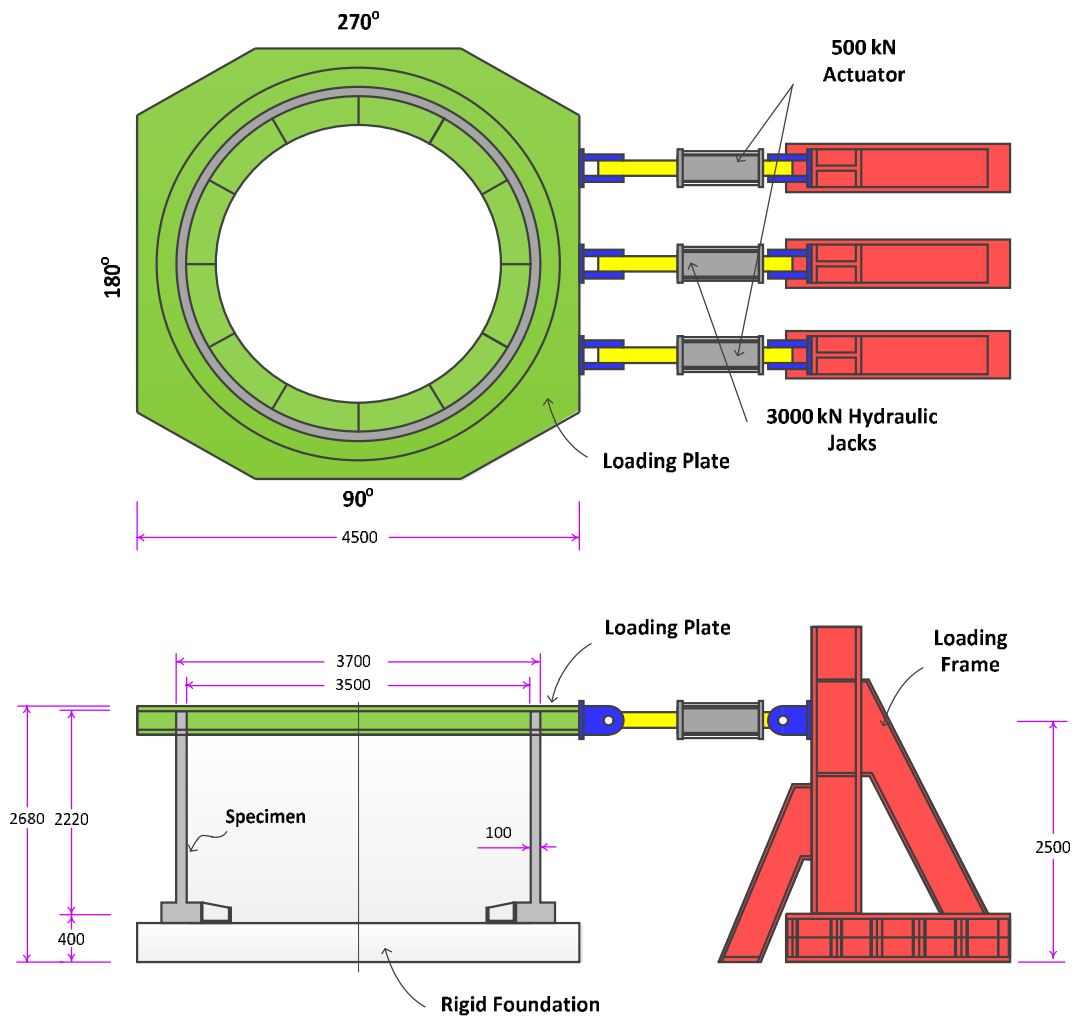


Figure 4.20 Dimensions and reinforcement details of RC cylindrical tank

**Table 4.4 Dimension and Material Properties of the RC Cylindrical Tank**

Specimen	$f'_c$ (MPa)	D (mm)	H (mm)	t (mm)	Vertical Reinforcement		Circumferential Reinforcement	
					$f_y$ (MPa)	$r_v$ (%)	$f_y$ (MPa)	$r_c$ (%)
1	28.0	3600	2000	100	384.0	0.8	410.0	0.8

Note :  $f'_c$  = Compressive strength of concrete; D = Diameter of the tank;  
 t = Thickness  $f_y$  = Yielding strength of steel; H = Effective height of the tank;  
 $r_v$  = Percentage of the vertical steel;  $r_c$  = Percentage of circumferential steel.



**Figure 4.21 Test setup of RC cylindrical tank**

#### 4.5.2 Analytical Model

A finite element analysis was carried out on the specimen. The specimen was modeled by the finite element mesh, as shown in Figure 4.22. The tank was modeled by 30 CSMMShellS8 elements, which were the CSMM-based shell element developed in this study. Ten layers of concrete and two layers of steel were assigned for each element using the CSMMLayer material module. All elements were assigned with 8% of reinforcement. The steel layers were defined at the exact locations of steel at the top and bottom of the cross-section of each element. The other ten RigidShellS8 elements, which are elastic 8-node shell elements with very high stiffness, are defined at the top of the model to simulate the rigid connection.

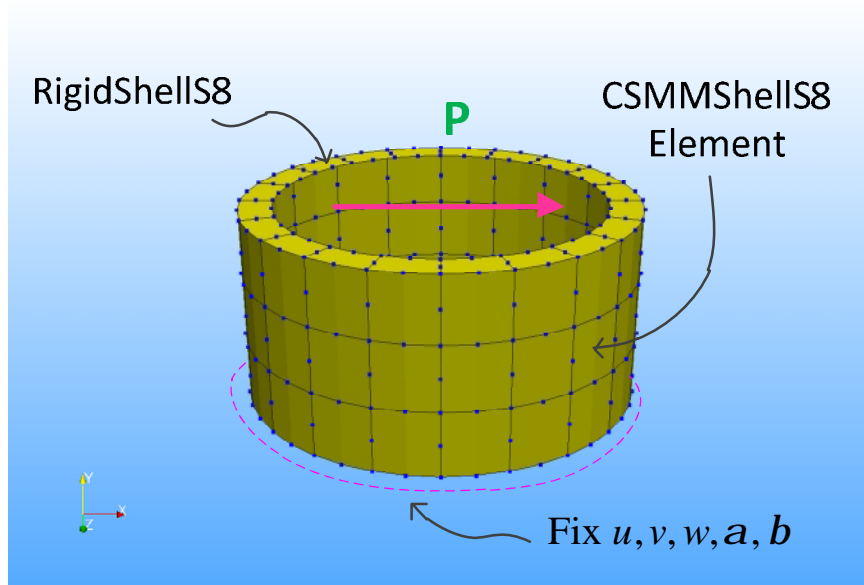
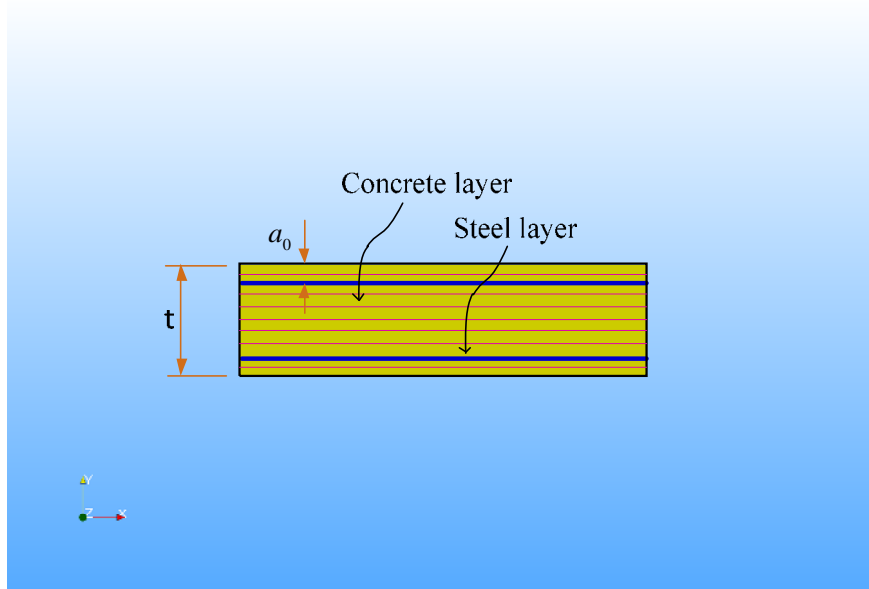


Figure 4.22 Finite element mesh used for RC cylindrical tank

All nodes at the bottom of the model were constrained to not allow any translations or rotations. Uniformly distributed loads were applied at all nodes along the perimeter at the

height level of the specimen, which satisfies the assumption that the horizontal loads were uniformly distributed on the top of the specimen. The analysis was performed by a predetermined displacement control scheme. The common displacement increment used in the analysis was 0.5 mm. The KrylovNewton method was used as the solution algorithm. The nodal displacement and corresponding horizontal forces were recorded at each converged displacement step, and the stress and strain of the elements were monitored.



**Figure 4.23** Cross-section mesh of the shell element used for RC cylindrical tank

### **4.5.3 Comparison of Analytical Results with Experimental Results**

The analytical horizontal force versus displacement relationships of the specimen obtained from the analytical model was compared with the experimental result, as shown in Figure 4.24. The analytical result and the experimental result are illustrated by a solid curve and a dotted curve, respectively. The analytical result was shown to provide a good correlation with experimental data. The specimen experienced a large deformation before

the load started to decrease. The analytical model predicted the large deformation and the starting point of the descending part. Overall, the primary backbone curve, the initial stiffness, the peak strength, the descending branch, and the failure characteristic of the analytical result matched closely with the experimental data. The analytical model accurately predicted the pinching effect and the unloading path.

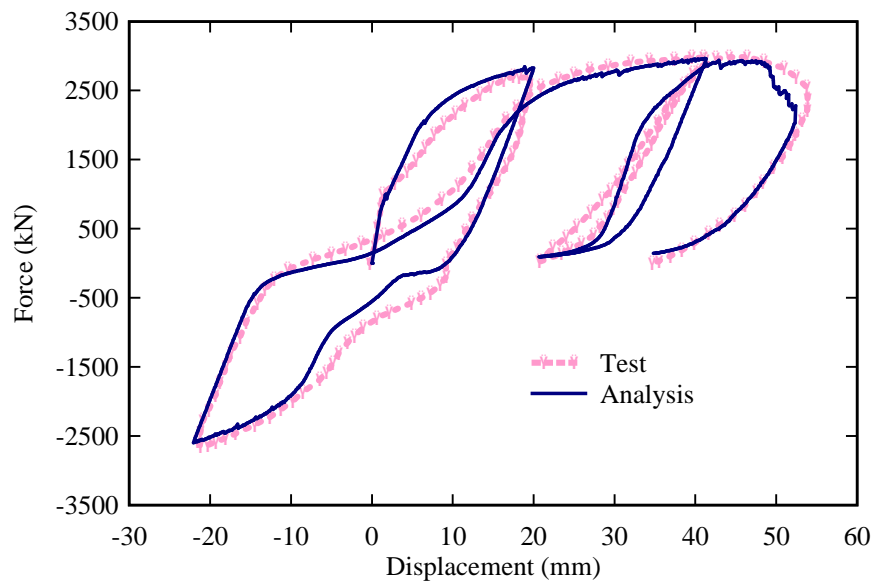


**Figure 4.24 Comparison between experimental and analytical load versus displacement for RC cylindrical tank**

## 4.6 Simulation of a 3D RC Shear Wall

### 4.6.1 Test Description

The proposed element was further validated by modeling a 3D reinforced concrete (RC) shear wall tested by Palermo and Vecchio (2002) at the University of Toronto, Toronto, Canada (Figure 4.25). The dimensions of the top and bottom slabs were 4415 x 4000 x 460 mm and 4415 x 4000 x 460 mm, respectively. The main specimens contained two parts: a web wall with the dimension of 2020 mm height and 75 mm thickness and

two flange walls with dimension of 2020 mm height and 95 mm thickness. Two layers of D6 reinforcing bars were provided vertically and horizontally within the specimen. The arrangement of the D6 reinforcing bars in the specimen is illustrated in Figure 4.26. The spacings of the D6 reinforcing bars in the web wall were 140 mm and 130 mm in the horizontal and vertical directions, respectively. Similarly, the spacing of 140 mm of D6 reinforcing bars was also used in the two flange walls in the horizontal direction. The arrangement of the D6 reinforcing bars in the vertical reinforcement of the two flange walls, however, was divided into two regions. The inner region, adjacent to the web wall, was reinforced with spacing of 140 mm, and the outer region, near the tip of the flanges, was reinforced with the spacing of 355 mm, as shown in Figure 4.26. The calculated amount of reinforcement and material properties of the specimen are summarized in Table 4.4. The average compressive strength of concrete used for the specimen was 21.7 MPa. The nominal yielding strength of 605 MPa was used for reinforcement in both longitudinal and transverse directions. Figure 4.27 illustrates the test setup of the specimen. The bottom slab was fixed to the laboratory strong floor to simulate a rigid foundation. An axial load of 940 kN was applied to the wall from four 600-kN-capacity hydraulic jacks. The simulated lateral earthquake load was applied through the top slab by two 1000-kN-capacity horizontal actuators.

**Table 4.5 Dimension and Material Properties of the 3D Shear Wall**

Wall Zone	$f'_c$ (MPa)	P (kN)	$\frac{P}{f'_c A_g}$	L (mm)	Longitudinal Reinforcement		Transverse Reinforcement	
					$f_y$ (MPa)	$r_l$ (%)	$f_y$ (MPa)	$r_s$ (%)
Web	21.7	940	0.054	2020	605.0	0.8	605.0	0.73
Inner Flange						0.62		0.58
Outer Flange						0.23		0.58

Note :  $f'_c$  = Compressive strength of concrete;  $A_g$  = Area of cross section;  
 $f_y$  = Yielding strength of steel;  $L$  = Effective height of the wall;  
 $r_l$  = Percentage of the longitudinal steel;  $r_s$  = Percentage of transverse steel.

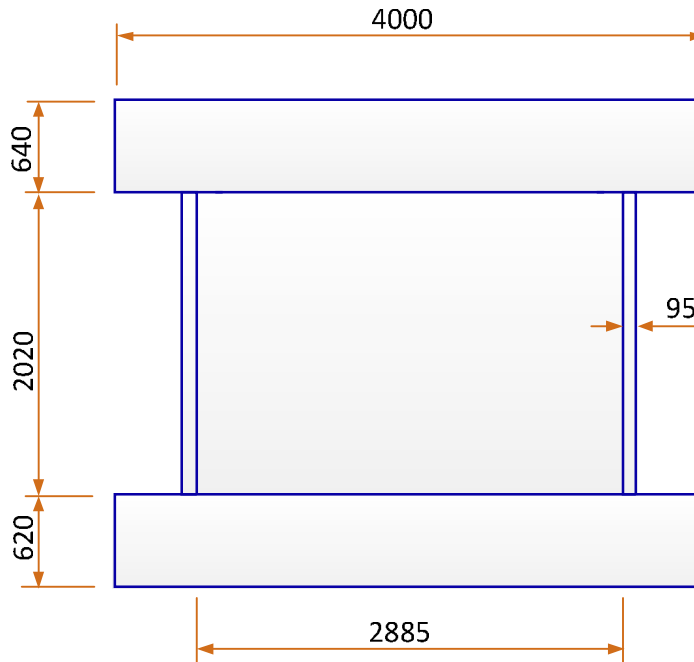


**Figure 4.25 Elevation view of 3D shear wall**

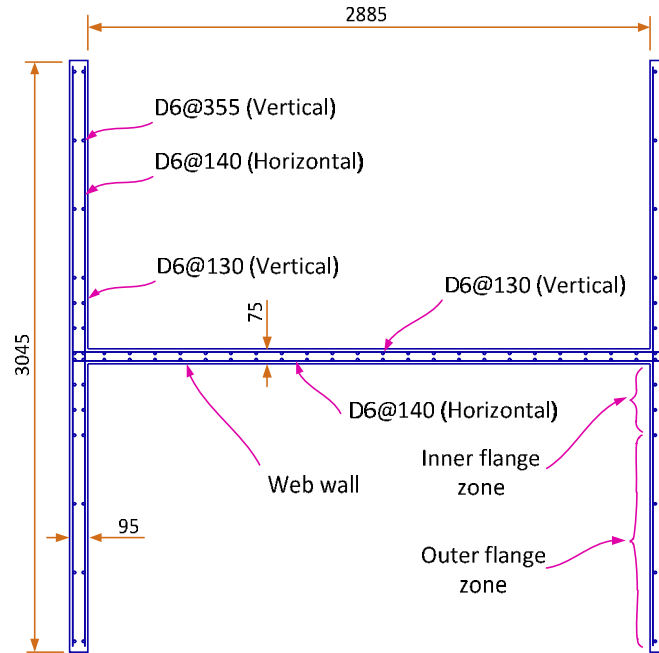


Figure 4.26 Dimensions and reinforcement details of 3D shear wall

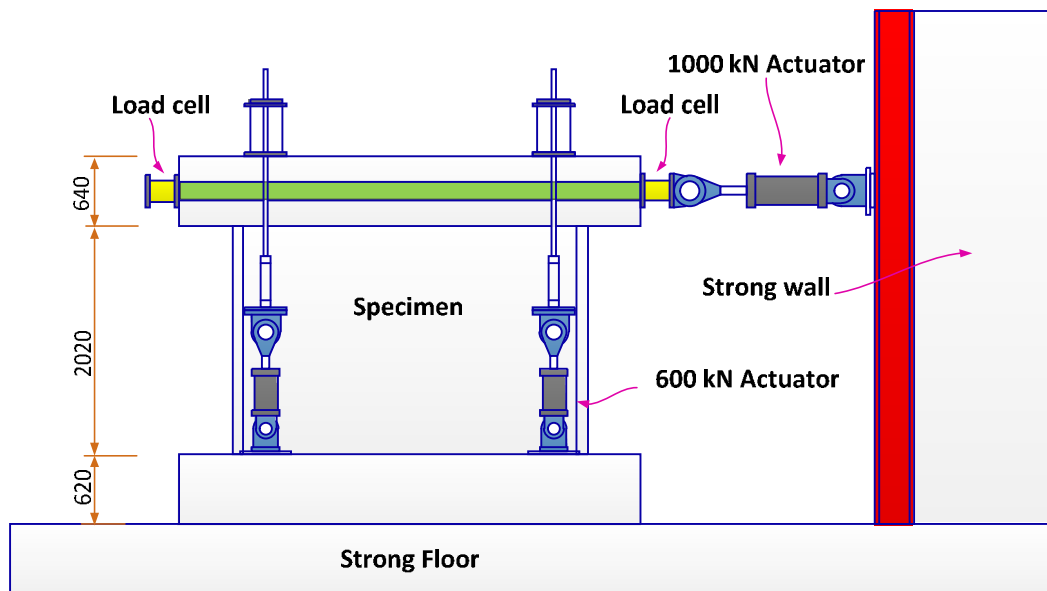


Figure 4.27 Test setup of the 3D shear wall

#### 4.6.2 Analytical Model

A finite element analysis was carried out on the specimen. The specimen was modeled by the finite element mesh, as shown in Figure 4.28. This mesh size was chosen to ensure the wall zones with different amount of steel were defined correctly. The web wall and each flange wall were modeled by 30 CSMMSHELLS8 elements each. Five layers of concrete and two layers of reinforcement were assigned for each element using the CSMMLayer material module. The steel layers were defined at the exact locations of reinforcement at the top and bottom of the cross-section of each element. The amount of reinforcement used in each element was defined equivalently to each region of the wall, as shown in Figure 4.26.

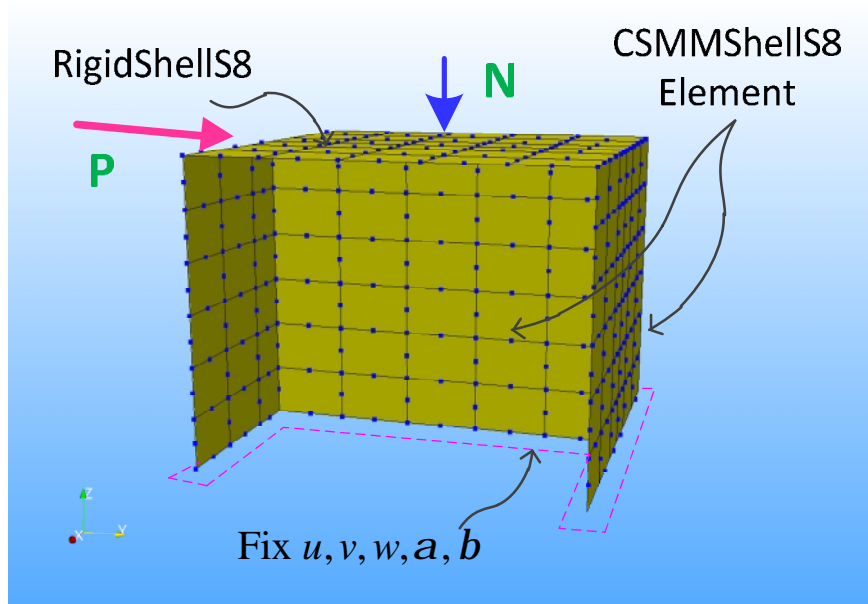
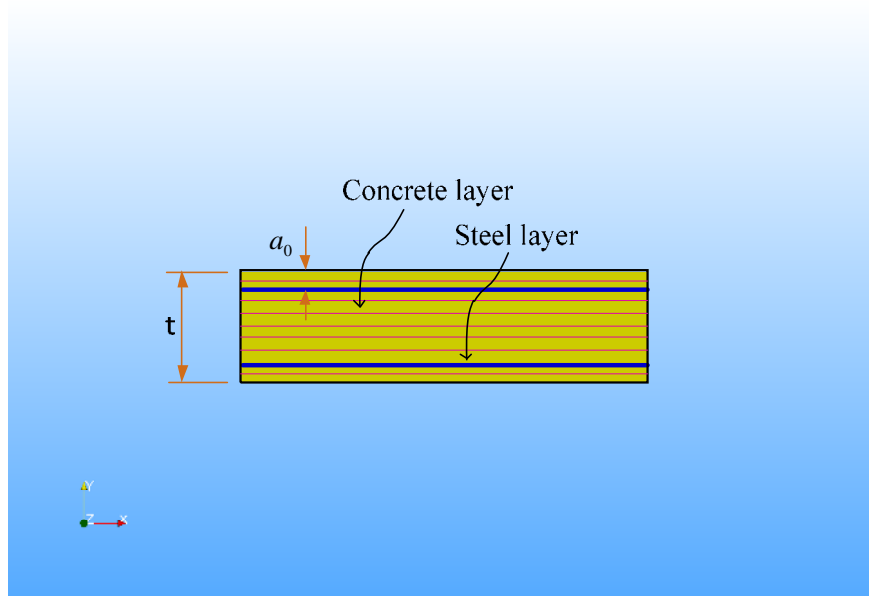


Figure 4.28 Finite element mesh used for RC cylindrical tank



**Figure 4.29** Cross section mesh of the shell element used for RC cylindrical tank

As shown in Figure 4.28, the top slab of the specimen was modeled by 30 RigidShellS8 elements, which were elastic 8-node shell elements with high stiffness. All nodes at the bottom of the model were constrained to not allow any translations or rotations to simulate the rigid foundation. Uniformly distributed loads were applied horizontally at all nodes along the two edges of the top slab to simulate the load applied from horizontal actuators. The analysis was performed by a predetermined displacement control scheme. The common displacement increment used in the analysis was 0.5 mm. The KrylovNewton method was used as the solution algorithm. The nodal displacement and corresponding horizontal forces were recorded at each converged displacement step, and the stress and strain of the elements were monitored.

#### **4.6.3 Comparison of Analytical Results with Experimental Results**

The analytical horizontal force versus displacement relationships of the specimen obtained from the analytical model were compared with the experimental result, as

shown in Figure 4.30. The analytical result and the experimental result are illustrated by solid curve and dotted curve, respectively. The analytical result was shown to provide a good correlation with the experimental data. Overall, the primary backbone curve, the initial stiffness, the peak strength, the descending branch, and the failure characteristic of the analytical result matched closely with the experimental data. The analytical model predicted accurately the pinching effect and the unloading path of the specimen.

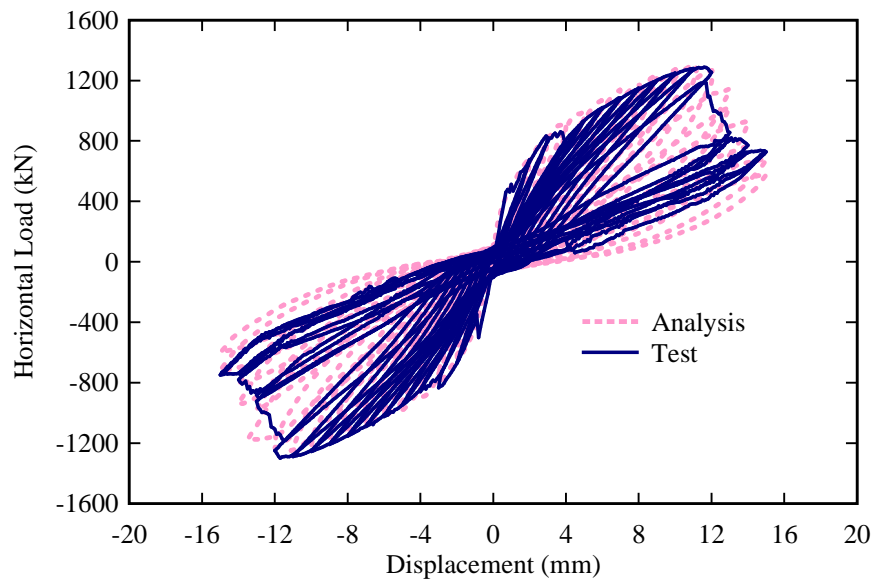


**Figure 4.30 Comparison between experimental and analytical load versus displacement for 3D RC shear wall**

## **4.7 Analysis of RC Hollow Bridge Piers**

### **4.7.1 Test Description**

Six full-scale RC rectangular and circular hollow bridge piers were tested under a constant axial load and horizontally reversed cyclic load at the National Center for Research on Earthquake Engineering (NCREE) in Taiwan (Yeh & Mo, 1999; Yeh et al., 2001). Details of the dimensions and reinforcement of the piers are shown in Figure 4.32,

in which all rectangular piers have had a cross section of 1500 x 1500 mm, and all circular piers had the inner diameter of 900 mm and the outer diameter of 1500 mm. The thickness of the reinforced concrete wall in each specimen was 300 mm. The variables in the test program including the lengths, axial load, amount of reinforcement, and material properties of the rectangular and circular specimens are listed in Table 4.6 and Table 4.7, respectively.

**Table 4.6 Loading and Material Properties of RC Hollow Rectangular Piers**

Specimen Name	$f'_c$ (MPa)	P (kN)	$\frac{P}{f'_c A_g}$	L (mm)	Longitudinal Reinforcement		Transverse Reinforcement	
					$f_y$ (MPa)	$r_l$ (%)	$f_y$ (MPa)	$r_s$ (%)
PS1	34.0	4000	0.082	6500	460.0	1.7	343.0	1.1
PI1	34.0	4000	0.082	4500	460.0	1.7	510.0	0.45
PI2	32.0	3600	0.078	3500	418.2	1.7	420.0	0.26

Note :  $f'_c$  = Compressive strength of concrete;  $A_g$  = Area of cross section;  
 $f_y$  = Yielding strength of steel;  $L$  = Effective height of the column;  
 $r_l$  = Percentage of the longitudinal steel;  $r_s$  = Percentage of transverse steel.

**Table 4.7 Loading and Material Properties of RC Hollow Circular Piers**

Specimen Name	$f'_c$ (MPa)	P (kN)	$\frac{P}{f'_c A_g}$	L (mm)	Longitudinal Reinforcement		Circumferential Reinforcement	
					$f_y$ (MPa)	$r_l$ (%)	$f_y$ (MPa)	$r_s$ (%)
PS1-C	31.7	3600	0.101	5500	418.2	2.15	410.0	0.9
PI1-C	33.8	3600	0.094	5500	418.2	2.15	410.0	0.3
PI2-C	30.9	3600	0.103	3500	418.2	2.15	410.0	0.26

Note :  $f'_c$  = Compressive strength of concrete;  $A_g$  = Area of cross section;  
 $f_y$  = Yielding strength of steel;  $L$  = Effective height of the column;  
 $r_l$  = Percentage of the longitudinal steel;  $r_s$  = Percentage of circumferential steel.

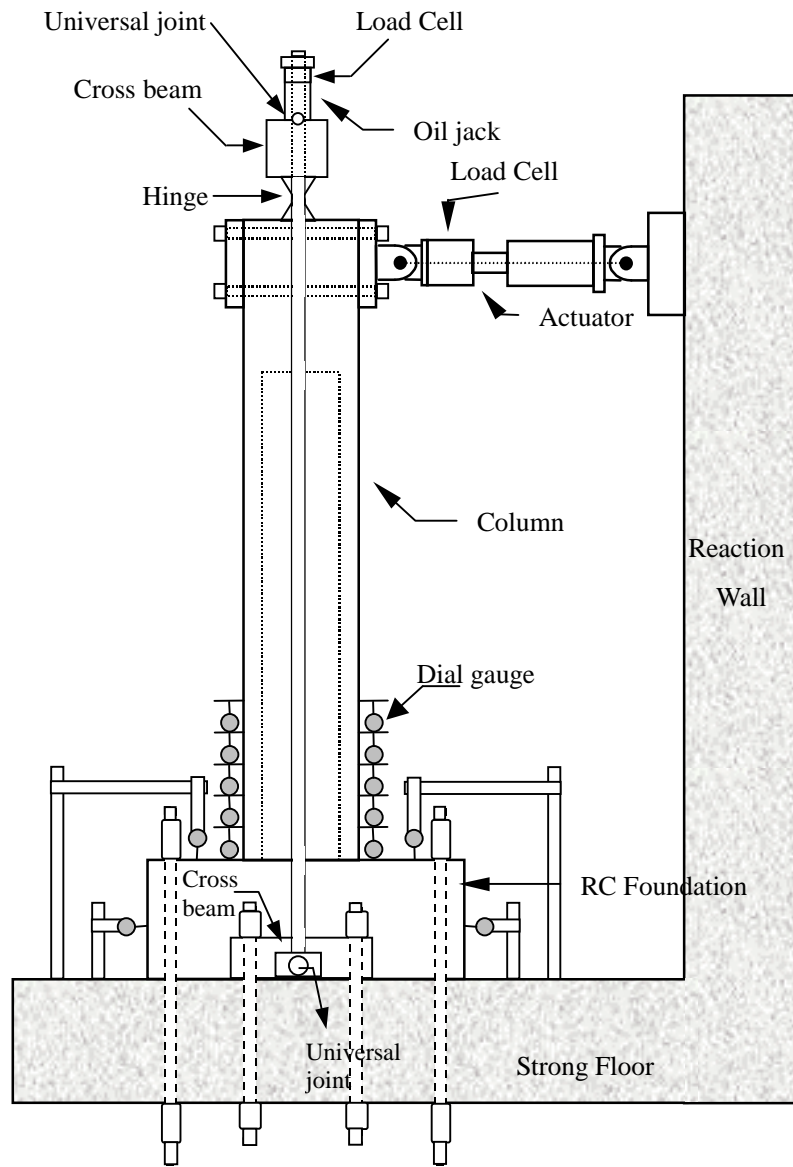


**Figure 4.31 Test setup of RC hollow columns**

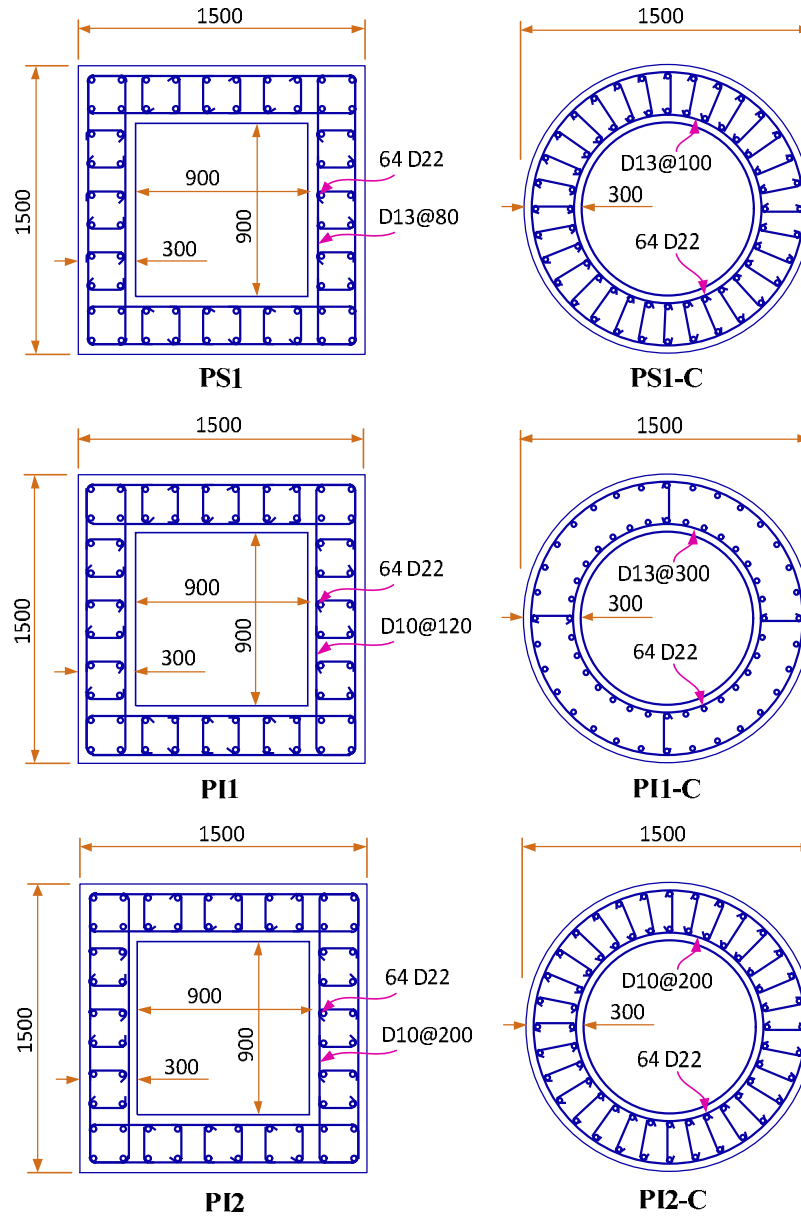


**Figure 4.32 Cross sections of RC hollow bridge piers**

The main parameter of the test program was the height to width ratio of the piers. For the rectangular hollow piers, the height to width ratios of the specimen PS1, PI1, and PI2 were 4.3, 3.0, and 2.3, respectively. For the circular hollow pier, only two values of the height to width ratios were investigated, which were 2.3 for specimen PI2-C and 3.7 for specimens PS1-C and PI1-C.

The test setup for each of the six specimens is shown in Figure 4.31. The bottom of the specimen was mounted on its reinforced concrete foundation, which was clamped to the laboratory floor. The top part of the specimen was casted as a solid cross section, which was connected with axial oil jacks and horizontal actuators. Each pier was subjected to a combination of lateral and axial loading. The constant applied axial load was first applied and maintained during the test by the oil jacks. The lateral displacements were imposed by three 1000-kN-capacity actuators that were horizontally mounted to a reaction wall.

#### **4.7.2 CSMM for Confined Concrete**

The concrete of the RC hollow piers had a confinement effect because of the special detailing of transverse reinforcement. As reported by Yeh et al. (2001), the confinement effect significantly enhanced the strength and the ductility of the piers. Therefore, a rational model of compressive stress-strain relationship for confined concrete needed to be used to accurately predict the behavior of the piers. At present, the CSMM does not take into account the confinement effect; therefore, the analytical model using the CSMM-based shell element may underestimate the strength as well as the ductility of the piers.

In the 2D model developed by Zhong (2005), the confinement effect of the piers was also considered, as shown in Figure 4.33. In the model, each specimen was divided into two parts: flanges and webs. The webs of the pier were modeled by PlaneStress Quadrilateral membrane elements. The flanges of the pier were modeled by Nonlinear-beam-column elements. As can be seen from the figure, the confinement effect was taken into the model by the modified Ken and Park model for confined concrete that was assigned to the core area of the concrete fiber cross section of the Nonlinear-beam-

column elements. However, the Nonlinear-beam-column elements were not used in a 3D model because the developed shell element, which can accurately capture in-plane shear and out-of-plane bending, was used to simulate both webs and flanges of the piers. As a result, the method to account for confinement effect used in the 2D model was not valid in the 3D model.

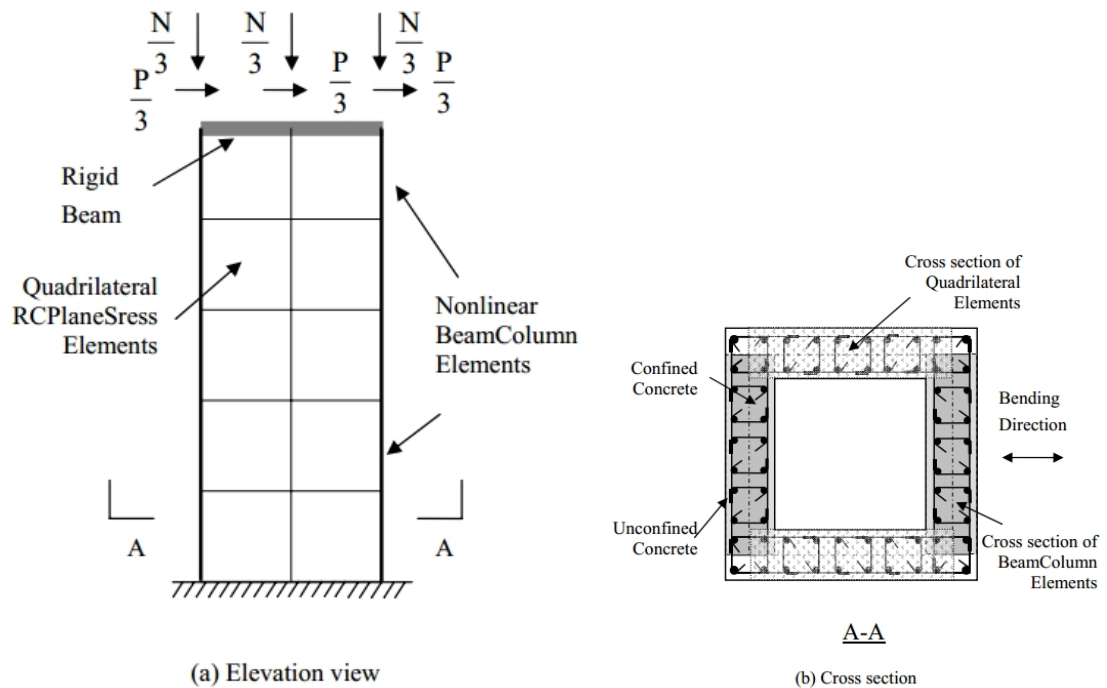


Figure 4.33 Finite element mesh of the RC hollow piers using 2D model (Zhong, 2005)

In this study, to improve the accuracy of the proposed 3D model, a new CSMM for confined concrete was proposed to account for the confinement effect. The model was extended from CSMM by modifying the envelope of the stress-strain curve of concrete in compression. The confined model for confined concrete proposed by Sheikh and Uzumeri (1982) was adopted. The proposed equations for the uniaxial stress-strain relationship of the confined concrete used for CSMM are summarized as follows:

$$s_c = Dz f'_{cc} \left[ 2 \left( \frac{\bar{e}}{ze_{01}} \right) - \left( \frac{\bar{e}}{ze_{01}} \right)^2 \right], \quad 0 \leq |\bar{e}| \leq |ze_{01}|, \quad (4.1)$$

$$s_c = Dz f'_{cc}, \quad |ze_{01}| \leq |\bar{e}| \leq |ze_{02}|, \quad (4.2)$$

$$s_c = Dz f'_{cc} [1 - Z(\bar{e} - e_{02})] \geq 0.3 Dz f'_{cc}, \quad |\bar{e}| > |ze_{02}|, \quad (4.3)$$

$$f'_{cc} = K_s f'_c, \quad (4.4)$$

$$K_s = 1.0 + \frac{A_{co}}{140 P_{occ}} \left[ \left( 1 - \frac{nc^2}{5.5 A_{co}} \right) \left( 1 - \frac{s}{2B} \right) \right] \sqrt{r_s f_{yh}}, \quad (4.5)$$

$$P_{occ} = 0.85 f'_c (A_{co} - A_s), \quad (4.6)$$

$$e_{01} = 80 \times 10^{-6} \cdot K_s \cdot f'_c, \quad (4.7)$$

$$e_{02} = 0.0022 \left[ 1 + \frac{248}{c} \left( 1 - 5 \left( \frac{s}{B} \right)^2 \right) \frac{r_s f_{yh}}{\sqrt{f'_c}} \right], \quad (4.8)$$

$$e_{85} = 0.225 r_s \sqrt{\frac{B}{s}} + e_{02}, \quad (4.9)$$

$$Z = \frac{0.15}{e_{85} - e_{02}}, \text{ and} \quad (4.10)$$

where  $A_{co}$  is the core area enclosed by the center line of the outer transverse reinforcement,  $A_s$  is the total area of longitudinal bars with the core area;  $s$  = spacing of transverse reinforcement,  $r_s$  is the ratio of the volume of total transverse reinforcement versus the core volume,  $n$  is the number of arcs created among longitudinal bars,  $c$  is the distance between center line of longitudinal bars,  $Z$  is slope of the descending part of the stress-strain curve,  $e_{s1}$  is the minimum strain corresponding to the maximum concrete stress,  $e_{s2}$  is the maximum strain corresponding to the maximum concrete stress,  $e_{85}$  is the strain value corresponding to 85% of the maximum concrete stress in the descending curve.

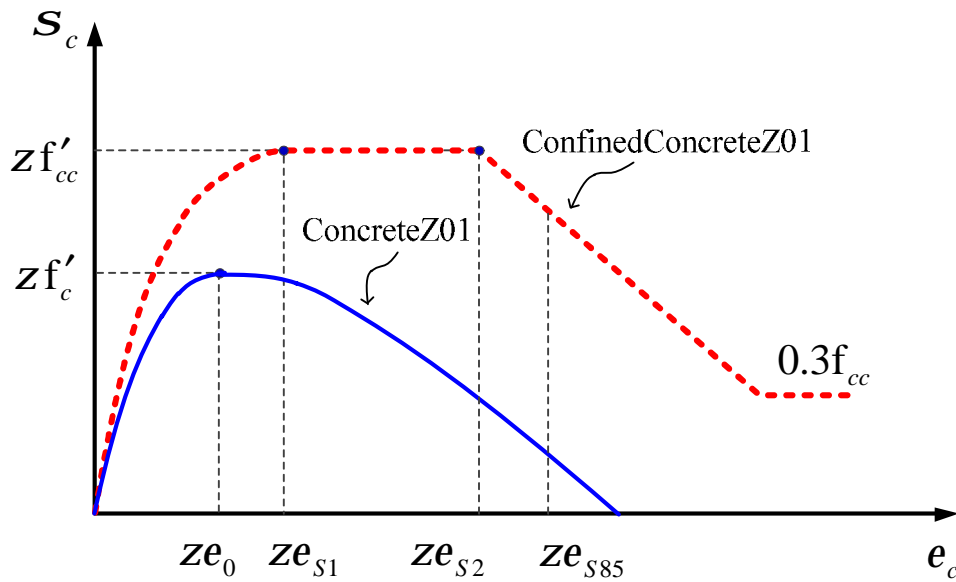


Figure 4.34 The proposed softened compressive stress-strain relationship for confined concrete

Based on the proposed equation, a new uniaxial material model, the ConfinedConcreteZ01, was developed in this study for confined concrete. The input parameters for ConfinedConcreteZ01 were as follows:

<code>uniaxialMaterial ConfinedConcreteZ01 \$mtag \$fc \$es1 \$es2 \$es85</code>
--

where \$mtag = unique integer tag identifying concrete material; \$fc = compressive strength of concrete; \$es1 = the minimum strain corresponding to the maximum concrete stress; \$es2 the maximum strain corresponding to the maximum concrete stress; \$es85 = the strain value corresponding to 85% of the maximum concrete stress in the descending curve. All the parameters should be in negative values.

### 4.7.3 Analytical Model

The specimens were modeled using the finite element meshes illustrated in Figure 4.35 and Figure 4.36. Two types of shell element were used in the model: CSMMSHELLS8

and ElasticShellS8. The CSMMShellS8 was used to simulate the piers; while, the ElasticShellS8 was used to simulate the rigid part at the top of the piers. For the RC rectangular hollow piers, the numbers of CSMMShellS8 elements were 72 for specimen PI2, and 80 for specimen PI1 and PS1. For the RC circular hollow piers, the numbers of CSMMShellS8 elements were 56 for specimen PI2, and 80 for specimen PI1 and PS1. Five layers of concrete and two layers of steel were assigned for each element using the CSMMLayer material module. The steel layers were defined at the exact locations of steel at the top and bottom of the cross-section. In the case of not considering confinement effects, all concrete layers were defined with the same properties of unconfined concrete, as shown in Figure 4.37. In the case of considering confinement effects, the cover concrete layers were defined with the properties of unconfined concrete, and the cover concrete layers were defined with the properties of the confined concrete developed in this study, as shown in Figure 4.38. The ElasticShellS8 elements were defined with very high stiffness to guarantee that the top part of the piers wasw totally rigid. For the boundary conditions, all nodes at the bottom of the model were constrained to not allow any translations or rotations. Equal horizontal and vertical loads were applied at all nodes along the perimeter of the top of the specimen based on the assumption that the loads were uniformly distributed. The magnitude of the axial loads acting remained constant during the analyses. The horizontal loads were changed according to the displacement control scheme.

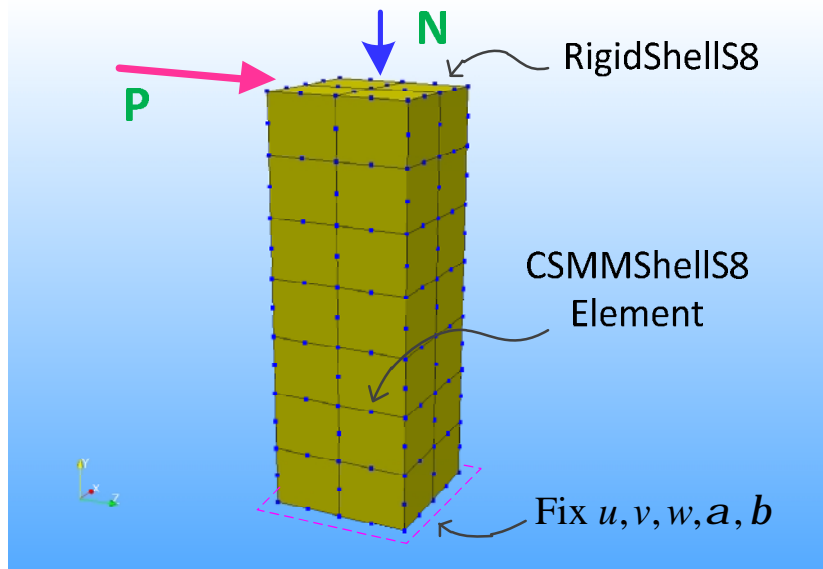


Figure 4.35 Finite element mesh used for RC hollow rectangular piers

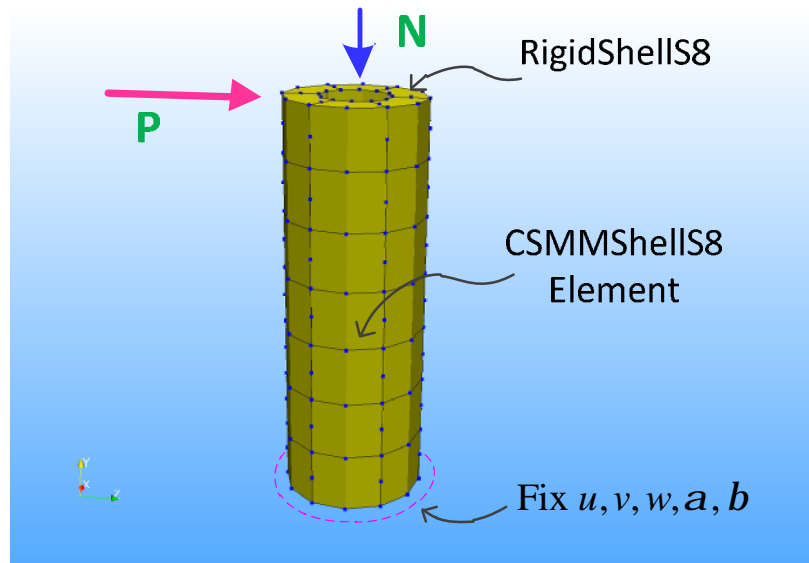
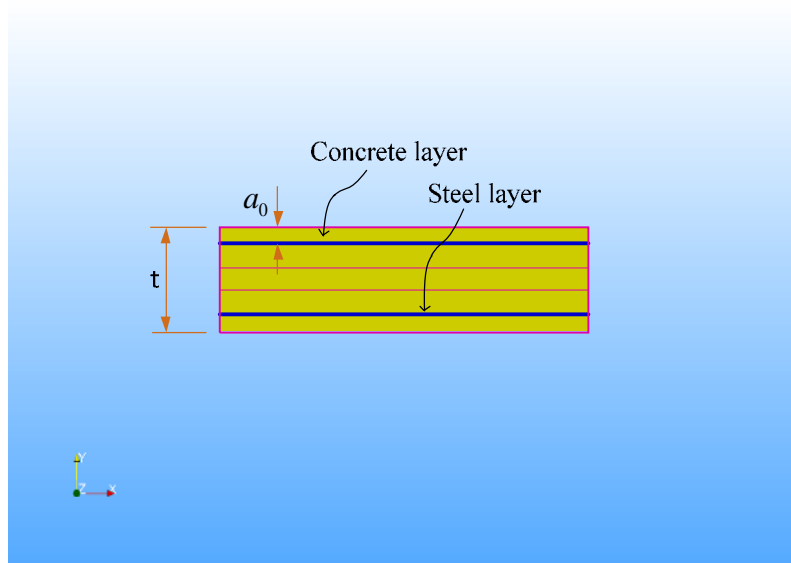
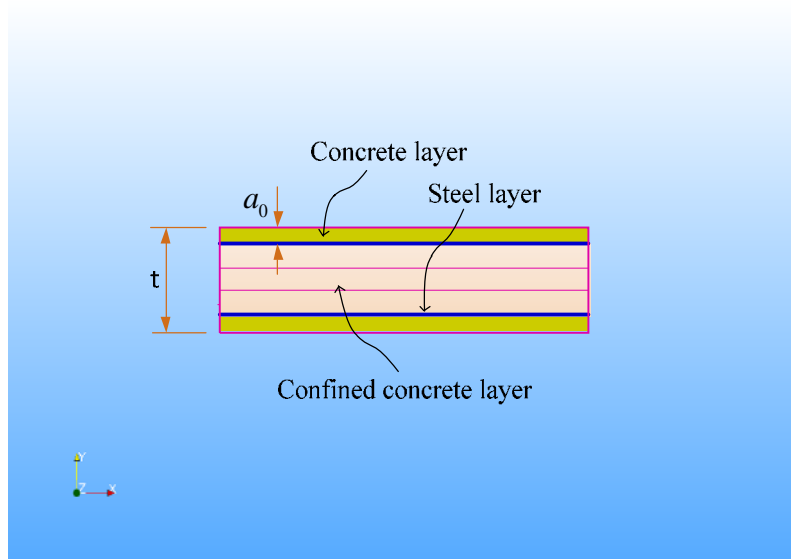


Figure 4.36 Finite element mesh used for RC hollow circular piers



**Figure 4.37 Cross section mesh of the shell element used for RC hollow piers (Unconfined)**



**Figure 4.38 Cross section mesh of the shell element used for RC hollow piers (Confined)**

The analyses were performed by a predetermined force control and displacement control schemes. The analysis procedure was separated into two steps. In the first step,

axial loads were applied to the columns using load control by ten load increments. In the second step, axial loads were kept constant and reversed cyclic horizontal loads were applied by the predetermined displacement control on the drift displacement. The common displacement increment used in the analyses was 0.5 mm. Convergence was obtained easily during the cyclic analyses. The Krylov-Newton method was used as the solution algorithm. The nodal displacement and corresponding horizontal forces were recorded at each converged displacement step, and the stress and strain of the elements were monitored.

#### **4.7.4 Comparison of Analytical Results with Experimental Results**

The monotonic curves of horizontal force versus displacement relationships of the unconfined analytical model and confined analytical model were calculated and compared with the experimental results, as illustrated in Figure 4.39 and Figure 4.40. The dotted curve represents the result using the unconfined model, and the solid curve represents the result using the confined model. The results shown in Figure 4.39 are for column PI2-C, which was governed by the flexural failure. The results shown in Figure 4.40 are for column PS1-C, which was governed by the flexural-shear failure. The results from both figures showed that the unconfined model can predict accurately the initial stiffness; however, the model underestimated the strength and the ductility of the structures. In contrast, the curves provided by the confined model had a good correlation with the experimental data in both cases. Hence, the confined model proposed in this section was appropriate to model the whole cyclic behavior of the hollow bridge piers.

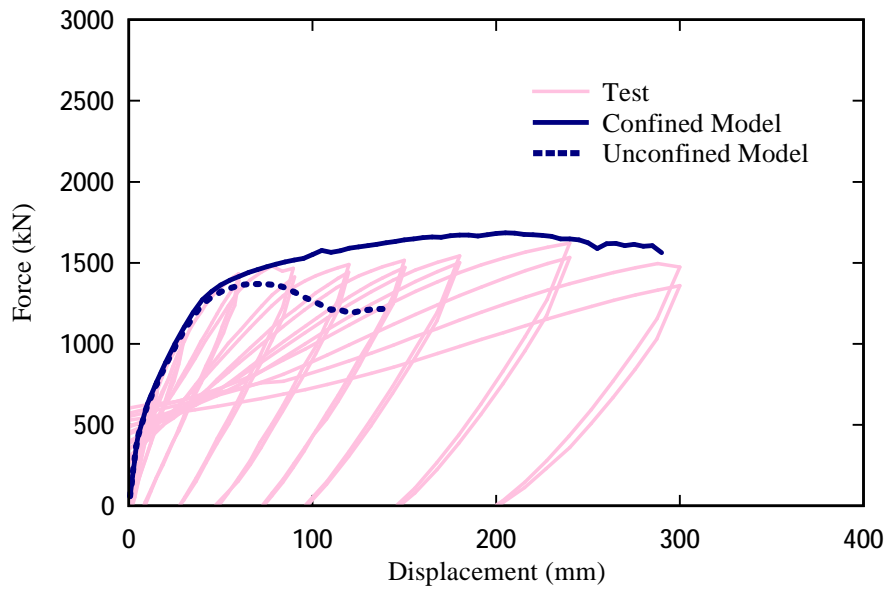


**Figure 4.39 Comparison between confined model and unconfined model for flexural-governed column (Column PS1-C)**

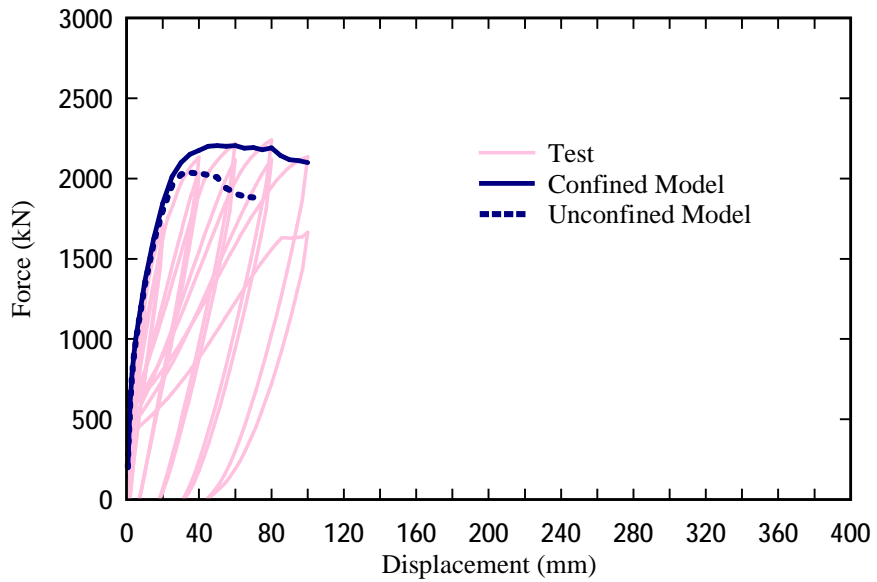


**Figure 4.40 Comparison between confined model and unconfined model for flexural-shear-governed column (Column PI2-C)**

The analytical horizontal force versus displacement relationships of the specimens were calculated by using the confined model and compared with the experimental data, as

demonstrated in Figure 4.41 through Figure 4.46. The analytical results are illustrated by solid curves and the experimental results are illustrated by dotted curves. The experimental failure modes and ductility levels of the specimens are different. The experimental results showed that specimens PS1, PI1, and PS1-C sustained flexural failure, specimens PI2 and PI2-C sustained flexural-shear failure, and specimen PI1-C failed due to buckling of longitudinal steel bars. The failure modes were reflected on the shape of the experimental force and displacement curve as well as the ductility levels. The flexural governed specimens have a long yield plateau in the envelop of force-displacement relationship and robust hysteresis loops. The flexural-shear governed specimens have much shorter yield plateau and provide much less energy dissipation.

As can be seen from the figures, the analytical results show a good correlation with the experimental results. The analytical force-displacement curves can accurately predict the different behavior of the specimens. The analytical results predict the initial stiffness, yield point, and ultimate strength of all specimens very well. In cases of the flexural governed specimens, the analytical results exhibit a long plateau and robust hysteresis loops, which were also observed in the experimental results. In cases of the flexural-shear specimens, although the analytical cannot accurately capture the whole descending part of the load-displacement curve, but the peak load is well predicted. For specimen PI1-C, the analytical model can only predict the behavior prior to buckling because the analytical model does not take into account the buckling failure mode. The analytical model also predicted accurately the pinching effect and the unloading path of all specimens.

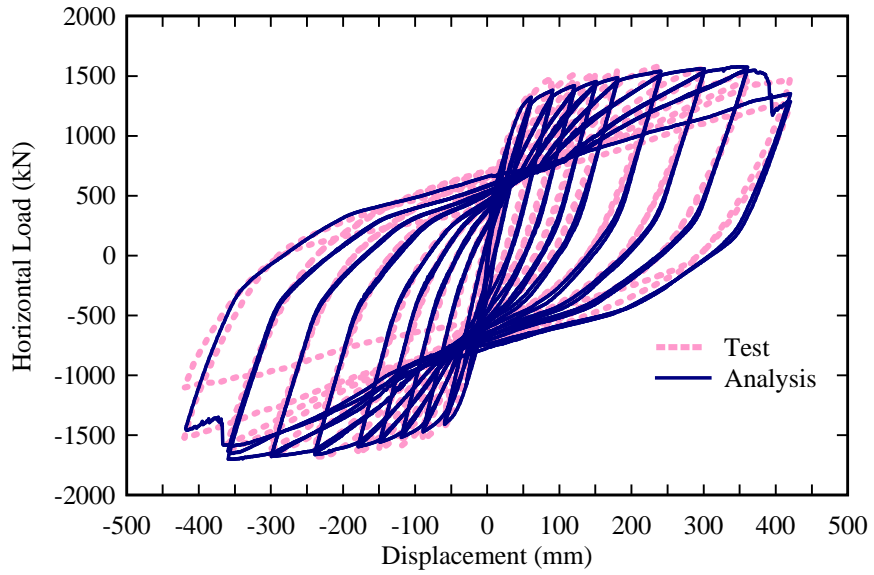


**Figure 4.41 Comparison between experimental and analytical load versus displacement for column PS1**

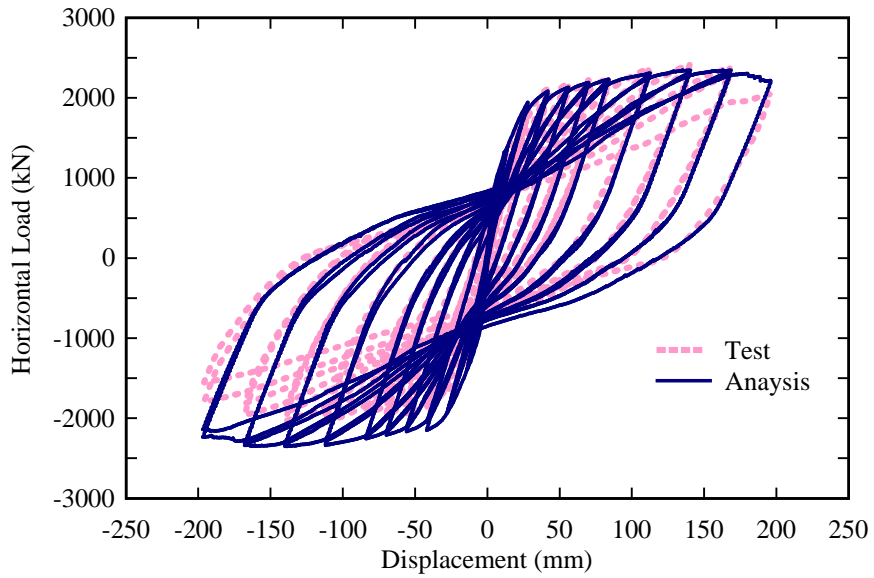


**Figure 4.42 Comparison between experimental and analytical load versus displacement for column PI1**

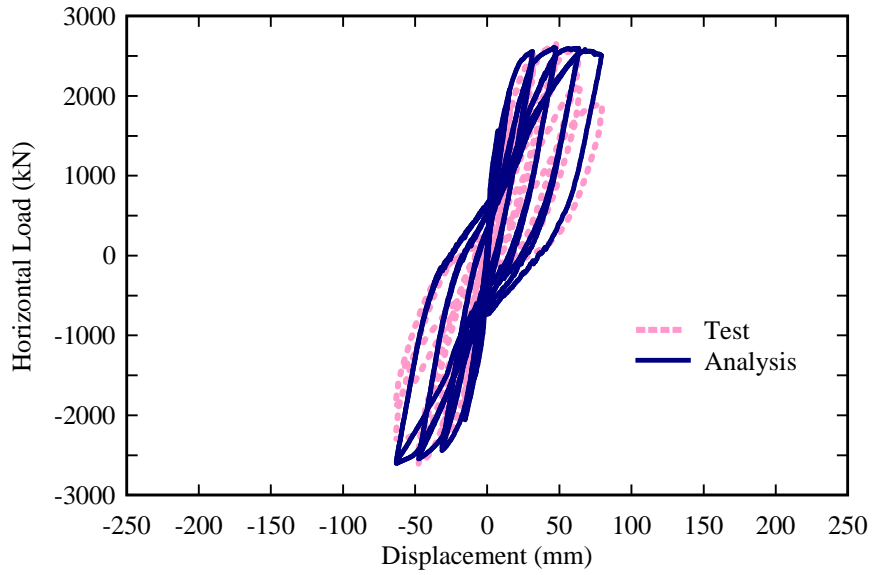


**Figure 4.43 Comparison between experimental and analytical load versus displacement for column PI2**

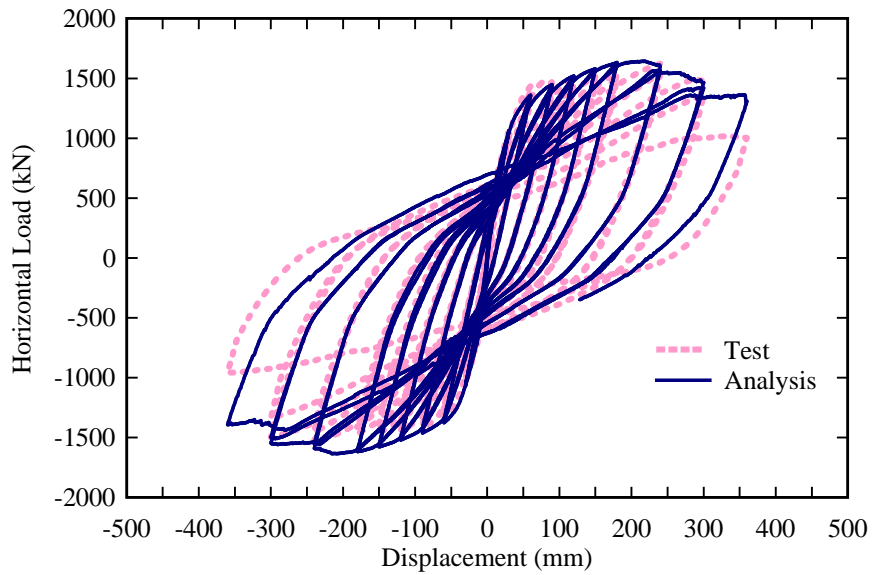


**Figure 4.44 Comparison between experimental and analytical load versus displacement for column PS1-C**

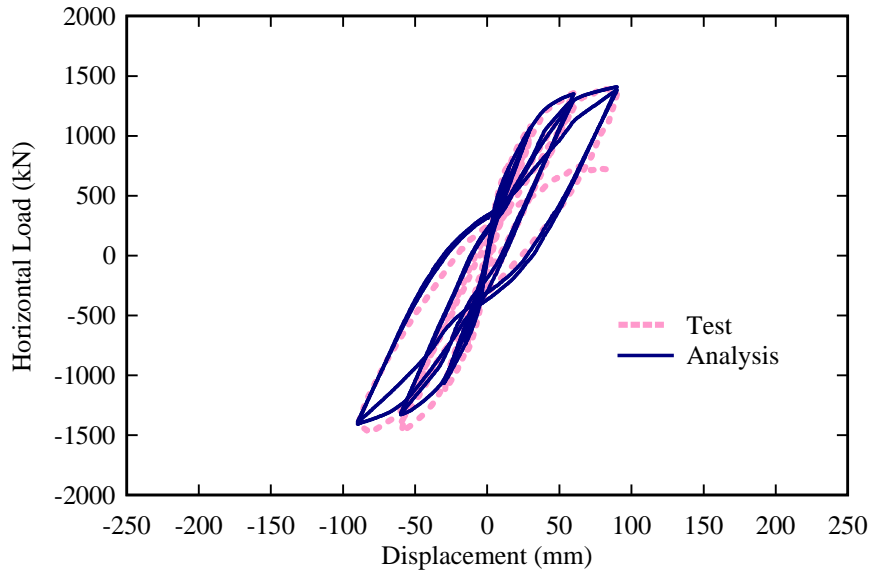


**Figure 4.45 Comparison between experimental and analytical load versus displacement for column PI1-C**

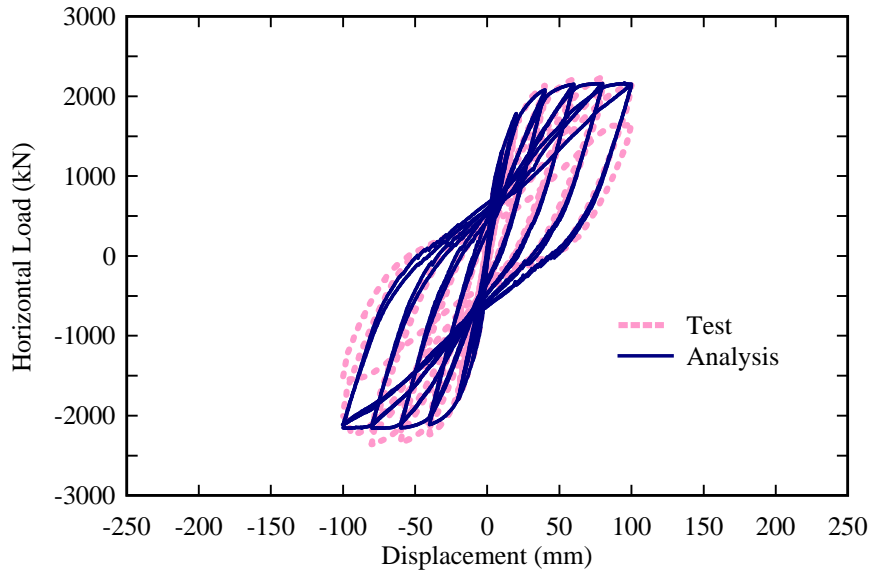


**Figure 4.46 Comparison between experimental and analytical load versus displacement for column PI2-C**

# **CHAPTER 5**

## **EXPERIMENT AND SIMULATION OF RC NUCLEAR CONTAINMENT VESSEL**

### **5.1 Introduction**

A nuclear containment vessel is a complex structure and needs significant safety requirements, such as pressure resistance, radiation leaking prevention, seismic and impact protection, etc. Considered to be a competitive material that satisfies the safety requirements of the containment structure, reinforced concrete has been used extensively from the beginning of the nuclear power industry. With the large dimensions of the structure, a reinforced concrete nuclear containment vessel often contains large sections and large diameter steel bars. The reinforced concrete nuclear containment vessel is classified as a shell-type structure with complex stress conditions, as shown in Figure 5.1, which involve various states. For example, internal pressure due to a leakage accident could produce large bi-axial tension, and an earthquake action could lead to seismic (tangential) shear, which has become a major design consideration. Airplane collisions, missile attacks, and other high local loads could lead to punching (peripheral) shear (Banerjee & Holley, 1978).

Under seismic loading, the nuclear containment vessel is subjected to cyclic flexural, axial, and shear forces. Shear behavior is an important consideration in a concrete containment wall, and a realistic assessment of shear strength and stiffness across cracks is essential to the design and analysis of concrete structures. Because of its critical importance to nuclear safety, the containment structure must be able to maintain

structural integrity while undergoing simultaneous stresses of internal pressure, earthquake action, and/or high local loads. Under these conditions, the accurate assessment of shear behavior poses a difficult design and analysis problem (Leombruni, Buyukozturk, & Connor, 1979).

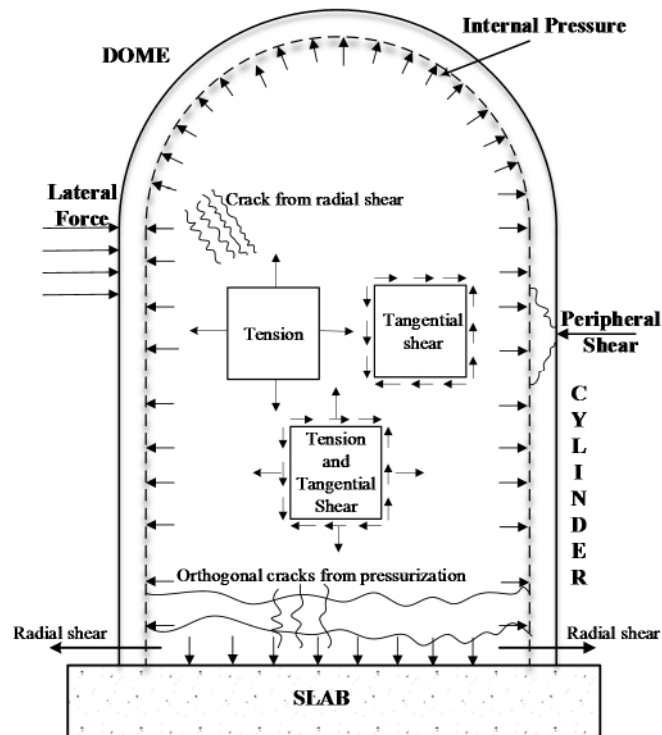


Figure 5.1 Stress states and resulting cracks in containment

From a structural point of view, a nuclear containment can be visualized as assemblies of many elements. This concept facilitates the analysis of the complex structure when the finite element analysis is used, accompanied by the rational constitutive laws of materials. The key to rational analysis of the structure is to understand fully the behavior of one element isolated from the structure. Once a rational model is developed to predict the behavior of one element, this rational model can be incorporated into a finite element

analysis program to predict the behavior of the whole structure under different kinds of loading.

Because of the complexity of testing conditions, in an element-based study only a few research groups with special testing equipment could conduct an experimental study of shell elements. Two famous systems for testing RC shell elements are the Shear Rig developed by Vecchio and Collins (1981a) at the University of Toronto and the Universal Panel Tester developed by Hsu, Belarbi, and Xiaobo (1995) at the University of Houston. Using the experimental results of the panel tests, many constitutive models for reinforced concrete have been proposed. The models are the Compression-Field Theory and Modified Compression Field Theory by (Vecchio & Collins, 1981b, 1982); Disturbed Stress Field Theory by Vecchio (2000); Rotating-Angle Softened Truss Model (RA-STM) (Belarbi & Hsu, 1995; Pang & Hsu, 1995); Fixed-Angle Softened Truss Model (FA-STM) (Pang & Hsu, 1996), the Softened Membrane Model (SMM) (Hsu & Zhu, 2002), and the Cyclic Softened Membrane Model (CSMM) (Mansour & Hsu, 2005). They all satisfy Navier's three principles of mechanics of materials and, thus, are rational. Among these constitutive models, the CSMM is the most versatile and accurate. The CSMM is capable of predicting the cyclic shear behavior of reinforced and prestressed concrete membrane elements including the stiffness, ultimate strength, descending branch, ductility, and energy dissipation.

In model-based simulation studies, many researchers have proposed analytical models to predict the behavior of an entire RC shell-type structure using FEA. This research included work by Hand, Pecknold, and Schnobrich (1972); Cervera, Hinton, and Hassan (1987); Scordelis and Chan (1987); Hu and Schnobrich (1991); Adebar and Collins

(1994); Polak and Vecchio (1994); Yamamoto and Vecchio (2001); Kim, Lee, and Shin (2002); Song, Shim, Byun, and Maekawa (2002); Maekawa et al. (2003); Zhang, Bradford, and Gilbert (2007); Lee (2010); and Xiang, Mo, and Hsu (2012). Most researchers use the approach of developing a RC shell element by combining a rational constitutive model of RC into FE formulations of a general shell element with a layered approach. The developed RC shell element is implemented into a finite element analysis development framework to form a FEA program for predicting the behavior of the entire structure. In contrast to the analytical study, the experimental studies in nuclear containment vessel under seismic loading are limited due to the high cost and complexity of testing.

In this chapter, tests and simulations of two 1/13-scaled nuclear containment vessel specimens subjected to reserved cyclic loadings are presented. First, the test program is described including test specimen, test setup, and loading method. Next, the seismic behavior of the nuclear containment vessel specimens is experimentally investigated. Finally, the nonlinear analyses of the nuclear containment vessel specimens are conducted using the developed finite element program SCS-3D, and the analytical results are compared with the test data. The tests were undertaken as part of an international collaboration project between the National Center for Research on Earthquake Engineering (NCREE), Taipei, Taiwan, and the University of Houston (UH), Houston, Texas. The NCREE performed the experimental work, and the specimen design and the experimental data were analyzed at UH.

## 5.2 Experimental Program

### 5.2.1 Specimen Design

To understand the fundamental behavior of structural component and system, structural testing must be performed. The size of test specimens should be as close as possible to the structure to properly represent its true behavior. However, to test full-scale specimens in laboratories is unfeasible because the nuclear containment structures often involve large dimensions of the structure, large sections, and large diameter steel bars. Based on the current capacity of testing equipment at the National Center of Research on Earthquake Engineering laboratory in Taipei, Taiwan, the experimental specimen of 1/13-scaled nuclear containment vessel was designed to investigate the behavior of a nuclear containment vessel isolated from a nuclear structure and subjected to the gravity and earthquake loads. This section describes the test specimens, material properties, construction process, test setup, instrumentation, and loading protocol.

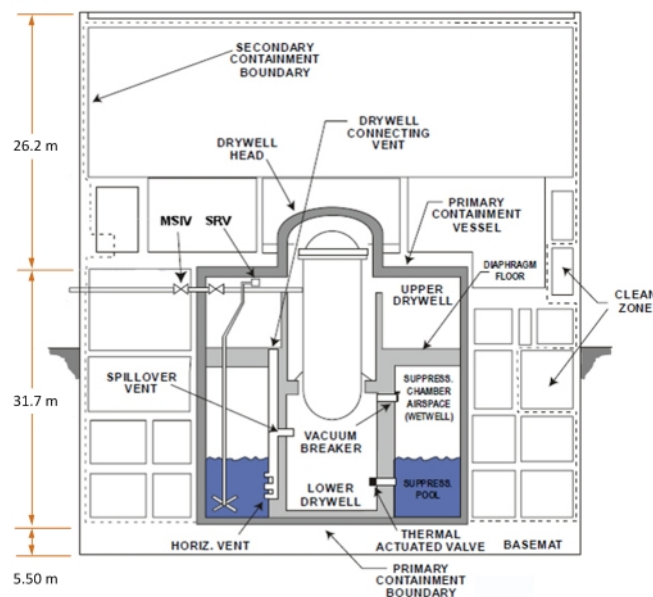
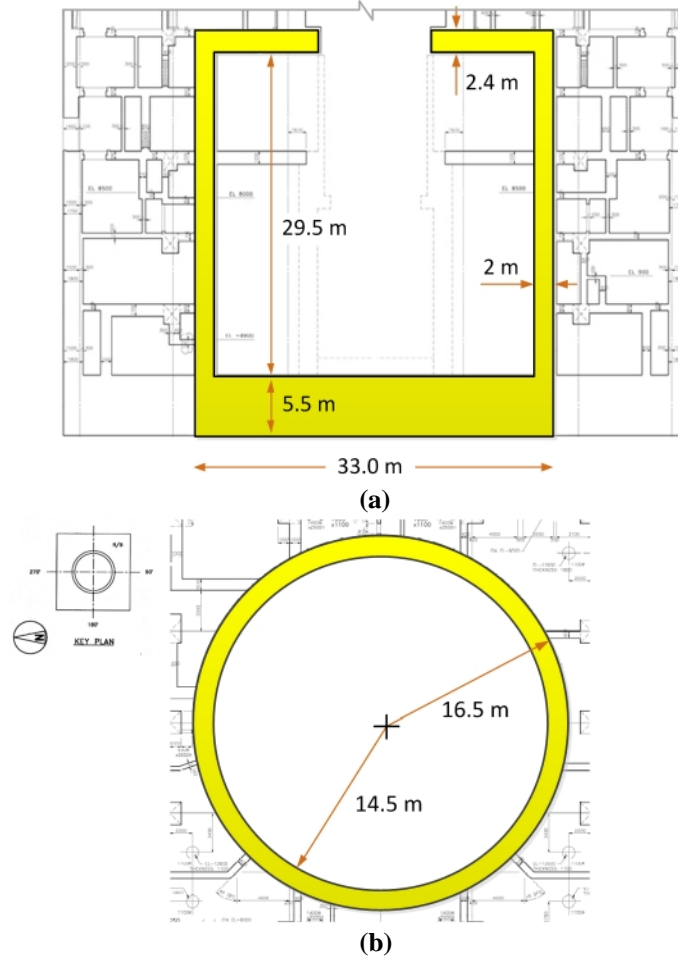
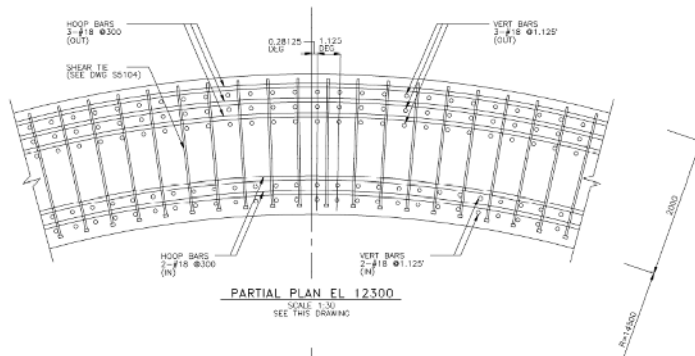
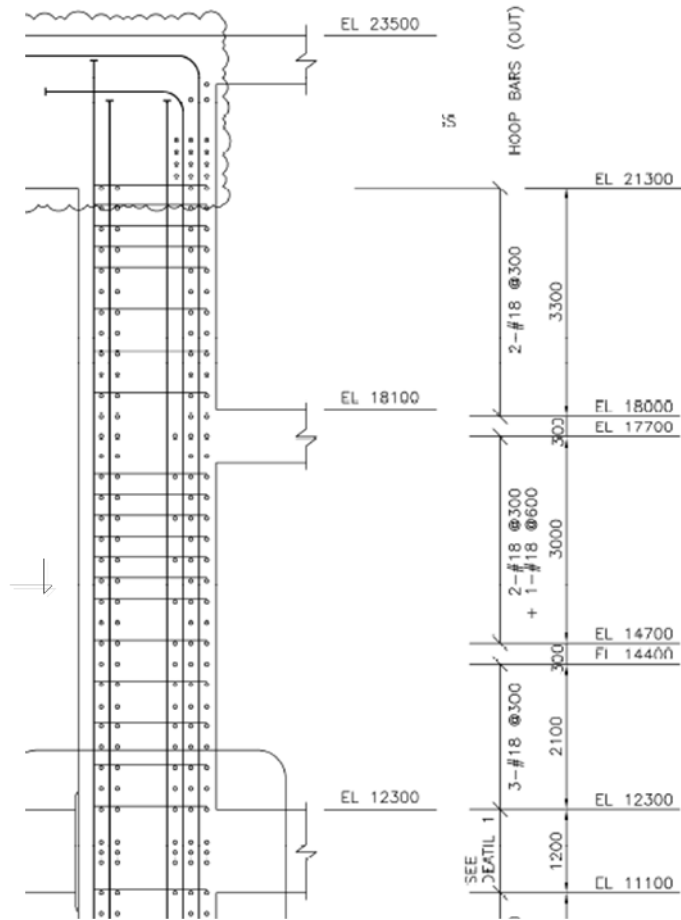


Figure 5.2 Elevation view of the Lungmen Nuclear Power Plant (NPP)



**Figure 5.3 RC containment vessel of Lungmen NPP: (a) Elevation view (b) Plan view**

The specimen was designed based on the prototype of Lungmen nuclear containment structure, as shown in Figure 5.2. The real-size containment has a height of 29.5 m, a radius of 15.5 m (center-line dimension), and a thick wall of 2.0 m, as shown in Figure 5.3. The reinforcement details of the containment are shown in Figure 5.4. To simulate the loads and keep the boundary conditions of the specimens as close to the real nuclear containment structure as possible, a computer-controlled static testing system with multiple displacement and force control modes was used. A control scheme was developed to apply the lateral load following a displacement history while maintaining a constant axial load and preventing rotation at the top of the specimen.



**Figure 5.4 Cross-section detail of Lungmen RCCV**

The experimental program included the construction and testing of two nuclear containment specimens under axial and lateral loading. The specimens had similar amount of reinforcement ratio compared to the real structure. The two test specimens had identical details and material properties. The test specimens, which were connected to

nearly rigid top and bottom slabs, were tested in double curvature. Due to their size and capacity, similar types of tests have not been reported in the literature; therefore, the tests are unique.

### **5.2.2 Specimen Description**

The dimensions of the test specimens are shown in Figure 5.5. Each specimen included three parts: the main containment, top slabs, and bottom slabs. The bottom slabs simulated the rigid foundation while the top slab simulated the rigid floor system, as shown in Figure 5.3. These slabs were designed conservatively to avoid significant deformation occurring in the slabs so that the nonlinearity took place only in the containment during the tests. Rotations of the top and base slabs in the vertical plane were prevented during the test to ensure the containments had double-curvature behavior during the tests. The containments had a height of 2.25 m and a radius of 1.175 m (center-line dimension). The outer and inner diameters of the containments were 2.5 m and 2.2 m, respectively. Thickness of the containment was 0.15 m. The top and bottom slabs of the specimens had a cross section of 3.5 m x 3.5 m and a depth of 0.73 m.

The reinforcement arrangement in the specimens is illustrated in Figure 5.6 through Figure 5.8. As shown in Figure 5.7, four layers of vertical and circumferential reinforcements were along the thickness of the containments. The #3 (diameter of 9.5 mm) steel bars were adopted in the test containment for both vertical and circumferential reinforcements, and the steel bars in the top and bottom slabs were #5 (diameter of 15.8 mm). The reinforcements were uniformly distributed around the perimeter and along the height of the tests containments with the same spacing. The percentage of the reinforcement ratio in the containment of Specimen No. 1 was 2% in both the vertical and

circumferential directions, as shown in Figure 5.6a. The vertical bars in the containments were continuous without lap splices. The clear concrete cover over the vertical bars was 17 mm. The circumferential bars were closed using welding lap splices with a length of  $30 d_b$ , where  $d_b$  was the bar diameter, as shown in Figure 5.9. The anchorage length of the vertical bars of the containments inside the top and bottom slabs was greater than the development length calculated using ACI 318-11. The joint connector nuts were provided at the end of the vertical bars to enhance the anchorage capacity during the tests, as shown in Figure 5.10.

**Table 5.1 Dimensions and Material Properties of RCCV Specimens**

Specimen No.	$f'_c$ (MPa)	$D$ (mm)	$H$ (mm)	$t$ (mm)	Vertical Reinforcement			Circumferential Reinforcement		
					$d_b$ (mm)	$f_y$ (MPa)	$r_v$ (%)	$d_b$ (mm)	$f_y$ (MPa)	$r_c$ (%)
RCCV #1	35	2350	2250	150	9.5	360	2	9.5	360	2
RCCV #2	35	2350	2250	150	9.5	360	2	9.5	360	2

Note :  $f'_c$  = Compressive strength of concrete;  $D$  = Diameter;  $H$  = Net height;  
 $t$  = Thickness;  $f_y$  = Yielding strength of steel;  $d_b$  = Diameter of steel bar;  
 $r_v$  = Steel ratio in the vertical direction;  $r_c$  = Steel ratio in circumferential direction

The reinforcement details of Specimen No. 2 is almost identical to Specimen No. 1 except that more vertical reinforcements (dowel bars) were added to each end of the containment to enhance its shear sliding capacity, resulting in the vertical reinforcement ratio of 4% in each of these two ends, as shown in Figure 5.6b. The cut-off points of the additional vertical reinforcement were arranged in a jagged manner to prevent cracking within the cut-off regions. The center line of the zigzag curve was at a quarter of the containment height. The details of dimensions and material properties of the specimens are summarized in Table 5.1.

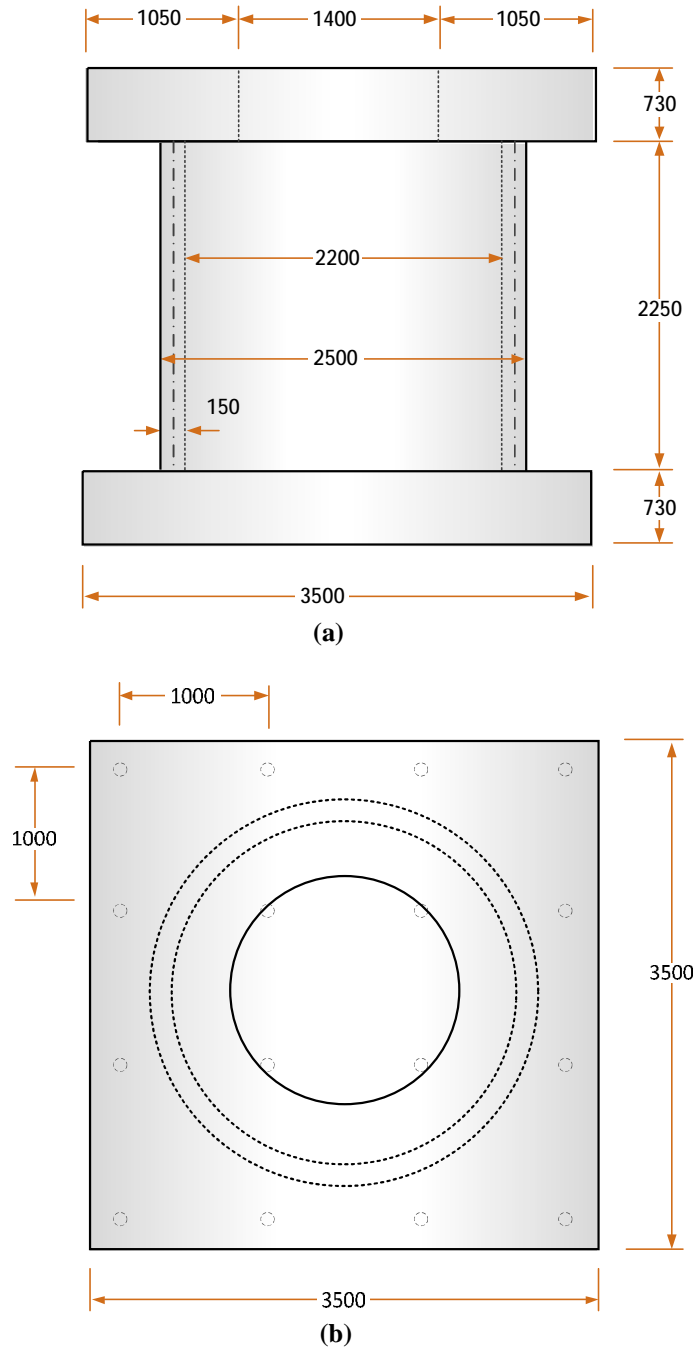
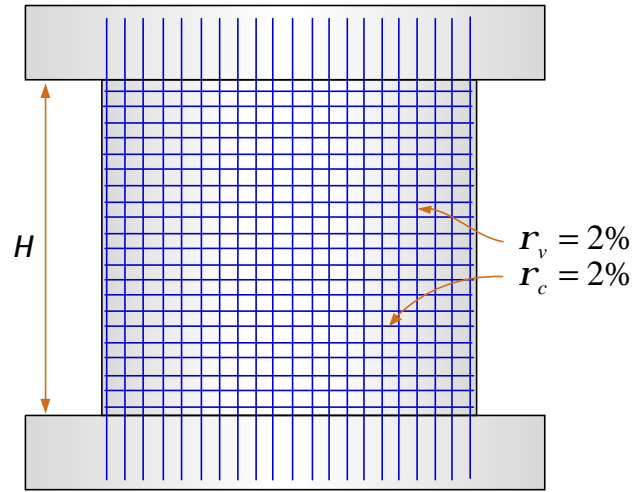
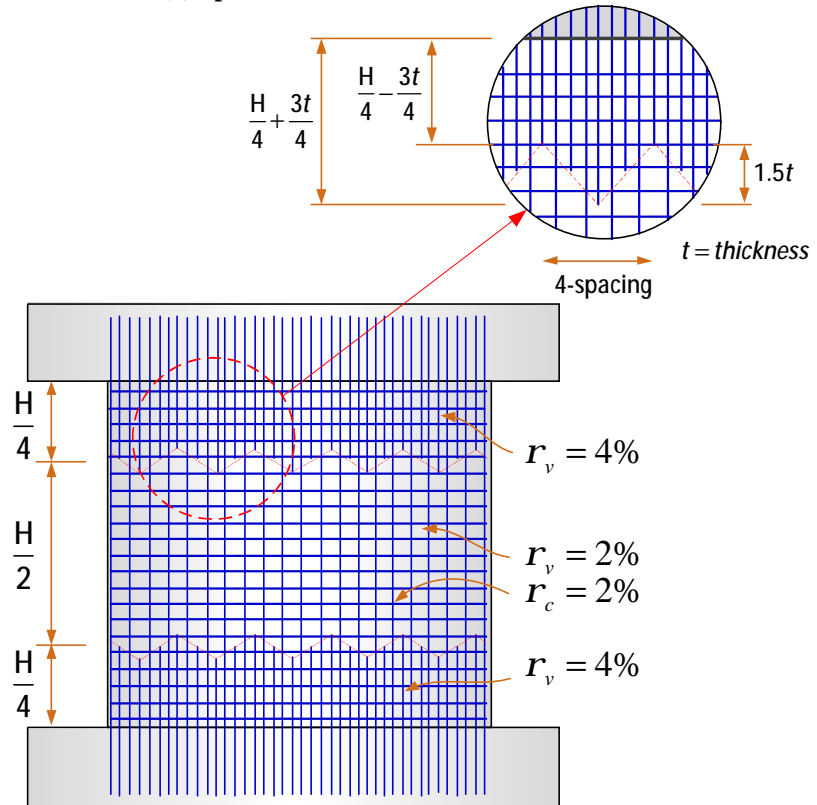


**Figure 5.5 Dimensions of the RCCV specimens: (a) Elevation view (b) Plan view**

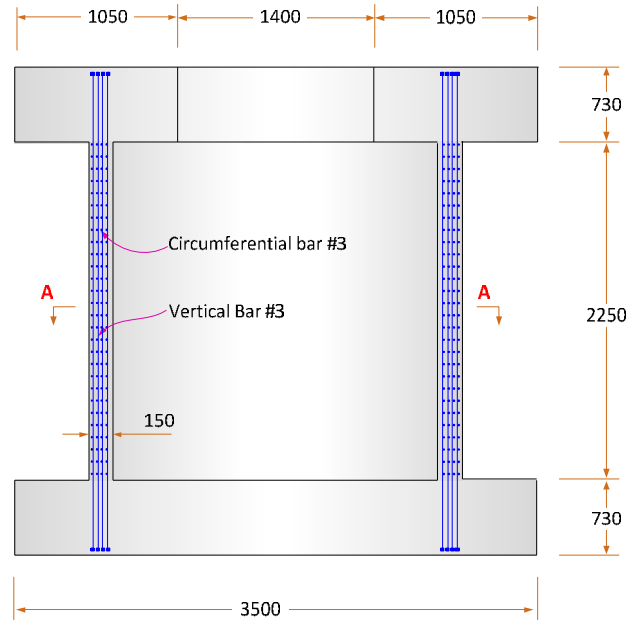


(a) Specimen No. 1

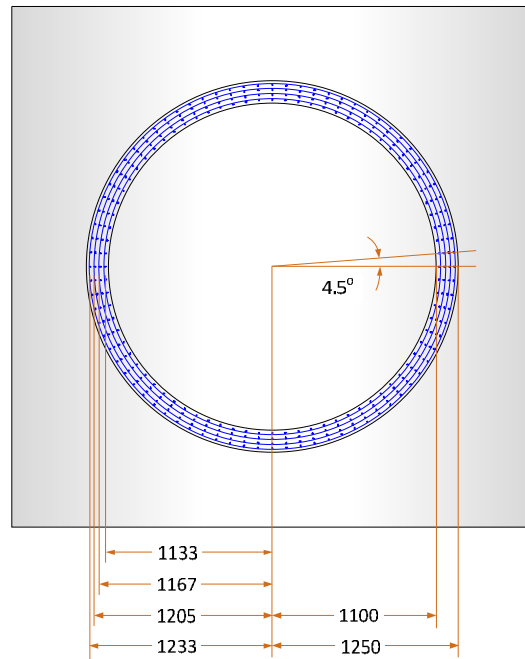


(b) Specimen No. 2

Figure 5.6 Reinforcement details of the RCCV specimens

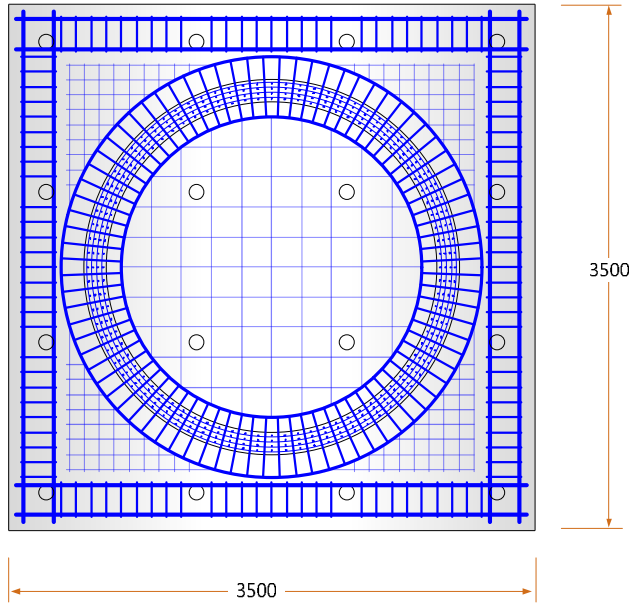


(a) Vertical cross section

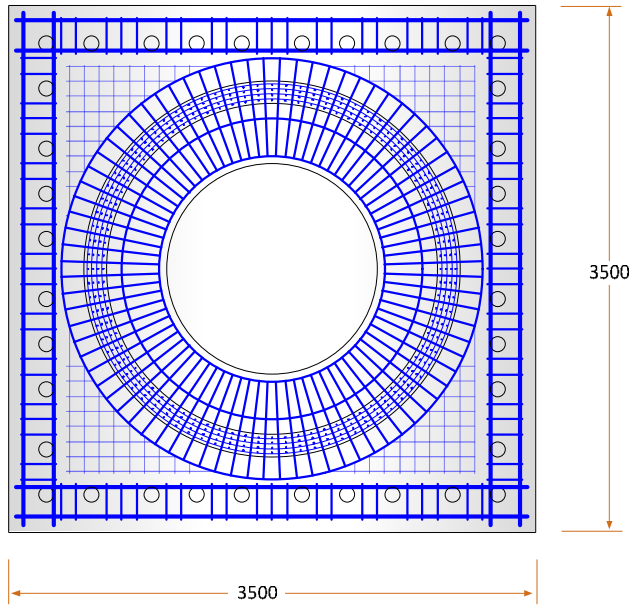


(b) Horizontal cross section

Figure 5.7 Reinforcement details of the RCCV specimens



**(a) Bottom slab**



**(b) Top slab**

**Figure 5.8 Reinforcement details of the top and bottom slabs**

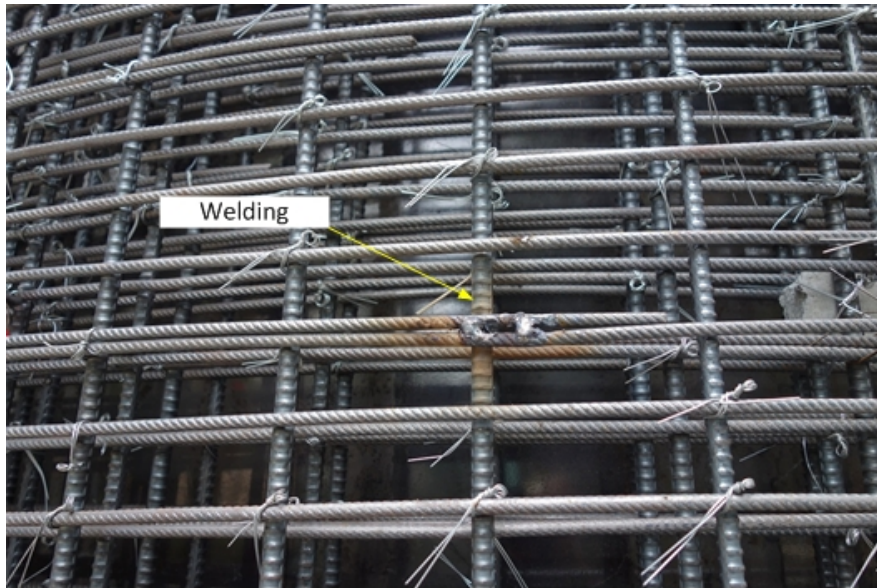


**Figure 5.9 Welding connection of the circumferential bars**

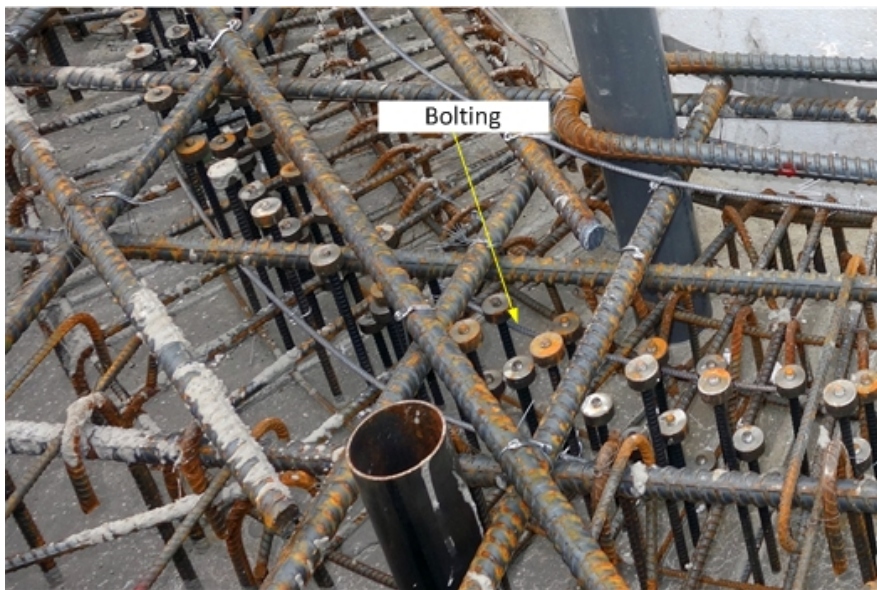


**Figure 5.10 Details of the end-bolt connection of the vertical bars**

### 5.2.3 Material

A local concrete company supplied the ready-mixed concrete for the test specimens. Similar concrete mixtures were used for both specimens. Because of the high amount of reinforcements placed in a slender wall of the containments, using traditional concrete would have caused difficulty in the concrete consolidation in such congested reinforced specimens. As a result, self-consolidating concrete (SCC) was used in the specimens. Self-consolidating concrete, also referred to as self-compacting concrete, has substantial commercial benefits because of the ease of placement in complex forms with congested reinforcements. The filling ability and flowability of the SCC mixture were tested using the slump flow test. The slump flow is the mean diameter of the horizontal spread of the concrete mass, after lifting the slump cone, as shown in Figure 5.11. The slump flow diameter of the SCC mixture was 75 cm, as shown in Figure 5.12. During the slump flow test, there was no restriction to the freely flowing SCC mixture. Hence, the flow spread recorded during this test was referred to as an unrestricted slump flow. For the hardening property, the compressive strength of concrete was determined from the compression tests of standards concrete cylinder (300 mm in height and 150 mm in diameter). The average compressive strength of concrete at Day 28 was 35 MPa (5 ksi). The nominal yielding strength of the reinforcements was 365 MPa (51.4 ksi). Two different types of steel bars were used for the structural components. The #3 bars were used as vertical and circumferential bars of the containments; the #5 bars were used as the vertical steel bars of the top and bottom slabs.



**Figure 5.11 Slump flow test of concrete**

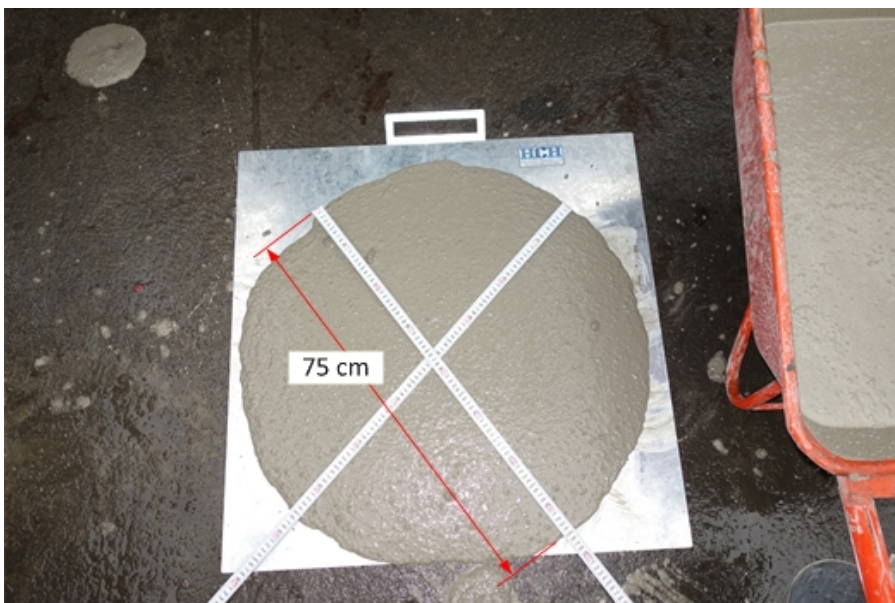


**Figure 5.12 Slump flow diameter of concrete**

## **5.2.4 Manufacturing**

The manufacture of each specimen was processed separately following similar processes. The first step was the fabrication of formwork. The arrangement of steel, casting of the bottom foundation, and the main body of the specimen were built outside the lab. A truck and crane moved the specimen into the lab. After the specimen was in the testing location, the top slab was casted.

### **5.2.4.1 Formwork**

The formwork was made of steel and was specifically designed for the specimens, as shown in Figure 5.13. The formwork of the top and bottom slabs of the specimens consisted of large steel plates, which were welded together to make one large piece. The formwork of the specimen body contained many small pieces. Each piece was designed with a similar curvature and was connected together by using bolt connections. The formwork of the top slab was lifted by a crane and was connected to the body formwork, as shown in Figure 5.14. A steel frame was designed to support the formwork and the self-weight of the concrete of the top slab before the concrete gained sufficient strength to support itself. Before the formwork was assembled, form release oil was applied inside the formwork so it could be removed easily after the concrete of the specimens hardened. Figure 5.15 shows the application of the form release oil. After casting the top slab, the formwork of the specimen body was removed. The formwork for both the top slab and the bottom foundation of the specimens were kept, as shown in Figure 5.16 through Figure 5.18.



**Figure 5.13 Formwork of the RCCV specimens**



**Figure 5.14 Formwork of the top slab**



**Figure 5.15 Applying oil to the formwork before casting**



**Figure 5.16 Removing the formwork**



**Figure 5.17** The specimen outside the laboratory after removing the formworks



**Figure 5.18** The RCCV specimen inside the laboratory before testing

#### 5.2.4.2 Arrangement of the Reinforcement

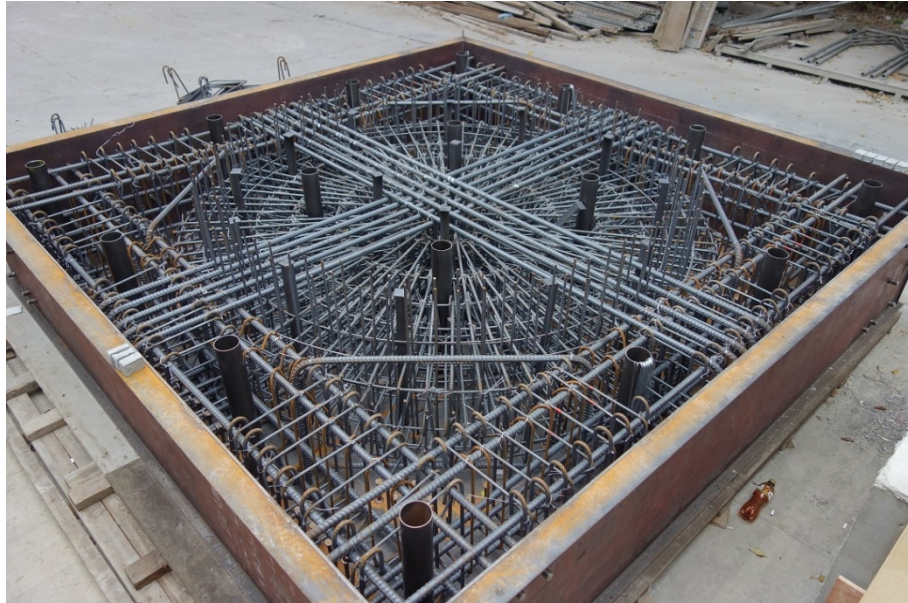
A local supplier cut and bent the reinforcing bars. The reinforcing cage was tied and the strain gauges were pasted on the reinforcing bars outside of the laboratory. The strain gauges were covered by coating agents and wrapped with vinyl mastic to protect them from damage during the concrete casting, as shown in Figure 5.28. A typical reinforcing cage of the containments is shown in Figure 5.19 and Figure 5.20. Typical reinforcement cages inside the top and bottom slabs are shown in Figure 5.21 and Figure 5.22.



Figure 5.19 Reinforcement detail of Specimen No. 1



**Figure 5.20 Reinforcement detail of Specimen No. 2**



**Figure 5.21 Typical reinforcement detail inside the bottom slab**



**Figure 5.22 Typical reinforcement detail inside the top slab**

### 5.2.4.3 Casting of the Concrete

The specimens were cast in the vertical direction. The process of concrete casting for the specimens was divided into three stages, each being a continuous pour. First, the bottom slab of the specimen was cast using one truckload of concrete. Second, the containment was poured from another batch of concrete. Third, the top slab was cast after the specimen was settled at the testing location. In the first step, the concrete was poured from the bottom to two-third of the thickness of the bottom slab. In the second step, the concrete was poured up to the height of one-third of the top slab. By doing so, no cold joint occurred between the containment and the top and bottom slabs. The casting of the top slab is shown in Figure 5.23 and Figure 5.24. A working frame was made to surround the specimen to allow workers to stand and control the concrete pipe. Vibrators were used to make sure the concrete had uniform distribution and that segregation was prevented.



**Figure 5.23 Pumping concrete from the truck inside the laboratory**



**Figure 5.24 Casting the top slab inside the laboratory**

#### **5.2.4.4 Transportation of the Specimen into the Test Position**

Because the test specimen was cast outside the lab, the specimen needed to be moved to the testing location. Because the specimen was heavy and a forklift could not move it, a special wheel system was assembled under the bottom of the specimen. This system allowed the specimen later to be pulled by a truck into the lab. After the specimen was moved into the lab, a crane system lifted and moved it toward the testing location. The process of moving the specimen is illustrated in Figure 5.25 and Figure 5.26. Figure 5.27 shows the testing location before the specimen was placed. A set of holes was created so that the specimen can be tightened onto the floor by using bolt connections. Before the specimen was placed, a layer of oil was applied onto the surface of the floor to make it easier to remove the specimen.

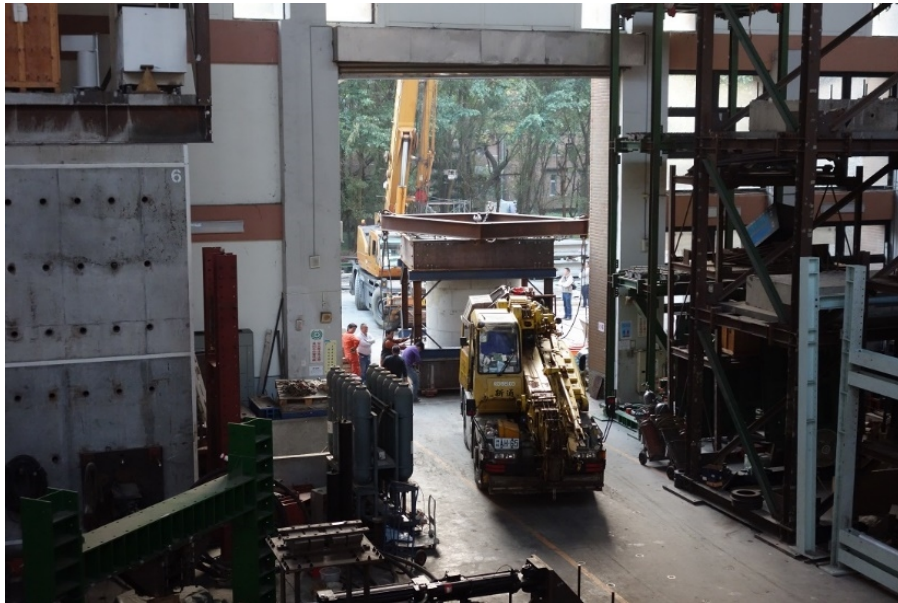


**Figure 5.25 Moving the specimen into the lab by truck**



**Figure 5.26 Lifting the specimen toward the testing location by crane**



**Figure 5.27 The testing location**

### **5.2.5 Instrumentations**

The overall system instrumentation used can be categorized into internal and external instrumentation systems. The internal instrumentation included the strain gauges used to measure the reinforcement strains at selected positions, as shown in Figure 5.28 and Figure 5.29. The external instrumentation encompassed load cells, Linear Voltage Displacement Transducer (LVDTs), dial gauges, and the Certus Position Sensor system (CPS) with NDI markers, as shown in Figure 5.30 and Figure 5.31. The load cells and LVDTs were used to measure the lateral and vertical loads; the dial gauges were used to measure the small slip displacements of the foundation.

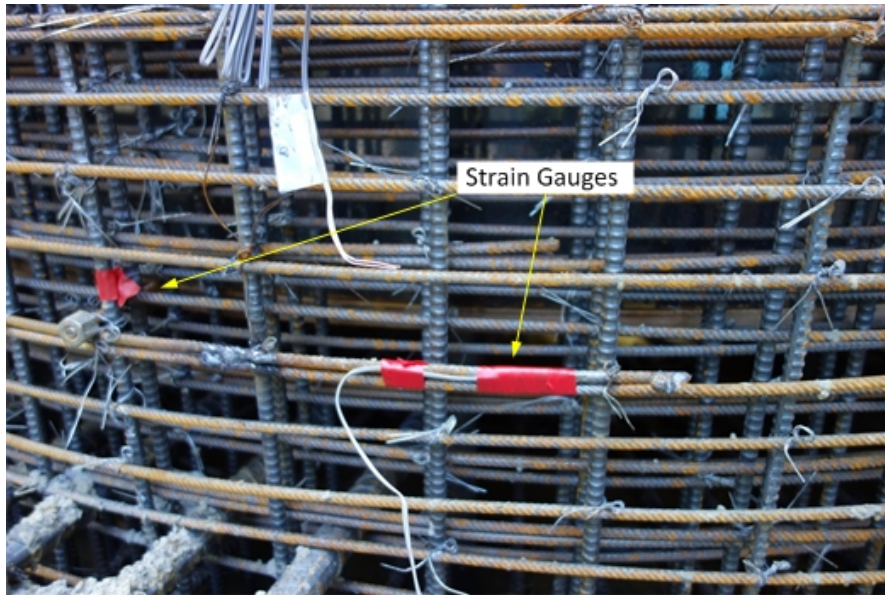


**Figure 5.28 Strain gauges were attached to the steel bars**



**Figure 5.29 Plastic pipes protected the strain gauge cables**

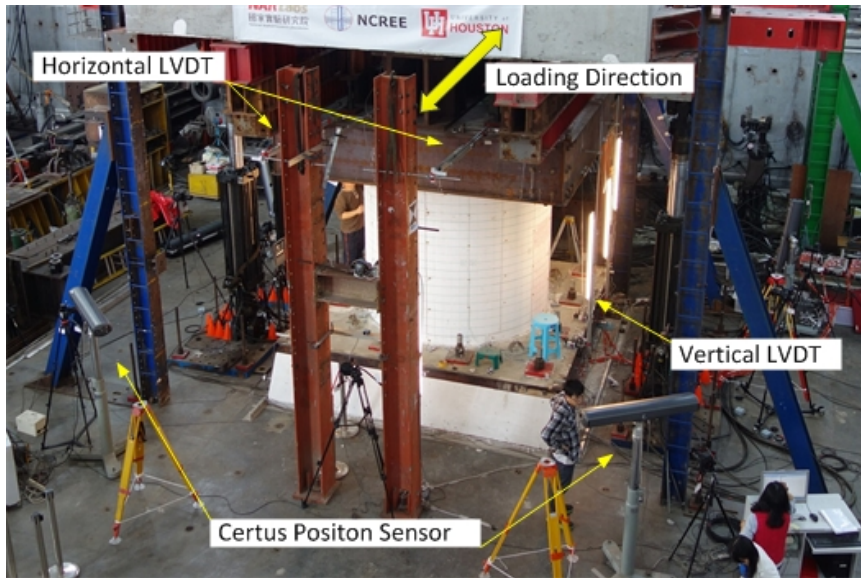


**Figure 5.30 Instruments outside of the specimen**

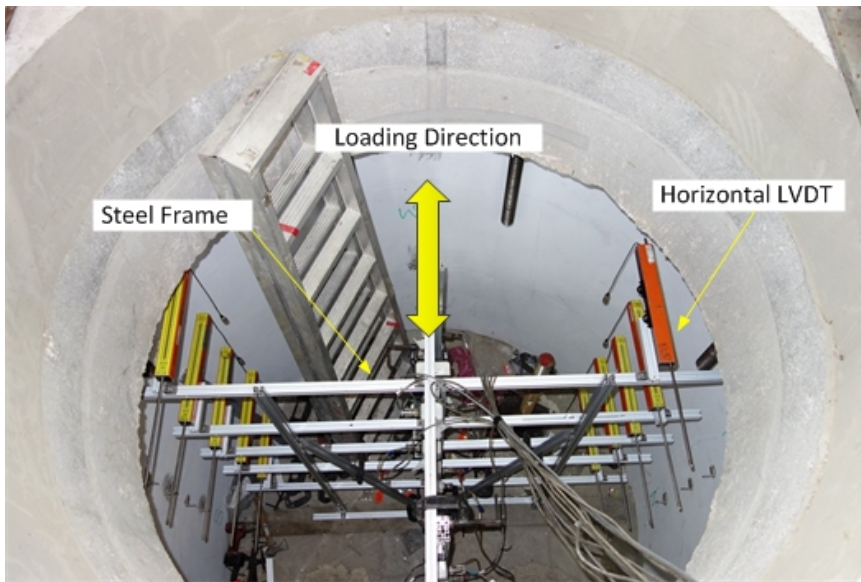


**Figure 5.31 Instruments inside the specimen**

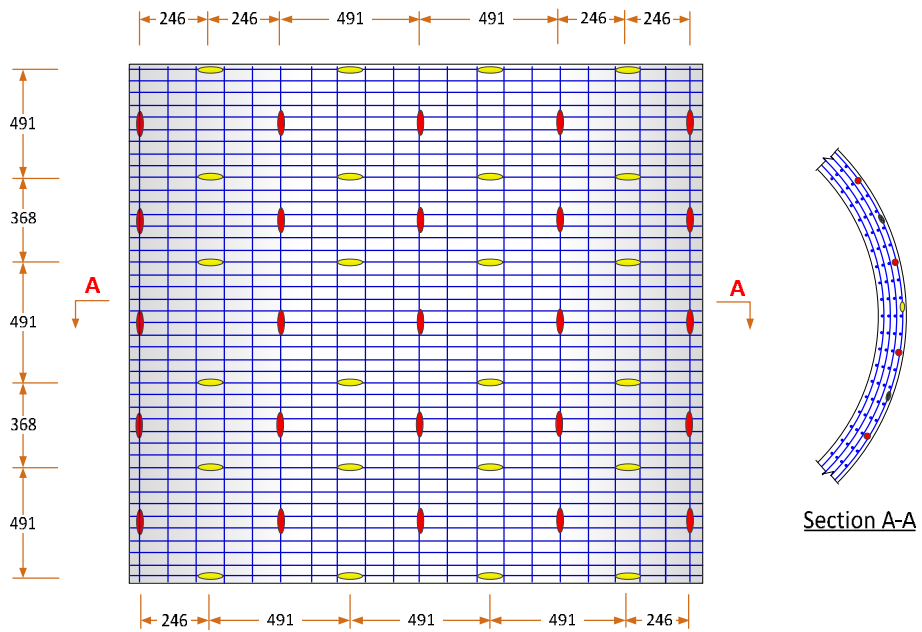


**Figure 5.32 Arrangement of the strain gauges for Specimen No. 1**

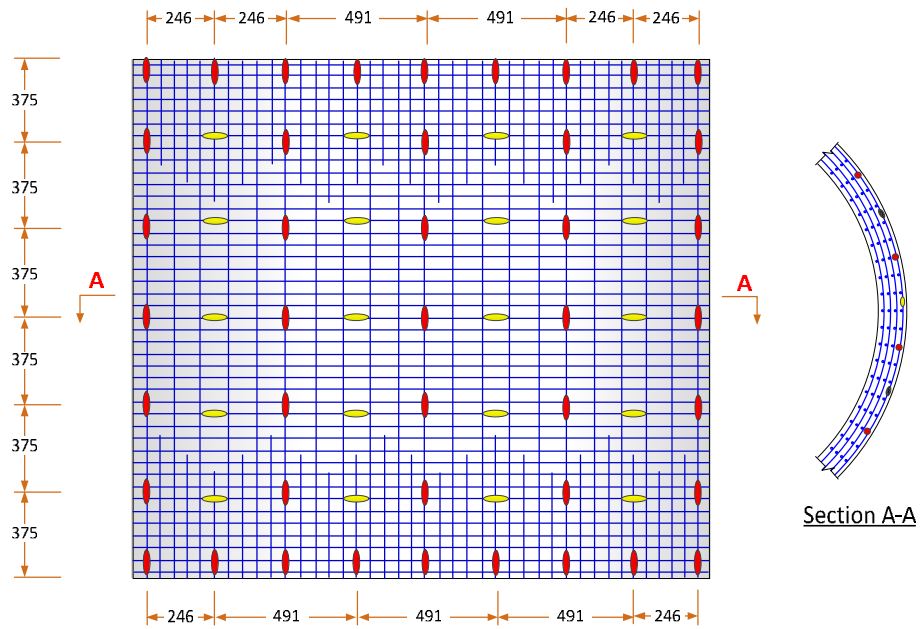


**Figure 5.33 Arrangement of the strain gauges for Specimen No. 2**

### 5.2.6 Test Setup

The test specimens were subjected to horizontal loading up to their maximum capacity with a set of specially built steel loading frames at National Center for Research on Earthquake Engineering, Taiwan, as shown in Figure 5.34. The test setup was used to simulate gravity and the lateral and vertical earthquake loads. Figure 5.35 shows the side view of the test setup. Figure 5.37 shows the overview of the test setup with various components in details, including the horizontal actuators, vertical actuators, steel loading frame systems, and the specimen and data acquisition systems.

The specimens were loaded axially using four 1000-kN capacity vertical hydraulic actuator. Pin connections were used at the end of the vertical actuators to minimize moment when transferred to the L-shaped steel loading frame. The simulated lateral earthquake load was applied by eight 1000-kN-capacity horizontal actuators under displacement control. As shown in Figure 5.36, the horizontal actuators were bolted to a rigid concrete reaction wall and the loading frame such that the center of the loading axis passed through the specimen's mid-height. The maximum stroke of the horizontal actuators was 200 mm. The specimens were connected to the strong floor with 16 31.75 mm (1.25 in.) diameter all-thread steel rods that went through the foundation. A steel plate was placed around each rod and mortared to the concrete surface, and nuts were screwed onto the plates to prevent the foundation from sliding against the solid floor. The loading frame was allowed to move freely in the vertical plane. Additional steel frames bolted to the solid floor were placed on the north and south sides of the specimen to prevent the horizontal out-of-plane displacement.

During the tests, the containment specimens were subjected to constant vertical axial loads and horizontal reversed-cyclic load until failure. Both the prescribed displacement and forces controlled the four vertical actuators. A prescribed horizontal displacement history controlled the eight horizontal actuators. A control modes in the computer-control testing system controlled the operation of the vertical and the horizontal actuators.

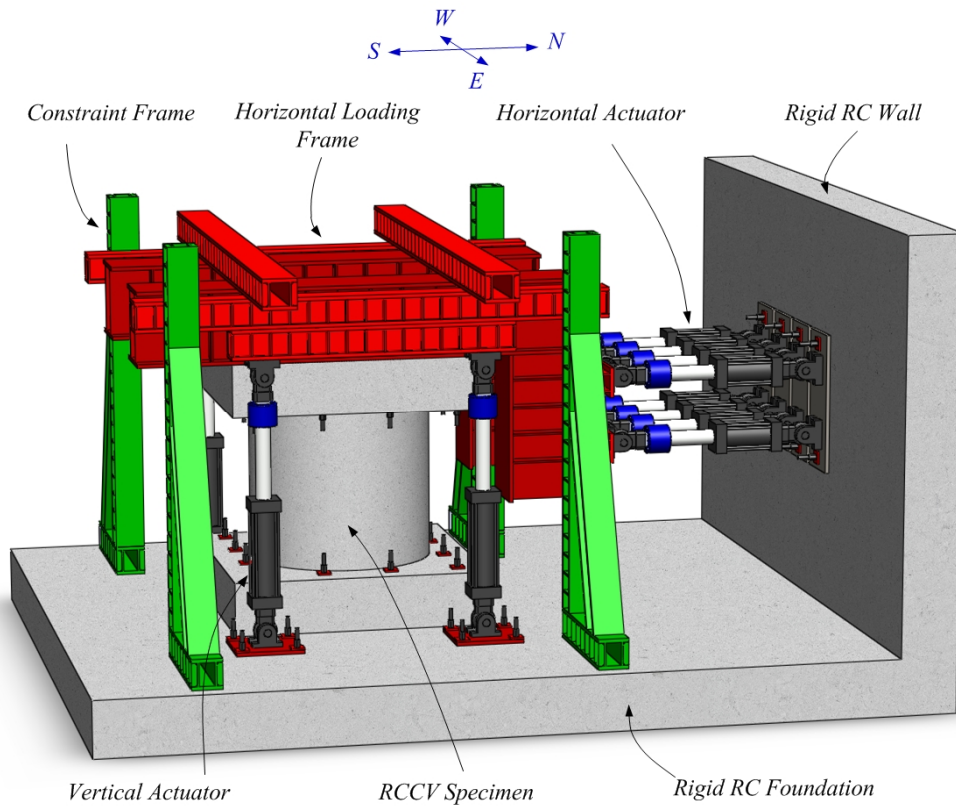


**Figure 5.34 Three-dimensional view of the test setup**

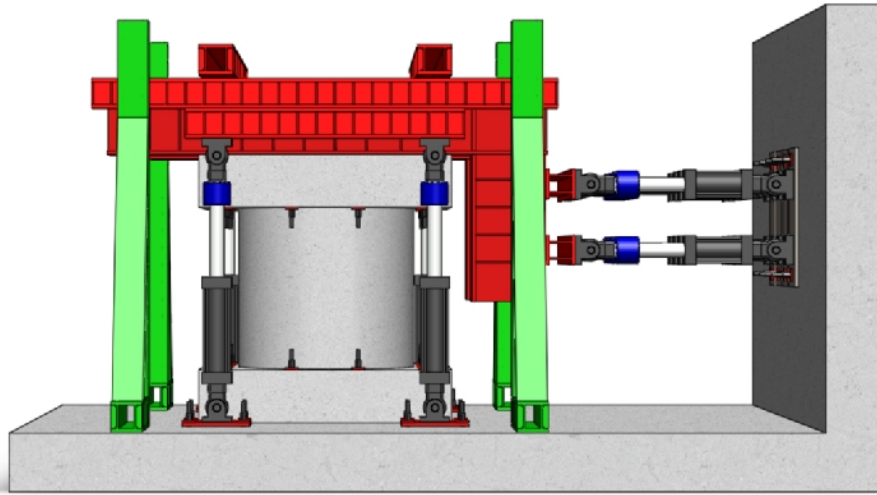


Figure 5.35 Side view of the test setup (East-West)

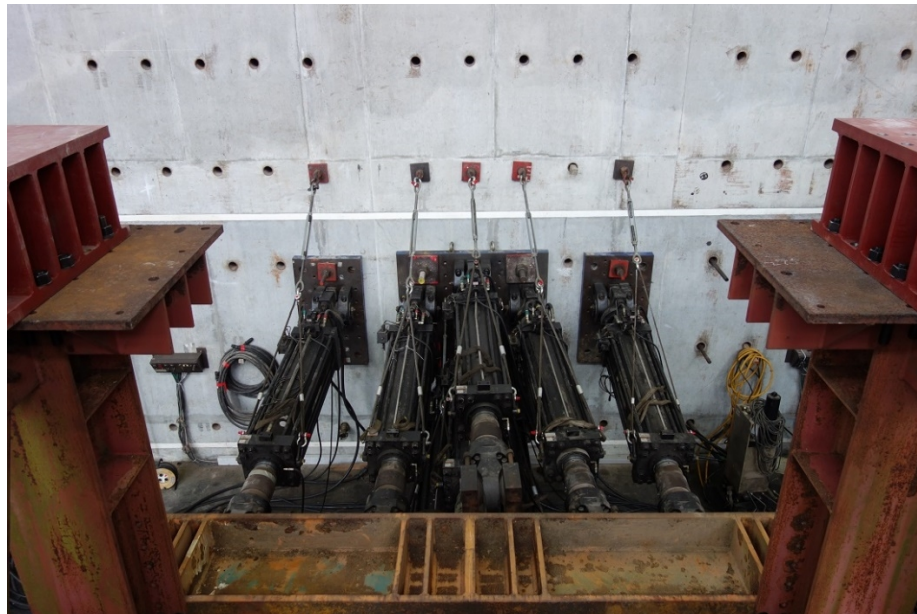


Figure 5.36 Horizontal actuators (Total capacity: 8000 kN)



Figure 5.37 Overview of the test set up

### 5.2.7 Loading Protocol

The first step of the loading protocol program was to apply an axial load that would remain constant during the course of the test. The total initial vertical load equaled 1.6% of the axial concrete capacity ( $f_c' A_g$ ) of each specimen, where  $f_c'$  is compressive strength of concrete and  $A_g$  is nominal area of the specimen. The axial concrete capacity was dependent on the compressive strength of the concrete ( $f_c'$ ); consequently, the total initial vertical load varied for each specimen.

After the axial load was applied, a reversed-cyclic load was added by eight 1000-kN-capacity horizontal actuators under displacement control. First, the test specimens were subjected to several cycles of small displacements for warming up, in which the specimen behaved elastically. Then, inelastic tests were performed by using the loading history consisting of the following drift cycles: 0.1%, 0.15%, 0.2%, 0.375%, 0.5%, 0.75%, 1.0%, 1.5%, 2.0%, 3.0%, and 4.0% as shown in Figure 5.38.

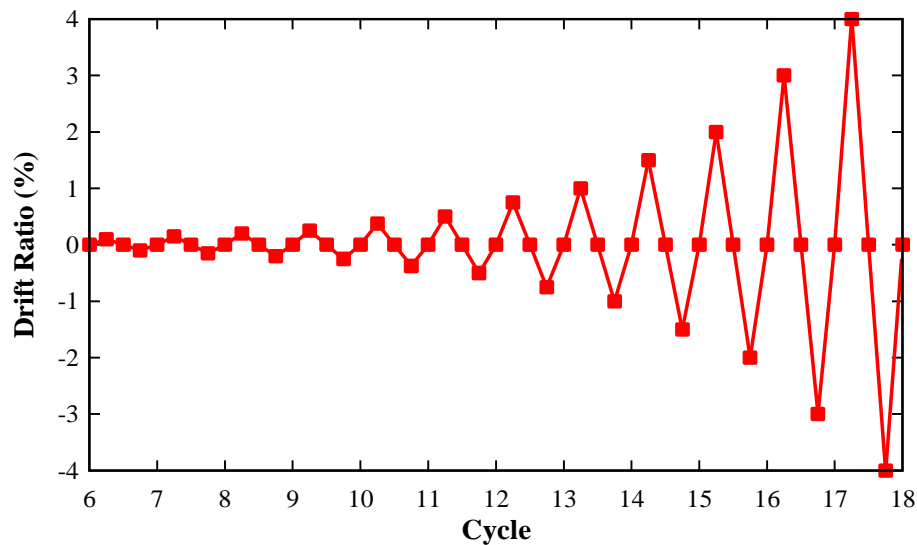


Figure 5.38 Horizontal displacement control scheme (Inelastic test)

## 5.3 Experimental Results

### 5.3.1 Cracking Patterns of Concrete

The typical cracking patterns of the RCCV specimens are shown in Figure 5.39 and Figure 5.40. Three types of cracks occurred in the specimen during the tests. The first cracks can be classified as flexural cracks located within the west-side and east-side of the wall panels, which were perpendicular to the loading direction. These cracks were in the horizontal direction and distributed along the height of the specimens. The second cracks can be classified as shear cracks located within the north-side and south-side of the wall panels, which were parallel to the loading direction. The shear cracks were distributed uniformly at an inclination angle varying from 40° to 60°. The third cracks occurred only in Specimen No. 1, which were considered to be shear sliding cracks that appeared at the junction of the body of the specimen and the top slab. The flexural cracks and the shear cracks occurred almost at the same time in the first several cycles of the test; meanwhile, the shear sliding crack occurred later.

In the both specimens, the initial flexural and shear cracks were observed when the drift ratio reached 0.25%. A similar pattern of cracks occurred in the specimen when the drift ratios were 0.375%, 0.5%, and 0.75%. The density of the cracks increased, and the width of the cracks opened wider when the drift of the specimen increased. The tests showed a drift of 0.75% with no major damage in the specimens, although flaking and scaling of the concrete cover were observed. In Specimen No. 1, sliding shear cracks started to occur from the drift of 0.5% and opened larger with the increasing of the drift. Spalling of the concrete was observed along the sliding shear crack.

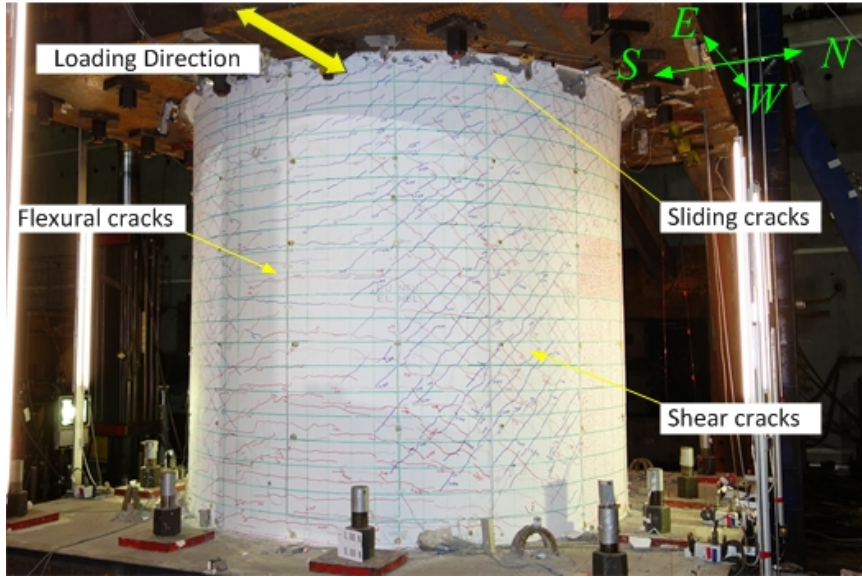


Figure 5.39 Typical cracking patterns of the RCCV specimens (north-east view)

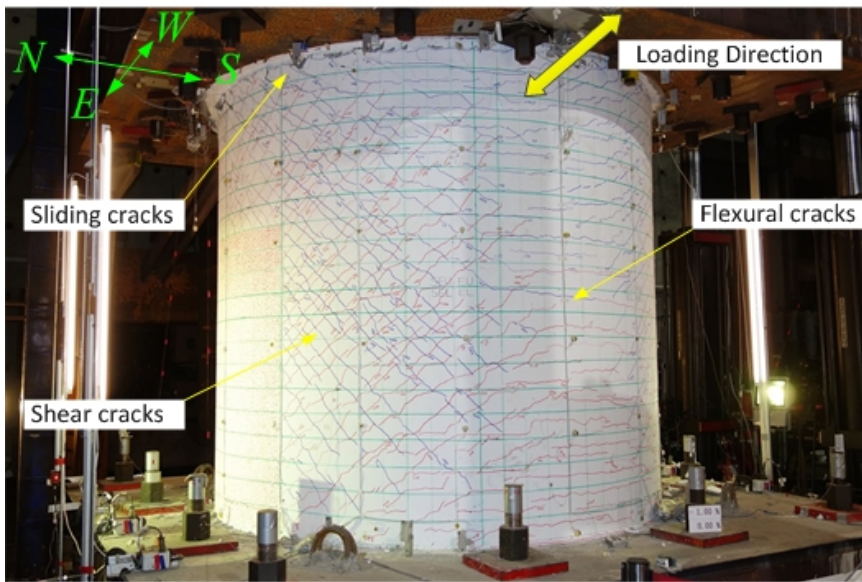


Figure 5.40 Typical cracking patterns of the RCCV specimens (north-west view)

### 5.3.2 Load-Displacement Characteristic

The horizontal load versus horizontal displacement relationships of the test specimens are shown in Figure 5.41 and Figure 5.42. These curves illustrate the load resisting mechanism of the nuclear containment vessels. The five critical points are noted in each curve, which correspond to the first cracking of concrete, the first yielding of vertical and circumferential steel bars, and the peak load in each specimen, as shown in Table 5.2. The envelope of curve of each specimen significantly changed its slope after the displacement exceeded 1.6 mm. The slope of the envelope curve often decreased when the stiffness of the specimen was reduced significantly after cracking. Therefore, the displacement of 1.6 mm could be considered as the cracking displacement of the specimens. With corresponding to the cracking displacement, the cracking loads of Specimen No. 1 and Specimen No. 2 were determined to be 1900 kN and 1880 kN, respectively.

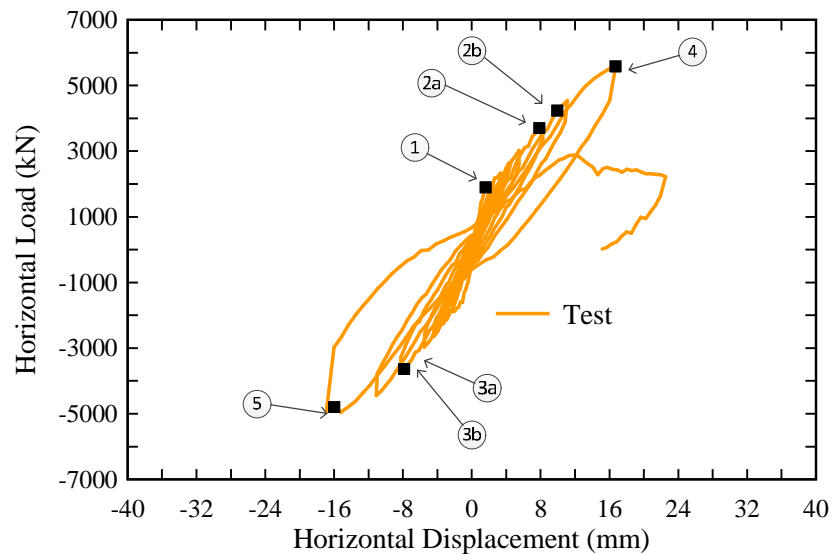
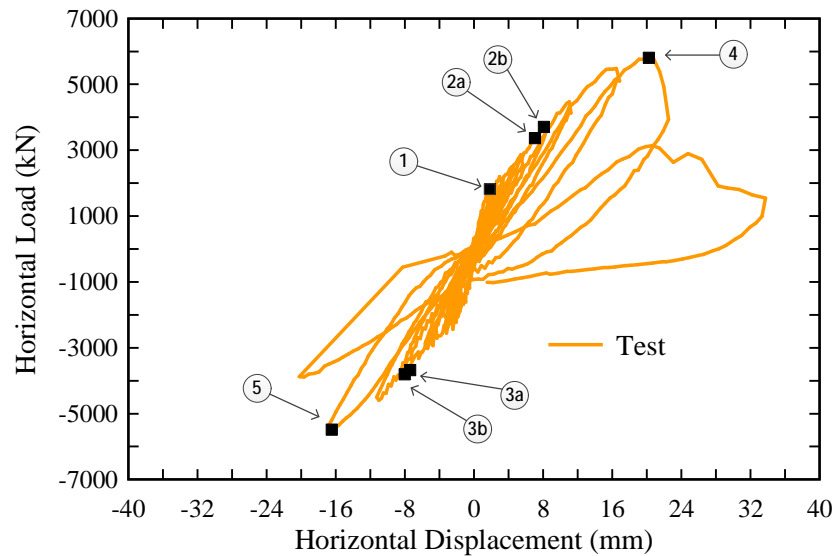


Figure 5.41 Horizontal load versus displacement curve of Specimen No. 1

By observing the strain data of all the steel bars at each step of loading, it is shown that both the vertical and circumferential steel bars of Specimen No. 1 yielded during the tests, and the yielding points of the steel bars were close to each other. In the positive loading direction, the vertical steel bars yielded first at the load of 3706 kN and the displacement of 7.84 mm; the circumferential steel bars yielded later at the load of 4234 kN and the displacement of 9.9 mm, as shown in Table 5.3 and Figure 5.41. In the negative loading direction, both of the steel bars yielded at the same time at the load of 3634 kN and the displacement of 7.86 mm, as shown in Table 5.3 and Figure 5.41.



**Figure 5.42 Horizontal load versus the displacement curve of Specimen No. 2**

Similarly, in case of Specimen No. 2, both the vertical and circumferential steel bars yielded during the test, and the circumferential steel bars reached yield before the vertical steel bars in both the positive and negative loading direction. In the positive loading direction, the circumferential steel bars yielded at the load of 3363 kN and the

displacement of 7.04 mm; the vertical steel bars yielded at the load of 3702 kN and the displacement of 8.1 mm, as shown in Table 5.3 and Figure 5.42. In the negative loading direction, the circumferential steel bars yielded at the load of 3675 kN and the displacement of 7.38 mm; the vertical steel bar yield at the load of 3805 kN and the displacement of 8.03 mm, as shown in Table 5.3 and Figure 5.42.

**Table 5.2 Demonstration of Critical Points on the Load Versus Displacement Curves**

Points	Status
1	First cracking of concrete
2a	First yield of vertical steel bars in the positive direction
2b	First yield of circumferential steel bars in the positive direction
3a	First yield of vertical steel bars in the negative direction
3b	First yield of circumferential steel bars in the negative direction
4	Peak load in the positive direction
5	Peak load in the negative direction

As shown in Table 5.3 and Figure 5.41, the recorded peak loads of Specimen No. 1 were 5580 kN and 4794 kN in the positive and negative loading directions, respectively. The displacements corresponding to the peak loads were 16.7 mm and 16.0 mm in the positive and negative loading directions, respectively. The recorded peak loads of Specimen No. 2 were 5805 kN and 5487 kN in the positive and negative loading directions, respectively. The displacements corresponding to the peak loads were 20.2 mm and 16.5 mm in the positive and negative loading directions, respectively, as shown

in Figure 5.42. It can be seen that the peak loads of Specimen No.2 were slightly higher than the peak loads of Specimen No.1 in both loading directions. In both specimens, the lateral strength dropped significantly after the peak load. Although the specimens were able to sustain the axial-load-carrying capacity, they sustained relatively large displacements until the end of the tests.

**Table 5.3 Ductility of the Test Specimen**

Specimen	Loading Direction	$\Delta_y$ (mm)	$P_y$ (kN)	$\Delta_{max}$ (mm)	$P_{max}$ (kN)	$m$
1	(+)	7.84	3706	16.7	5580	2.13
	(-)	7.86	3634	16.0	4794	2.04
2	(+)	7.04	3363	20.2	5805	2.87
	(-)	7.38	3675	16.5	5487	2.23

As observed from the load versus displacement curves, because the steel bars yielded before the loads reached the peak, it can be concluded that the specimens had ductile behavior. The ductility coefficients of the two specimens in both positive and negative loading directions are shown in Table 5.3. The coefficients were calculated as the ratio of displacement at the peak load divided by the first yielding displacement of the specimens. As seen in Table 5.3, Specimen No. 2 had higher ductility than Specimen No. 1 in both positive and negative loading direction. In the positive loading direction, the ductility coefficients of Specimen No. 1 and Specimen No. 2 are 2.13 and 2.87, respectively. In the negative loading direction, the ductility coefficients of Specimen No. 1 and Specimen No. 2 are 2.04 and 2.23, respectively.

### **5.3.3 Behaviors of Steel Bars**

Investigating the behavior of reinforcement was important to understand the inelastic behavior of the test specimens. Therefore, many strain gauges were installed on the vertical and circumferential steel bars of the specimens to measure the strains of the steel bars during the test, as shown in Figure 5.32 and Figure 5.33. The measurements from the strain gauges are presented in the Appendix. In this section, the data obtained from the strain gauges were plotted as contour diagrams to show the strain distributions in the vertical and circumferential steel bars over the surface of the specimen. In the contour diagram, the upper limit of the legend of the diagram was set to be equal to the yielding tensile strain of the steel bars, 0.002, so that the diagram would show all the yielding locations of the steel bars.

#### **5.3.3.1 At the First Yielding**

The strain distribution in the vertical steel bars over the surface of the test Specimen No. 1 at the yielding points are illustrated in Figure 5.43 and Figure 5.44, which correspond to Point 2 and Point 3 on the load vs. displacement curves, as shown in Figure 5.41. As shown in the figures, the vertical steel bars had high tensile strain values along the diagonal direction of the specimen. The highest value of tensile strains was located at the top and bottom corners of the specimen, which also were where the first yielding in the vertical steel bars occurred.

The strain distribution in the vertical steel bars over the surface of the test Specimen No. 2 at yielding points are illustrated in Figure 5.45 and Figure 5.46 which correspond to Point 2 and Point 3 on the load vs. displacement curves, as shown in Figure 5.42. Similar to Specimen No. 1, the vertical steel bars in Specimen No. 2 had a high tensile strain

values along the diagonal direction of the specimen. However, the largest value of the tensile strains was not concentrated at the top and bottom corners of the specimen. Instead, they were located near the cut-off point of the dowel steel bars that were added to the specimen to prevent sliding shear. As a result, the first yielding of the vertical steel bars occurred at the position near the cut-off point of the dowel bars.

The strain distribution in the circumferential steel bars over the surface of Specimen No. 1 and Specimen No. 2 at the yielding points are illustrated in Figure 5.47 through Figure 5.50. The strain distributions of the circumferential steel bars of the two specimens were similar. The circumferential steel bars had intense tensile strain values in the mid-height region of the specimen, and the first yielding occurred in this region. This result indicated that the specimens had critical shear behavior.

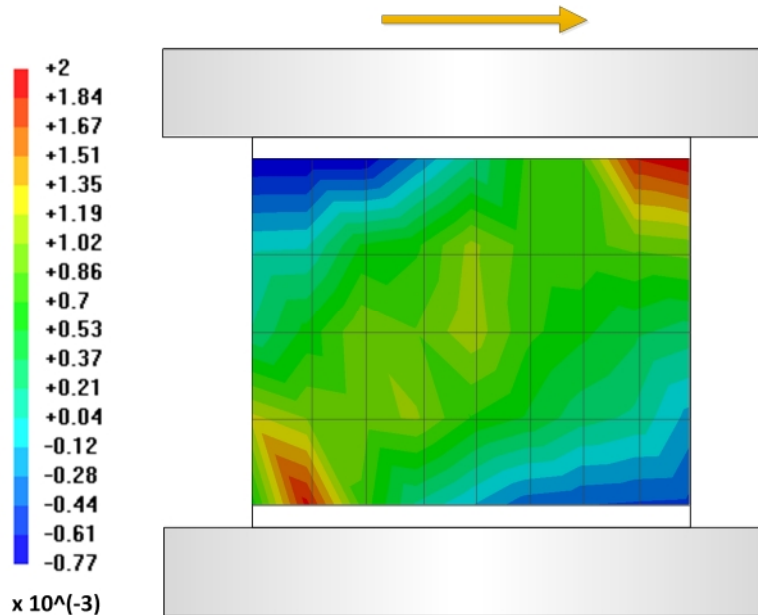


**Figure 5.43 Strains of the vertical steel bars in Specimen No. 1 (at the stage of the first yielding of the vertical steel bars in the positive direction)**

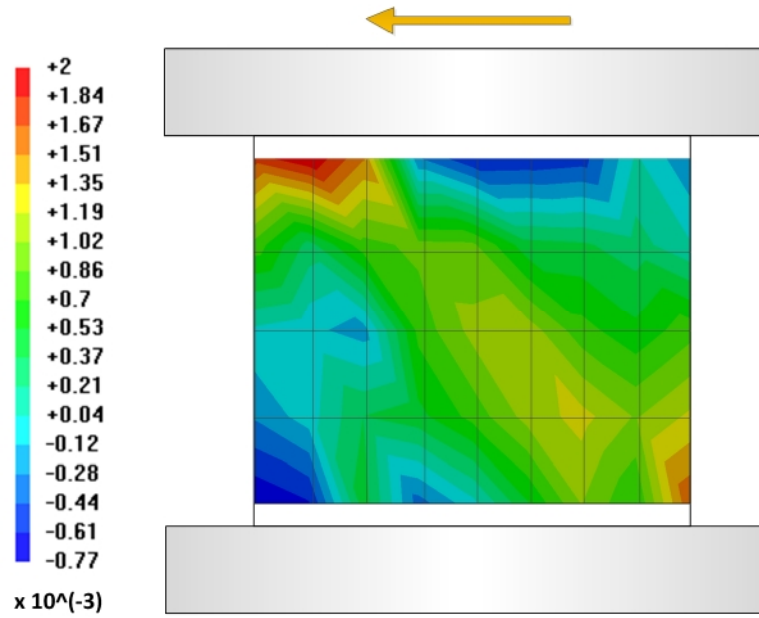


Figure 5.44 Strains of the vertical steel bars in Specimen No. 1 (at the stage of the first yielding of the vertical steel bars in the negative direction)

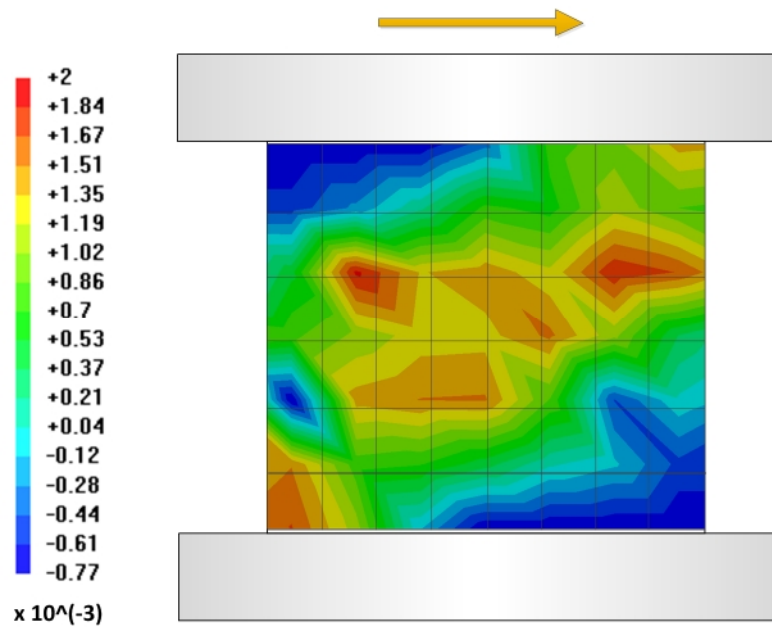


Figure 5.45 Strains of the vertical steel bars in Specimen No. 2 (at the stage of the first yielding of the vertical steel bars in the negative direction)

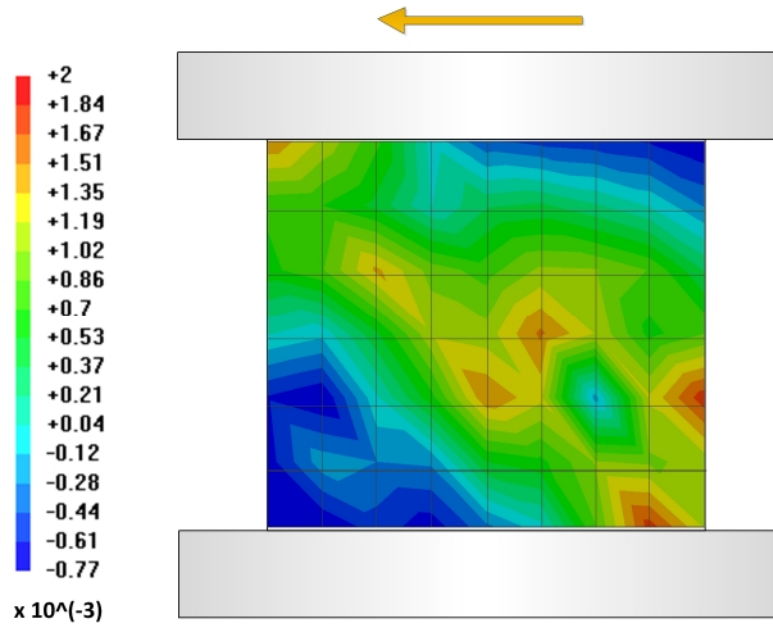


Figure 5.46 Strains of the vertical steel bars in Specimen No. 2 (at the stage of the first yielding of the vertical steel bars in the negative direction)

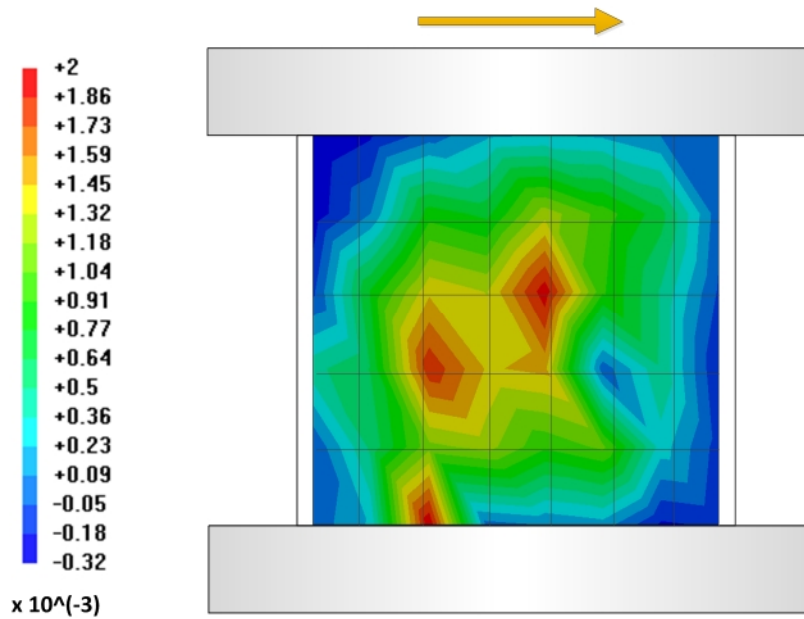


Figure 5.47 Strains of the circumferential steel bars in Specimen No. 1 (at the stage of the first yielding of the circumferential steel bars in the positive direction)

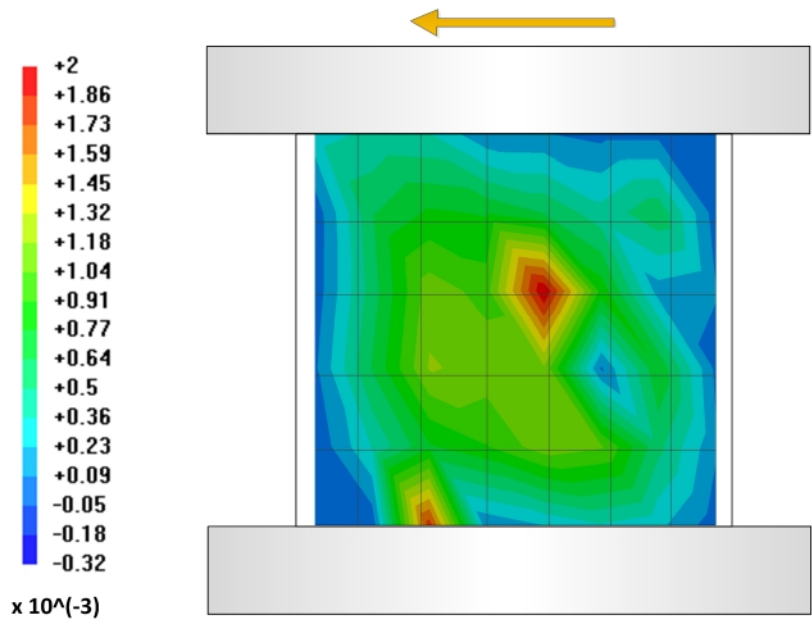


Figure 5.48 Strains of the circumferential steel bars in Specimen No. 1 (at the stage of the first yielding of the circumferential steel bars in the positive direction)

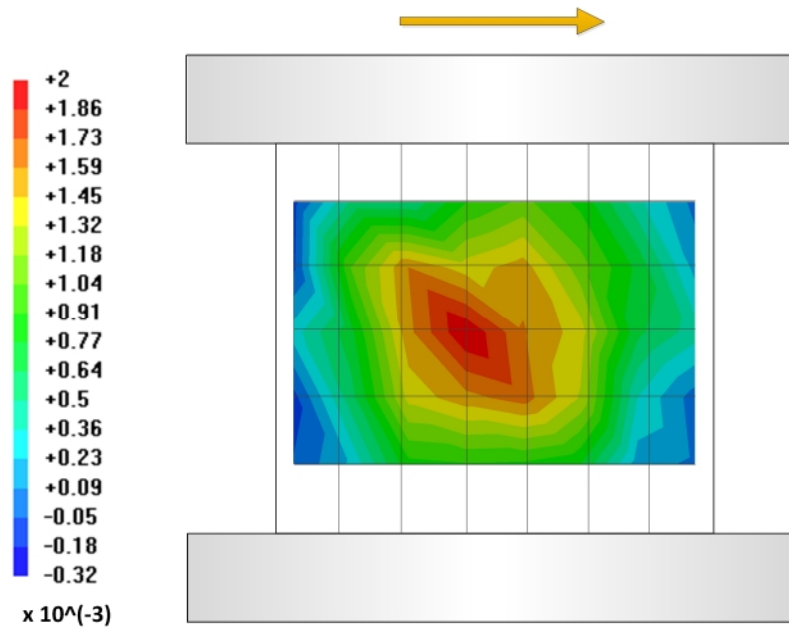
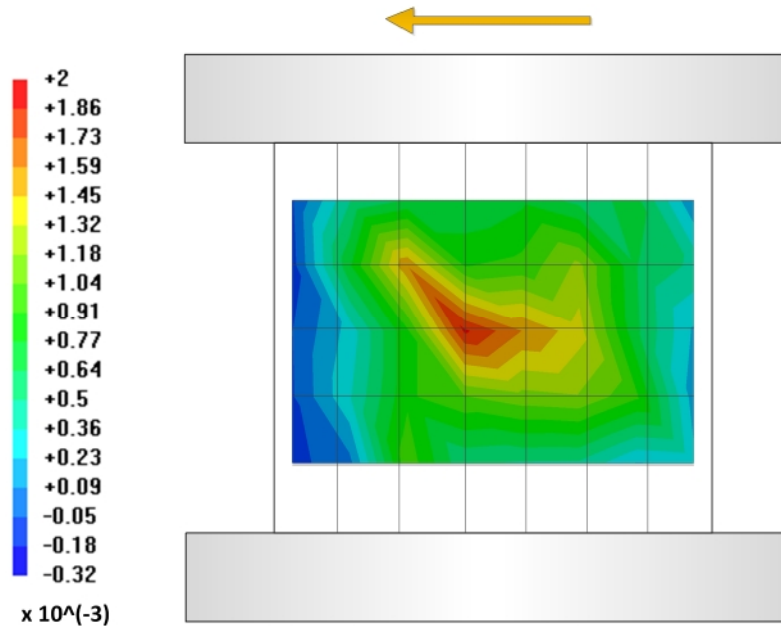


Figure 5.49 Strains of the circumferential steel bars in Specimen No. 2 (at the stage of the first yielding of the circumferential steel bars in the negative direction)



**Figure 5.50 Strains of the circumferential steel bars in Specimen No. 2 (at the stage of the first yielding of the circumferential steel bars in the negative direction)**

### **5.3.3.2 At the Peak Load**

The strain distribution in the vertical steel bars over the surface of Specimen No. 1 at the peak load points is illustrated in Figure 5.51, which correspond to Point 4 on the load vs. displacement curves, as shown in Figure 5.41. The yielding region of the vertical steel bars was spread out to a large region on the surface of the specimen. The yielding region formed diagonally from the bottom to the top corners of the specimen. A similar strain distribution observed in the vertical steel bars of Specimen No. 2 at the peak load points are illustrated in Figure 5.52 which correspond to Point 4 on the load vs. displacement curves, as shown in Figure 5.42.. However, one point in the strain contour diagram does not show along the diagonal direction because the strain gauge at this location was damaged during the test.

The strain distribution in the circumferential steel bars over the surface of the both specimens at the peak load points are illustrated in Figure 5.53 and Figure 5.54. The yielding zone of the circumferential steel bars was expanded to a large region on the surface of the specimen. Unlike the yielding region formed diagonally from the bottom to the top corners of the specimen, the yielding region of the circumferential steel bars concentrated only in the mid-height region of the specimens.

Overall, the results showed that the specimens had a ductile behavior because the vertical and circumferential steel bars yielded significantly. However, no clear yielding plateau was in the envelope of the load vs. displacement curve of the specimen because the steel bars in many locations are in elastic behaviors and their stresses continued to increase. As a result, the load gradually increased from the first yielding point to the peak load and then dropped when the concrete was damaged.

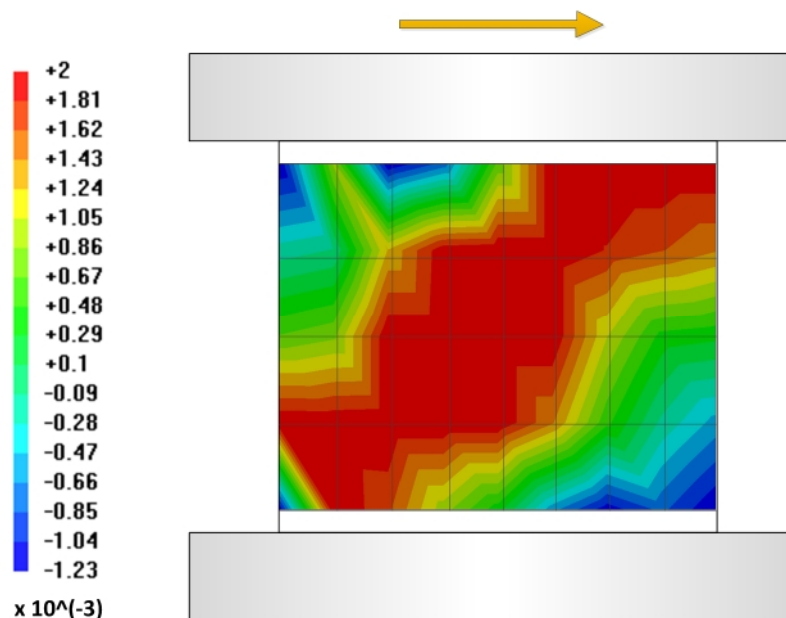


**Figure 5.51 Strains of the vertical steel bars in Specimen No. 1 (at the stage of the peak load in the positive direction)**

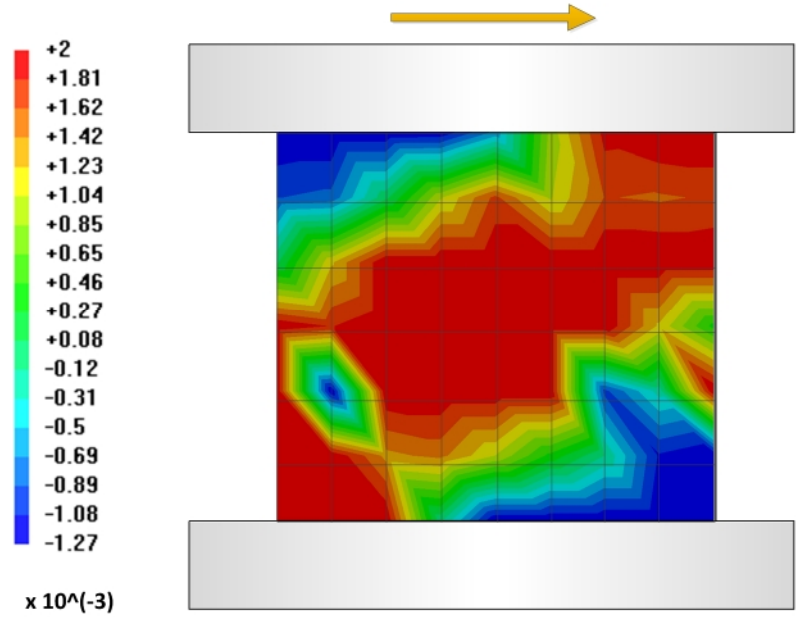


Figure 5.52 Strains of the vertical steel bars in Specimen No. 2 (at the stage of the peak load in the positive direction)

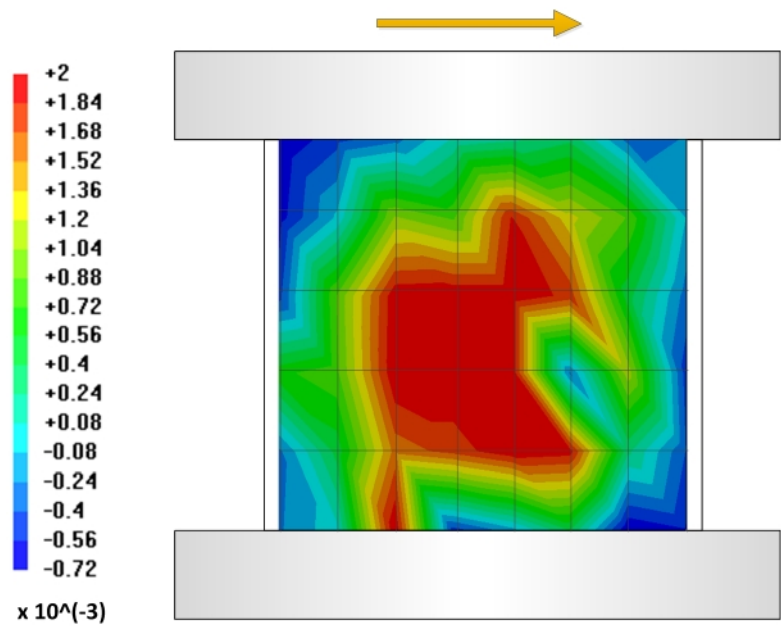
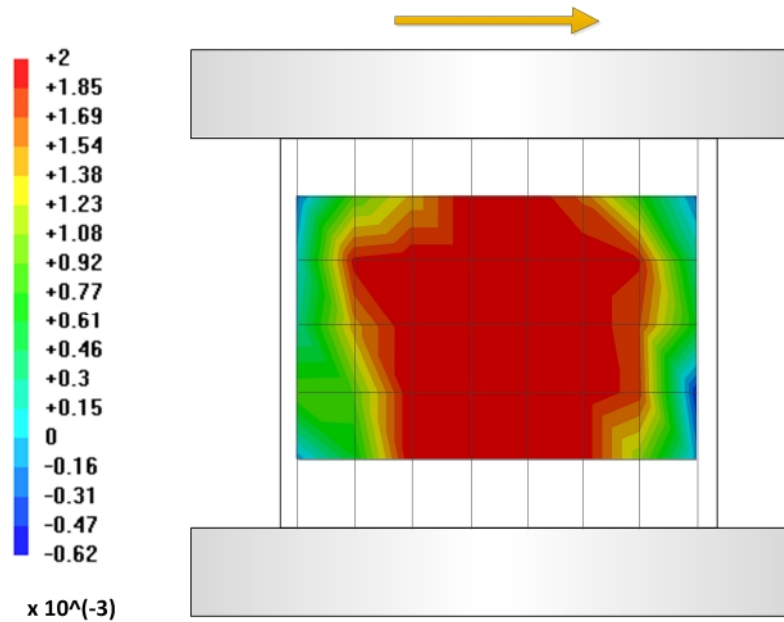


Figure 5.53 Strains of the circumferential steel bars in Specimen No. 1 (at the stage of the peak load in the positive direction)



**Figure 5.54** Strains of the circumferential steel bars in Specimen No. 2 (at the stage of the peak load in the positive direction)

### 5.3.4 Failure Modes

The two test specimens were almost identical; however, the failure modes of the two specimens were different. Specimen No. 1 failed due to sliding shear that happened at the top of the specimen, as shown in Figure 5.55. The peak load of Specimen No. 1 might have been higher if the sliding shear had not occurred. The sliding shear cracks started to occur on the top of the specimen from the drift of 0.5% and became larger when the load increased. Before the sliding shear failure, no critical damage of the concrete and reinforcement was observed in the specimens. Learning from the failure of Specimen No. 1, additional vertical steel bars, called dowel bars, were added on the top and bottom of Specimen No. 2 to prevent the sliding shear failure. As observed from the test, the method was successful when not only no sliding shear failure occurred but also the severe sliding shear cracks on the top of the specimen were eliminated. As a result, the specimen was able to reach a higher peak load and deformation until it failed when the concrete

crushed in the mid-height region. This failure can be classified as web shear failure, as shown in Figure 5.56

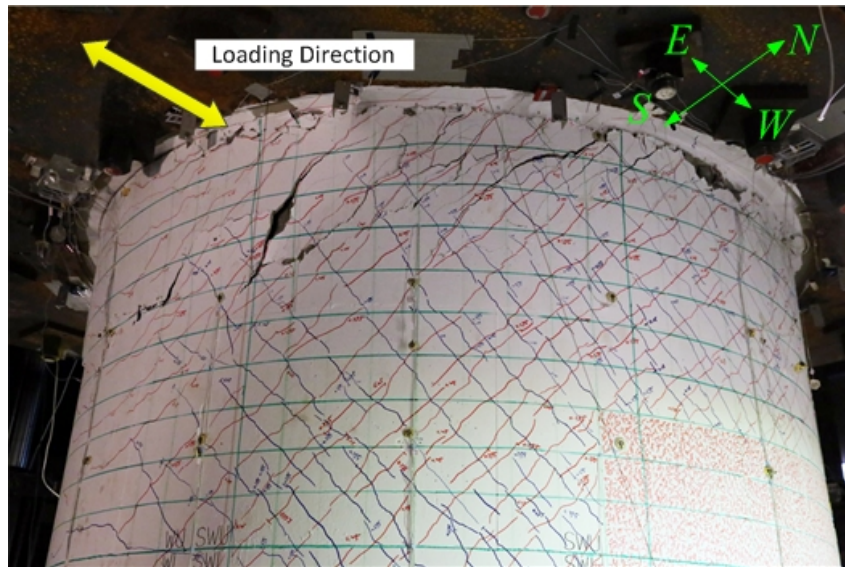


**Figure 5.55 Failure due to sliding shear of Specimen No. 1**

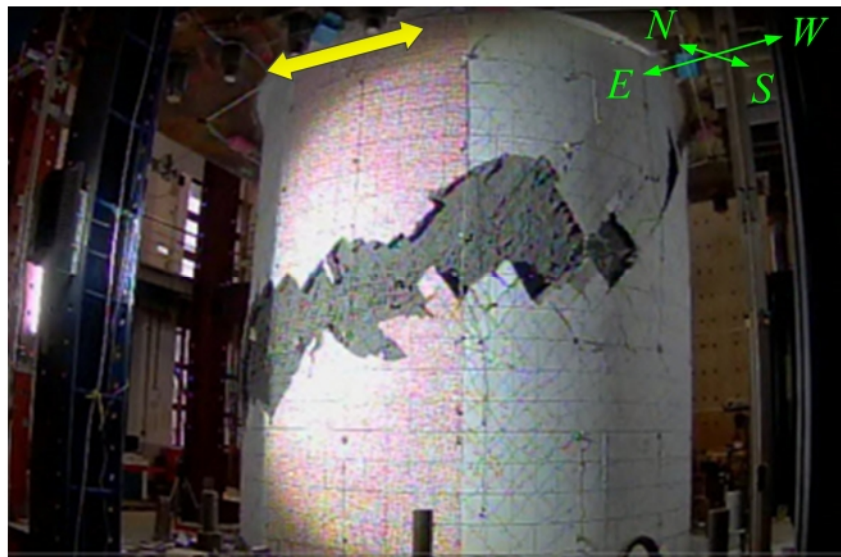


**Figure 5.56 Failure due to web shear of Specimen No. 2**

## 5.4 Analytical Model

### 5.4.1 Finite Element Mesh

In this section, the tested RCCV specimens were analyzed by using the CSMM-based shell element that was discussed in Chapter 3 to validate the capacity of the element in predicting the behavior of shell-type structures such as nuclear containment vessel under reversed cyclic loading. The specimens were modeled using the finite element mesh illustrated in Figure 5.58. For each specimen, the cylindrical wall of the vessel was defined by 40 CSMMShellS8 elements. Ten layers of concrete and two layers of steel were assigned for each element using the CSMMLayer material module, as shown in Figure 5.57. Mesh sensitivity analyses, which will be presented in the next section, were conducted before the analysis to ensure that the predicted results were not sensitive to the finite element size under the current mesh used. The steel layers were defined at the exact locations of the steel within the cross section of the specimen. In Specimen No. 1, all shell elements were assigned with 2% of reinforcement in both vertical and circumferential directions. The percentage of steel used in shell elements of Specimen No. 2 was almost identical to Specimen No. 1, except the shell elements located within the distance of one-fourth of the net height at the top and bottom of the specimen were assigned with 4% of vertical reinforcement.

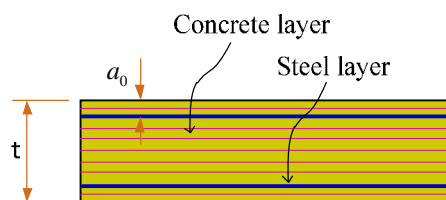
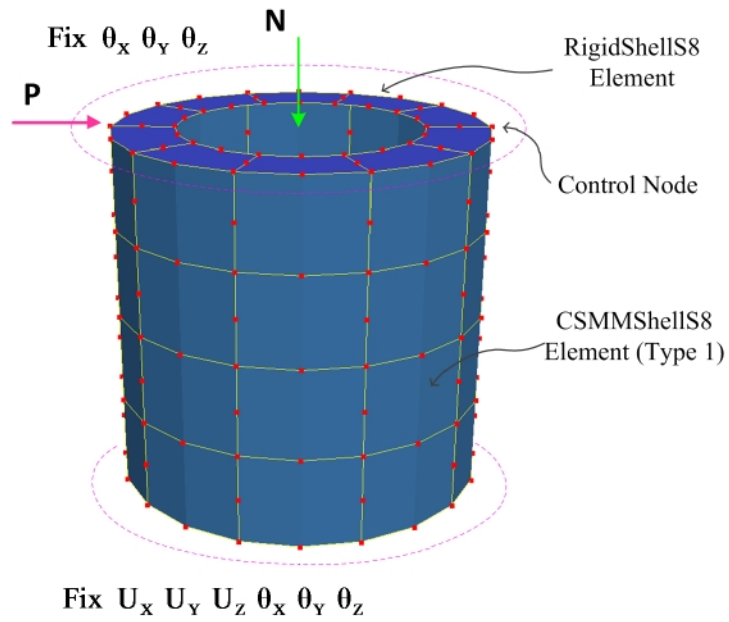
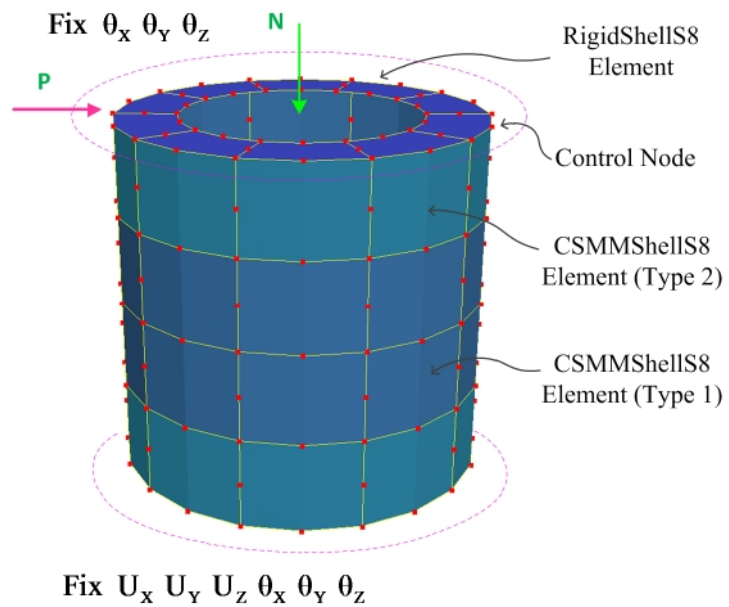


Figure 5.57 Finite element mesh along the thickness of the RCCV specimens



(a) Specimen No. 1



(b) Specimen No. 2

Figure 5.58 Finite element mesh of the RCCV specimens

The top slab of each RCCV specimen was defined as a rigid body by using ten CSMMSHELLS8 elements with high stiffness. For the boundary conditions, all nodes at the bottom of the model were constrained to not allow any translations or rotations. Equal horizontal and vertical loads were applied at all nodes along the perimeter at the height level of the specimen based on the assumption that the loads were uniformly distributed. The axial loads acting on the cap were applied with the direction and magnitude of the loads remaining constant in the analysis. The horizontal loads were changed according to the displacement control scheme.

#### **5.4.2 Analytical Algorithm**

The analysis was performed by a predetermined force control and displacement control schemes. The analysis procedure was separated into two steps. In the first step, axial loads were applied to the columns using load control by ten load increments. In the second step, axial loads were kept constant and reversed cyclic horizontal loads are applied by the predetermined displacement control on the drift displacement. The common displacement increment used in the analysis was 0.5 mm. Convergence was obtained smoothly during the cyclic analysis. The KrylovNewton method was used as the solution algorithm. The nodal displacement and corresponding horizontal forces were recorded at each converged displacement step, and the stress and strain of the elements were also monitored.

#### **5.4.3 Sensitivity Analysis**

To ensure that the predicted results were not sensitive to the finite element size, sensitivity analyses were performed to examine the proper size of the elements as well as number of layer used in the finite element analysis of each RCCV specimen. Four

different mesh sizes were chosen for sensitivity analysis, as shown in Figure 5.59. Results of the analysis were plotted for comparison, as shown in Figure 5.60.

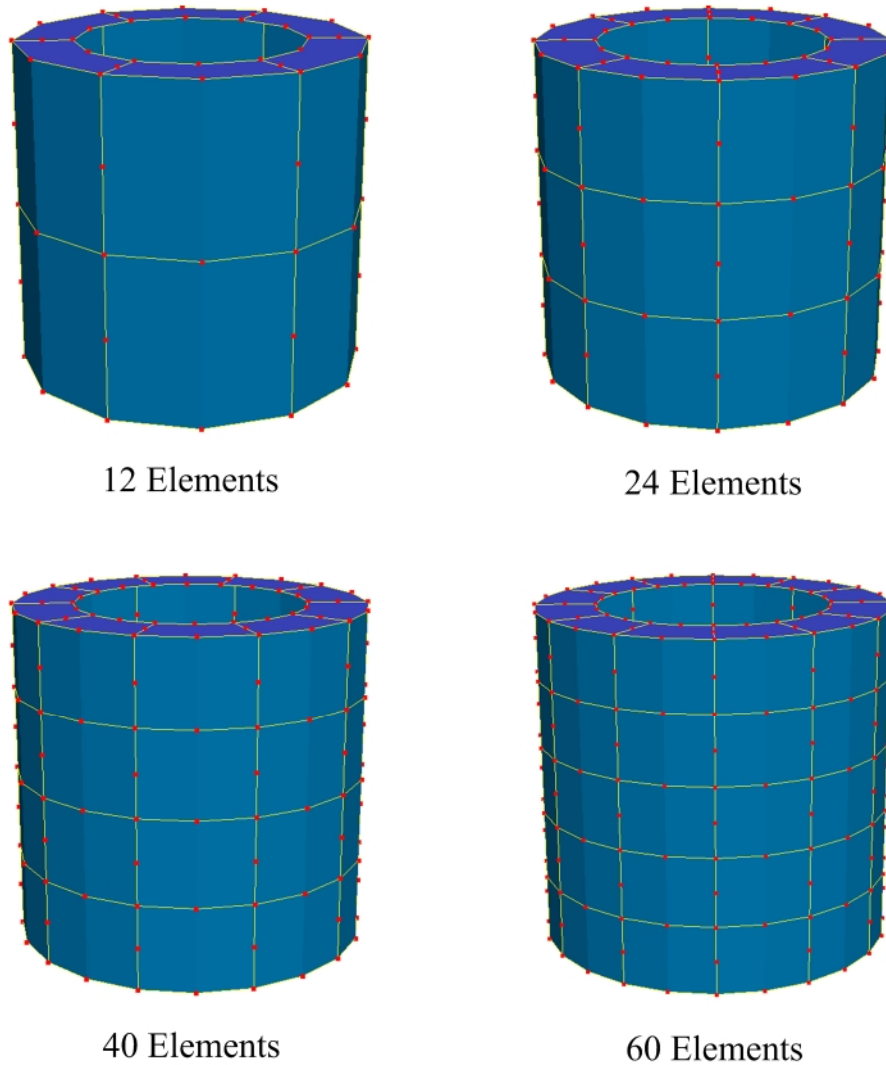


**Figure 5.59** Finite element meshes of the RCCV specimens for sensitivity analysis

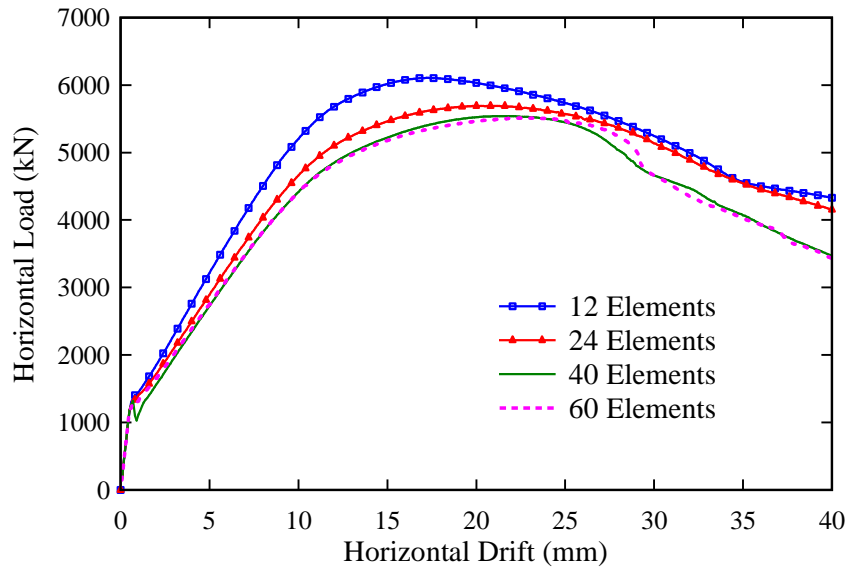


**Figure 5.60 Comparison of results of different mesh sizes**

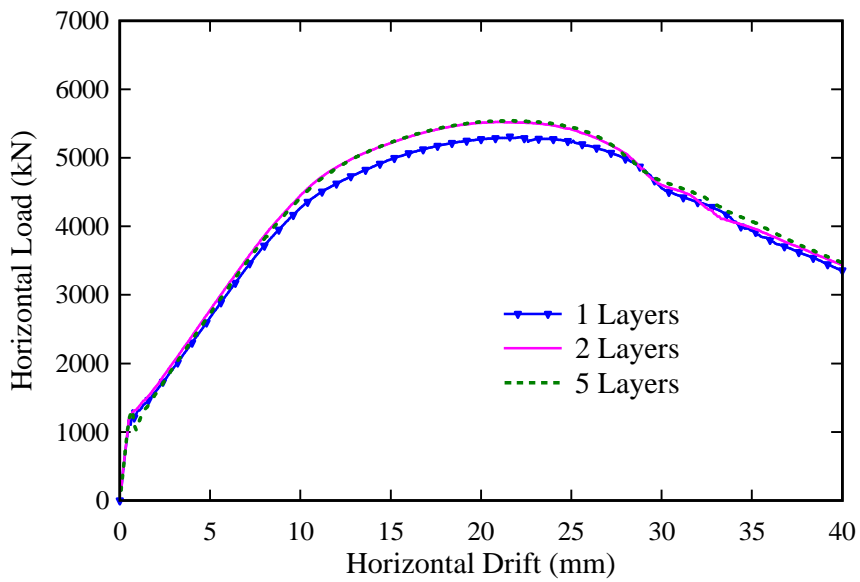


**Figure 5.61 Comparison of results on different numbers of layer**

Figure 5.60 shows that the analytical results obtained from the model using fewer numbers of elements were higher than those using a larger number of elements. The analytical curve using only 12 elements had the highest prediction among all selected

cases. The prediction using 24 elements was close to those using higher elements. The results obtained by using 40 elements and 60 elements were almost identical in both ascending and descending parts. The results obtained from analysis of models using different number of concrete layers were compared in Figure 5.61. The curves obtained by using 2 concrete layers and 5 layers were almost identical. The results of the sensitivity analysis showed that using 40 elements with 2 layers was sufficient for finite element analysis of RCCV specimens. These results were consistent with the conclusion provided by Zhong (2005) that an accurate solution would be achieved even with fewer number of elements or large mesh size of elements.

## **5.5 Comparison of Analytical Results with Experimental Outcomes**

### **5.5.1 Analytical Load-displacement Relationships**

The horizontal load versus the horizontal displacement relationships of the test specimens are shown in Figure 5.62 and Figure 5.63. Five critical points were listed in each curve to compare the analytical results with the experimental data. The critical points corresponded to the first cracking of concrete, the first yielding of vertical and circumferential steel bars, and the peak load in each specimen, as shown in Table 5.2. The analytical cracking loads of Specimen No. 1 and Specimen No. 2 were 1443 kN and 1490 kN, respectively. The analytical cracking loads were smaller than the cracking loads obtained from the tests.

The analytical model accurately predicted the yielding condition of steel bars, in which it showed that the vertical and the circumferential steel bars both yielded during the test and that the first yielding points of the vertical and circumferential steel bars were

close to each other. In Specimen No. 1, the analytical model predicted that the vertical steel bars yielded first in both the positive and negative loading direction. In the positive loading direction, the first yielding load was 3829 kN at the yielding displacement of 7.8 mm, respectively. In the negative loading direction, the first yielding load was 3764 kN at the yielding displacement of 7.6 mm, as shown in Figure 5.62 and Table 5.4. In Specimen No. 2, the analytical model predicted that the circumferential steel bars yielded first in both the positive and negative loading direction. In the positive loading direction, the first yielding load was 3897 kN at the yielding displacement of 7.9 mm. In the negative loading direction, the first yielding load was 3873 kN at the yielding displacement of 7.8 mm, as shown in Figure 5.63 and Table 5.4. The predicted yielding loads and yielding displacements of the tests specimens are shown to have good correlations with the experimental data, as shown in Figure 5.64 and Figure 5.65.

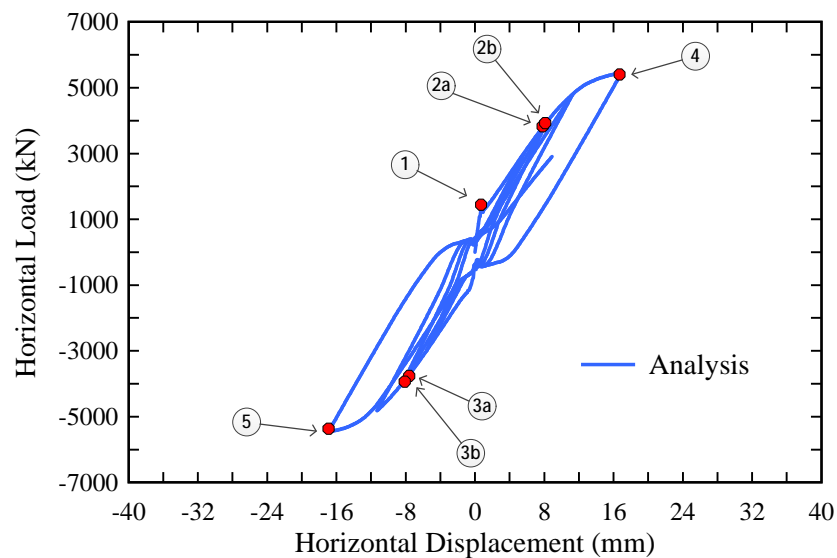


**Figure 5.62 Analytical load versus displacement curve of Specimen No. 1**

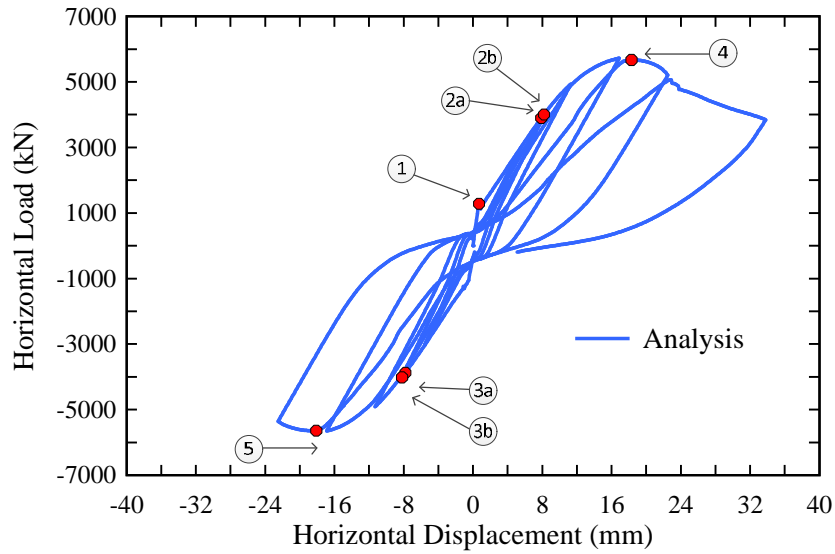


**Figure 5.63 Analytical load versus displacement curve of Specimen No. 2**

**Table 5.4 Ductility of the Test Specimen from the Analytical Results**

Specimen	Loading Direction	$\Delta_y$ (mm)	$P_y$ (kN)	$\Delta_{max}$ (mm)	$P_{max}$ (kN)	$m$
1	(+)	7.8	3829	16.7	5400	2.14
	(-)	7.6	3764	16.9	5367	2.22
2	(+)	7.9	3897	18.3	5669	2.31
	(-)	7.8	3873	18.1	5640	2.32

As shown in Table 5.4, for Specimen No. 1, the peak loads predicted were 5400 kN and 5367 kN in the positive and negative loading directions, respectively. The displacements corresponding to the peak loads were 16.7 mm and 16.9 mm in the positive and negative loading directions, respectively. For Specimen No. 2, the peak loads predicted were 5669 kN and 5640 kN in the positive and negative loading directions,

respectively. The displacements corresponding to the peak loads were 18.3 mm and 18.1 mm in the positive and negative loading directions, respectively. The predicted peak loads and peak displacements of the tests specimens are shown to have good correlations with the experimental data, as shown in Figure 5.64 and Figure 5.65.

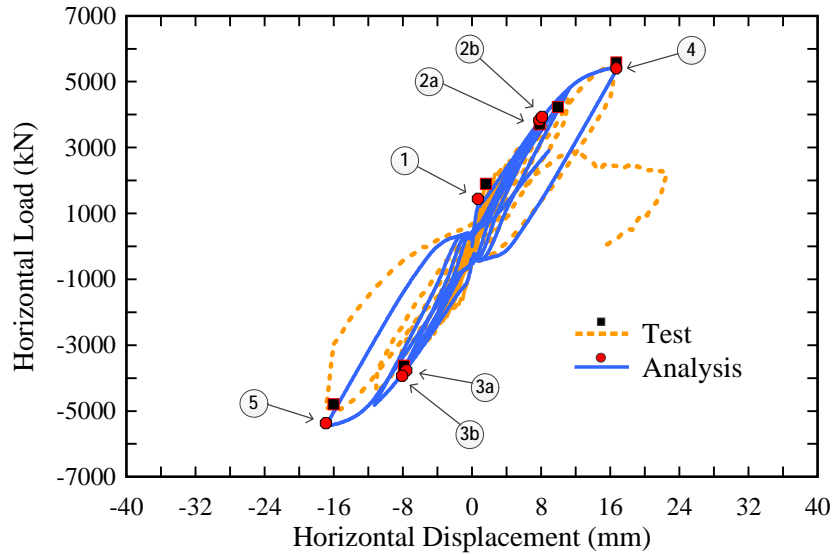


**Figure 5.64 Analytical load versus horizontal displacement curve of RCCV Specimen No. 1**

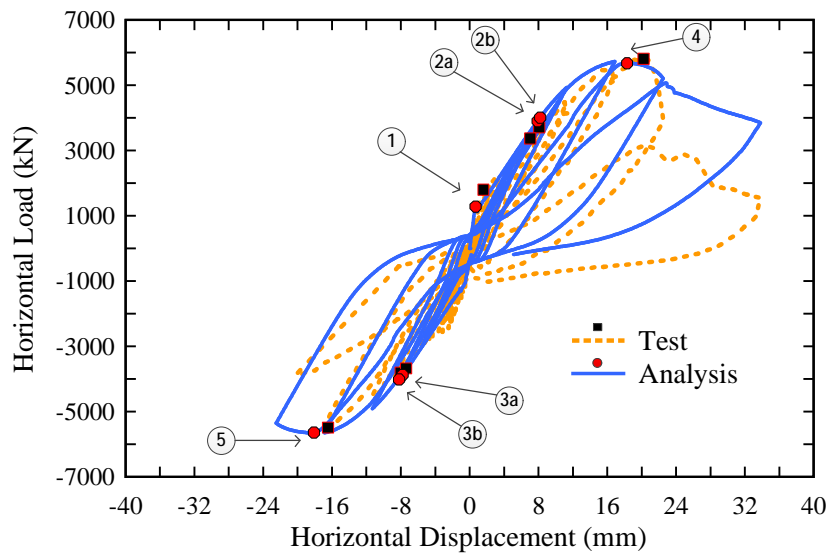


**Figure 5.65 Analytical load versus horizontal displacement curve of RCCV Specimen No. 2**

The analytical horizontal force versus displacement relationship of the test specimens were compared with the experimental results, as shown in Figure 5.64 and Figure 5.65. The experimental result and the analytical result are illustrated by a dashed curve and a solid curve, respectively. The analytical result provided a good correlation with the experimental data. Although the predicted initial stiffness was higher compared to the experimental stiffness, the analytical model accurately predicted behaviors in the both positive and negative directions, including the primary backbone curve, the initial stiffness, the yield points, and the peak strength. The model, however, did not predict well the behavior of Specimen No. 1 in the positive direction and the last cycle of Specimen No. 2 in the negative direction. The reasons for the poor prediction in these cycles will be explained in the next sections. Furthermore, the unloading path and pinching behavior were well simulated.

Figure 5.64 shows that the analytical model did not accurately predict the failure of Specimen No. 1. In the last cycle, the force predicted by the analytical model increased, while the experimental force decreased after reaching 3000 kN because the analytical model did not take into account the sliding shear failure mode, which happened locally at the junction between the vessel and the top slab. The model was based on the smeared finite element approach and could only capture the failure if it occurred within the element, such as the crushing of diagonal concrete or yielding of steel bars. A further study needs to be conducted to improve the prediction on the sliding shear failure.

As compared to the experimental hysteretic loops of Specimen No. 2, shown in Figure 5.65, the accuracy of the analytical model was excellent up to the peak load, which represented the point at which the concrete at mid-height of the specimen started to spall

and the specimen started to lose its lateral capacity. After the load drop, the descending parts of the load vs. displacement curve, however, were not captured well by the analytical model. The descending parts of the experimental hysteretic loops were steeper compared to the predicted results. Two reasons might have contributed to the steeper descending loops. First, the loss of the concrete cover due to spalling reduced the cross section of the cylinder wall. Second, in a wall element subjected to reversed cyclic loading, the negative cycles appeared to have a more damaging effect than anticipated on the positive cycles. A parametric study is provided at the end of this chapter to try to improve the prediction on the descending branch of the load vs. displacement curve of the specimen.

The critical points on the load vs. displacement curve of the test specimens were determined based on investigating the stress and strain conditions at each layer of the concrete and steel bar of the specimen. The stresses and strains in the exterior concrete and steel bar layers represented the general stress and strain conditions of all the concrete and steel bar layers of the shell element. Therefore, only the stresses and strains of the exterior concrete and steel bar layers of each shell element were plotted and are discussed in the following sections.

## **5.5.2 Behaviors of Concrete and Steel Bars at the First Cracking**

### **5.5.2.1 Cracking Patterns**

To investigate the cracking patterns of the two specimens, the principal coordinates had to be determined, which defined the cracking orientations. As presented in Chapter 3, for each layer of concrete in the shell element, the 1-2 coordinate represented the principal stress directions of the applied stresses. The 1- and 2- axes of the principal

coordinate had an angle  $\theta_1$  with respect to the  $x'$ - and  $y'$ - axes of the local coordinate, respectively.  $\theta_1$  is called the principal stress angle. Based on CSMM, if the stress corresponding to one of the principal axes was under tension and the tensile stress exceeded the cracking stress of concrete, the principal axis would represent the cracking orientation of concrete. For both specimens, the angles of the principal coordinates of the exterior concrete layer were obtained from the analytical models at the drift of 0.5% and plotted in Figure 5.66. The angles were determined for both positive and negative loadings. The angle of principal direction varied from  $40^\circ$  to  $60^\circ$  in the entire middle region of the specimens in both cases of loading directions. Hence, if cracks were formed in the middle region, they would be inclined cracks and be classified as shear cracks. At the corners of the specimen, the angle of principal direction was approximately  $90^\circ$  or  $0^\circ$  in cases of positive and negative loading directions, respectively. Hence, if cracks formed in this area, they would be horizontal cracks and be classified as flexural cracks. The results of the cracking angle obtained from the analytical model matched well with the cracking patterns of the specimens observed from the tests shown in Figure 5.39 and Figure 5.40.

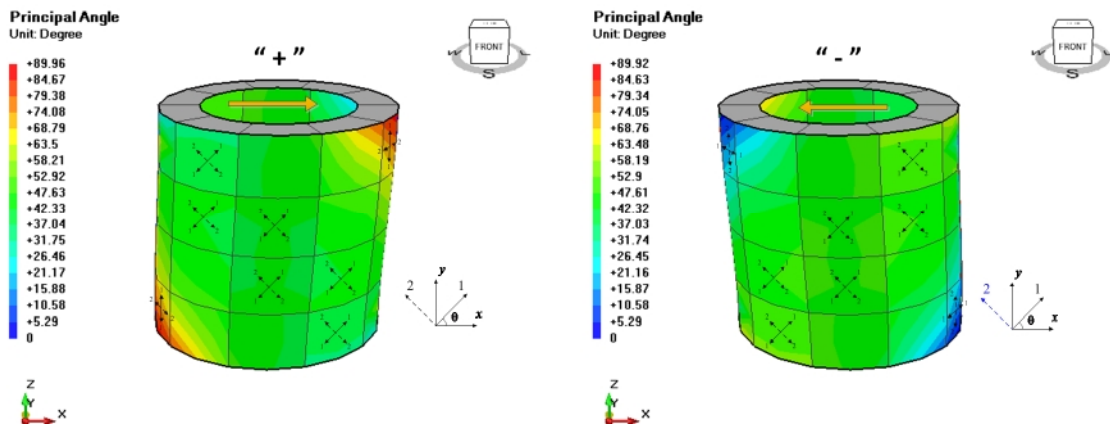


**Figure 5.66 Analytical cracking orientation of Specimen No. 1 and Specimen No. 2 in the positive and negative directions (at the drift of 0.375%)**

Figure 5.67 shows the stress conditions of the exterior concrete layer when the specimen has elastic behavior. The figure indicates that when the specimen was subjected to the positive loading direction, the stresses of concrete corresponding to the 1-axis of the principal coordinate was tensile stress. Hence, the 1-axis represents the cracking orientation in the positive loading direction. In contrast, when the specimen was subjected to the negative loading direction, the stresses of concrete corresponding to the 2-axis of the principal coordinate was tensile stress. Hence, the 2-axis represents the cracking orientation in the negative loading direction. These interpretations of the 1-axis and 2-axis for cracking orientations in the positive and negative directions did not change when the specimens went into the inelastic behavior in the further loading steps. The stress and strain results for the cases of the positive and negative loading direction were almost identical; therefore, only the stress and strain conditions for case of the positive loading direction are discussed in this section.

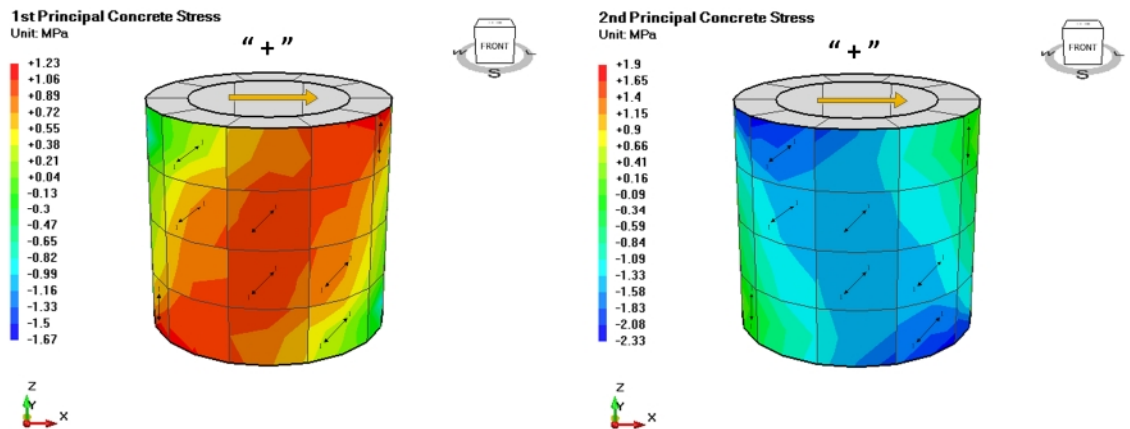


**Figure 5.67 Analytical stresses of concrete in Specimen No. 1 and Specimen No. 2 in case of positive loading direction (elastic)**

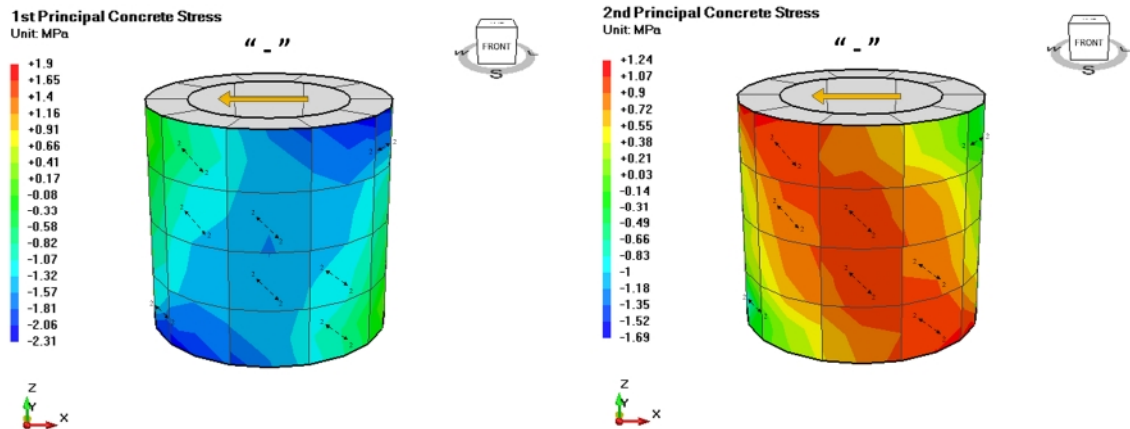


Figure 5.68 Analytical stresses of concrete in Specimen No. 1 and Specimen No. 2 in case of negative loading direction (elastic)

### 5.5.2.2 Stresses and Strains

The contour diagrams of the stresses and strains of the exterior concrete and steel bar layers of Specimen No. 1 when the first cracks occurred are illustrated in Figure 5.69 through Figure 5.72, which correspond to Point 1 on the load vs. displacement curve, as shown in Figure 5.62. Based on CSMM, the first cracking point of concrete was defined when the strains of concrete reached 0.00008. The region of the concrete, which had the strain exceed the cracking strain, was distributed diagonally in the surface of the specimen. The maximum principal tensile and compressive stresses in the concrete were 1.88 MPa and -3.51 MPa, respectively. The figures show that the stresses and strains of the steel bars had higher values at the top and bottom corner of the specimen, compared to other locations. The maximum tensile and compressive stresses in the vertical steel bars of the specimen were 22.29 MPa and -28.27 MPa, respectively.

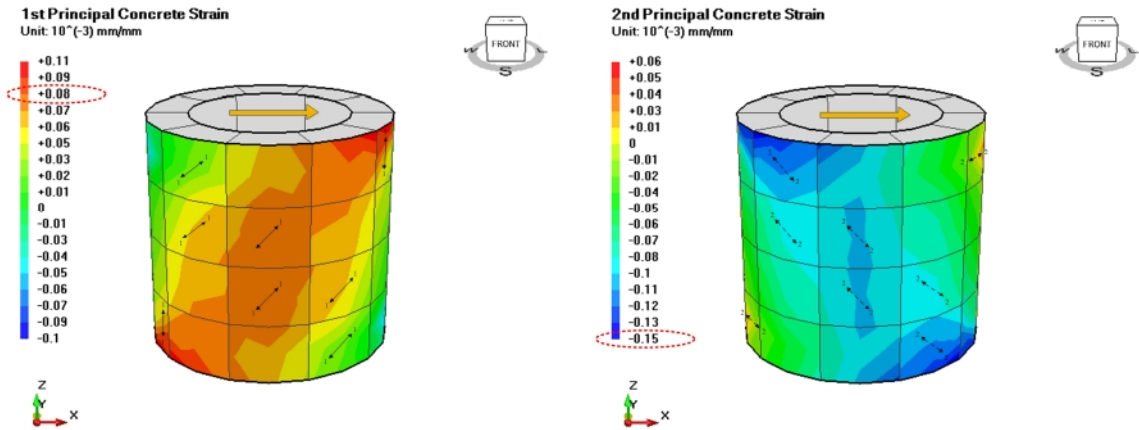


Figure 5.69 Analytical strains of concrete in Specimen No. 1 (at the stage of the first cracking of concrete)

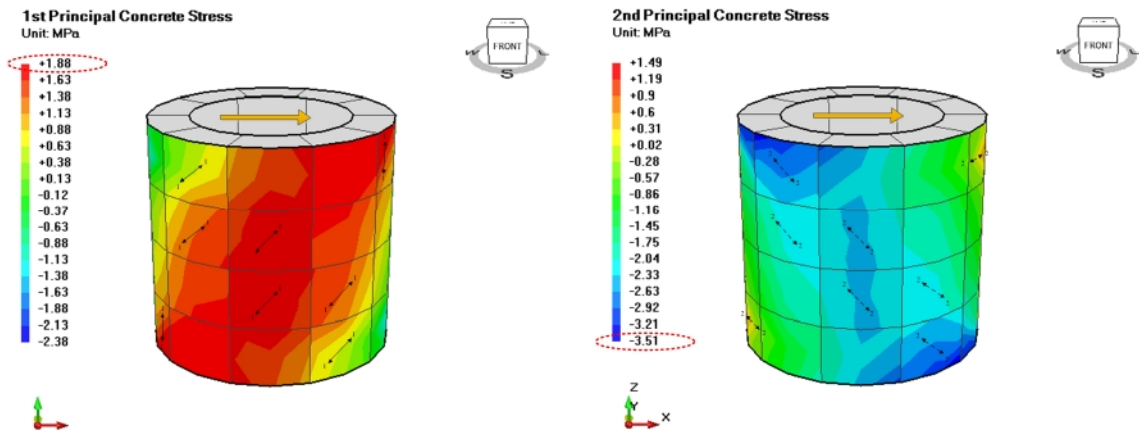


Figure 5.70 Analytical stresses of concrete in Specimen No. 1 (at the stage of the first cracking of concrete)

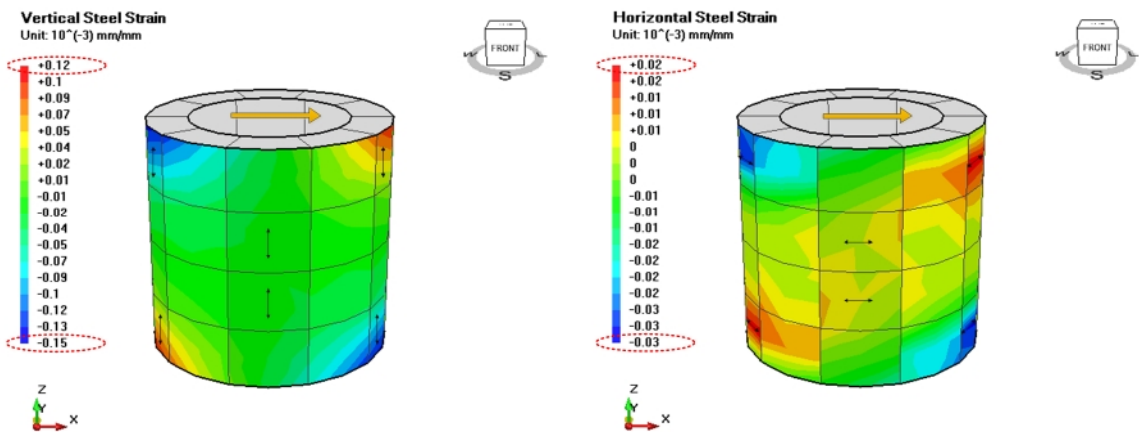
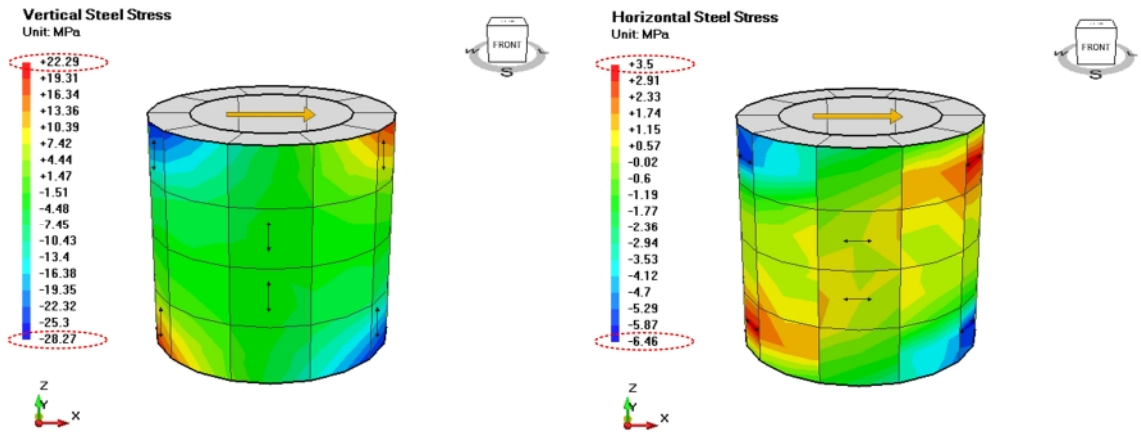


Figure 5.71 Analytical strains of steel bars in Specimen No. 1 (at the stage of the first cracking of concrete)



**Figure 5.72 Analytical stresses of steel bars in Specimen No. 1 (at the stage of the first cracking of concrete)**

The contour diagrams of the stresses and strains of the exterior concrete and steel bar layers of Specimen No. 2 when the first cracks occurred in the concrete are illustrated from Figure 5.73 through Figure 5.76, which correspond to Point 1 on the load vs. displacement curve, as shown in Figure 5.63. The maximum tensile and compressive stresses of the vertical steel bars were 21.64 MPa and 25.33 MPa, respectively. The maximum principal tensile and compressive stresses of the concrete were 2.01 MPa and -3.69 MPa, respectively. The values of stresses and strains of concrete and steel bars of Specimen No. 2 were almost identical to Specimen No. 1. The analytical result was reasonable because the dimensions, reinforcement detailing, and material properties of both specimens were almost identical, with the exception that the amount of vertical reinforcement at the top and bottom of Specimen No. 2 was doubled to increase the sliding shear capacity.

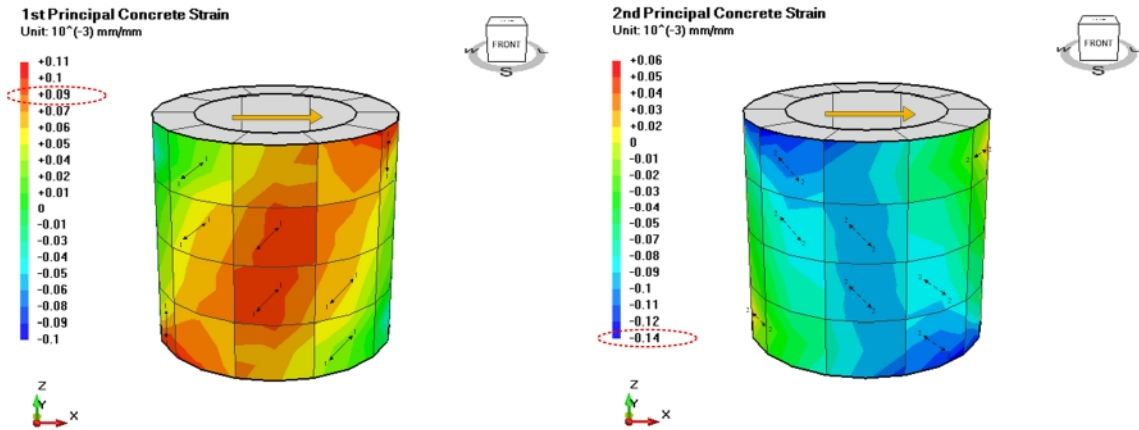


Figure 5.73 Analytical strains of concrete in Specimen No. 2 (at the stage of the first cracking of concrete)

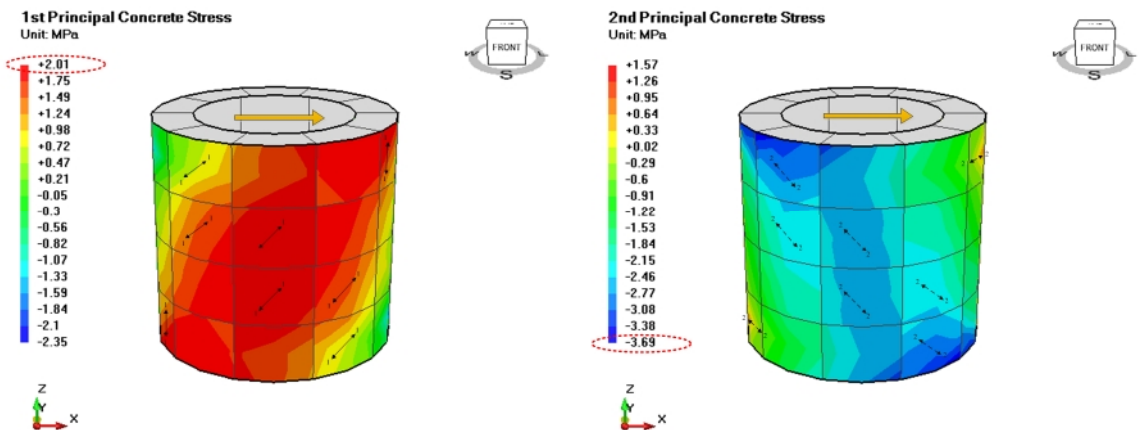


Figure 5.74 Analytical stresses of concrete in Specimen No. 2 (at the stage of the first cracking of concrete)

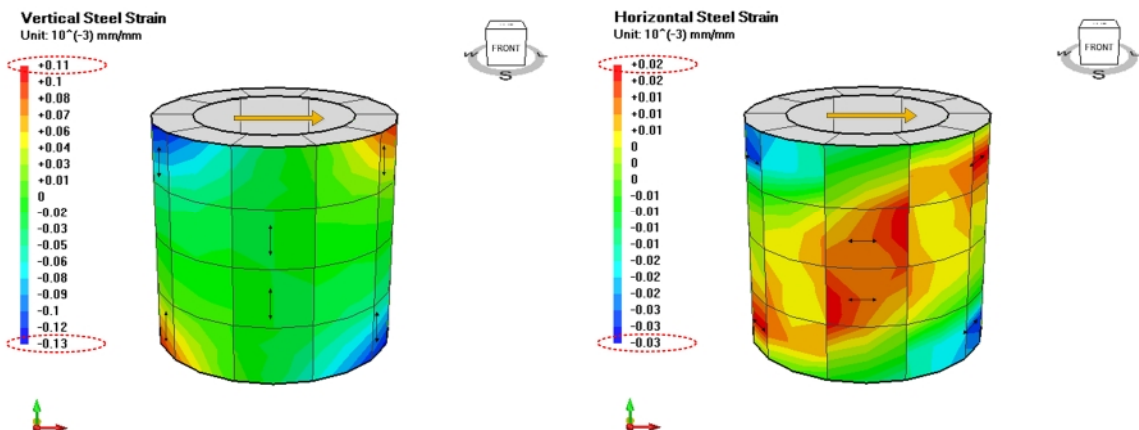
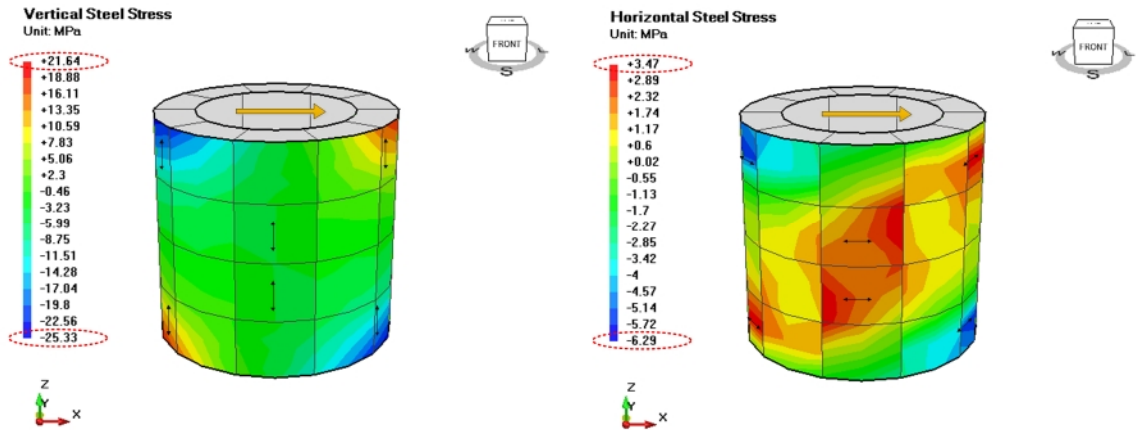


Figure 5.75 Analytical strains of steel bars in Specimen No. 2 (at the stage of the first cracking of concrete)



**Figure 5.76 Analytical stresses of steel bars in Specimen No. 2 (at the stage of the first cracking of concrete)**

### 5.5.3 Behaviors of Concrete and Steel Bars at First Yielding of Steel Bars

The contour diagrams of the stresses and strains of the exterior concrete and steel bar layers of Specimen No. 1 when the first yielding of the steel bars occur are illustrated from Figure 5.77 through Figure 5.80, which correspond to Point 2 on the load vs. displacement curve, as shown in Figure 5.62. The first yielding point was defined when the strains of the steel bars start to reach the yielding strain of 0.002. Figure 5.77 shows that when the vertical steel bars reached the yielding strains, the maximum strain of the circumferential steel bars was 0.00196, which was slightly less than the yielding strains. Hence, the vertical steel bars yielded first. The result also revealed that the first yielding point of both vertical and circumferential steel bars were close. Figure 5.78 shows that the maximum tensile of the vertical and circumferential steel bars were 341.85 MPa and 341.61 MPa, respectively. The yielding of the vertical steel bars was located at the top and bottom corners, and the yielding of the circumferential steel bars was located in the mid-height region of the specimen. The yielding order and yielding location of the steel

bars in the analytical results of the specimen were similar to the results obtained from the tests shown from Figure 5.43 through Figure 5.50.

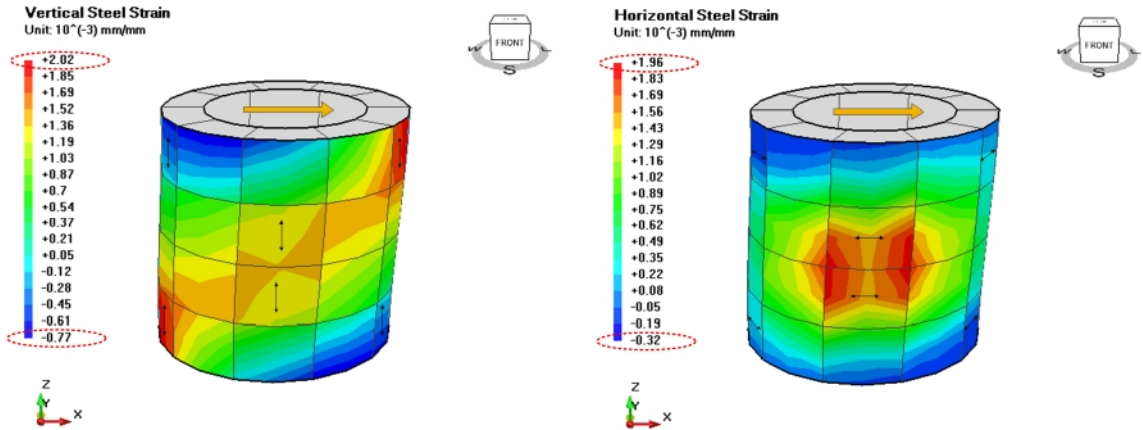


Figure 5.77 Analytical strains of steel bars in Specimen No. 1 (at the stage of first yield of the vertical steel bars in the positive direction)

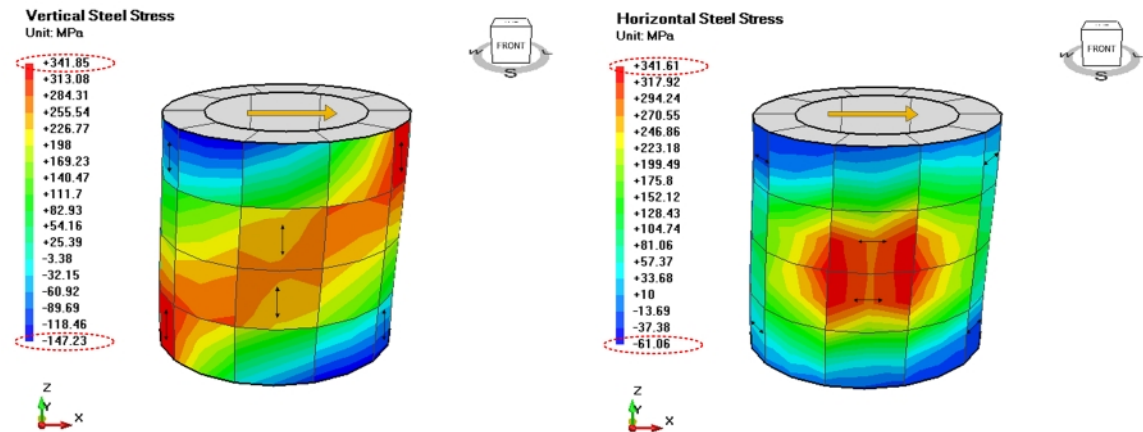


Figure 5.78 Analytical stresses of steel bars in Specimen No. 1 (at the stage of first yield of the vertical steel bars in the positive direction)

The contour diagrams of stresses and strains of the exterior concrete of Specimen No. 1 are shown in Figure 5.79 and Figure 5.80. Similar to the first cracking stage, the principal stresses and strains of the concrete had high values along the diagonal directions of the specimens. Especially, the high value principal tensile strains of concrete were concentrated in the mid-height region of the specimen. The maximum principal tensile and compressive strains in the concrete were 0.00358 and -0.0019, respectively. Due to

the tensile stiffening property of concrete, the stress of concrete was reduced as the strain increases. At this yielding stage, the maximum principal tensile strain of concrete was far beyond the cracking strain. As a result, the concrete lost its tensile resisting capacity and the cracking widths were opened significantly, especially in the middle region where the high value strains of concrete were concentrated.

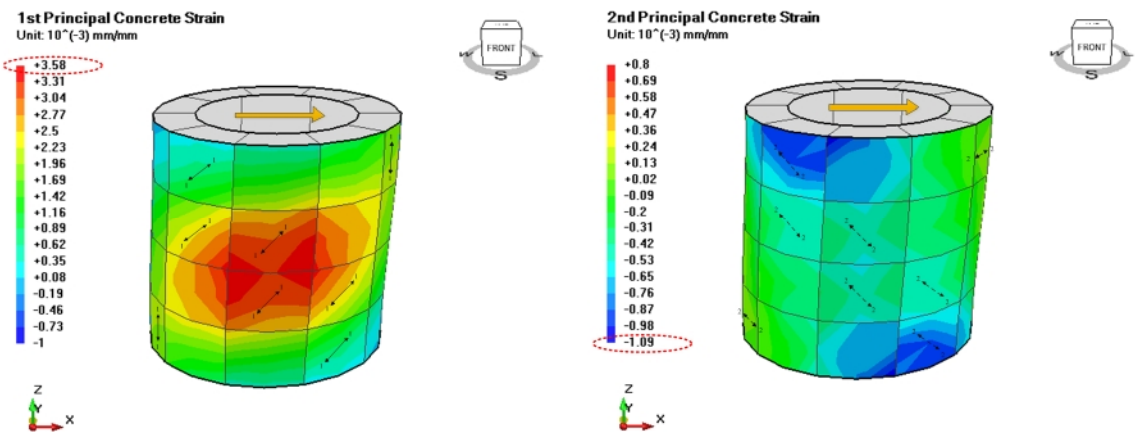


Figure 5.79 Analytical strains of concrete Specimen No. 1 (at the stage of first yield of steel bars in the positive direction)

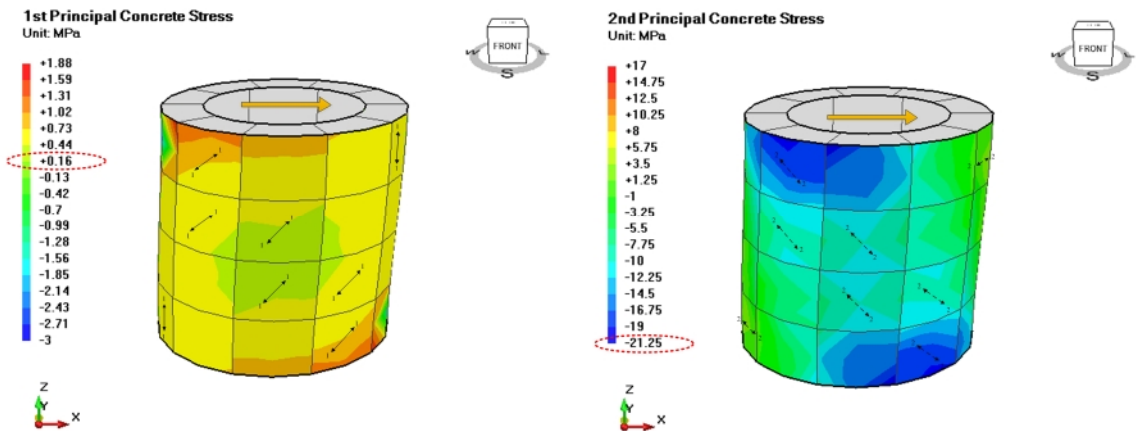


Figure 5.80 Analytical stresses of concrete Specimen No. 1 (at the stage of first yield of steel bars in the positive direction)

The contour diagrams of stresses and strains of the exterior concrete and steel bar layers of Specimen No. 2 when first yielding of steel bars occur are illustrated from Figure 5.81 through Figure 5.84, which correspond to Point 2 on the load vs. displacement curve, as shown in Figure 5.63. Figure 5.81 shows that when the circumferential steel bars reached the yielding strains, the strains of the vertical steel bars were 0.00194, which was slightly smaller than the yielding strains. Hence, the circumferential steel bars yielded first. The result indicated that the first yielding point of both vertical and circumferential steel bars were very close. Similar to Specimen No. 1, the yielding of the circumferential steel bars occurred in the mid-height region of the specimen. However, the yielding of the vertical steel bars of Specimen No. 2 was not located at the top and bottom corners as it happened in Specimen No. 1. Instead, the yielding of the vertical steel bars were located near the cut-off point of the dowel bars that were added in Specimen No. 2 to prevent sliding shear. The yielding order and yielding location of the steel bars in the analytical results of the specimen were similar to the results obtained from the tests shown from Figure 5.43 through Figure 5.50. This results were reasonable and can be explained as follows. Because the dowel bars were added at the top and bottom of the specimen, the amount of vertical reinforcement in this location was higher than that in Specimen No. 1. As a result, the vertical steel bars at the top and bottom corners is prevented to reach yielding early as happened in Specimen No. 1. Moreover, the yielding shifted to the location where the amount of the vertical reinforcement was smaller.

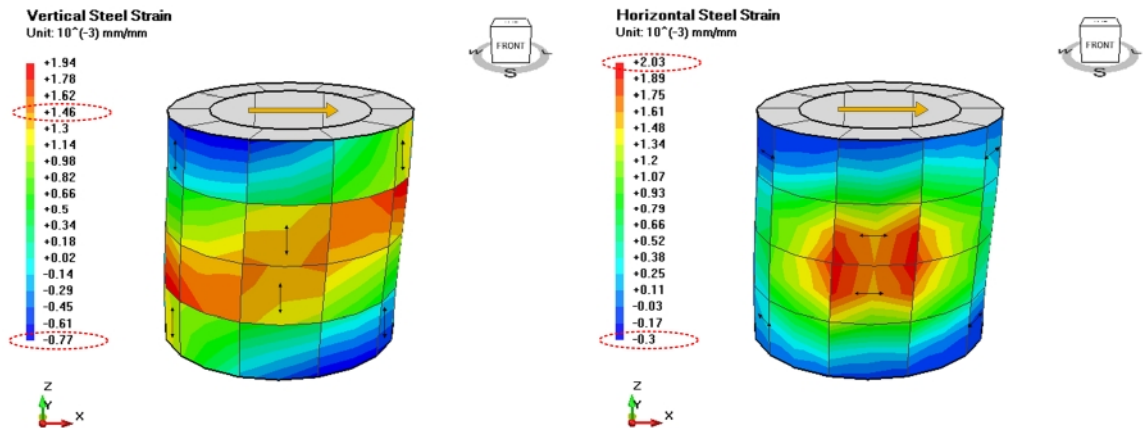


Figure 5.81 Analytical strains of steel bars in Specimen No. 2 (at the stage of first yield of the circumferential steel bars in the positive direction)

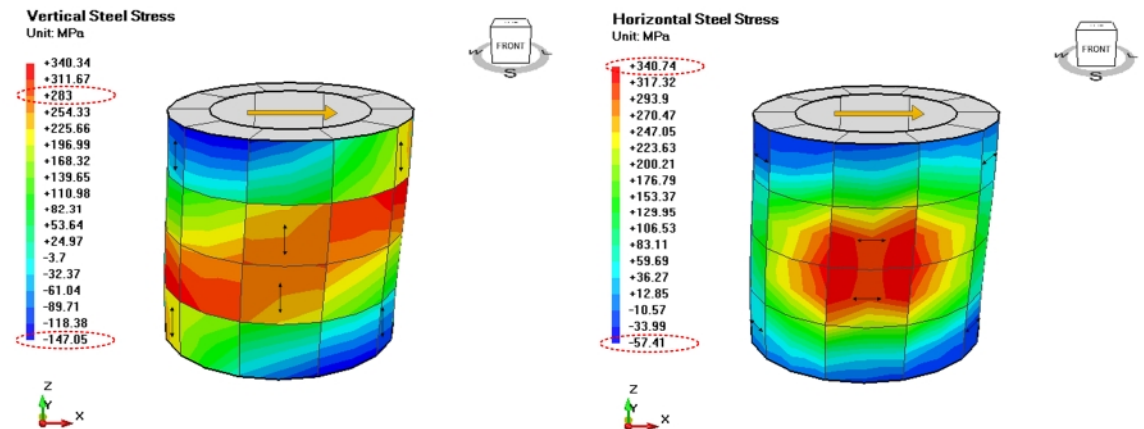


Figure 5.82 Analytical stresses of steel bars in Specimen No. 2 (at the stage of first yield of the circumferential steel bars in the positive direction)

Similar to Specimen No. 1, the stresses and strains of concrete had high values along the diagonal directions of the specimens and the high values of the principal tensile strains of concrete were concentrated in the mid-height region of the specimen. The maximum principal tensile and compressive strains of the concrete were 0.00373 and -0.00105, respectively.

In both specimens, although the steel bars started to yield, the maximum principal compressive strain of concrete was small, approximately -0.001, which indicated that

concrete had not crushed or reached its maximum compressive strength yet. Therefore, it can be concluded that the structural behavior of the specimens was ductile behavior. The yielding stress of the steel bars were approximately 340 MPa, which was less than the defined yielding stress, 365 MPa. These results occurred because the steel bars used in the model were based on the smeared cracking concept of CSMM, in which, the stresses in the steel bars between the cracks would be less than the yield stress at the cracks because part of the tensile force was resisted by the surrounding concrete.

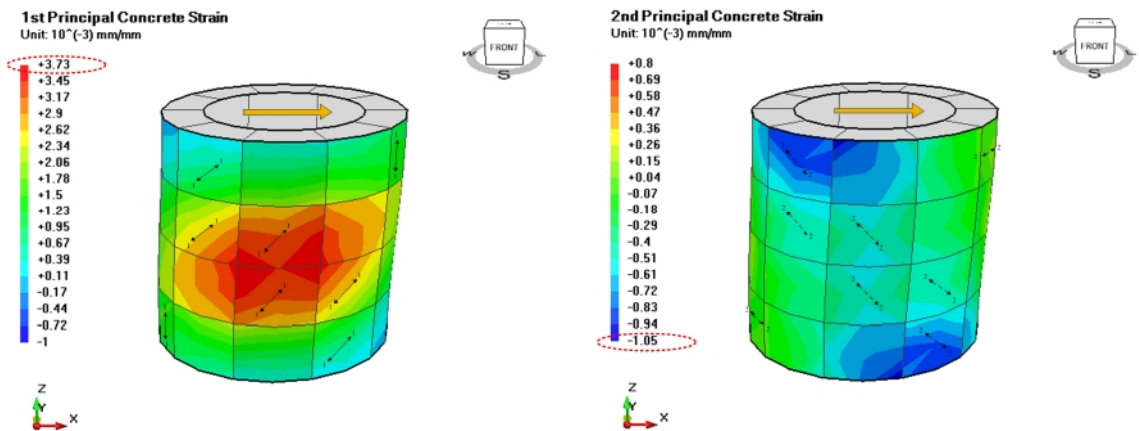


Figure 5.83 Analytical strains of concrete Specimen No. 2 (at the stage of first yield of steel bars in the positive direction)

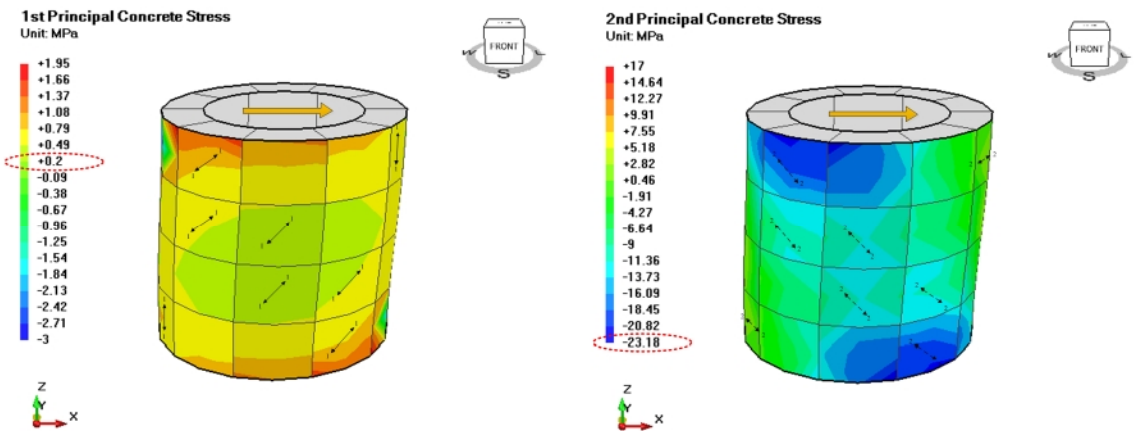


Figure 5.84 Analytical stresses of concrete Specimen No. 2 (at the stage of first yield of steel bars in the positive direction)

#### **5.5.4 Behaviors of Concrete and Steel Bars at the Peak Load**

The contour diagrams of the stresses and strains of the exterior concrete and steel bar layers of Specimen No. 1 when the horizontal load reached its peak load are illustrated from Figure 5.85 to Figure 5.88, which related to Point 4 on the load vs. displacement curve, as shown in Figure 5.62. As shown in Figure 5.85, the tensile strains grew considerably in both the vertical and circumferential steel bars. The vertical steel bar strain reached its maximum tensile value of 0.008 at the top and bottom corners of the specimen while the circumferential rebar strain reached its maximum tensile value of 0.0054 in the mid-height of the specimen. The yielding areas of both steel bars also expanded significantly up to two-thirds of the area of the specimen walls. In contrast to the tensile strain, the compressive strains of the steel bars were still in the elastic region. The maximum compressive strains of the vertical and circumferential steel bars were 0.0012 and 0.00072, respectively. Unlike the tensile strains, the tensile stress of the steel bars raised slightly compared to its value at the first yielding point. Hence, the yielding area of steel bars was observed easier in the stress diagram, as shown in Figure 5.86. It can be seen that the yielding regions of the vertical and circumferential steel bars were spread out to a large region on the surface of the specimen. The yielding region of the vertical steel bars formed diagonally from the bottom to the top corners of the specimen; meanwhile, the yielding region of the circumferential steel bars concentrated only in the mid-height region of the specimens. The yielding distribution of the steel bars obtained from the analysis matched very well with the the experimental results illustrated from Figure 5.51 through Figure 5.54.

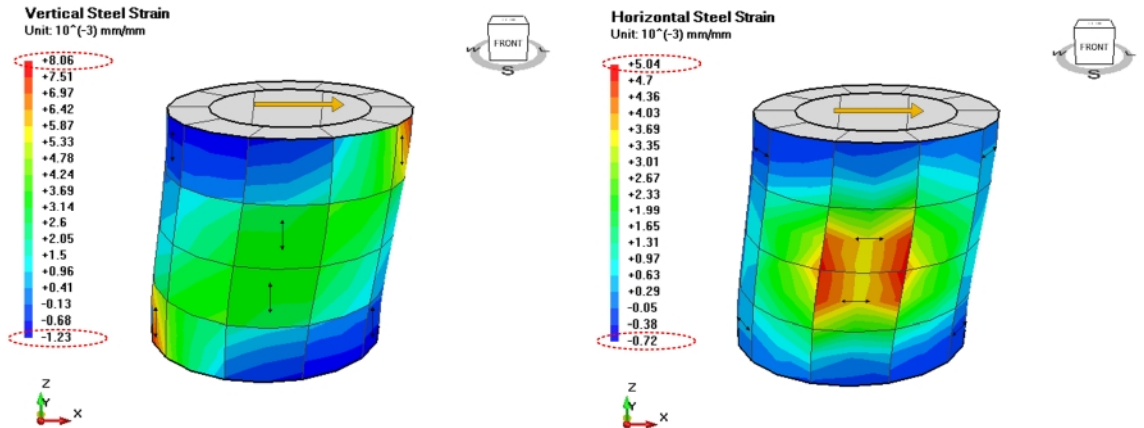


Figure 5.85 Analytical strains of steel bars in Specimen No. 1 (at the stage of the peak load in the positive direction)

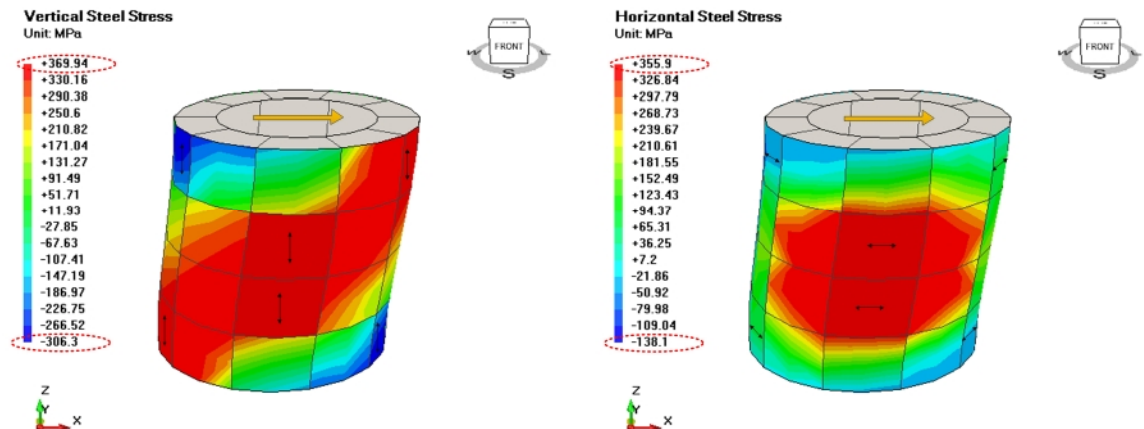


Figure 5.86 Analytical stresses of steel bars in Specimen No. 1 (at the stage of the peak load in the positive direction)

Because the specimen reached its maximum capacity in this stage, the concrete probably reached its compressive strength. However, the contour strain diagram only indicated the critical location in which the concrete was shown to have high strain value. It does not reveal the current response of the concrete. Unlike normal concrete, the response of the cracked concrete cannot be determined by looking at its strain value in the contour diagram because the compressive stress and strain curve of the cracked concrete in one direction depended on the value of the tensile strain in the perpendicular

direction. The entire stress and strain curve of the concrete needed to be plotted to determine the correct response of concrete at the investigated loading step.

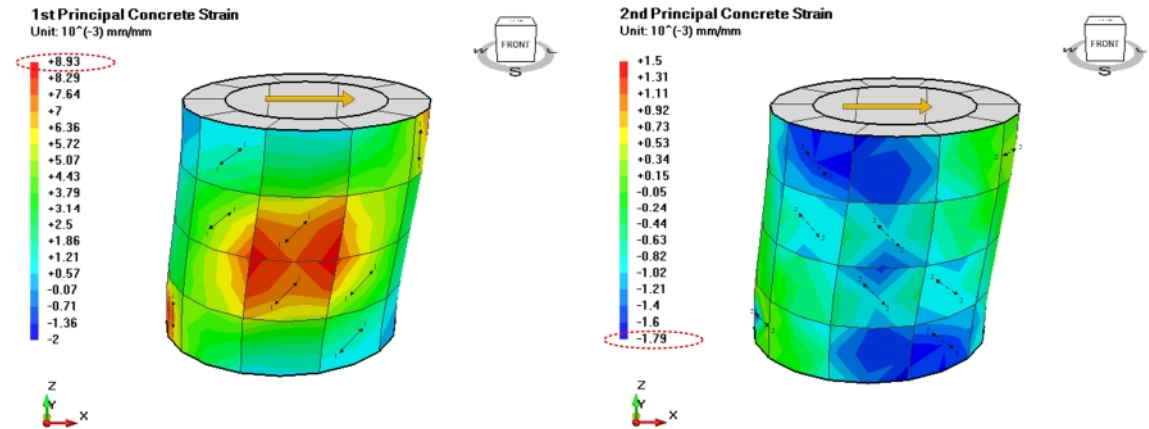


Figure 5.87 Analytical strains of concrete in Specimen No. 1 (at the stage of the peak load in the positive direction)

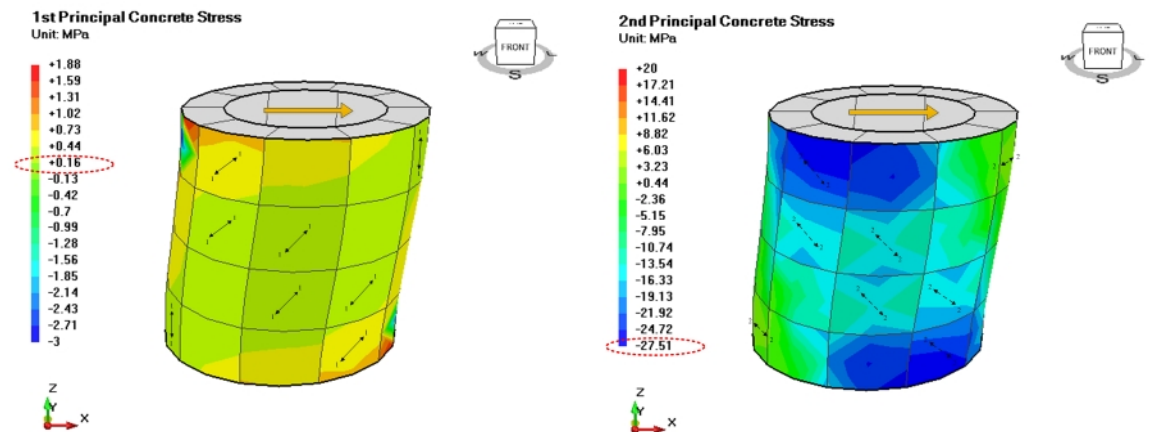
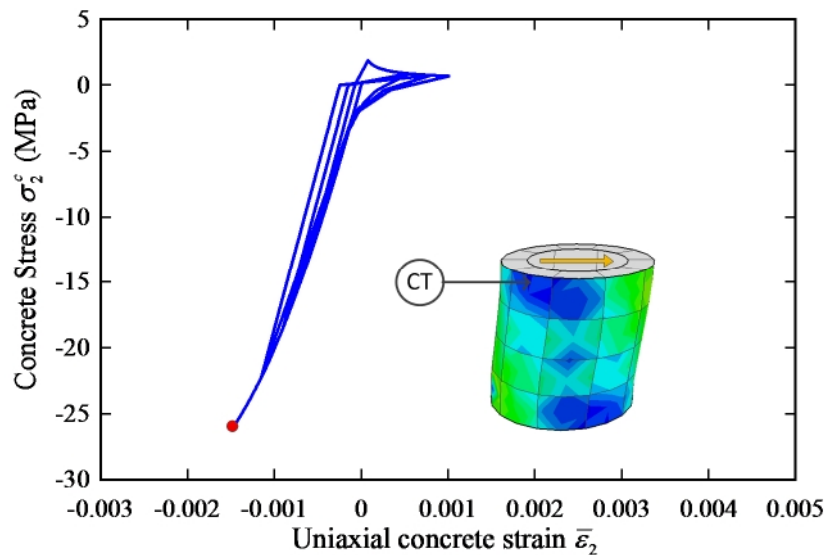


Figure 5.88 Analytical stresses of concrete in Specimen No. 1 (at the stage of the peak load in the positive direction)

As shown in Figure 5.87, the maximum principal compressive strain of the concrete was approximately  $-0.00179$  and occurred at the top and bottom corner of the specimen. The concrete in the mid-height had lower compressive strain; however, the maximum tensile strain of approximately  $0.0089$  was located within this region. Therefore, the top and bottom corner and the mid-height were considered to be critical area. The stress and

strain curves of two selected points from the critical region were plotted to investigate the response of concrete at the current loading step, as shown in Figure 5.89 and Figure 5.90. The figures reveal that the stress of concrete at the top and bottom corners was less than the compressive strength, while the stress of concrete in the mid-height already reached the compressive strength. From the stress and strain curve, the compressive strength of the concrete in the mid-height region was determined to be about 18 MPa, which was much smaller than the defined compressive strength of concrete, 35 MPa. This result indicated that the severe opening of the cracks within this region caused the decrease in the strength of concrete to 48%. The concrete had no damage in this stage because the stress and strain curve of the concrete had not yet developed its descending branch.



**Figure 5.89** Stress-strain curve of concrete at the point CT in Specimen No. 1 (at the stage of the peak load in the positive direction)

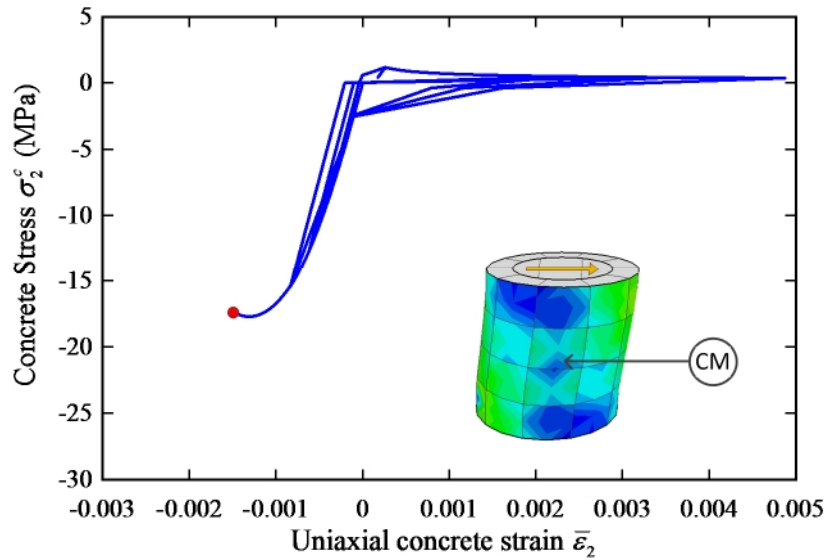


**Figure 5.90 Stress-strain curve of concrete at the point CM in Specimen No. 1 (at the stage of the peak load in the positive direction)**

The contour diagrams of the stresses and strains of the exterior concrete and steel bar layers of Specimen No. 2 when the horizontal load reached its peak load are illustrated from Figure 5.91 through Figure 5.94, which correspond to Point 4 on the load vs. displacement curve, as shown in Figure 5.63. Similar to Specimen No. 1, the tensile strains grew considerably in both the vertical and circumferential steel bars, as shown in Figure 5.91. However, the maximum tensile strain of the vertical steel bars was located in different location as stated in the previous section. The vertical steel bar strain reached its maximum tensile value of 0.0084, while the circumferential rebar strain reached its maximum tensile value of 0.0042. In this stage, the steel bars at the top and bottom corners already yielded. Similar to Specimen No. 1, the yielding areas of both steel bars also expanded significantly up to two-thirds of the area of the specimen walls which matched very well with the the experimental results illustrated from Figure 5.51 through Figure 5.54. In compression, both the vertical and circumferential steel bars were still in

elastic with the maximum compressive strains of 0.0015 and 0.00062, respectively, as shown in Figure 5.91

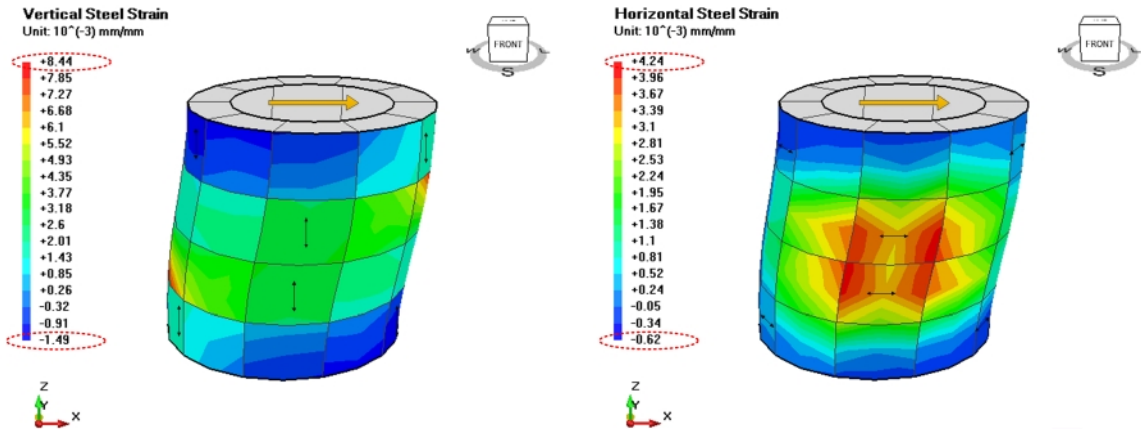


**Figure 5.91 Analytical strains of steel bars in Specimen No. 2 (at the stage of the peak load in the positive direction)**

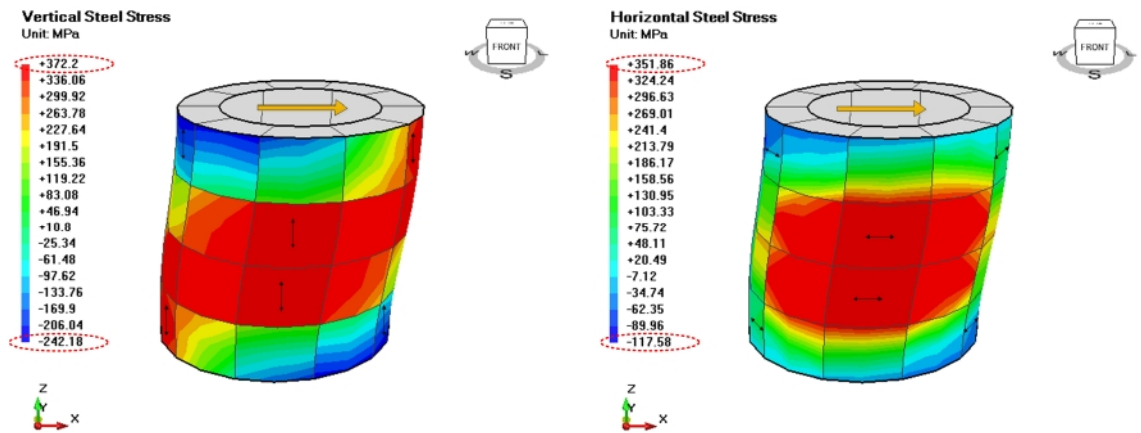


**Figure 5.92 Analytical stresses of steel bars in Specimen No. 2 (at the stage of the peak load in the positive direction)**

As shown in Figure 5.93, the maximum values of both principal tensile and compressive strains of the concrete occurred in the mid-height of the specimen. Therefore, the mid-height of the specimen was considered to be the most critical area. The stress and strain curves of a selected points from the mid-height region was plotted to investigate the response of concrete at the current loading step, as shown in Figure 5.95.

From the stress and strain curve, the compressive strength of the concrete in the mid-height region was determined to be about 18 MPa, which was significantly smaller than the defined compressive strength of concrete, 35 MPa. This result indicated that the severe opening of the cracks within this region caused the decrease in the strength of concrete of 48%, similar to Specimen No. 1. The figures revealed that both the stresses and strains of the concrete in the mid-height region moved further to the descending branch. Therefore, the concrete reached the damage in this stage.

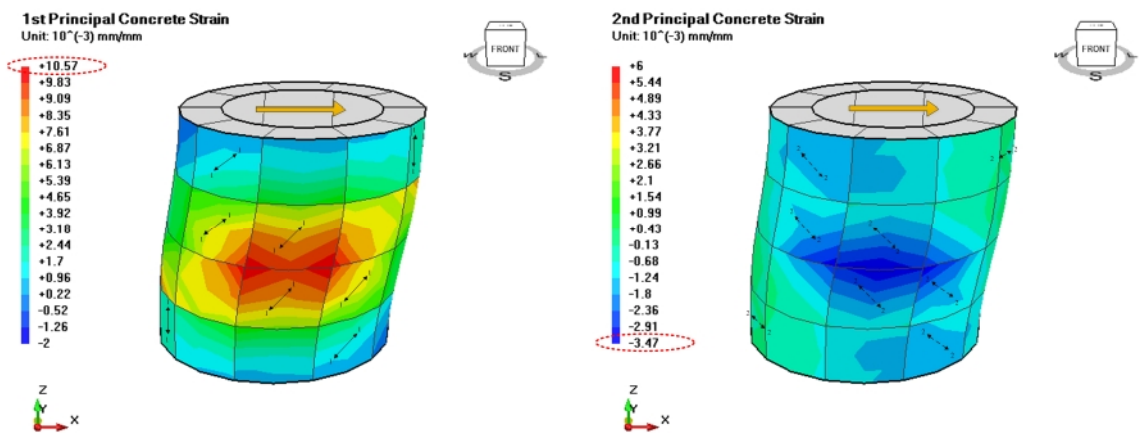


Figure 5.93 Analytical strains of concrete in Specimen No. 2 (at the stage of the peak load in the positive direction)

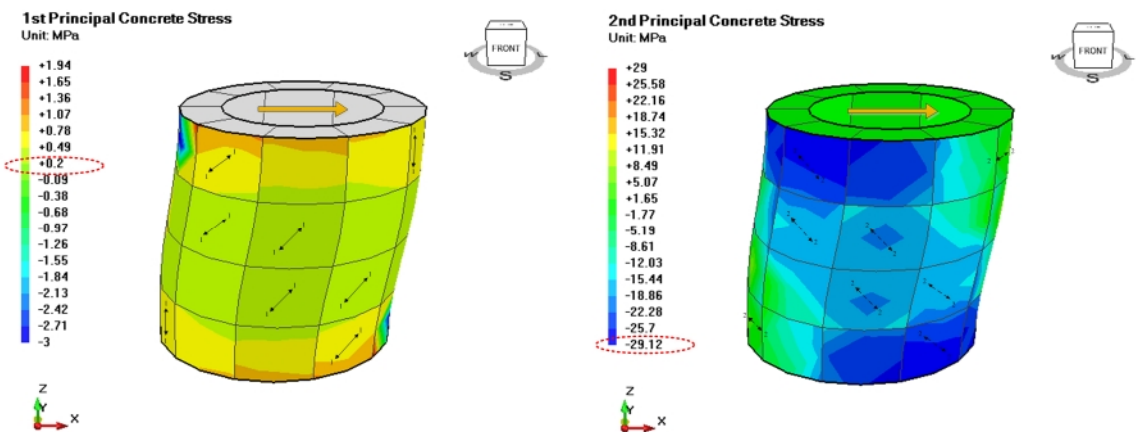


Figure 5.94 Analytical stresses of concrete in Specimen No. 2 (at the stage of the peak load in the positive direction)

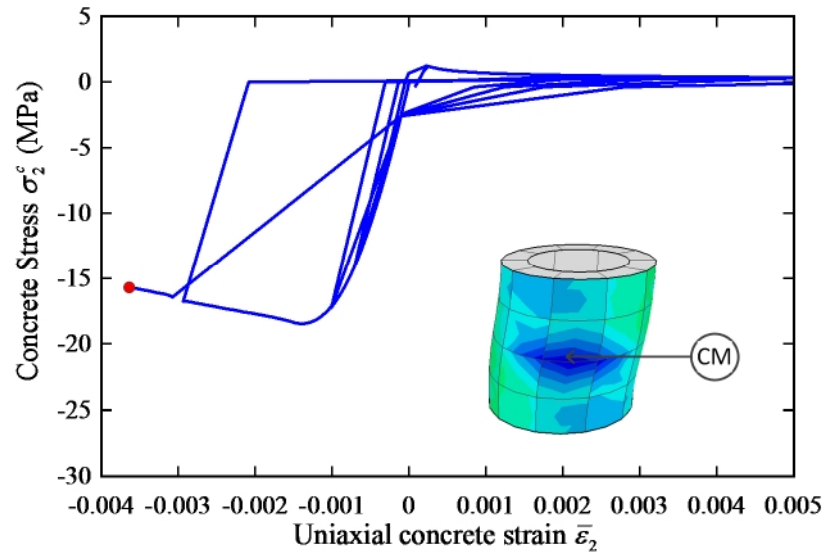


Figure 5.95 Stress-strain curve of concrete at the point S2 in Specimen No. 2 (at the stage of the peak load in the positive direction)

## 5.6 Further Analytical Studies

### 5.6.1 Improving Sliding Shear Failure Prediction of Specimen No. 1

For the purpose of making more accurate predictions for the analytical simulation in terms of the sliding shear that occurred in Specimen No. 1, a sliding shear failure mechanism stated by Paulay et al. (1982) was applied, as shown in Figure 5.96. Based on the mechanism, when the flexural cracks had not yet occur at the junction of the vessel and the top slab, the shear force from the top slab was transmitted to the vessel through entire cross section of the vessel. After several cycles, flexural cracks occurred throughout entire cross section at the junction of the vessel and the top slab, and the shear force was transferred across the flexural compression zone. Before the cracks close to form the compression zone, the shear force was carried mainly by the dowel action of the vertical reinforcement. When all of the vertical reinforcement within the compression zone of the current cycle had yielded in tension from the previous cycle, the compression

zone could not be formed before the shear force reached the dowel capacity of the vertical reinforcement. As a result, when the shear force exceeded the dowel capacity shear sliding failure occurred.

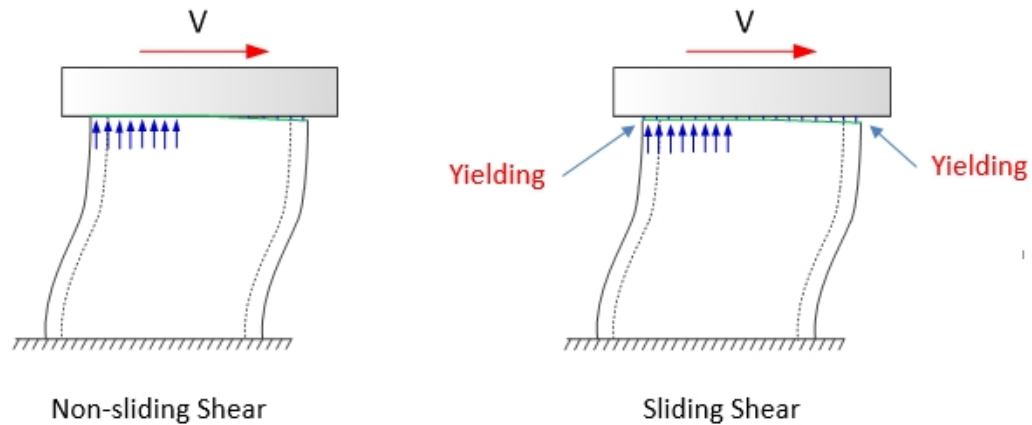


**Figure 5.96 Sliding shear failure mechanism**

The sliding shear failure was considered to be local failure and should be simulated by a discrete model approach. However, the CSMM-based shell element, which was developed based on a smeared cracking model approach in this research, could be used to accurately predict sliding shear failure by using an appropriate analytical algorithm. In this research, an analytical algorithm with sliding shear checking condition was proposed, as shown in Figure 5.97. The analytical algorithm required the program users to look at the stress and strain diagram of the vertical reinforcement at the junction of the vessel with the top and bottom slab and use the checking condition to specify the step at which the sliding shear failure may happen. The checking condition was based on the assumption that the sliding shear only happens when all of the vertical reinforcement located within the compression zone of the current cycle has yielded in tension in the previous cycle. When the checking condition was satisfied, the current shear force was

compared with sliding shear limit, which was the dowel capacity of the vertical reinforcement, taken as  $0.4A_s f_y$ .

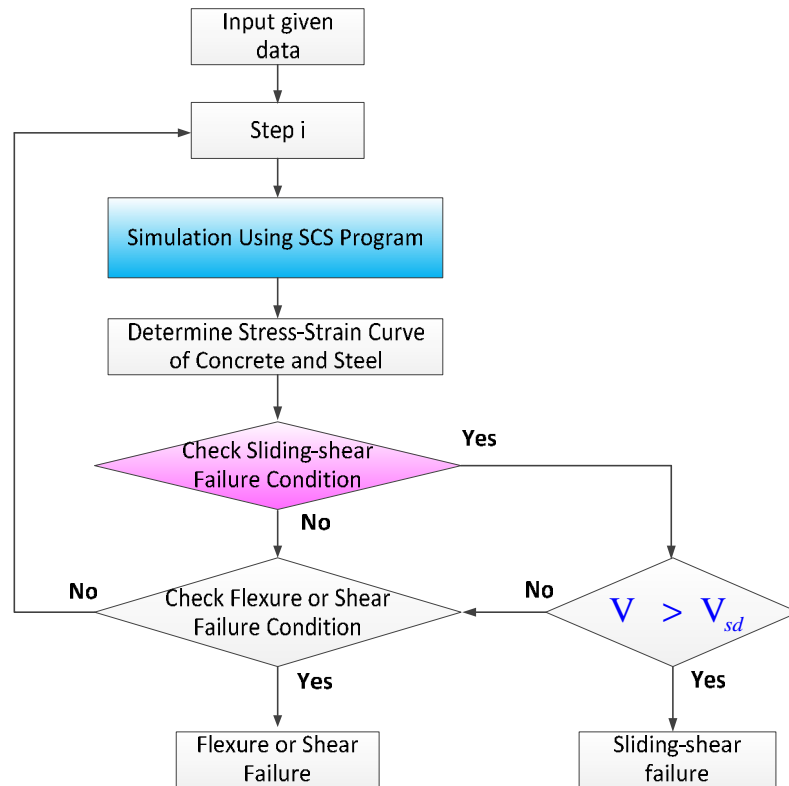


**Figure 5.97 Analytical algorithm with sliding shear checking**

Figure 5.98 shows the analytical result obtained by using the analytical algorithm with sliding shear checking. The model accurately predicted the cyclic in which sliding shear started to occur. This cycle started from Point 5, which corresponded to the peak load in the negative direction, to Point 2, which indicated the predicted sliding shear failure, in positive direction. Point 2 was the intersection between the original analytical curve and the horizontal line, which was specified by the sliding shear limit. The analytical results indicate that if the sliding shear occurred in the cycle mentioned above, the stresses and strains of the vertical steel bars needed to be investigated at this cycle.

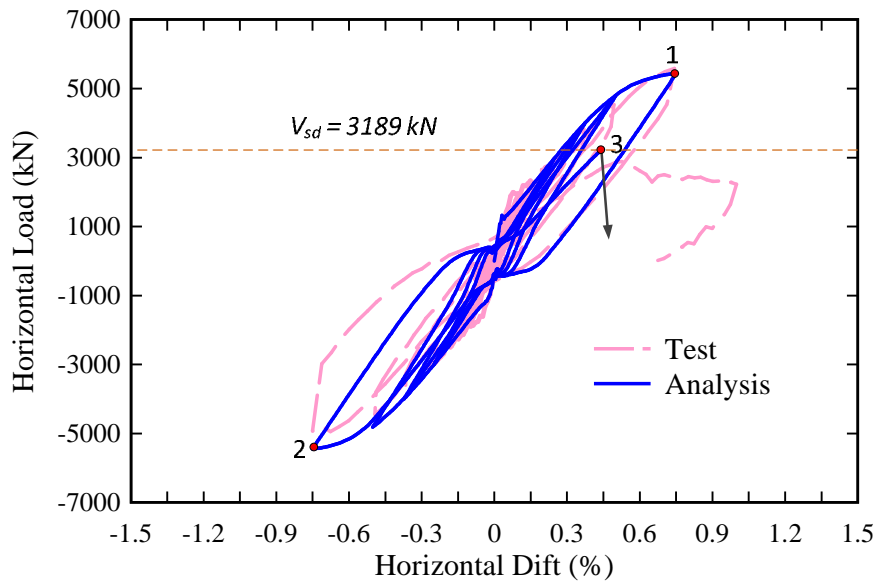


**Figure 5.98 Analytical load versus horizontal drift ratio curve of RCCV Specimen No. 1**

The strain distributions of the vertical steel bars corresponding to Point 5 and Point 6 are illustrated in Figure 5.99 and Figure 5.100, respectively. The figures indicate that the top left corner region of the specimen, which is compressed in Figure 5.100, yielded in tension in the previous cycle, as shown in Figure 5.99. The Point ST located at the boundary of the compression zone of the top left corner in Figure 5.99 was peaked and the stress and strain curve of the vertical steel bars at this point were plotted, which corresponded to Point 5 and Point 6 in Figure 5.98. The stresses and strains of the vertical steel bars at the point ST were in the unloading path after reaching yielding value in the previous cycle. These results satisfied the checking condition in Figure 5.97, and, therefore, indicated that the sliding shear may occur in this cycle and the sliding shear limit of the specimen needed to be checked. In the case of Specimen No. 1, the sliding shear limit was about 3189 kN, which was significantly smaller than the peak load of the specimen. Hence, the specimen did fail due to sliding shear.

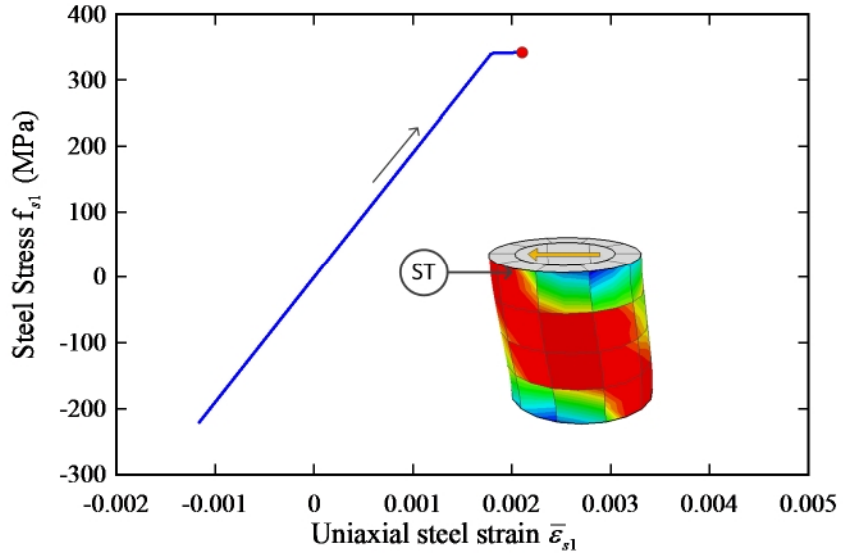


Figure 5.99 Stress-strain curve of steel bars at the point ST in Specimen No. 1 (at the stage of maximum load in the negative direction - Point 5)

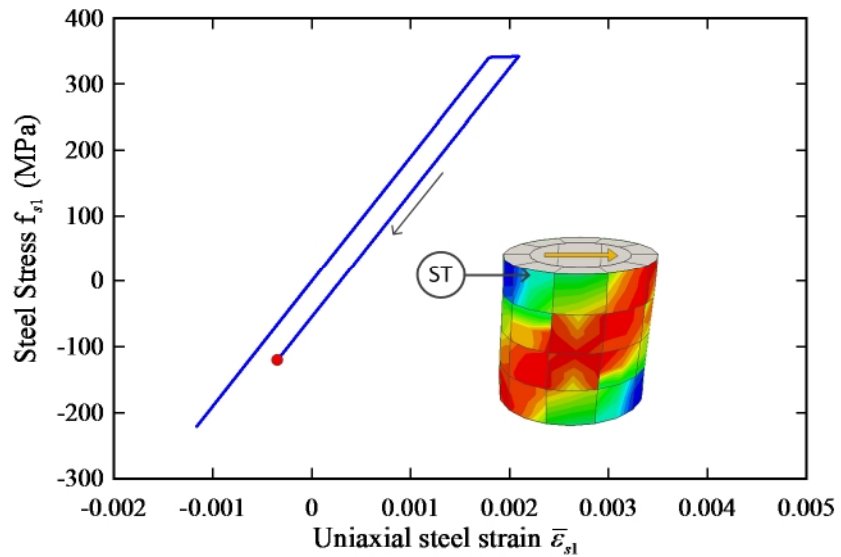


Figure 5.100 Stress-strain curve of concrete at the point S2 in Specimen No. 2 (at the stage of sliding shear failure - Point 6)

Based on the analytical algorithm with sliding shear-checking method, it can be predicted that no sliding shear occurred in Specimen No. 2 for two reasons. First, the yielding region of the vertical steel bars was minimized by adding the dowel bars at the top of the specimen. Second, the dowel bars helped increase the sliding shear resistance of the specimen by two times, which exceeded the peak load of the specimen. Because the two conditions in the proposed sliding shear checking method were not satisfied, the specimen did not fail due to sliding shear.

### **5.6.2 Improving the Prediction for the Descending Branch of Specimen No. 2**

As stated in the previous section, as compared to the experimental hysteretic loops of Specimen No. 2 shown in Figure 5.65, the descending part of the experimental hysteretic loops were steeper compared to the predicted results. The steeper descending part could depend on many factors. One factor that could have directly affected the slope of the descending part was the shape of the stress and strain curve of the concrete material. The analyses conducted using three models of the stress-strain curve of concrete are shown in Figure 5.101, in which the curve with the maximum strain of  $4e_0$  is the current model of concrete used in the analytical model. The analytical results were compared with the experimental data, as shown in Figure 5.102. The figure shows that the descending branch of the load became steeper as the maximum strain in the stress and strain curve of concrete model decreased. However, one disadvantage of decreasing the maximum strain was that it made the maximum displacement at the peak load smaller compared with the experimental results.

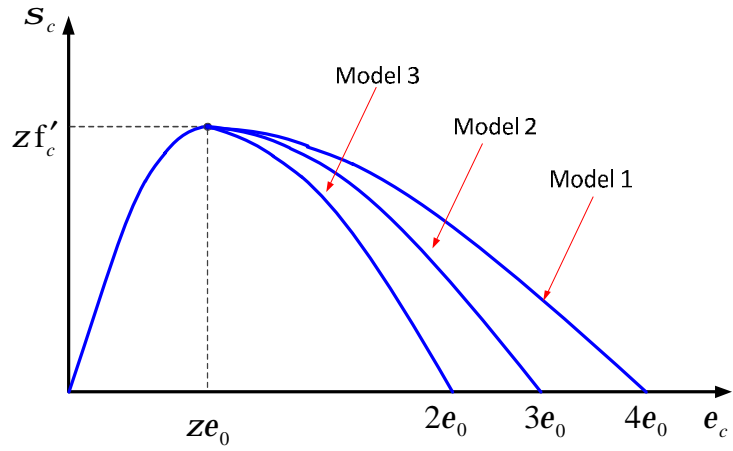


Figure 5.101 Stress-strain curve of concrete

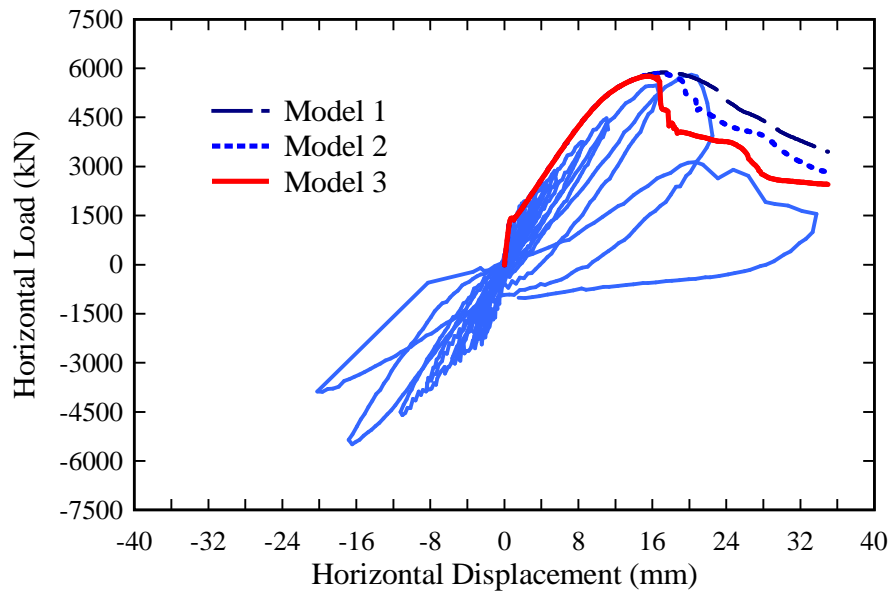


Figure 5.102 Parametric study on the load-displacement curve of Specimen No. 2

# **CHAPTER 6**

## **SIMULATION OF A TWO-STORY UNSYMMETRICAL REINFORCED CONCRETE BUILDING**

### **6.1 Introduction**

One of the important aspects of the proposed shell element is its capacity to simulate the 3D behavior of RC shear walls. The proposed shell element can be used with beam-column elements to simulate the behavior of an entire RC building structure, which is a combination of various types of components such as beams, columns, and shear walls. In this chapter, tests and simulation of a two-story unsymmetrical reinforced concrete building subjected to bi-directional reserved cyclic loadings are presented. First, the test program including a test specimen, test setup, and loading method are described. Next, the experimental behavior of a whole two-story unsymmetrical RC building specimen is investigated. Finally, an analytical study of the two-story unsymmetrical RC building specimen are conducted using the proposed shell element, and the analytical results are compared with the test data.

### **6.2 Test Description**

#### **6.2.1 Specimen**

The tests were undertaken as part of an international collaboration project between the National Center for Research on Earthquake Engineering (NCREE) in Taipei, Taiwan, and the University of Houston, Houston, Texas (Tseng, Hwang, Mo, Yeh, & Lee, 2009). The full-scale test specimen was a two-story unsymmetrical reinforced concrete (RC)

building, as shown in Figure 6.1. The specimen was 3 m x 9 m in plan and approximately 4.3 m in height with one bay in the short direction and two bays in the long direction. The bay widths in the long direction were 3.5 m and 5.5 m, respectively. The net height of column on the first floor was 2 m and on second floor was 1.5 m. The specimen consisted of six columns on each floor and total three walls. Figure 6.2 illustrates the plan view and elevation view of the specimen. All beams had the cross section of 300 mm x 400 mm, and all columns had the cross section of 400 mm x 400 mm. The thickness of slab was 200 mm in both floors.



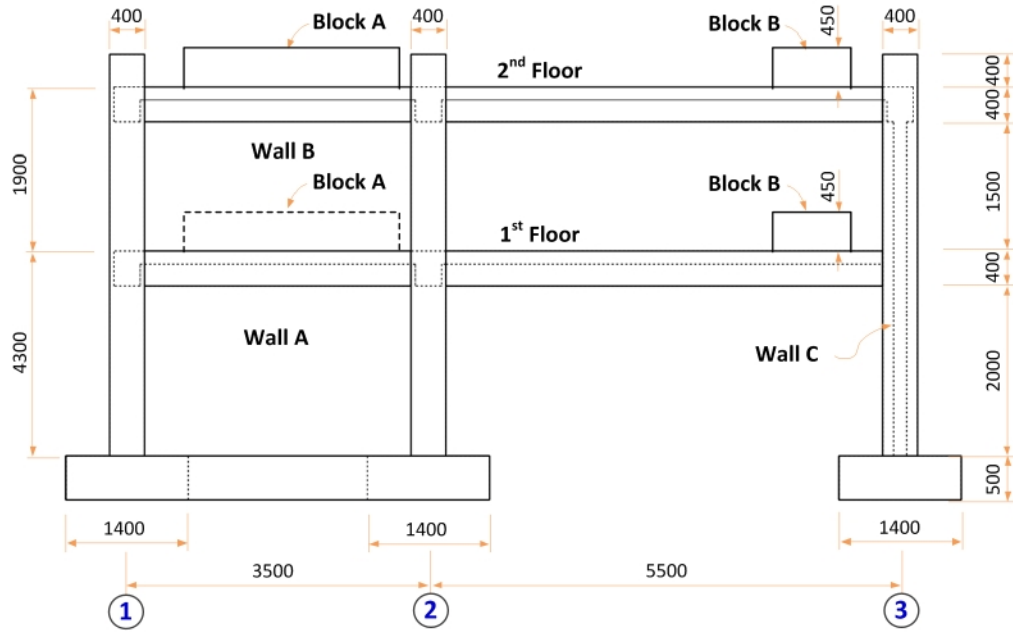
**Figure 6.1 Three-dimensional view of the two-story unsymmetrical RC building specimen**

The dimensions and arrangement of the longitudinal and transverse reinforcement in the columns are shown in Figure 6.3. Twelve No. 6 deformed longitudinal bars were placed uniformly around the perimeter of the column's cross section resulting in a longitudinal reinforcement ratio,  $\rho_{sl} = A_{sl} / A_g = 0.025$ , where  $A_{sl}$  = total cross-sectional

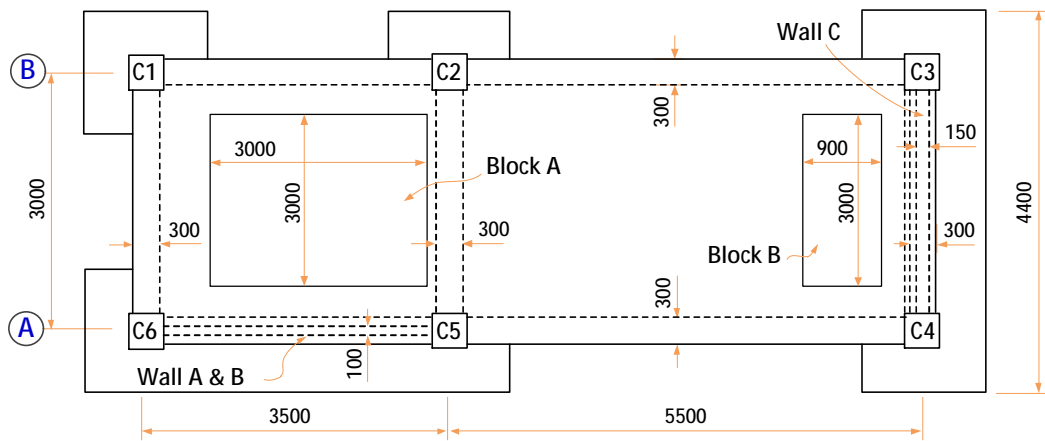
area of longitudinal reinforcement,  $A_g$  = gross area of the cross section of the column. The longitudinal bars were assembled continuously without lap splices. No. 3 deformed bars were used for the transverse reinforcement.

For the purpose of studying the structural behavior of the columns under various behaviors such as flexure, shear, or torsion, the columns were classified into three types based on the arrangement of transverse reinforcement and height-to-width ratio. Type 1 included all columns on the first floor (C1-F1, C2-F1, C3-F1, C3-F1, C4-F1, C5-F1, C6-F1) that have the height-to-width ratio of 5.0 with very dense spacing of the transverse reinforcement of 100 mm. Type 2 included two columns on the second floor that are adjunct to Wall C (C3-F2, C4-F2). The column had a height-to-width ratio of 3.75, and the transverse reinforcement was spaced uniformly at 100 mm. Type 3 included four columns on the second floor (C1-F2, C2-F2, C5-F2, C6-F2) that had a height-to-width ratio of 3.75 with light spacing of the transverse reinforcement of 280 mm. Based on the designed height-to-width ratio, the columns in Type 1 and Type 2 were expected to be critical in flexure, and the columns in Type 3 were expected to be critical in shear.

Cross-section details of the beams and slabs are shown in Figure 6.4. The beams and slabs were designed to have enough strength and ductility so that the failure of the building will happen only in the columns or the walls. Each beam had eight No. 6 longitudinal reinforcing bars and No. 3 stirrups with the spacing of 100 mm. Two layers of No. 3 reinforcing bars with spacing of 150 mm were arranged at the top and bottom of the slab on each floor.



(a)

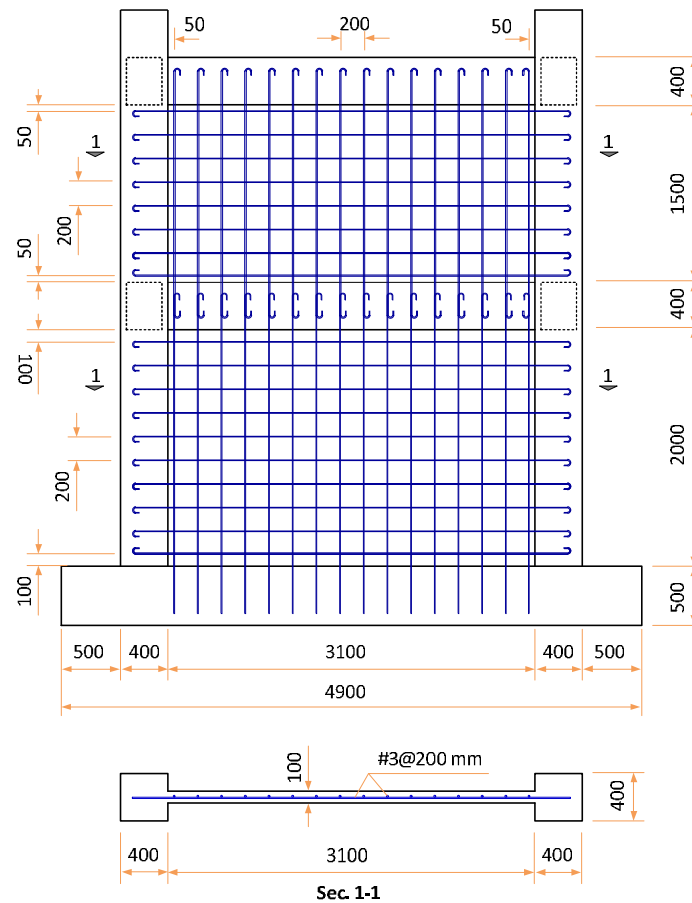


(b)

**Figure 6.2 Dimension of the two-story unsymmetrical RC building specimen in (a) Elevation view (b) Plan view**

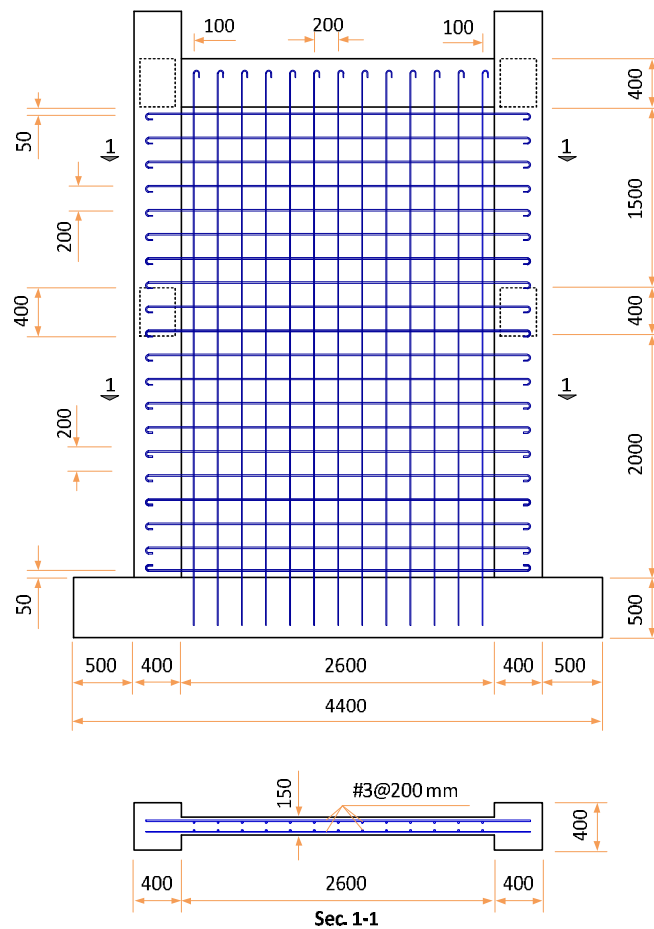


Figure 6.5 and Figure 6.6 illustrate the details of the reinforced concrete walls. To test the torsional effect, the walls of the building were arranged asymmetrically. Wall A and Wall B with the thickness of 100 mm were located on the east side, and Wall C with the thickness of 150 mm was located on the north side of the building, as shown in Figure 6.1. The walls were divided into two categories. Wall A and Wall B, which had the height to width ratio of 0.64 and 0.48 respectively, were classified as low-rise shear walls. Wall C, which had the height to width ratio of 1.5, was classified as a mid-rise shear wall. With such design, Wall A and Wall B were expected to be critical in shear behavior; Wall C was expected to be critical in both shear and flexural behaviors.



**Figure 6.5 Dimensions and details of Wall A and Wall B**

Figure 6.5 illustrates the dimensions and detailings of Wall A and Wall B. One layer of the No. 3 deformed bars with the spacing of 200 mm is used in both horizontal and vertical directions, resulting in a steel ratio of 0.36%. Figure 6.6 illustrates the dimensions and detailings of Wall C. Two layers of No. 3 deformed bars with the spacing of 200 mm are used in both horizontal and vertical directions, resulting in a steel ratio of 0.48%.



**Figure 6.6 Dimensions and detailings of Wall C**

During the test, forces were generated by the hydraulic power supply actuators and applied to the building through RC blocks (Figure 6.2), which transmit the forces to the slab and eventually to the other structure component elements. Two different

configurations of the blocks were designed. RC block Type A dimensions were sized and designed as 2000 mm × 2500 mm × 450 mm; RC block Type B was sized and designed as 900 mm × 2000 mm × 450 mm. Reinforcement detailings of the RC blocks are shown in Figure 6.7. The calculations took into consideration that the RC block was subjected to shear force, shear reinforcement and preloaded bolts were installed in the blocks. Four bolts were installed on the Type A blocks and eight bolts on the Type B Blocks (Figure 6.7). Each preloaded bolt was capable of supporting loads up to 80 tons (in tension). In this manner, slip displacement between the blocks and the floor slabs was minimized.

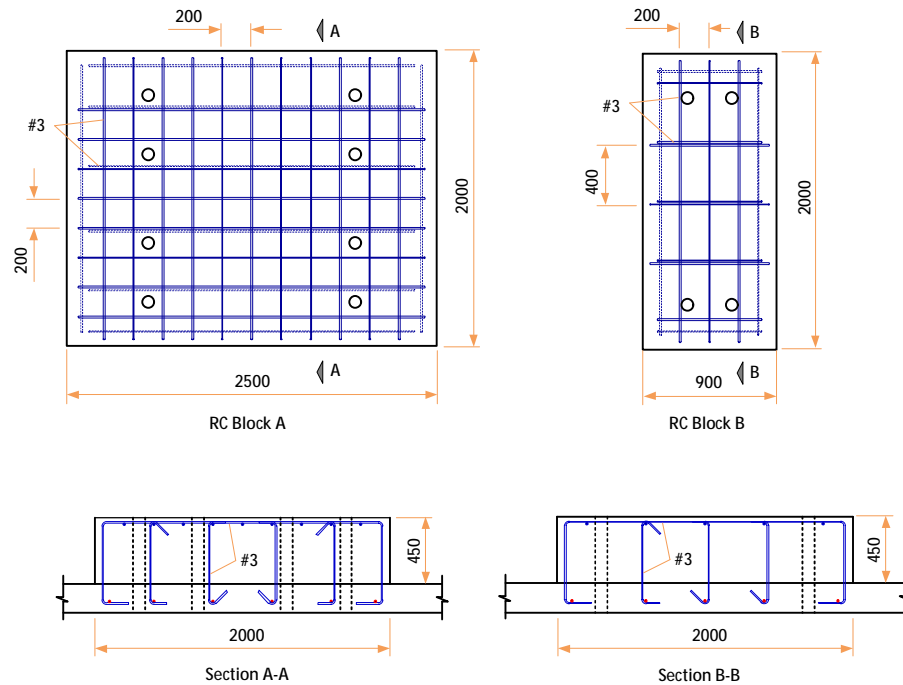


**Figure 6.7 Dimensions and detailings of the RC blocks**

### 6.2.2 Material Properties

Ready-mix concrete companies provided six batches of concrete with target specified compressive strengths of 27.5 MPa. The compressive strength of concrete was determined from the compression tests of standards concrete cylinder (300 mm in height

and 150 mm in diameter). Results of the compression tests of concrete are tabulated in Table 6.1.

**Table 6.1 Result of Compressive Strength Tests of Concrete**

Batch No.	Curing days	$f'_c$ (Mpa)
1	28	28.6
	113	35.0
2	28	32.6
	100	39.2
3	28	29.1
	77	30.0
4	71	29.1
5	62	28.4
6	56	26.0

The nominal yielding strength of reinforcement was 420 MPa. Table 6.2 shows the results of the tension tests of reinforcing rebars used for the specimen. Two different types of rebars were used for the main structural components, such as beams, columns, and walls. Bar No. 6 was used as the longitudinal bars of columns and beams while Bar No. 3 was used as the stirrup of columns and beams or as horizontal and vertical bars of walls.

**Table 6.2 Results of Tensile Tests of Reinforcement**

Bar Type	Tensile Strength	Specimen 1 (Mpa)	Specimen 2 (Mpa)	Specimen 3 (Mpa)	Specimen 4 (Mpa)
#3	$f_y$	453.2	448.7	442.5	443.5
	$f_u$	690.6	681.8	681.3	682.3
#6	$f_y$	455.2	431.1	427.2	425.5
	$f_u$	662	654.8	660.1	678

### 6.2.3 Test setup and Instruments

The test setup of the specimen is illustrated in Figure 6.8. Ten sets of static hydraulic actuators, each with a capacity of 981kN, were used for the experiment. Five sets of actuators were allocated in the long direction, in which, two sets on the first floor and three sets on the second floor, while there were two sets of actuators on the first floor and another three sets on the second floor in the short direction. Figure 6.9 shows the notation of the actuators used in each floor. This test is mainly designed to investigate the torsional effect of the two-story unsymmetrical RC building structure, which consists both RC frames and shear walls. For the purpose of this investigation, the loading history was required to satisfy two conditions. First, to control the center of mass on the second floor, the displacement ratio of the long to short direction was set at 1:2. Second, the horizontal force ratio of the second story to the first story was set at 1.83, equal to the ratio of the story height. Additionally, a vertical loading system was designed with a capacity of 850 kN to apply an axial load on column C1 to investigate the vertical loading effect on a single column.

The overall system instrumentation used can be categorized into internal and external instrumentation systems. The internal instrumentation included the strain gauges used to measure the reinforcement strains at selected positions. The external instrumentation encompassed load cells, cable-extension position transducers, and dial gauges. The load cells were used to measure the lateral and vertical loads; the cable-extension position transducer was used to measure the displacement of the beam-column joint; and the dial gauges were used to measure the small slip displacements of the foundation.

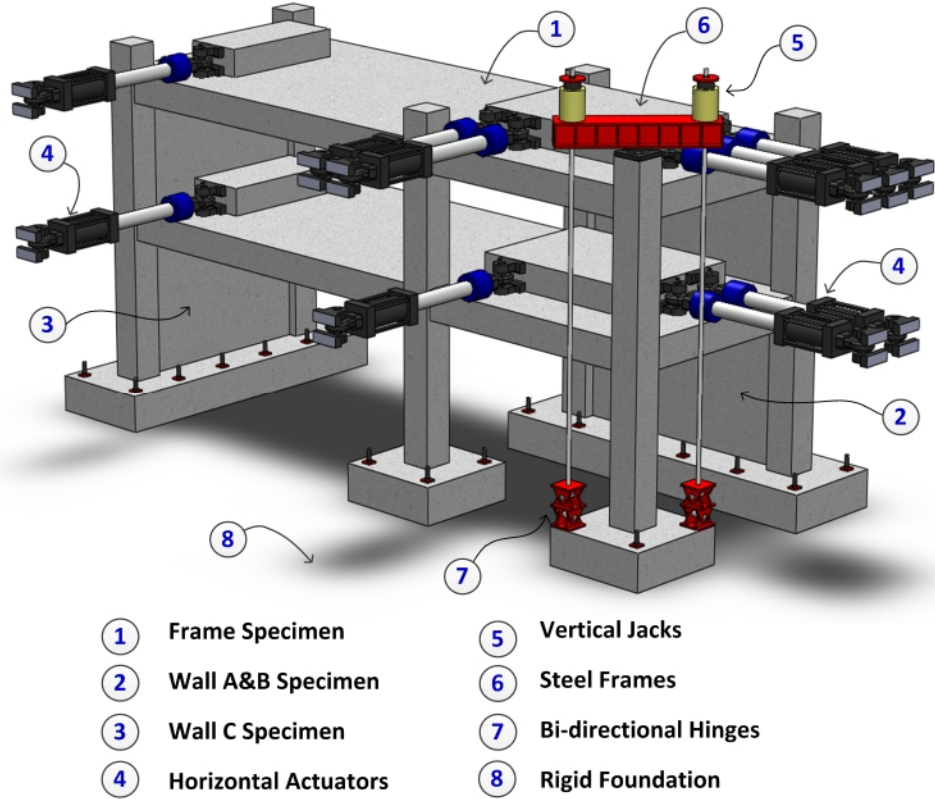
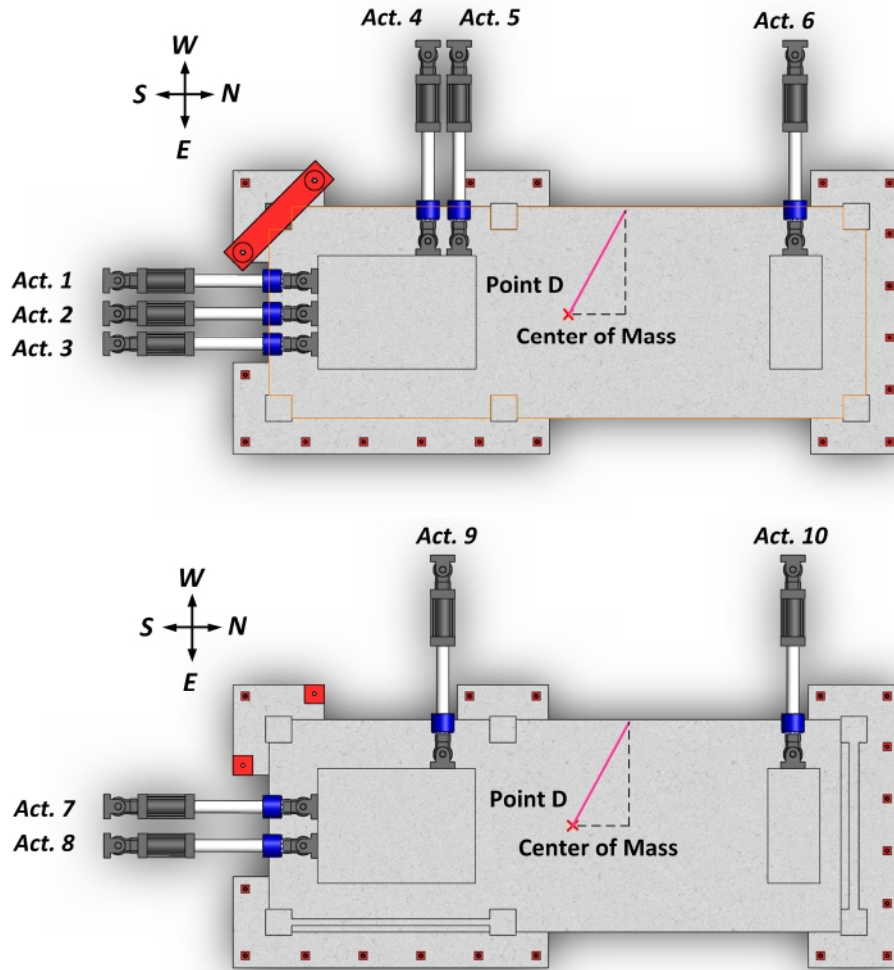


Figure 6.8 Notations of the actuators

#### 6.2.4 Loading Procedure

For the purpose of this investigation, the loading history must satisfy two conditions. First, to control the mass center displacement on the second floor, the displacement ratio of the short to long direction must be equal to  $\tan(q)$ , where  $q$  is the angle between the moving direction of the mass center and the horizontal direction. Second, the ratio of horizontal force was set to be equal to the ratio of the story height. The height from the foundation to the center of the second floor was 4200 mm whereas the height from the foundation to the center of the first floor was 2300mm. Therefore, the ratio of the horizontal force was set equal to 1.83, equivalent to the ratio of the story height.



**Figure 6.9 Test setup of the two-story unsymmetrical RC building specimen**

To meet the objectives of the experiment, each actuator had its own control mode. The control method of the six sets of actuators on the second floor must produce the straight reversed cyclic movement of the mass center on the second floor. At the same time, the resultant force needed to pass through the vertical projection location of the mass center. According to the designed reversed cyclic loading history, the mass center on the second floor can control. The control modes of the four actuators on the first floor were all set in the force mode and were distributed based on the story height. All control modes of the

actuators are listed in Table 6.3. Fig. 15 shows the loading history consisting of the following drift cycles: 0.25%, 0.375%, 0.5%, 0.75%, 1.0%, 1.5%, 2.0%, 3.0%, with each loading having three cycles. In this experiment, the loading history is referred to as Cmd\_D (Table 6.3).

**Table 6.3 Control Modes and Equations of Actuators**

Actuator No.	Control Mode	Equation
1	Force / Calculation	$F1 = F2$
2	Calculation / Command	$D2 = Cal\_D2 = - Cmd\_D \times \cos(\theta)$
3	Force / Calculation	$F3 = F2$
4	Force / Calculation	$F4 = F5$
5	Calculation / Command	$Cal\_D5 = Cmd\_D \times \sin(\theta)$
6	Force / Calculation	$F6 = 4/7 \times (F4 + F5)$
7	Force / Calculation	$F7 = 0.5 (F1 + F2 + F3) / 1.83$
8	Force / Calculation	$F8 = 0.5 (F1 + F2 + F3) / 1.83$
9	Force / Calculation	$F9 = (F4 + F5) / 1.83$
10	Force / Calculation	$F10 = F6 / 1.83$

Note: F(i) = Force applied from the actuator "i". Cmd\_D = Displacement at the control node on the second floor.  $\theta$  = angle between the movement direction of the control node and the horizontal direction.

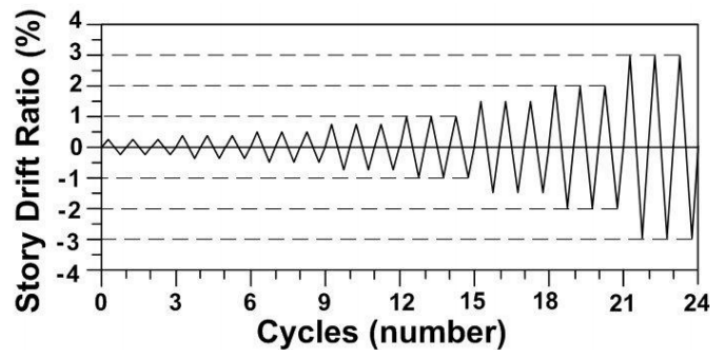
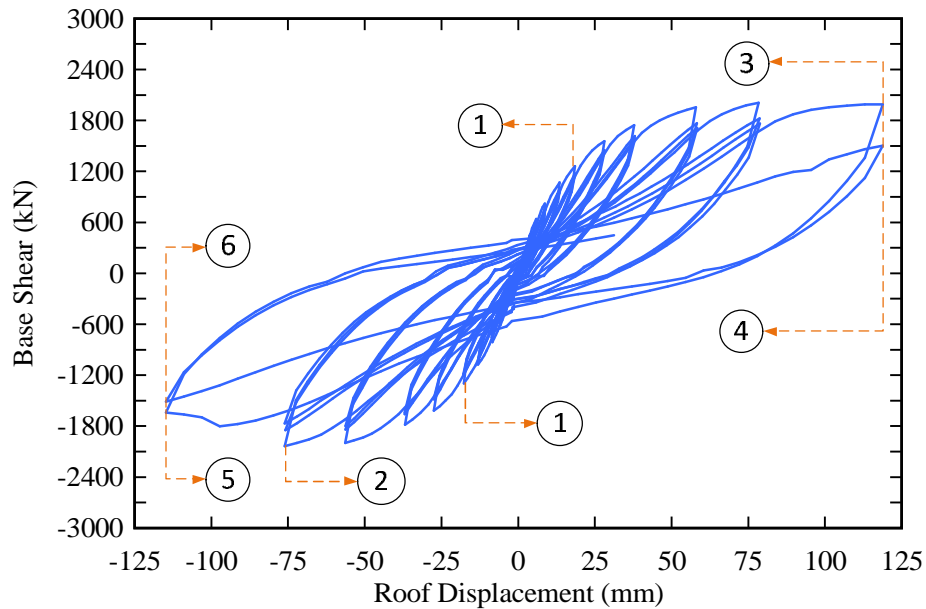


**Figure 6.10 Loading protocol**

### 6.2.5 Experimental Results

Figure 6.11 shows the relationship between the base shear and the roof displacement. In the figure, the base shear is compared against the roof displacement hysteresis loops. When the story drift was -2% at the third cycle, buckling occurred at the column C6-1F reinforcement. When the story drift was +3% at the first cycle, buckling occurred at the column C1-1F reinforcement. On the other hand, when the story drift was +3% at the first cycle, shear failure occurred at column C2-2F. Lastly, when the story drift was -3% at the second cycle, the column C1-2F reinforcement experienced collapse. Diagonal cracks happened in all of the RC walls; however, they did not have severe damage during the test. Photos of the failure sequences are shown in Figure 6.12.



- |                                |                                 |
|--------------------------------|---------------------------------|
| ① +0.5 % : C1-1F rebar yield   | ④ +3.0 % : C1-1F rebar buckle   |
| ② - 2.0 % : C6-1F rebar buckle | ⑤ - 3.0 % : C1-2F shear failure |
| ③ +3.0 % : C2-2F shear failure | ⑥ - 3.0 % : C1-2F collapse      |

**Figure 6.11 The experimental base shear versus roof displacement relationship**

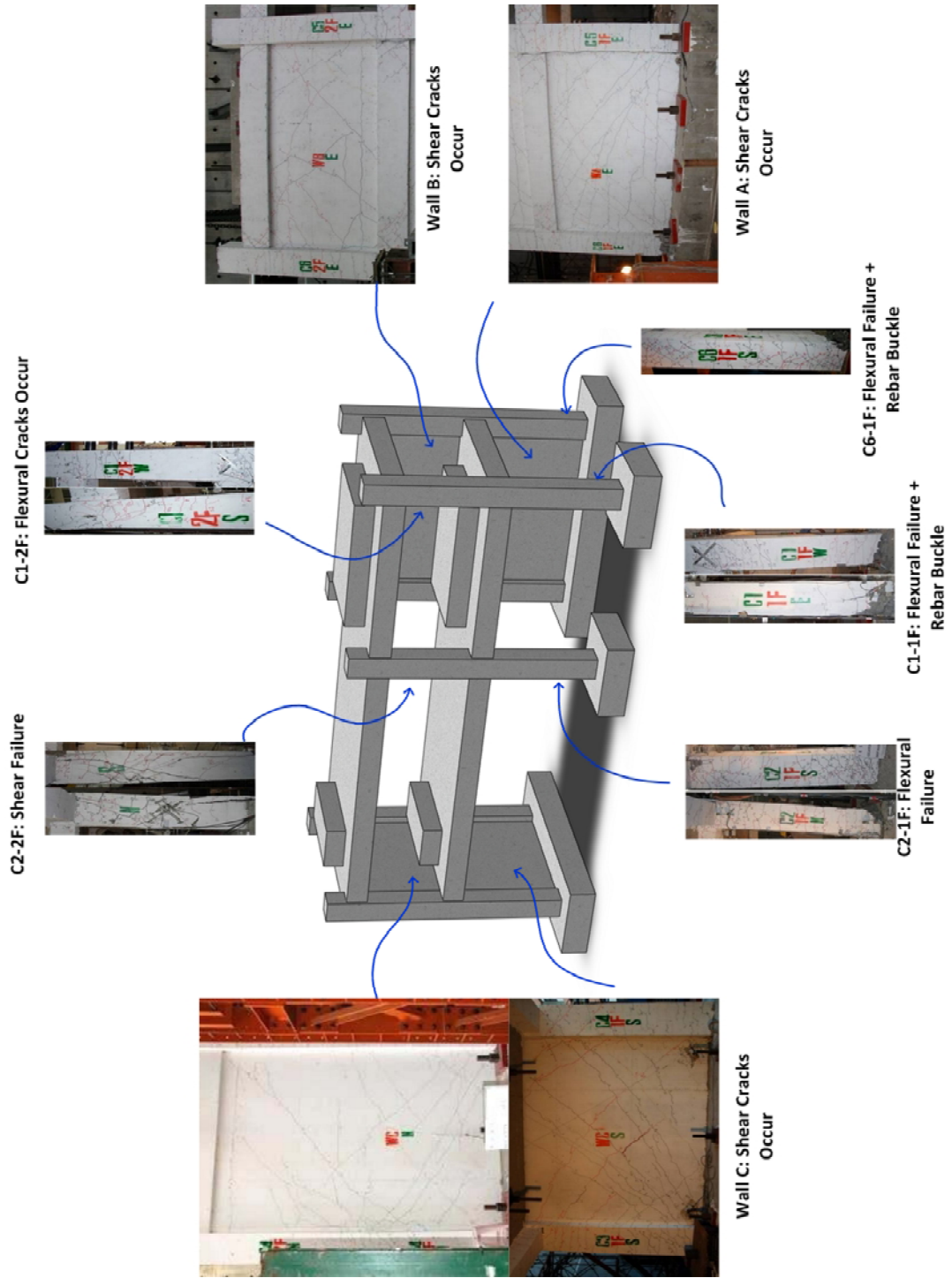


Figure 6.12 Failure sequences of the two-story unsymmetrical RC building specimen

## 6.3 Description of Analytical Model

The analytical model described in this section is a relatively complex 3D model that consists of three different types of elements. The elastic beam-column element was used to simulate the slabs. The nonlinear fiber beam-column element was used to simulate the beams and columns that compose the structure's frame. The developed CSMM-based shell element was used to simulate the shear walls and the shear-governed columns. Details of the model are described in the following sections.

### 6.3.1 Modeling Slabs

The purpose of the test was to force failure to happen at the vertical components; therefore, the slabs of the building were designed to have significant thickness and high amounts of reinforcement. From the test observation, no damage was found on the slabs. Therefore, for computer efficiency, the slabs were modeled with elastic beam column element.

The isotropic elastic material used for the elastic beam column element required the definition of two parameters: the elastic modulus and Poisson ratio. The elastic modulus of concrete was calculated using the ACI empirical equation

$$E_c = 4700\sqrt{f'_c}, \quad (6.1)$$

The Poisson ratio of concrete under uniaxial compressive stress ranged from 0.15 to 0.22 with a representative value of 0.19 or 0.2 (ASCE, 1982). In this study, the Poisson ratio of concrete was assumed to be 0.2.

### 6.3.2 Modeling Beams and Columns

The beams and columns of the building were modeled by using the fiber element named NonlinearBeamColumn (NBC) element, which is available in the present library of OpenSees, as shown in Figure 6.13. In the finite element mesh, each beam and column were modeled using four NBC elements with three control sections in each element. Figure 6.14 demonstrates the discretization used in the fiber section of the beam and column. The fiber section was meshed in both directions so that the element was able to capture biaxial bending. Each section of the column was discretized into 28 x 28 fibers of concrete and 12 fibers of steel. Each section of the beam was discretized into 20 x 28 fibers of concrete and 8 fibers of steel.

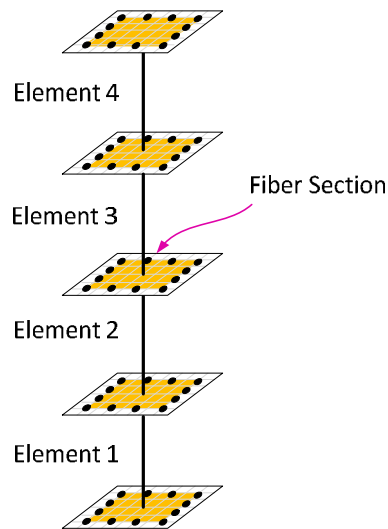
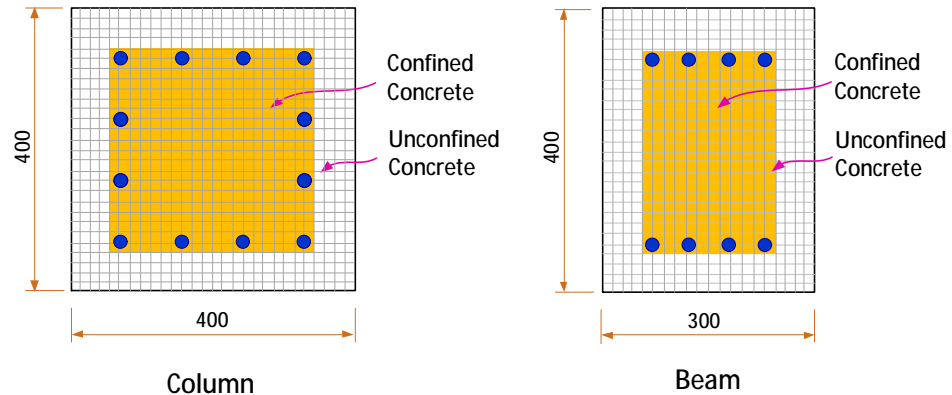


Figure 6.13 NonlinearBeamColumn element

Three different type of fibers were used in each section of the NBC element in the model. As shown in Figure 6.14, the white cells represent the confined fibers, the grey cells represent the confined concrete, and the black cells represent the reinforcing steel

fibers. Each fiber in the section of the NBC element was assigned with a uniaxial material corresponding to the material in that fiber.



**Figure 6.14 Discretization of fiber sections of the beams and the columns**

Concrete01 material model, which is available in OpenSees, was chosen to represent the concrete model, as shown in Figure 6.15. The models, which can be used for both confined and unconfined concrete, were based on the constitutive stress-strain relationship proposed by Kent and Park (1971) with degraded linear unloading and reloading paths proposed by Karsan and Jirsa (1969), as shown in Figure 6.16. Unconfined concrete model was assigned on the concrete cover while confined concrete was assigned to the concrete core surround by transverse reinforcement, as shown in Figure 6.14. The model did not consider any tensile strength of concrete. The input parameters were at the concrete compressive strength at 28 days, concrete strain at maximum strength, and concrete strain at crushing. After crushing, the concrete strength remained constant.

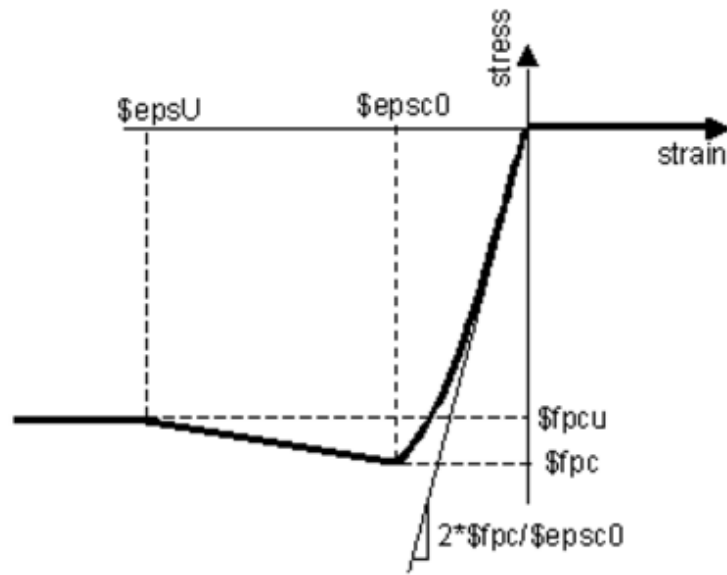


Figure 6.15 Concrete01 model for concrete (OpenSees, 2013)

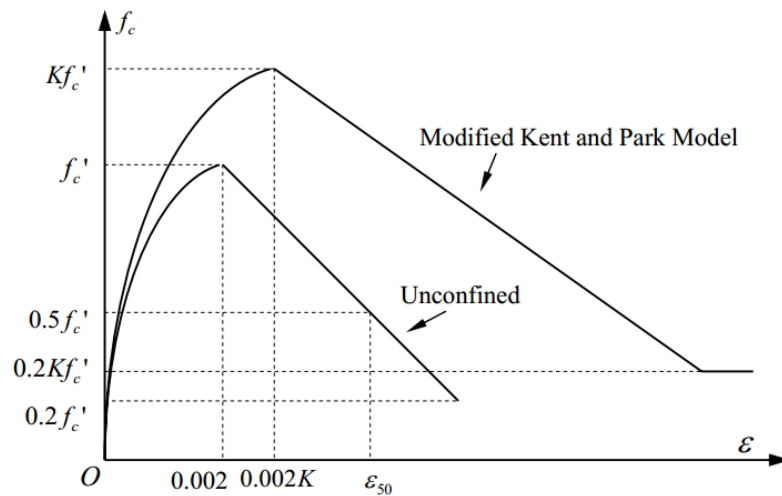


Figure 6.16 Modified Kent and Park Model for confined concrete

To model the beams and columns of the building that only had flexural-governed behaviors, the Steel01 material model, which is available in OpenSees, was used for the steel, as shown in Figure 6.17. The model consisted of two segments: the elastic linear branch and the strain-hardening branch. The bilinear model should not be defined with a

negative slope in the post-yield region to ensure that damage only occurs at the columns or the shear walls. This definition helps prevent the situation in which the reduction in strength and stiffness of the total performance of the whole specimen could be caused by a failure response of the beams.

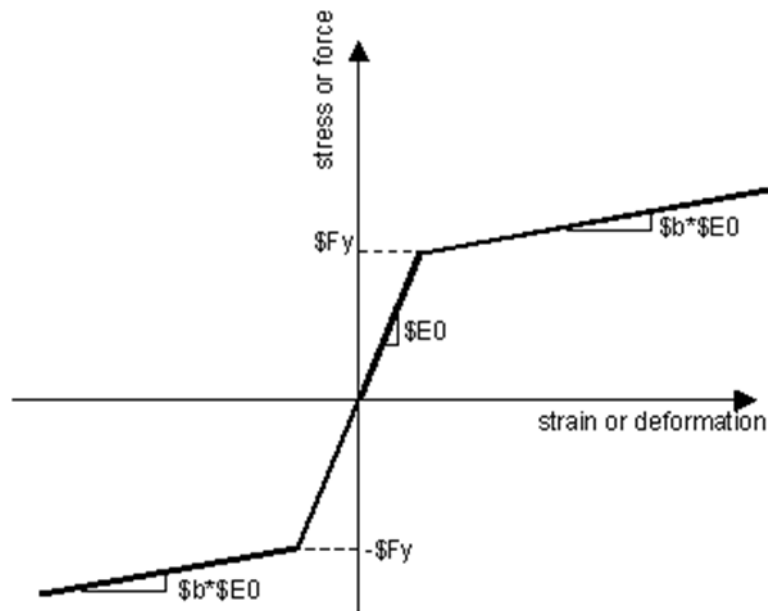
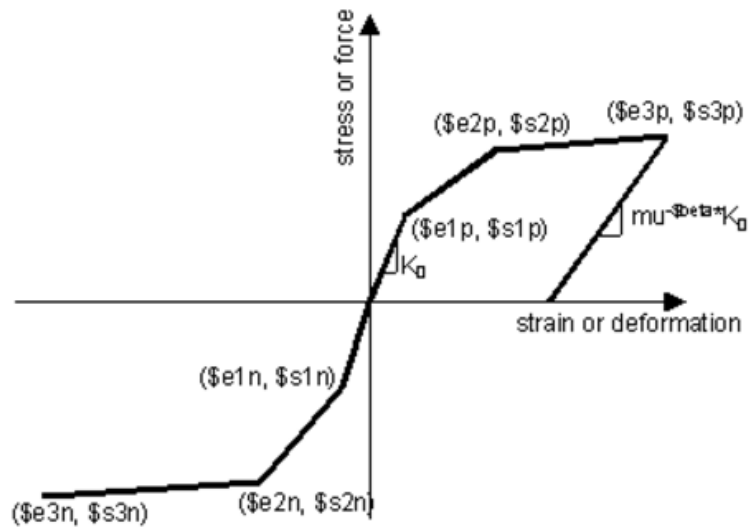


Figure 6.17 Steel01 model for concrete (OpenSees, 2013)

The hysteretic material model, which is available in OpenSees, was chosen to represent the steel model, as shown in Figure 6.18. This material model had two advantages. First, the model provided a better convergence as compared to other steel models. Second, the model allowed the user to modify its envelope by providing different values for three control points of the stress-strain curve. Hence, a low-cycle fatigue material model, which requires negative slope stress-strain curve, could be easily implemented.



**Figure 6.18 Hysteretic model for steel (OpenSees, 2013)**

To model columns that have buckling effects, a trilinear model was used for modeling of the steel used in the columns of the building. The model consisted of three segments: the elastic linear branch, the strain hardening branch, and the descending branch, which represented the buckling effect of the rebar. The model was based on the low-cycle fatigue model proposed by Mander, Panthaki, and Kasalanti (1994). The stress-strain curve of the model is shown in Figure 6.19. The strain corresponding to the maximum stress in the condition of low-cycle fatigue was approximately 3 to 5 times the yield strain, and the ultimate strain and stress was approximately 70% of that obtained in a tensile test. This concept was employed in the stress-strain relationship of longitudinal rebars in the analytical model by modifying the envelope of the hysteretic model.

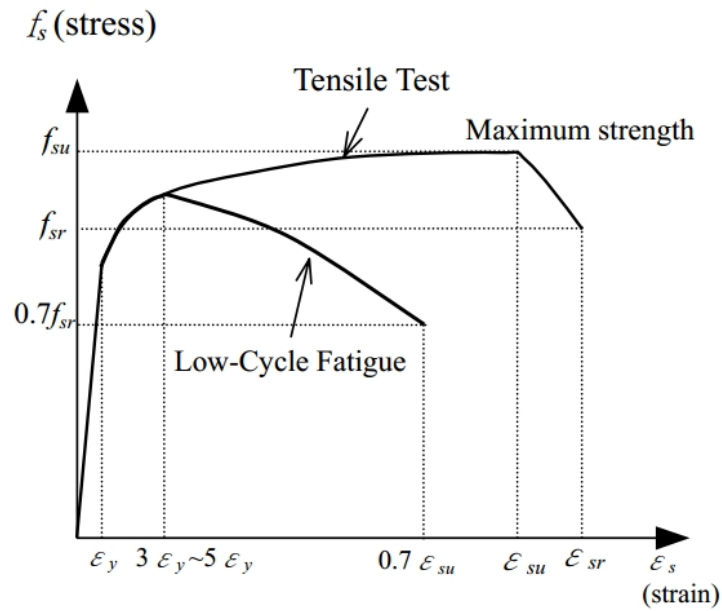
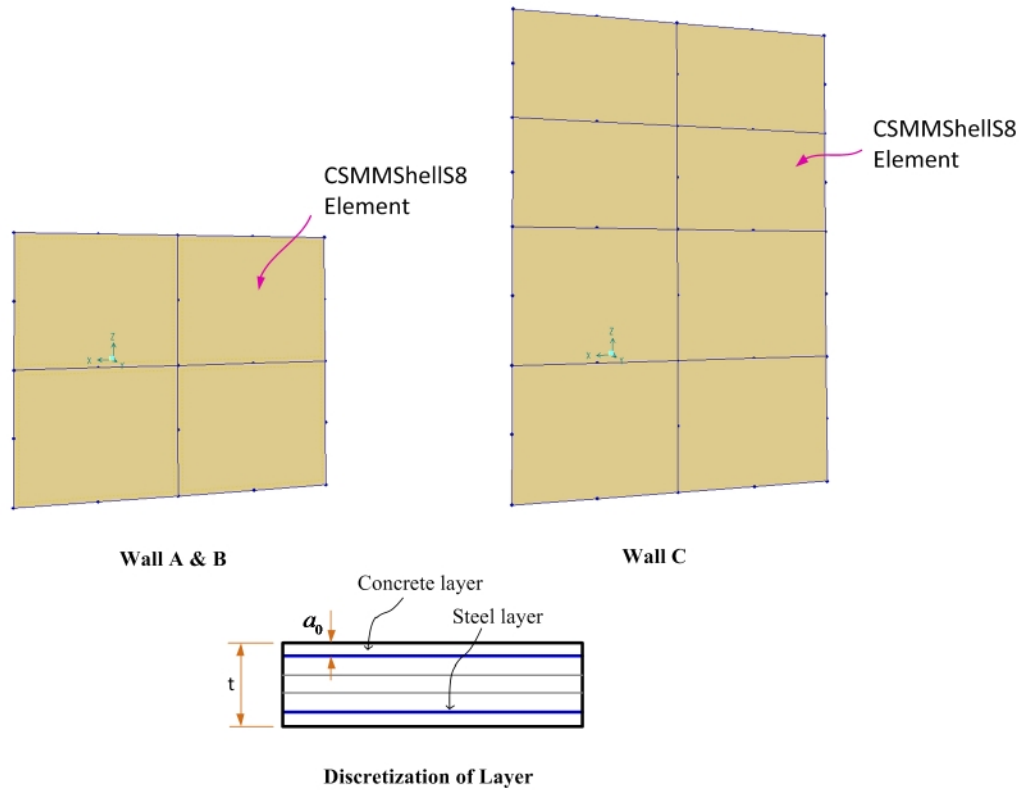


Figure 6.19 Low-cycle fatigue stress-strain curve of steel

### 6.3.3 Modeling Shear Walls

The shear walls of the building were modeled by using the CSMMShellS8 elements, which are the CSMM-based curved shell elements developed in this work. The finite element meshes of the shear walls are shown in Figure 6.20. Wall A and Wall B were modeled by four shell elements, and the wall C was modeled by eight shell elements. The steel ratio of the shear walls was defined in the CSMMLayer material. Ten layers of concrete and two layers of steel were assigned for each element. The steel layers were defined at the exact locations of steel at the top and bottom of the cross section of each element. SteelZ01 and ConcreteZ01 were used to create uniaxial constitutive laws of steel and concrete, respectively. To ensure that the shell elements worked together with the building frame, the shear walls were tied with the beams and the columns at the boundary nodes.



**Figure 6.20 Finite element mesh of shear walls**

### 6.3.4 Modeling Shear-governed Columns

As can be seen from the configuration and reinforcement detailing of the columns in Figure 6.13, columns C1-2F and C2-2F on the second floor were designed with a low height-to-width ratio and a large spacing of transverse reinforcement. With such design, these columns were expected to have shear behavior. The shear-governed columns could not be modeled accurately by the NBC element because this element was appropriate only for predicting flexural behavior. In this model, the shear-governed column was simulated using the using the CSMMSHELLS8 elements.

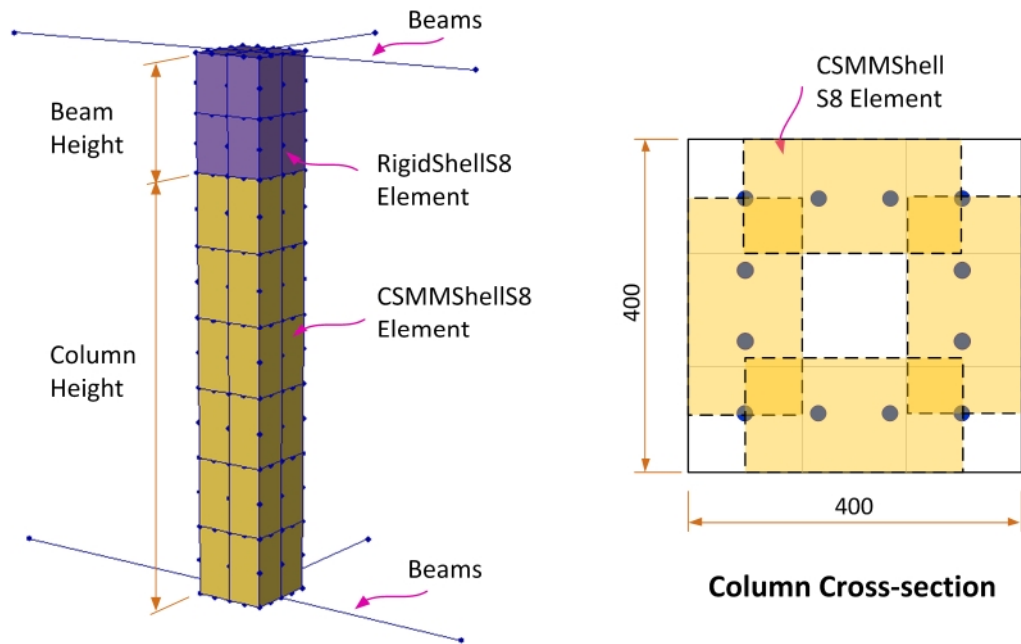


**Figure 6.21 Finite element mesh of column C1-2F and column C2-2F**

Finite element meshes of the column are shown in Figure 6.19. The column was modeled by 48 shell elements. The thickness of the shell element was equal to two times of the distance from center of the longitudinal rebar to the extreme fiber of concrete. Five layers of concrete and one layers of steel were assigned for each element. Material properties assigned for the shell element used for the columns were similar to shear walls.

The joined region on top of the column, which was the intersection between the column and the beam, was considered to be rigid. This rigid region was modeled using ElasticShellS8 elements. The stiffness of the ElasticShellS8 elements was defined to be high to guarantee that the top part of the column was totally rigid.

### 6.3.5 Applying Load

Loads were applied on the level of each floor of the building at the locations of the corresponding set of actuators. The load ratio was determined based on the control equation of actuators (Table 6.3) so that the load resultant would pass through the control points, which was the mass center of the building specified by the test program. The direction of the load resultant matched with the designed moving direction of the control points, as shown in Figure 6.22. The load resultant ratio between the second floor and the first floor was set equal to 1.83, equivalent to the ratio of the story height, so that it was consistent with the experimental program, as shown in Figure 6.23.

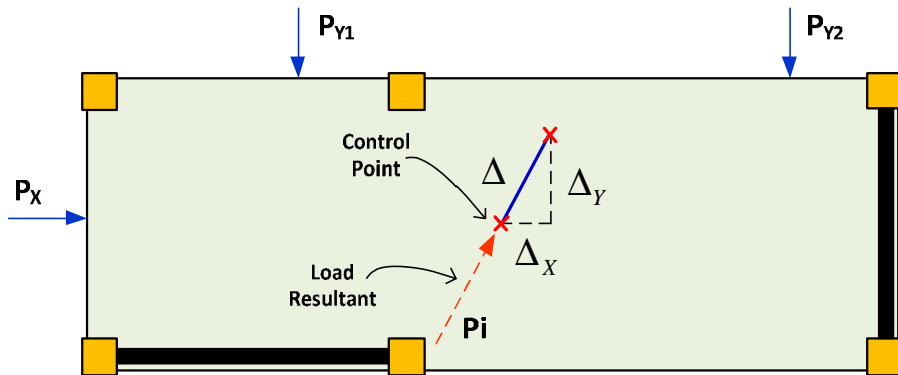


Figure 6.22 Conceptual deformation of the specimen

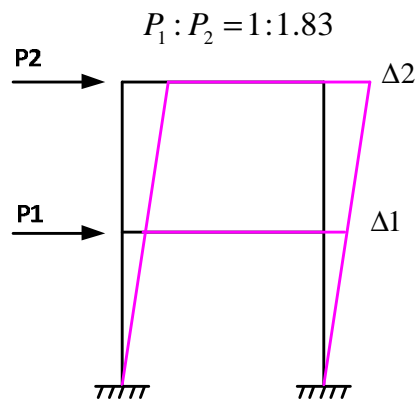


Figure 6.23 Force distribution of the specimen

### **6.3.6 Solution algorithm**

The analysis was performed by a predetermined force control and displacement control schemes. The analysis procedure was separated into two steps. In the first step, axial loads were applied to the columns using load control by ten load increments. In the second step, axial loads were kept constant and reversed cyclic horizontal loads were applied by the predetermined displacement control on the drift displacement. The common displacement increment used in the analysis was 0.5 mm. Convergence was obtained quite smoothly during the cyclic analysis. The modified Newton-Raphson method was used as the solution algorithm. The nodal displacement and corresponding base-shear forces were recorded at each converged displacement step, and the stress and strain of the elements were monitored.

## **6.4 Effects of Modeling Assumption on the Analytical Results**

### **6.4.1 Effect of RC Walls**

To investigate the effect of the RC wall, three analytical models were created and compared. The first model contained only the RC frame that included the slabs, beams, and columns, as shown in Figure 6.24. The second and third models were the combination of both RC frame and RC walls. The difference between the second model and the third model was the type of element to model the RC walls. In the second model, the RC walls were modeled by 8-node elastic shell elements, as shown in Figure 6.25. In the third model, the RC walls were modeled by the CSMM-based shell elements, as shown in Figure 6.26. The results obtained from the analyses of the three analytical models were compared to each other and with the experimental data in the positive direction, as shown in Figure 6.27.

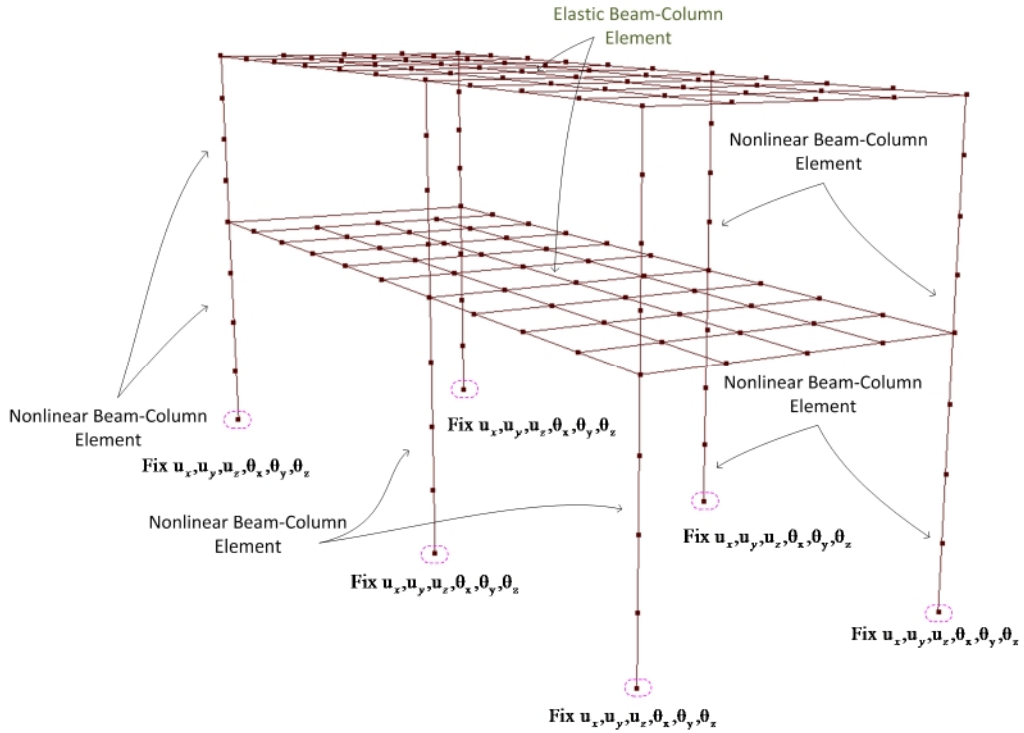


Figure 6.24 Finite element mesh of the building specimen (Model 1: Frame only)

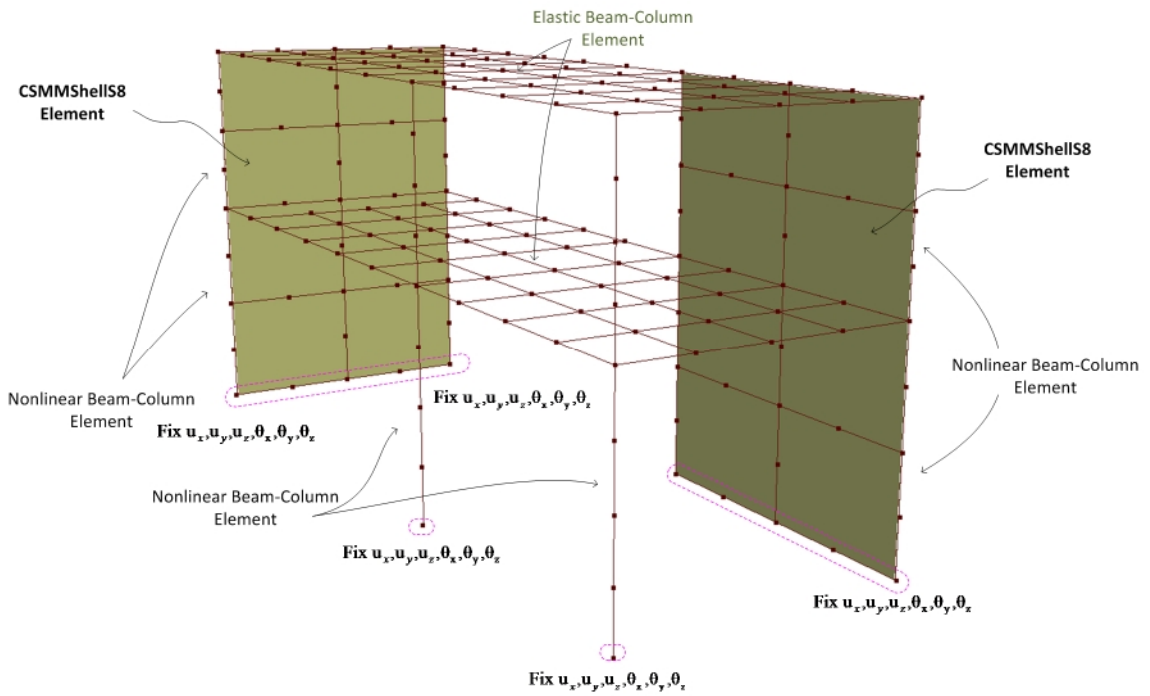
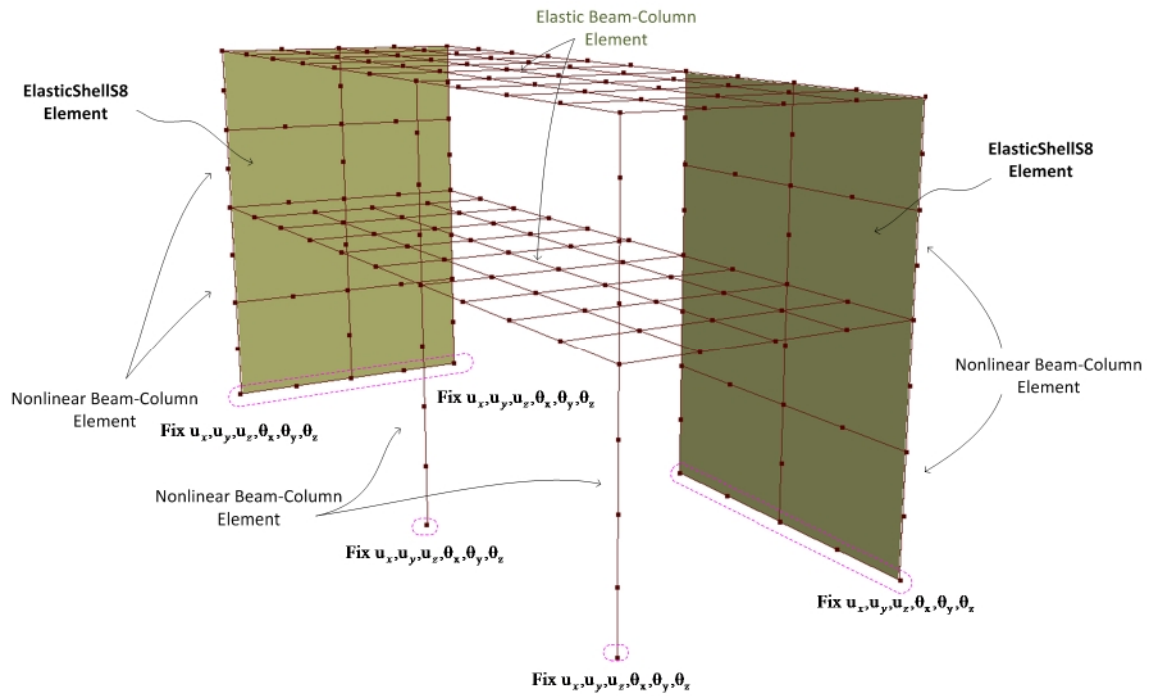


Figure 6.25 Finite element mesh of the building specimen (Model 2: Frame + Elastic Wall)



**Figure 6.26 Finite element mesh of the building specimen (Model 3: Frame + CSMM Wall)**

The result obtained from the first model, which is the dotted curve in Figure 6.27, showed a much lower strength as well as stiffness compared to the experimental result. This result was expected because it only represented the contribution of the RC frame in the total loading resistance of the whole building. By investigating this result, it could be seen that the contribution of the RC wall in the total loading resistance of the whole building was extremely large. The existence of the RC walls increased both the stiffness and strength of the building by approximate 40%.

The result obtained from the second model is illustrated as the dashed curve in Figure 6.27. This model predicted well the behavior of the specimen up to the displacement of 10 mm. After that the model overestimated the stiffness and the strength of the response of the building specimen. The displacement of 10 mm, both the stiffness of the predicted curve and the experimental curve started to change significantly. This change in stiffness

could be explained that one or many of the components of the structure started to behave inelastically. Because the frame was modeled by the nonlinear-beam-column element with fiber sections, it was assumed that the inelastic behavior occurring in the frame could be captured. Hence, the difference between the analytical result and the experimental result might have been caused by the inelastic of the RC wall, which could not be predicted by the elastic shell element.

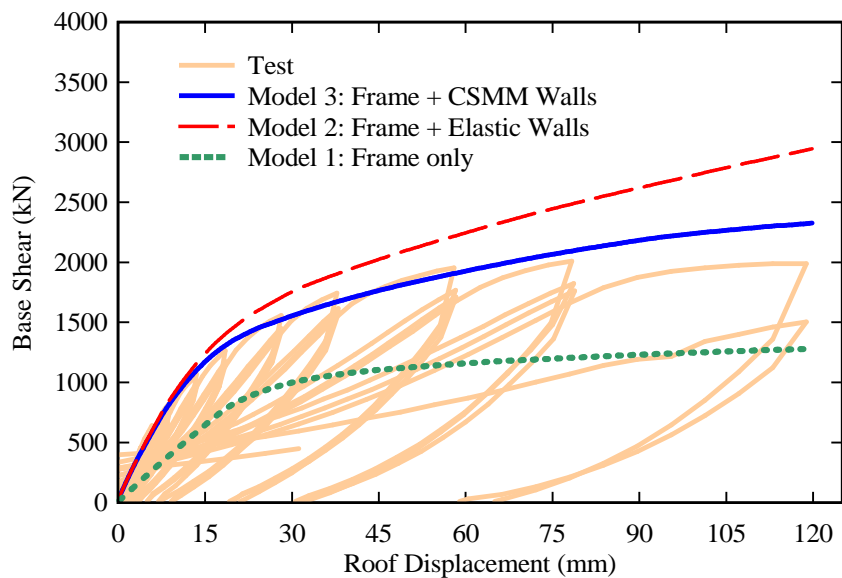


**Figure 6.27 Effect of RC walls on the base shear versus second-tory displacement relationship**

The result obtained from the third model is illustrated as the solid curve in Figure 6.27. In this model, because the CSMM-based shell element was able to predict accurately the inelastic behavior of RC walls, this model predicted the behavior of the specimen in both the elastic and inelastic parts up to the displacement of 50 mm. The results of the third model showed that the CSMM-based shell element was an appropriate a model for RC walls and the analytical model combining nonlinear-beam-column element and CSMM-

based shell element could serve as a powerful tool to predict the behavior of entire RC building structure. After the displacement reached 50 mm, the base shear of the building almost remained constant and slightly decreased. The experimental test of the specimen in this region showed some damage in some components. The redistribution of resistances among the damaged and undamaged components caused the base shear cannot increase. More rigorous models to account for the damage of the structure will be discussed in the next sections.

#### **6.4.2 Effect of Shear-governed Columns**

As reported in the test description, the columns 1-2F and 2-2F on the second floor were designed to have a low height-to-width ratio and little amount of transverse reinforcement so that it would be critical in shear behavior. The experimental results showed that both columns were damaged due to shear failure. This damage of the columns caused the base shear to remain at a constant value for which the previous models could not predict because the nonlinear-beam-column element used in the models was not effective for the simulation of the shear-critical columns. To have better predict, which can account for the shear behavior of column, the fourth model was created, as shown in Figure 6.28. This model was similar to the third model except that the two shear-critical columns were modeled by a series of CSMM-based shell elements as presented in Section 6.3.4. The results obtained from the third and fourth models are illustrated as the solid and dashed curves in Figure 6.29, respectively. The figure shows that the fourth model had better prediction compared with the third model. The region of the total base shear versus the displacement curve, in which the base shear remained constant, was captured.

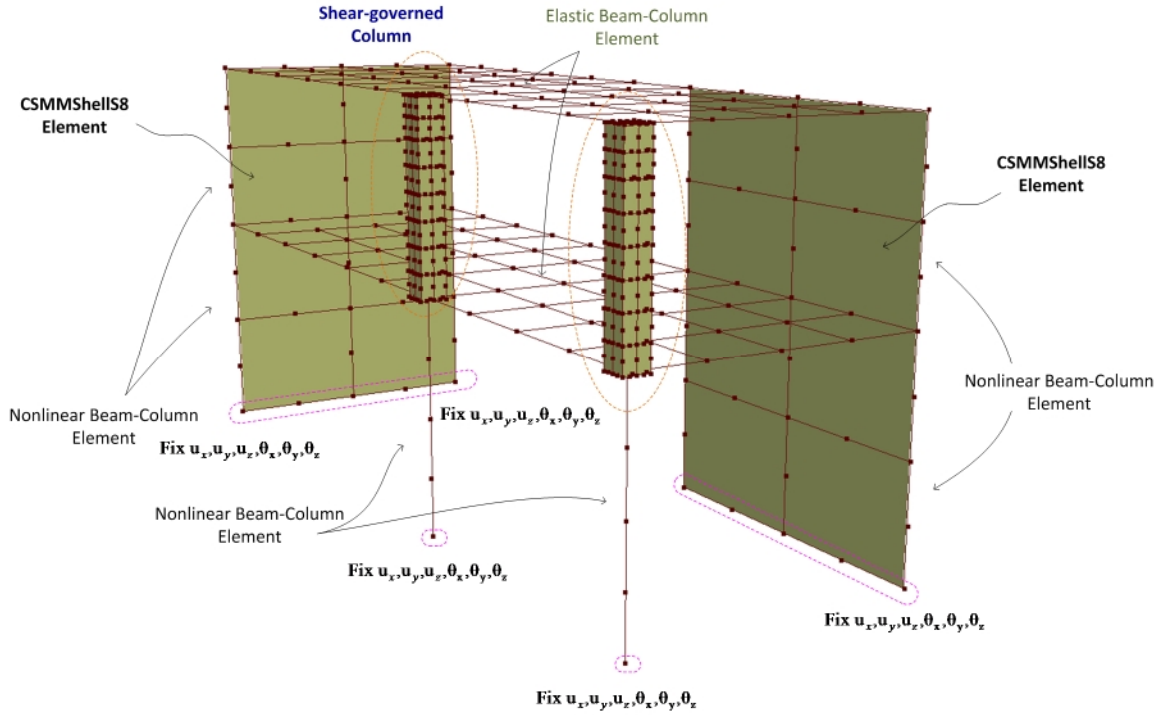


**Figure 6.28** Finite element mesh of the building specimen (Model 4: Frame + CSMM Wall + Shear-governed column)

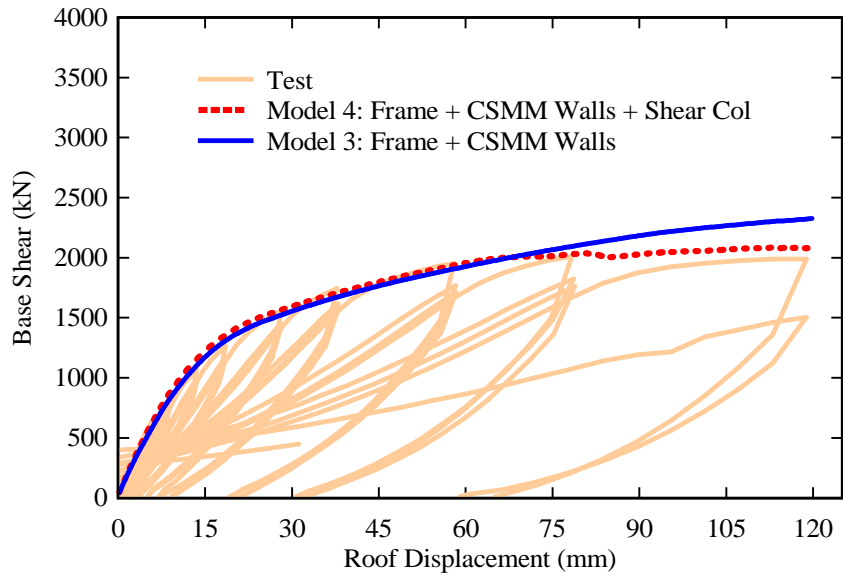


**Figure 6.29** Effect of the shear-governed column on the base shear versus the roof displacement relationship

### 6.4.3 Effect of Buckling Columns

The fifth model was created to investigate the effect of buckled columns on the total base shear and displacement curve. Two columns on the first floor were modeled using the low-cycle fatigue steel material, as shown in Figure 6.30. The results obtained from the fifth model are illustrated as the solid curve in Figure 6.31. As shown in the figure, this model had the capability of predicting the descending part of the total base shear and displacement curve. This model took into account all the possible failure mechanisms and, therefore, was an appropriated analytical model to simulate the entire hysteretic response of the building specimen.

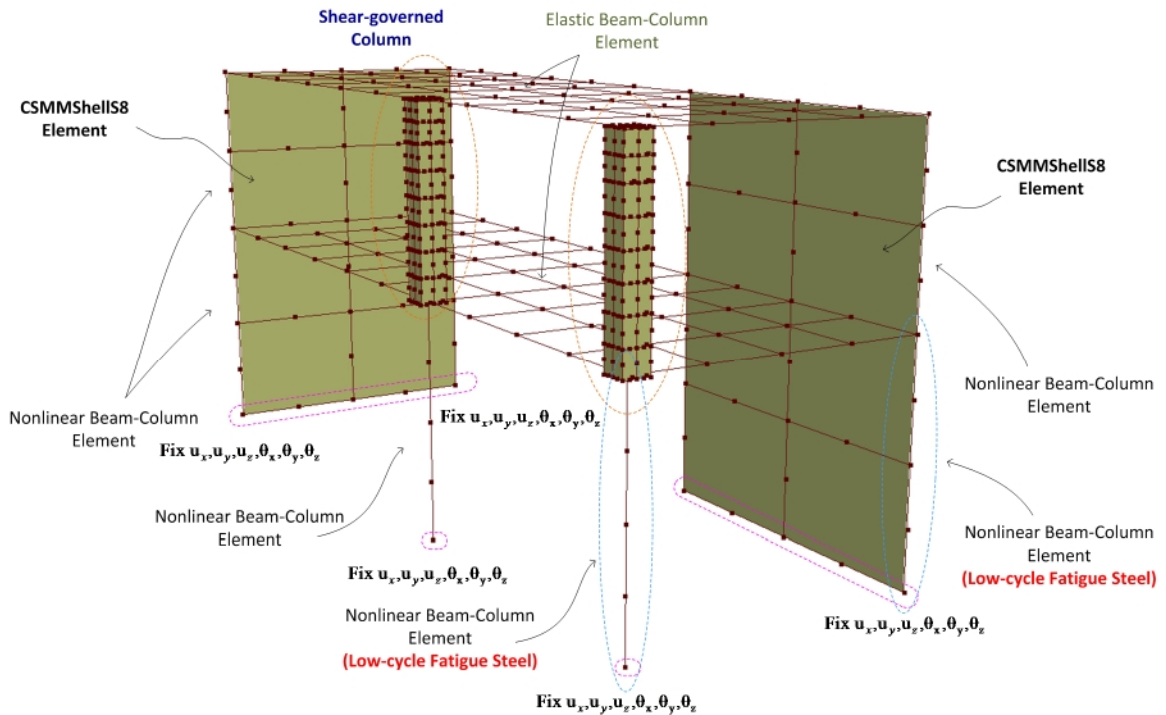
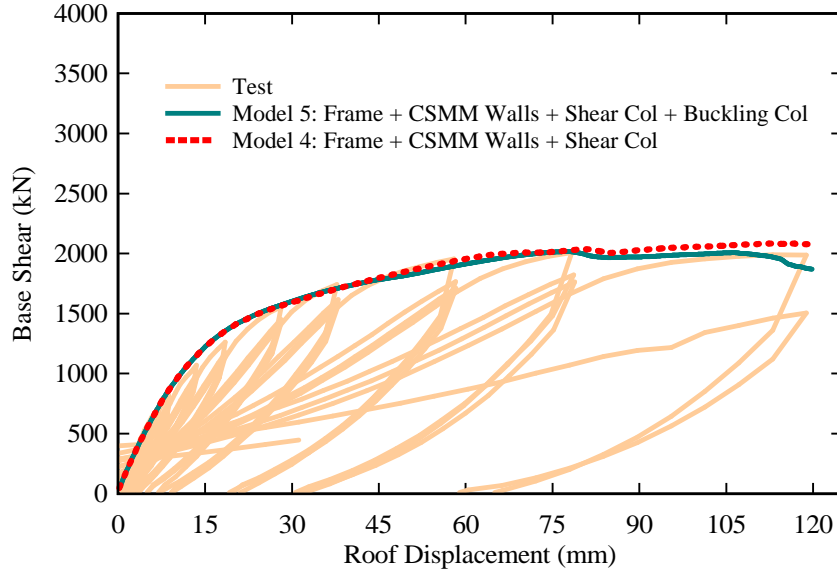


Figure 6.30 Finite element mesh of the building specimen (Model 5: frame + CSMM wall + shear-governed & buckled column)



**Figure 6.31 Effect of buckling columns on the base shear versus roof displacement relationship**

## 6.5 Comparison of Analytical Result with Experimental Outcome

The hysteretic response of the specimen was predicted using the fifth model, which was discussed in Section 6.4.3. The finite element mesh of the model is shown in Figure 6.32. The analytical results were compared with the experimental data regarding the total base shear and the roof displacement, as shown in Figure 6.32. The analytical result and the experimental result are illustrated by solid curve and dotted curve, respectively. The analytical result was shown to provide a good correlation with the experimental data in the positive direction, including the initial stiffness, the ultimate strength, and strength degradation in the descending branch. The analytical model also predicted accurately the pinching effect and the unloading path of the specimen. The model, however, could not predict accurately the ultimate strength of the specimen in the negative direction.

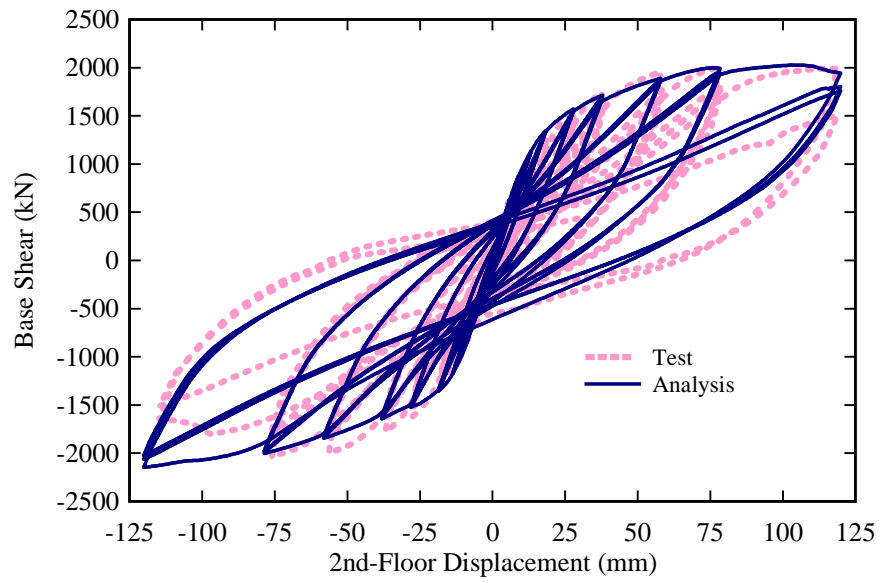


**Figure 6.32 Effect of RC walls on the base shear versus roof displacement relationship**

# CHAPTER 7

## SUMMARY AND CONCLUSIONS

### 7.1 Summary

In this dissertation, a new shell element, the CSMM-based shell element, was developed and implemented into the finite element program SCS-3D to predict the nonlinear behavior of RC shell-type structures. The research was conducted by a model-based simulation approach that included four steps: modeling, implementation, validation, and application. The CSMM-based shell element was developed by utilizing formulation of the degenerated shell theory with layered approach (Cook, 2002; Hinton & Owen, 1984), and taking into account the Cyclic Softened Membrane Model (CSMM) (Hsu & Mo, 2010). The formulations of CSMM were extended from 2D to 3D so that they could be implemented into each layer of the shell element. The model based simulation (MBS) approach was proposed by the National Science Foundation (Chen 2000) and was considered to be the focus of structural engineering research. Therefore, the entire study in this research could be interpreted as a MBS for reinforced concrete shell structures subjected to static and reversed cyclic loadings.

The capacity in predicting the behavior of RC shell structures of the analytical models using the developed CSMM-based shell element was verified by experimental data from several large-scale tests of RC shell structures subjected to seismic loadings. The structures selected for validations included a panel tested under pure shear (Mansour & Hsu, 2005a; Pang & Hsu, 1996), panels tested under pure bending and combination of shear and bending (Polak & Vecchio, 1994), a 3D RC cylindrical tank (Maekawa,

Okamura, & Pimanmas, 2003), a RC shear wall (Palermo & Vecchio, 2002), and six RC rectangular and circular hollow bridge piers (Yeh & Mo, 1999; Yeh, Mo, & Yang, 2001).

The developed CSMM-based shell element was applied to investigate the structural behavior of the reinforced concrete nuclear containment vessel under seismic loadings. Two 1/13-scaled RCCV specimens were designed and tested at the National Center for Research on Earthquake Engineering (NCREE). The behaviors of the specimens were experimentally investigated. The nonlinear finite element analysis of the nuclear containment vessel specimens was conducted through the finite element program SCS-3D using the proposed CSMM-based shell element. The analytical investigations were divided into two steps. In the first step, preliminary analyses were performed to blindly predict the behaviors of the test specimens. The analytical results of the first step were used to design the specimens to ensure that their strengths and deformations did not exceed the capacity of the testing equipment. In the second step, the experimental data was used to calibrate the analytical model to obtain better simulations.

The versatile application of the developed finite element analysis program SCS-3D was further investigated by the modeling of a two-story unsymmetrical reinforced concrete building specimen subjected to bi-directional reserved cyclic loadings. The analytical model of the two-story unsymmetrical RC building specimen was created by combining the proposed CSMM-based shell element and the nonlinear beam-column element, which is available in OpenSees. The analytical results were compared with the test data.

## 7.2 Conclusions

The following general conclusions are drawn from this study:

The developed CSMM-based shell element could be used to create analytical models that accurately predict the inelastic behavior of RC shell structures. Several types of RC structures were selected to validate the analytical models including RC panels, a RC cylindrical tank, a 3D RC shear wall, and circular and rectangular RC hollow bridge piers. Agreements were obtained when comparing analytical results with experimental data. Overall, the primary backbone curves, the initial stiffness, the peak strength, the descending branch, and the failure characteristics were accurately predicted. The hysteretic behavior provided accurate measurements of the pinching effect, the residual displacement, the ductility, and the energy dissipation capacity. Hence, the new developed CSMM-based shell element could be a powerful and versatile analytical tool for studying the cyclic response of both curved and flat RC shell structures.

In the analysis of RC shell structures, the modified Newton-Raphson method with Krylov subspace acceleration, in which the tangent stiffness matrix was updated at every iteration, provided stable and smooth solutions with an appropriate convergence rate. The analysis using displacement control scheme was stable and had the ability to predict the entire hysteretic load and displacement curves of the structures, including both ascending and descending parts while the load control scheme could only predict the ascending branch.

The 8-node degenerated curved shell element adopted for the development of the CSMM-based shell element was proved in the literature to provide appropriate accuracy for both the curved and flat shell structures. One disadvantage of using the element was

that the shear-locking phenomenon existed in the element when applied to the shell structures with a thin thickness. However, no locking phenomenon was experienced in the analysis of the RC shell structures in this study because the RC shell structures investigated in this study had either thick or moderate thin thickness.

The constitutive model of reinforced concrete material used for the CSMM-based shell element was based on the Cyclic Softening Membrane Model (CSMM). This model was developed based on the concept of a smeared-crack model in which the cracked concrete and the embedded steel bars were considered as a continuum. Therefore, it was not necessary to use a small mesh size of elements to achieve more accurate solutions.

Numerical problems might have been encountered when performing an analysis of the RC shell structures using the proposed finite element model. Sometimes getting convergence was difficult when the response of the structure approached the cracking point due to the discontinuity in the tensile stress-strain curve of the concrete model. These numerical problems could be overcome by changing the increment size or by increasing the number of iteration in most cases.

The confined CSMM, which took into account the confinement effect of concrete, was able to predict the structural behavior of RC hollow bridge piers, which have special detailing with confinement transverse reinforcement to increase strength and ductility. The model accurately captured the different failure modes of the structures.

The developed CSMM-based shell element could be combined with the nonlinear beam-column element, which is available in OpenSees, to create an analytical model that can accurately predict the inelastic behavior of a two-story unsymmetrical reinforced concrete building specimen subjected to bi-directional reserved cyclic loadings.

A visualization module was developed for the finite element program SCS-3D. Using this module, we can plot the contour diagram of stress and strain of the concrete and steel at each layer over the entire shell structure. The module helps us to identify whether yielding happens in steel or concrete crushes during the response of the shell structure. Also, we can determine the exact location of the specimens where the yielding and damage happen.

With respect to the experimental and analytical results of the reinforced concrete nuclear containment vessel specimens subjected to reversed cyclic loading, the following conclusions can be made:

Two 1/13-scale nuclear containment vessel specimens were successfully designed and tested under reversed cyclic loading. Both shear and flexural cracks developed in the specimen during the tests. Specimen No. 1 had sliding shear cracks occur at the top of the specimen.

In the two test specimens, the vertical and circumferential steel bars both yielded during the tests and indicated that the specimens had ductile behavior. The first yielding points of the vertical and circumferential steel bars were close to each other. The average ductility of the two test specimens was observed to be approximately 2.5.

The first specimen failed due to the sliding shear failure, and the second specimen failed due to web shear failure.

The analytical model accurately predicted the behavior of the specimens including the cracking patterns, the first yielding points, yielding distributions of the steel bars, and the overall hysteretic loops of the load and displacement curve.

The analytical model accurately predicted the two failure modes, the sliding shear and web shear failure. However, the analytical model overestimated the initial stiffness and the slope of the descending branch of the experimental hysteretic loops.

### **7.3 Recommendations for future research**

Related to this research, several other subjects have been identified that need further investigation. The experimental and analytical research needs are summarized below.

The CSMM-base shell element currently is being developed to be used for RC shell structures whose response is dominated by in-plane shear and out-of-plane bending. The out-of-plane shear effect such as punching shear has not been taken into account.

The CSMM-base shell element currently is to be used only for RC shell structures. The element should be extended to be used for the shell structures with different materials such as prestressed concrete or steel-fiber concrete by modifying the current constitutive model of the implemented material.

The constitutive law of reinforced concrete material used for the developed CSMM-base shell element is time-independent. Therefore, time-dependent effects, such as creep, shrinkage, and relaxation of prestressing steel, should be considered in the future. These effects need to be factored into the analysis of prestressed RC shell structures.

The loading rate effect should be considered in the constitutive law of reinforced concrete material used for the developed CSMM-base shell element so that the element can be used for the analyses of RC shell structures under impact loading.

A new analytical model, which can take into account the slip deformation of steel bars at the top and bottom of the specimens, needs to be developed so that the initial stiffness of the specimen can be better predicted.

The CSMM-based shell element was derived based on the small displacement assumption in which the strains were taken as a first-order derivative of the displacements. This assumption provided suitable predictions for the RC shell structures investigated in this study. In the future, the CSMM-based shell element derived based on large displacement assumption should be examined. Numerical problems encountered in the analysis should be further studied by improving the solution algorithm.

This research concentrated in the simulations of RC shell structures under static loading. However, the CSMM-based shell element was developed to be used for both static and dynamic loading. More research should be conducted to examine the capacity of the shell element for predicting the behavior of RC shell structures under dynamic loading.

More tests on the RC nuclear containment vessels with more considering parameters should be performed to fully understand and to find the way to improve its behavior under seismic loading. The suggested test parameters include the aspect ratios such as the height-to-diameter ratio and the diameter-to-thickness ratio, the compressive strength of concrete, the mount, and the orientation of reinforcement. Dynamic shaking table tests should be carried out to understand the behavior of the RC nuclear containment under real earthquake loading.

## REFERENCES

- Adebar, P., & Collins, M. P. (1994). Shear Design of Concrete Offshore Structures. *ACI Structural Journal*, 91(3).
- Ahmad, S., Irons, B. M., & Zienkiewicz, O. C. (1970). Analysis of Thick and Thin Shell Structures by Curved Finite Elements. *International Journal for Numerical Methods in Engineering*, 2(3), 419-451.
- Ayoub, A. (1995). *Nonlinear Finite Element Analysis of Reinforced Concrete Sub Assemblages*. (PhD dissertation), University of California, Berkeley, Dept. of Civil Engineering.
- Ayoub, A., & Filippou, F. C. (1998). Nonlinear Finite-Element Analysis of RC Shear Panels and Walls. *Journal of Structural Engineering*, 124(3), 298-308.
- Balakrishnan, S., & Murray, D. W. (1988a). Concrete Constitutive Model for NLFE Analysis of Structures. *Journal of Structural Engineering, ASCE*, 114(7), 1449-1466.
- Balakrishnan, S., & Murray, D. W. (1988b). Strength of Reinforced Concrete Panels. *Canadian Journal of Civil Engineering*, 15(5), 900-911.
- Balakrishnan, S., & Murray, D. W. (1988c). Prediction of R/C Panels and Deep Beam Behavior by NLFEA. *Journal of Structural Engineering, ASCE*, 114(10), 2323-2342.
- Banerjee, A. K., & Holley, M. J. (1978). Research Requirements for Improved Design of Reinforced Concrete Containment Structures. *Nuclear Engineering and Design*, 50, 33-39.

- Bathe, K. J., & Bolourchi, S. (1980). A Geometric and Material Nonlinear Plate and Shell Element. *Computers & structures*, 11(1), 23-48.
- Batoz, J. L., & Dhat, G. (1979). Incremental Displacement Algorithms for Nonlinear Problems. *International Journal for Numerical Methods in Engineering*, 14, 1262-1266.
- Belarbi, A., & Hsu, T. T. C. (1994). Constitutive Laws of Concrete in Tension and Reinforcing Bars Stiffened By Concrete. *ACI Structural Journal*, 91(4), 9.
- Belarbi, A., & Hsu, T. T. C. (1995). Constitutive Laws of Softened Concrete in Biaxial Tension Compression. *ACI Structural Journal*, 92(5), 562-573.
- Belletti, B., Cerioni, R., & Iori, I. (2001). Physical Approach for Reinforced-Concrete (PARC) Membrane Elements. *Journal of Structural Engineering*, 127(12), 1412-1426.
- Carlson, N. N., & Miller, K. (1998). Design and Application of A Gradient-weighted Moving Finite Element Code I: in One Dimension. *SIAM Journal of Science Computing*, 19(3), 728-765.
- Cedolin, L., & Dei Poli, S. (1977). Finite Element Studies of Shear-Critical R/C Beams. *Journal of the Engineering Mechanics Division*, 103(3), 395-410.
- Cervera, M., Hinton, E., & Hassan, O. (1987). Nonlinear Analysis of Reinforced Concrete Plate and Shell Structures using 20-noded Isoparametric Brick Elements. *Computers & structures*, 25(6), 845-869.
- Chan, E. C. (1983). *Nonlinear Geometric, Material and Time Dependent Analysis of Reinforced Concrete Shells with Edge Beams*. (PhD. Dissertation), University of California, Berkeley.

- Collins, M. P., & Vecchio, F. (1982). The Response of Reinforced Concrete to In-plane Shear and Normal Stresses. *University of Toronto*.
- Cook, R. D. (2002). *Concepts and Applications of Finite Element Analysis*: Wiley. com.
- Crisfield, M. A. (1981). A Fast Incremental/iterative Solution Procedure That Handles ‘Snap Through’. *Computers and Structures*, 13, 55-62.
- Crisfield, M. A. (1991). *Non-Linear Finite Element Analysis of Solids and Structures* (Vol. 1, Essentials): Wiley: Chichester.
- Crisfield, M. A., & Wills, J. (1989). Analysis of R/C Panels Using Different Concrete Models. *Journal of Engineering Mechanics, ASCE*, 115(3), 578-597.
- Fenves, G. L. (2001). Annual Workshop on Open System for Earthquake Engineering Simulation. *Pacific Earthquake Engineering Research Center, UC Berkeley*, <http://opensees.berkeley.edu/>.
- Gao, X. D. (1999). *Framed Shear Walls under Cyclic Loading*. University of Houston, Houston.
- Haisler, W. E., Stricklin, J. A., & Key, J. E. (1977). Displacement Incrementation in Non-linear Structural Analysis by the Self-Correcting Method. *International Journal for Numerical Methods in Engineering*, 11, 3-10.
- Hand, F. R., Pecknold, D. A., & Schnobrich, W. C. (1972). A Layered Finite Element Nonlinear Analysis of Reinforced Concrete Plates and Shells: University of Illinois Engineering Experiment Station. College of Engineering. University of Illinois at Urbana-Champaign.

- Harada, M., Onituka, S., Adachi, M., & Matsuo, T. (2001). Experimental Study on Deformation Performance of Cylindrical Reinforced Concrete Structure. *Proc. of JCI*, 23(3), 1129-1134.
- Hinton, E., & Owen, D. R. J. (1984). *Finite Element Software for Plates and Shells* (Vol. 91): Pineridge Press Swansea, UK.
- Hsu, T. T. C., Belarbi, A., & Xiaobo, P. (1995). A Universal Panel Tester. *Journal of testing and evaluation*, 23(1), 41-49.
- Hsu, T. T. C., & Mo, Y. L. (2010). *Unified Theory of Concrete Structures*: John Wiley & Sons.
- Hsu, T. T. C., & Zhang, L. X. (1996). Tension Stiffening in Reinforced Concrete Membrane Elements. *ACI Structural Journal*, 93(1), 108-115.
- Hsu, T. T. C., & Zhang, L. X. (1997). Nonlinear Analysis of Membrane Elements by Fixed-Angle Softened-Truss Model. *ACI Structural Journal*, 94(5), 483-492.
- Hsu, T. T. C., & Zhu, R. R. H. (2002). Softened Membrane Model for Reinforced Concrete Elements in Shear. *ACI Structural Journal*, 99(4), 460-469.
- Hu, H. T., & Schnobrich, W. C. (1991). Nonlinear Finite Element Analysis of Reinforced Concrete Plates and Shells under Monotonic Loading. *Computers & structures*, 38(5), 637-651.
- Hughes, T. J. R., & Liu, W. K. (1981). Nonlinear Finite Element Analysis of Shells: Part I. Three-dimensional Shells. *Computer Methods in Applied Mechanics and Engineering*, 26(3), 331-362.

- Ile, N., & Reynouard, J. M. (2000). Nonlinear Analysis of Reinforced Concrete Shear Wall under Earthquake Loading. *Journal of Earthquake Engineering*, 4(02), 183-213.
- Irons, B. M. (1976). The Semi-loof Shell Elements. In D. G. Ashwell & R. H. Gallagher (Eds.), *Finite Elements for Thin Shells and Curved Members* (pp. 25): John Wiley, Chichester, Sussex.
- Izumo, J., Shin, H., Maekawa, K., & Okamura, H. (1992). An Analytical Model for RC Panels Subjected to In-plane Stresses. *Concrete shear in earthquakes. Elsevier Applied Science, London and New York*, 206-215.
- Javaherian, H., Dowling, P. J., & Lyons, L. P. R. (1980). Nonlinear Finite Element Analysis of Shell Structures using the Semi-Loof Element. *Computers & structures*, 12(1), 147-159.
- Karsan, I. D., & Jirsa, J. O. (1969). Behavior of Concrete under Compressive Loadings. *Journal of the Structural Division, ASCE*, 95(ST 12).
- Kaufmann, W., & Marti, P. (1998). Structural Concrete: Cracked Membrane Model. *Journal of Structural Engineering*, 124(12), 1467-1475.
- Kent, D. C., & Park, R. (1971). Flexure Members with Confined Concrete. *Journal of the Structural Division, ASCE*, 97(7), 1969-1990.
- Kim, T. H., Lee, K. M., & Shin, H. M. (2002). Nonlinear Analysis of Reinforced Concrete Shells using Layered Elements with Drilling Degree of Freedom. *ACI Structural Journal*, 99(4).
- Kupfer, H., Hilsdorf, H. K., & Rusch, H. (1969). Behavior of Concrete Under Biaxial Stresses. *American Concrete Institute*, 66(8), 656-666.

- Kwon, M., & Spacone, E. (2002). Three-Dimensional Finite Element Analyses of Reinforced Concrete Columns. *Computers & structures*, 80(2), 199-212.
- Laskar, A. (2009). *Shear Behavior and Design of Prestressed Concrete Members*: University of Houston.
- Lee, H. P. (2011). Shell Finite Element of Reinforced Concrete for Internal Pressure Analysis of Nuclear Containment Building. *Nuclear Engineering and Design*, 241, 515-525.
- Leombruni, P., Buyukozturk, O., & Connor, J. J. (1979). Analysis of Shear Transfer in Reinforced Concrete with Application to Containment Wall Specimens: Massachusetts Inst. of Tech., Cambridge (USA).
- Li, B., & Maekawa, K. (1988). Contact Density Model for Stress Transfer across Cracks in Concrete. *Concrete Engineering, JCI*, 26(1), 123-137.
- Macneal, R. H., & Harder, R. L. (1988). A Refined Four-Noded Membrane Element with Rotational Degrees of Freedom. *Computers & structures*, 28(1), 75-84.
- Maekawa, K., Okamura, H., & Pimanmas, A. (2003). *Non-linear Mechanics of Reinforced Concrete*: CRC Press.
- Mander, J. B., Panthaki, F. D., & Kasalanti, A. (1994). Low Cycle Fatigue Behavior of Reinforcing Steel. *Journal of Structural Engineering*, 6(4), 453-468.
- Mansour, M. (2001). *Behavior of Reinforced Concrete Membrane Elements under Cyclic Shear: Experiment to Theory*. University of Houston, Houston.
- Mansour, M., & Hsu, T. T. C. (2005). Behavior of Reinforced Concrete Elements under Cyclic Shear: Part 1 – Experiments. *Journal of Structural Engineering, ASCE*, 131(1), 44-53.

- Mansour, M., & Hsu, T. T. C. (2005a). Behavior of Reinforced Concrete Elements under Cyclic Shear. I: Experiments. *Journal of Structural Engineering*, 131(1), 44-53.
- Mansour, M., & Hsu, T. T. C. (2005b). Behavior of Reinforced Concrete Elements under Cyclic Shear. II: Theoretical Model. *Journal of Structural Engineering, ASCE*, 131(1), 54-65.
- Mansour, M., Lee, Y. H., & Hsu, T. T. C. (2001). Cyclic Stress-Strain Curves of Concrete and Steel Bars in Membrane Elements. *Journal of Structural Engineering, ASCE*, 127(12), 1402-1411.
- Mo, Y. L., Zhong, J., & Hsu, T. T. C. (2008). Seismic Simulation of RC Wall-type Structures. *Engineering Structures*, 30(11), 3167-3175.
- Okamura, H., Maekawa, K., & Izumo, J. (1987). *RC plate element subjected to cyclic loading*. Paper presented at the IABSE Colloquium Delft.
- OpenSees. (2013). *Annual Workshop on Open System for Earthquake Engineering Simulation*. Paper presented at the Pacific Earthquake Engineering Research Center, UC Berkeley.
- Palermo, D., & Vecchio, F. J. (2002). Behavior of Three-dimensional Reinforced Concrete Shear Walls. *ACI Structural Journal*, 99(1).
- Palermo, D., & Vecchio, F. J. (2003). Compression Field Modeling of Reinforced Concrete Subjected to Reversed Loading: Formulation. *ACI Structural Journal*, 100(5), 616-625.
- Pang, X. B. (1991). *Constitutive Laws of Reinforced Concrete in Shear*. (PhD dissertation), University of Houston, Houston.

- Pang, X. B., & Hsu, T. T. C. (1995). Behavior of Reinforced Concrete Membrane Elements in Shear. *ACI Structural Journal*, 92(6), 665-679.
- Pang, X. B., & Hsu, T. T. C. (1996a). Fixed-Angle Softened-Truss Model for Reinforced Concrete. *ACI Structural Journal*, 93(2), 197-207.
- Pang, X. B., & Hsu, T. T. C. (1996b). Fixed Angle Softened Truss Model for Reinforced Concrete. *ACI Structural Journal*, 93(2), 197-207.
- Polak, M. (1998). Shear Analysis of Reinforced Concrete Shells using Degenerate Elements. *Computers & structures*, 68(1), 17-29.
- Polak, M. A. (1992). Nonlinear Analysis of Reinforced Concrete Shell.
- Polak, M. A., & Vecchio, F. (1993). Nonlinear Analysis of Reinforced-Concrete Shells. *Journal of Structural Engineering*, 119(12), 3439-3462.
- Polak, M. A., & Vecchio, F. J. (1994). Reinforced Concrete Shell Elements Subjected to Bending and Membrane Loads. *ACI Structural Journal-American Concrete Institute*, 91(3), 261-268.
- Ramakrishan, V., & Anathanarayana, Y. (1968). Ultimate Strength of Deep Beams in Shear. *ACI Journal*, 65, 87-98.
- Reddy, J. N. (2004). *Mechanics of Laminated Composite Plates and Shells: Theory and Analysis/JN Reddy*: CRC press.
- Riks, E. (1972). The Application of Newton's Method to the Problem of Elastic Stability. *Journal of Applied Mechanics*, 39, 1060-1066.
- Scordelis, A. C., & Chan, E. C. (1987). Nonlinear Analysis of Reinforced Concrete Shells. *ACI Special Publication*, 98.

- Sheikh, S. A., & Uzumeri, S. (1982). Analytical Model for Concrete Confinement in Tied Columns. *Journal of the Structural Division*, 108(12), 2703-2722.
- Shima, H., Chou, L. L., & Okamura, H. (1987). Micro and Macro Models for Bond in Reinforced Concrete. *Journal of the Faculty of Engineering*, 39(2), 133-194.
- Shin, H., Maekawa, K., & Okamura, H. (1992). Analytical Models for Reinforced Concrete Shear Walls under Reversed Cyclic Loading. *Concrete shear in earthquakes. Elsevier Applied Science, London and New York*, 289-298.
- Sittipunt, C., & Wood, S. L. (1995). Influence of Web Reinforcement on the Cyclic Response of Structural Walls. *ACI Structural Journal*, 92(6), 745-756.
- Song, H., Shim, S., Byun, K., & Maekawa, K. (2002). Failure Analysis of Reinforced Concrete Shell Structures using Layered Shell Element with Pressure Node. *Journal of Structural Engineering*, 128(5), 655-664. doi: doi:10.1061/(ASCE)0733-9445(2002)128:5(655)
- Sunidja, H., Foutch, D. A., & Gamble, W. L. (1982). Response of Prestressed Concrete Plate-Edge Column Connections: University of Illinois Engineering Experiment Station. College of Engineering. University of Illinois at Urbana-Champaign.
- Taylor, R. L. (2000). *FEAP - A Finite Element Analysis Program, Version 7.2 Users Manual* (Vol. 1 and 2).
- Tseng, C.-C., Hwang, S.-J., Mo, Y., Yeh, Y.-K., & Lee, Y.-T. (2009). *Experiment of Torsionally-Coupled RC Building Subjected to Bi-directional Cyclic Loading*. Paper presented at the Proceedings of the 3rd International Conference on Advances in Experimental Structural Engineering. San Francisco.
- Ugural, A. C. (2009). *Stresses in Beams, Plates, and Shells*: CRC Press.

- Vecchio, F., & Collins, M. P. (1981a). *Stress-Strain Characteristics of Reinforced Concrete in Pure Shear*. Paper presented at the Reports of the Working Commissions (International Association for Bridge and Structural Engineering).
- Vecchio, F. J. (2000). Disturbed Stress Field Model for Reinforced Concrete: Formulation. *Journal of Structural Engineering*, 126(9), 1070-1077.
- Vecchio, F. J. (2001). Disturbed Stress Field Model for Reinforced Concrete: Implementation. *Journal of Structural Engineering*, 127(1), 12-20.
- Vecchio, F. J., & Collins, M. P. (1981b). Stress-strain Characteristics of Reinforced Concrete in Pure Shear. *IABSE Colloquium, Advanced Mechanics of Reinforced Concrete, International Association of Bridge and Structural Engineering, Delft*, 211-225.
- Vecchio, F. J., & Collins, M. P. (1982). Response of Reinforced Concrete to In Plane Shear and Normal Stresses (pp. 211-225): University of Toronto, Department of Civil Engineering.
- Wang, J. (2006). *Constitutive Relationships of Prestressed Concrete Membrane Elements*. (Doctoral), University of Houston.
- Wang, T., Bradford, M., & Gilbert, I. (2005). Short-term Experimental Study of a Shallow Reinforced Concrete Parabolic Arch. *Australian Journal of Structural Engineering*, 6(1), 53.
- Xiang, H. J., Mo, Y. L., & Hsu, T. T. C. (2012). Seismic Simulation of RC Wall-type Structures using Softened Shell Model.
- Yamamoto, T., & Vecchio, F. J. (2001). Analysis of Reinforced Concrete Shells for Transverse Shear and Torsion. *ACI Structural Journal*, 98(2), 191-200.

- Yeh, Y. K., & Mo, Y. L. (1999). Full Scale Tests on Ductility, Shear Strength and Retrofit of Reinforced Concrete Hollow Columns (I).
- Yeh, Y. K., Mo, Y. L., & Yang, C. Y. (2001). Seismic Performance of Hollow Circular Bridge Piers. *ACI Structural Journal*, 98(6).
- Zhang, Y. X., Bradford, M. A., & Gilbert, R. I. (2007). A Layered Cylindrical Quadrilateral Shell Element for Nonlinear Analysis of RC Plate Structures. *Advances in Engineering Software*, 38(7), 488-500.
- Zhong, J. (2005). *Model-Based Simulation of Reinforced Concrete Plane Stress Structures*. University of Houston, Houston.
- Zhu, R. R. H., & Hsu, T. T. C. (2002). Poisson Effect in Reinforced Concrete Membrane Elements. *ACI Structural Journal*, 99(5), 631-640.
- Zhu, R. R. H., Hsu, T. T. C., & Lee, J. Y. (2001). Rational Shear Modulus for Smeared-Crack Analysis of Reinforced Concrete. *ACI Structural Journal*, 98(4).
- Zienkiewicz, O. C. (1971). Incremental Displacement in Non-Linear Analysis. *International Journal for Numerical Methods in Engineering*, 3, 587-592.
- Zienkiewicz, O. C., & Taylor, R. L. (2005). *The Finite Element Method for Solid and Structural Mechanics*: Butterworth-heinemann.
- Zienkiewicz, O. C., Taylor, R. L., & Too, J. M. (1971). Reduced Integration Technique in General Analysis of Plates and Shells. *International Journal for Numerical Methods in Engineering*, 3(2), 275-290.
- Zingoni, A. (1997). *Shell Structures in Civil and Mechanical Engineering: Theory and Closed-Form Analytical Solutions*: Thomas Telford.

# APPENDIX A

## INPUT FILE OF RCCV SPECIMEN 1

The input file for the reserved cyclic analysis of the nuclear containment specimen No. 1 described in Chapter 5 is presented as below.

---

```
# Input file for RCCV1 Specimen

# Unit: N, mm, sec, MPa

# Create ModelBuilder
model BasicBuilder -ndm 3 -ndf 6

# Set dimensions and mesh for the specimen
set H 2250;
set R 1175;
set Rhole 400;
set deltaH 562.5
set deltaTheta 36;
set deltaRhole 400;
set neleH [expr round($H/$deltaH)];
set neleTheta [expr 360/$deltaTheta];
set neleRhole [expr $Rhole/$deltaRhole];
set nH [expr 2*$neleH+1];
set nTheta [expr 2*$neleTheta];
set nRhole [expr 2*$neleRhole];
set DtoR [expr 3.14159/180];

# Define Nodes
set kk 1

for {set j 0} {$j < [expr $nH]} {incr j} {
  for {set i 0} {$i < $nTheta} {incr i} {
    if {[expr $j % 2] == 0} {
      node [expr $kk] [expr $R*cos((0.5*$deltaTheta*$DtoR)*$i)] [expr
$R*sin((0.5*$deltaTheta*$DtoR)*$i)] [expr $j*0.5*$deltaH]
      set kk [expr $kk+1]
    } else {
      if {[expr $i % 2] == 0} {
```

```

        node [expr $kk] [expr $R*cos((0.5*$deltaTheta*$DtoR)*$i)] [expr
$R*sin((0.5*$deltaTheta*$DtoR)*$i)] [expr $j*0.5*$deltaH]
        set kk [expr $kk+1]
    }
}

}

}

for {set j 1} {$j < [expr $nRhole+1]} {incr j} {
    for {set i 0} {$i < $nTheta} {incr i} {
        if {[expr $j % 2] == 0} {
            node [expr $kk] [expr ($R-
($j)*0.5*$deltaRhole)*cos((0.5*$deltaTheta*$DtoR)*$i)] [expr ($R-
($j)*0.5*$deltaRhole)*sin((0.5*$deltaTheta*$DtoR)*$i)] $H
            set kk [expr $kk+1]
        } else {
            if {[expr $i % 2] == 0} {
                node [expr $kk] [expr ($R-
($j)*0.5*$deltaRhole)*cos((0.5*$deltaTheta*$DtoR)*$i)] [expr ($R-
($j)*0.5*$deltaRhole)*sin((0.5*$deltaTheta*$DtoR)*$i)] $H
                set kk [expr $kk+1]
            }
        }
    }
}

}

}

# Define Constraints
fixZ 0.0 1 1 1 1 1 1
fixZ $H 0 0 0 1 1 1

# Set Parameters for Materials
set pi 3.141592654
set wfc 37.0
set ec0 0.003
set wfy 380.0
set wE 190000.0
set wGs [expr 3875.0*sqrt($wfc)/(2.4)]
set afa1 [expr 0.0*$pi]
set afa2 [expr 0.5*$pi]
set t0 150
set rou1v 0.02
set rou1h 0.02
set a0 30

```

```

# Define Materials

# Steel Material
uniaxialMaterial SteelZ01 11 $wfy $wE $wfc $rou1h
uniaxialMaterial SteelZ01 12 $wfy $wE $wfc $rou1v

# Concrete Material
uniaxialMaterial ConcreteZ01 13 [expr -$wfc] [expr -$ec0]
uniaxialMaterial ConcreteZ01 14 [expr -$wfc] [expr -$ec0]

# Material Layer for CSMMShellS8
nDMaterial CSMMLayer 16 0.0 11 12 13 14 $afa1 $afa2 $rou1h $rou1v $wfc
$wfy $wE $ec0 $wGs 1
nDMaterial CSMMLayer 17 0.0 11 12 13 14 $afa1 $afa2 $rou1h $rou1v $wfc
$wfy $wE $ec0 $wGs 0
set mat1 "16"
set mat2 "17"

# Material Layer for RigidShellS8
set E 9.e10
set v 0.2
set rho 1
set to 500.0
nDMaterial LinearFiber 20 $E $v $rho

set mat3 "20"

# Define CSMMShellS8 Elements
set nlay 5
set k 1
for {set i 0} {$i < $neleTheta} {incr i} {
  for {set j 0} {$j < $neleH} {incr j} {

    set node1 [expr 3*$j*$nTheta/2+2*$i+1]

    if {$i < [expr $neleTheta-1]} {
      set node2 [expr 3*$j*$nTheta/2+2*$i+3]
    } else {
      set node2 [expr 3*$j*$nTheta/2+1]
    }

    if {$i < [expr $neleTheta-1]} {
      set node3 [expr 3*($j+1)*$nTheta/2+2*$i+3]
    } else {
      set node3 [expr 3*($j+1)*$nTheta/2+1]
    }
  }
}

```

```

}

set node4 [expr 3*($j+1)*$nTheta/2+2*$i+1]
set node5 [expr 3*$j*$nTheta/2+2*$i+2]

if {$i < [expr $neleTheta-1]} {
  set node6 [expr 3*$j*$nTheta/2+$nTheta+$i+2]
} else {
  set node6 [expr 3*$j*$nTheta/2+$nTheta+1]
}

set node7 [expr 3*($j+1)*$nTheta/2+2*$i+2]
set node8 [expr 3*$j*$nTheta/2+$nTheta+$i+1]

element CSMMShellS8 [expr $k] $node1 $node2 $node3 $node4 $node5 $node6
$node7 $node8 $nlay $t0 $a0 $mat1 $mat2

set k [expr $k+1]

}
}

# Define RigidShells8 Elements
for {set j $neleH} {$j < [expr $neleH+$neleRhole]} {incr j} {
  for {set i 0} {$i < $neleTheta} {incr i} {

    set node1 [expr 3*$j*$nTheta/2+2*$i+1]

    if {$i < [expr $neleTheta-1]} {
      set node2 [expr 3*$j*$nTheta/2+2*$i+3]
    } else {
      set node2 [expr 3*$j*$nTheta/2+1]
    }

    if {$i < [expr $neleTheta-1]} {
      set node3 [expr 3*($j+1)*$nTheta/2+2*$i+3]
    } else {
      set node3 [expr 3*($j+1)*$nTheta/2+1]
    }

    set node4 [expr 3*($j+1)*$nTheta/2+2*$i+1]
    set node5 [expr 3*$j*$nTheta/2+2*$i+2]

    if {$i < [expr $neleTheta-1]} {
      set node6 [expr 3*$j*$nTheta/2+$nTheta+$i+2]

```

```

    } else {
      set node6 [expr 3*$j*$nTheta/2+$nTheta+1]
    }

    set node7 [expr 3*($j+1)*$nTheta/2+2*$i+2]
    set node8 [expr 3*$j*$nTheta/2+$nTheta+$i+1]

    element ElasticShells8 [expr $j*$neleTheta+$i+1] $node1 $node2 $node3 $node4
    $node5 $node6 $node7 $node8 $to $mat3

  }
}

# Define Output Files
set dataDir Analyze1Cyclic
file mkdir $dataDir/

ExportVTK NodeAll $dataDir/kennode.dat
ExportVTK Element8 $dataDir/keneleS.dat
ExportVTK Recorderdisp $dataDir/Recorderdisp.tcl $dataDir/nodedisp.dat
source "$dataDir/Recorderdisp.tcl"

set numEle [expr $neleH*$neleTheta]
recorder Element -eleRange 1 $numEle -time -file $dataDir/ConcreteStrain1.dat
ConcreteStrain1
recorder Element -eleRange 1 $numEle -time -file $dataDir/ConcreteStress1.dat
ConcreteStress1
recorder Element -eleRange 1 $numEle -time -file $dataDir/ConcreteStrain2.dat
ConcreteStrain2
recorder Element -eleRange 1 $numEle -time -file $dataDir/ConcreteStress2.dat
ConcreteStress2
recorder Element -eleRange 1 $numEle -time -file $dataDir/SteelStrain1.dat
SteelStrain1
recorder Element -eleRange 1 $numEle -time -file $dataDir/SteelStress1.dat
SteelStress1
recorder Element -eleRange 1 $numEle -time -file $dataDir/SteelStrain2.dat
SteelStrain2
recorder Element -eleRange 1 $numEle -time -file $dataDir/SteelStress2.dat
SteelStress2
recorder Element -eleRange 1 $numEle -time -file $dataDir/PrincipalAngle.dat
PrincipalAngle

set Rnode1 132
recorder Node -file $dataDir/FDH$Rnode1.dat -time -node $Rnode1 -dof 1 disp
recorder Node -file $dataDir/FDV$Rnode1.dat -time -node $Rnode1 -dof 3 disp

```

```

# Define Applying Loads

set N 640000;
set Ni [expr $N/10.0]

set Ni23 [expr (2.0/3.0)*$Ni]
set Ni13 [expr (1.0/3.0)*$Ni]

set Ni23 [expr (2.0/3.0)*$Ni]
set Ni13 [expr (1.0/3.0)*$Ni]

# Define Gravity Loads
pattern Plain 1 "Linear" {

    for {set i 0} {$i < $nTheta} {incr i} {
        if {[expr $i % 2] == 0} {
            load [expr ($nH-1)/2*(3*$nTheta/2)+$i+1] 0 0 -$Ni13 0 0 0
        } else {
            load [expr ($nH-1)/2*(3*$nTheta/2)+$i+1] 0 0 -$Ni23 0 0 0
        }
    }
}

# Define Analysis Parameter
system BandGeneral
constraints Plain
numberer Plain

# Define Create the Integration Scheme
test NormDispIncr 1.0e-3 100 5
integrator LoadControl 0.1

# Define Solution Algorithm
algorithm KrylovNewton
analysis Static

# Perform the Analysis
analyze 10

# Print out the state of nodes
puts "Finish Fst Analysis Step"
print node $Rnode1

# Solution 2: Applying horizontal load
loadConst -time 0.0

```

```

# Define Applying Loads

set P 1000;
set Pi [expr $P/10.0]

set Pi23 [expr (2.0/3.0)*$Pi]
set Pi13 [expr (1.0/3.0)*$Pi]

# Define Gravity Loads
pattern Plain 2 "Linear" {

    for {set i 0} {$i < $nTheta} {incr i} {
        if {[expr $i % 2] == 0} {
            load [expr ($nH-1)/2*(3*$nTheta/2)+$i+1] $Pi13 0 0 0 0 0
        } else {
            load [expr ($nH-1)/2*(3*$nTheta/2)+$i+1] $Pi23 0 0 0 0 0
        }
    }
}

}

# Define Analysis Parameter
system BandGeneral
constraints Plain
numberer Plain

# Define Create the Integration Scheme
test NormDispIncrVaryIter 0.5 17 3 numStep 56 112 140 168 197 226 282 338 394 450
563 676 788 900 1125 1350 735 numIter 150 150 150 150 150 150 150 150 150
150 150 150 150 150 150 150
integrator DisplacementPath $Rnode1 1 17 numStep 56 112 140 168 197 226 282 338
394 450 563 676 788 900 1125 1350 735 increment 0.1 -0.1 0.1 -0.1 0.1 -0.1 0.1 -0.1
0.1 -0.1 0.1 -0.1 0.1 -0.1 0.1 -0.1 0.1

# Define Solution Algorithm
algorithm KrylovNewton
analysis Static
initialize

# Perform the Analysis
set time1 [clock clicks -milliseconds]
analyze 1913
set time2 [clock clicks -milliseconds]

```

```
# Print out the state of nodes
puts "Finish Second Analysis Step"
puts "Elapsed time is [expr ($time2-$time1)/1000] seconds"
print node $Rnode1
```

The output file for load-displacement curve is presented as below

---

load (kN)	displacement (mm)
0	-3.00986e-07
235.175	0.0999926
482.439	0.199993
716.879	0.299993
956.549	0.399993
1186.79	0.499993
1086.66	0.599993
1317.84	0.699993
1375.61	0.799993
1257.4	0.899993
1385.89	0.999993
1389.02	1.09999
1444.47	1.19999
1459.39	1.29999
1490.02	1.39999
1524.02	1.49999
1557.48	1.59999
1592.08	1.69999
1627.69	1.79999
1663.79	1.89999
1700.16	1.99999
1737.23	2.09999
1774.24	2.19999
1811.2	2.29999
1849.03	2.39999
1887.07	2.49999
1925.35	2.59999
1963.61	2.69999
2002.01	2.79999
2040.52	2.89999
2078.81	2.99999
2116.99	3.09999
2155.65	3.19999
2194.4	3.29999
2233.3	3.39999
2272.36	3.49999
2311.59	3.59999
2350.77	3.69999
.....	

# APPENDIX B

## INPUT FILE OF RCCV SPECIMEN 2

The input file for the reserved cyclic analysis of the nuclear containment specimen No. 2 described in Chapter 5 is presented as below.

---

```
# Input file for RCCV2 Specimen

# Unit: N, mm, sec, MPa

# Create ModelBuilder
  model BasicBuilder -ndm 3 -ndf 6

# Set dimensions and mesh for the specimen
  set H 2250;
  set R 1175;
  set Rhole 400;
  set deltaH 562.5
  set deltaTheta 36;
  set deltaRhole 400;
  set neleH [expr round($H/$deltaH)];
  set neleTheta [expr 360/$deltaTheta];
  set neleRhole [expr $Rhole/$deltaRhole];
  set nH [expr 2*$neleH+1];
  set nTheta [expr 2*$neleTheta];
  set nRhole [expr 2*$neleRhole];
  set DtoR [expr 3.14159/180];

# Define Nodes
  set kk 1

  for {set j 0} {$j < [expr $nH]} {incr j} {
    for {set i 0} {$i < $nTheta} {incr i} {
      if {[expr $j % 2] == 0} {
        node [expr $kk] [expr $R*cos((0.5*$deltaTheta*$DtoR)*$i)] [expr
$R*sin((0.5*$deltaTheta*$DtoR)*$i)] [expr $j*0.5*$deltaH]
        set kk [expr $kk+1]
      } else {
        if {[expr $i % 2] == 0} {
```

```

        node [expr $kk] [expr $R*cos((0.5*$deltaTheta*$DtoR)*$i)] [expr
$R*sin((0.5*$deltaTheta*$DtoR)*$i)] [expr $j*0.5*$deltaH]
        set kk [expr $kk+1]
    }
}

}

}

for {set j 1} {$j < [expr $nRhole+1]} {incr j} {
    for {set i 0} {$i < $nTheta} {incr i} {
        if {[expr $j % 2] == 0} {
            node [expr $kk] [expr ($R-
($j)*0.5*$deltaRhole)*cos((0.5*$deltaTheta*$DtoR)*$i)] [expr ($R-
($j)*0.5*$deltaRhole)*sin((0.5*$deltaTheta*$DtoR)*$i)] $H
            set kk [expr $kk+1]
        } else {
            if {[expr $i % 2] == 0} {
                node [expr $kk] [expr ($R-
($j)*0.5*$deltaRhole)*cos((0.5*$deltaTheta*$DtoR)*$i)] [expr ($R-
($j)*0.5*$deltaRhole)*sin((0.5*$deltaTheta*$DtoR)*$i)] $H
                set kk [expr $kk+1]
            }
        }
    }
}

}

}

# Define Constraints
fixZ 0.0 1 1 1 1 1 1
fixZ $H 0 0 0 1 1 1

# Set Parameters for Materials
set pi 3.141592654
set wfc 37.0
set ec0 0.003
set wfy 380.0
set wE 190000.0
set wGs [expr 3875.0*sqrt($wfc)/(2.4)]
set afa1 [expr 0.0*$pi]
set afa2 [expr 0.5*$pi]
set t0 150
set rou1v 0.04
set rou1h 0.02
set a0 30

```

# Define Materials

# Steel Material

```
uniaxialMaterial SteelZ01 11 $wfy $wE $wfc $rou1h  
uniaxialMaterial SteelZ01 12 $wfy $wE $wfc $rou1v
```

# Concrete Material

```
uniaxialMaterial ConcreteZ01 13 [expr -$wfc] [expr -$ec0]  
uniaxialMaterial ConcreteZ01 14 [expr -$wfc] [expr -$ec0]
```

# Material Layer for CSMMShellS8 (Type 2)

```
nDMaterial CSMMLayer 16 0.0 11 12 13 14 $afa1 $afa2 $rou1h $rou1v $wfc $wfy  
$wE $ec0 $wGs 1  
nDMaterial CSMMLayer 17 0.0 11 12 13 14 $afa1 $afa2 $rou1h $rou1v $wfc $wfy  
$wE $ec0 $wGs 0
```

```
set mat1 "16"  
set mat2 "17"
```

# Set Prameters

```
set rou2v 0.02  
set rou2h 0.02
```

# Steel Material

```
uniaxialMaterial SteelZ01 21 $wfy $wE $wfc $rou2h  
uniaxialMaterial SteelZ01 22 $wfy $wE $wfc $rou2v
```

# Concrete Material

```
uniaxialMaterial ConcreteZ01 23 [expr -$wfc] [expr -$ec0]  
uniaxialMaterial ConcreteZ01 24 [expr -$wfc] [expr -$ec0]
```

# Material Layer for CSMMShellS8 (Type 1)

```
nDMaterial CSMMLayer 26 0.0 21 22 23 24 $afa1 $afa2 $rou2h $rou2v $wfc $wfy  
$wE $ec0 $wGs 1  
nDMaterial CSMMLayer 27 0.0 21 22 23 24 $afa1 $afa2 $rou2h $rou2v $wfc $wfy  
$wE $ec0 $wGs 0
```

```
set mat3 "26"  
set mat4 "27"  
set nlay 5
```

# Material Layer for RigidShellS8

```
set E 9.e10  
set v 0.2
```

```

set rho 1
set to 500.0
nDMaterial LinearFiber 30 $E $v $rho

set mat5 "30"

# Define CSMMShellS8 Elements
set nlay 5
set k 1
for {set i 0} {$i < $neleTheta} {incr i} {
  for {set j 0} {$j < $neleH} {incr j} {

    set node1 [expr 3*$j*$nTheta/2+2*$i+1]

    if {$i < [expr $neleTheta-1]} {
      set node2 [expr 3*$j*$nTheta/2+2*$i+3]
    } else {
      set node2 [expr 3*$j*$nTheta/2+1]
    }

    if {$i < [expr $neleTheta-1]} {
      set node3 [expr 3*($j+1)*$nTheta/2+2*$i+3]
    } else {
      set node3 [expr 3*($j+1)*$nTheta/2+1]
    }

    set node4 [expr 3*($j+1)*$nTheta/2+2*$i+1]
    set node5 [expr 3*$j*$nTheta/2+2*$i+2]

    if {$i < [expr $neleTheta-1]} {
      set node6 [expr 3*$j*$nTheta/2+$nTheta+$i+2]
    } else {
      set node6 [expr 3*$j*$nTheta/2+$nTheta+1]
    }

    set node7 [expr 3*($j+1)*$nTheta/2+2*$i+2]
    set node8 [expr 3*$j*$nTheta/2+$nTheta+$i+1]

    if {$j == 0 || $j == [expr $neleH-1]} {
      element Shell8SF6K02 [expr $k] $node1 $node2 $node3 $node4 $node5 $node6
      $node7 $node8 $nlay $t0 $a0 $mat1 $mat2
      #puts "element Shell8SF6K02 [expr $k] $node1 $node2 $node3 $node4 $node5
      $node6 $node7 $node8 $nlay $t0 $a0 $mat1 $mat2"
    }
  }
}

```

```

    } else {
      element Shell8SF6K02 [expr $k] $node1 $node2 $node3 $node4 $node5 $node6
      $node7 $node8 $nlay $t0 $a0 $mat3 $mat4
      #puts "element Shell8SF6K02 [expr $k] $node1 $node2 $node3 $node4 $node5
      $node6 $node7 $node8 $nlay $t0 $a0 $mat3 $mat4"

    }

    set k [expr $k+1]

  }
}

```

# Define RigidShells8 Elements

```

for {set j $neleH} {$j < [expr $neleH+$neleRhole]} {incr j} {
  for {set i 0} {$i < $neleTheta} {incr i} {

```

```

    set node1 [expr 3*$j*$nTheta/2+2*$i+1]

```

```

    if {$i < [expr $neleTheta-1]} {
      set node2 [expr 3*$j*$nTheta/2+2*$i+3]
    } else {
      set node2 [expr 3*$j*$nTheta/2+1]
    }

```

```

    if {$i < [expr $neleTheta-1]} {
      set node3 [expr 3*($j+1)*$nTheta/2+2*$i+3]
    } else {
      set node3 [expr 3*($j+1)*$nTheta/2+1]
    }

```

```

    set node4 [expr 3*($j+1)*$nTheta/2+2*$i+1]
    set node5 [expr 3*$j*$nTheta/2+2*$i+2]

```

```

    if {$i < [expr $neleTheta-1]} {
      set node6 [expr 3*$j*$nTheta/2+$nTheta+$i+2]
    } else {
      set node6 [expr 3*$j*$nTheta/2+$nTheta+1]
    }

```

```

    set node7 [expr 3*($j+1)*$nTheta/2+2*$i+2]
    set node8 [expr 3*$j*$nTheta/2+$nTheta+$i+1]

```

```
    element Shell8SF6K01 [expr $j*$neleTheta+$i+1] $node1 $node2 $node3 $node4
    $node5 $node6 $node7 $node8 $to $mat5
```

```
  }
}
```

```
# Define Output Files
```

```
set dataDir Analyze1Cyclic
file mkdir $dataDir/
```

```
ExportVTK NodeAll $dataDir/kennode.dat
ExportVTK Element8 $dataDir/keneleS.dat
ExportVTK Recorderdisp $dataDir/Recorderdisp.tcl $dataDir/nodedisp.dat
source "$dataDir/Recorderdisp.tcl"
```

```
set numEle [expr $neleH*$neleTheta]
recorder Element -eleRange 1 $numEle -time -file $dataDir/ConcreteStrain1.dat
ConcreteStrain1
recorder Element -eleRange 1 $numEle -time -file $dataDir/ConcreteStress1.dat
ConcreteStress1
recorder Element -eleRange 1 $numEle -time -file $dataDir/ConcreteStrain2.dat
ConcreteStrain2
recorder Element -eleRange 1 $numEle -time -file $dataDir/ConcreteStress2.dat
ConcreteStress2
recorder Element -eleRange 1 $numEle -time -file $dataDir/SteelStrain1.dat
SteelStrain1
recorder Element -eleRange 1 $numEle -time -file $dataDir/SteelStress1.dat
SteelStress1
recorder Element -eleRange 1 $numEle -time -file $dataDir/SteelStrain2.dat
SteelStrain2
recorder Element -eleRange 1 $numEle -time -file $dataDir/SteelStress2.dat
SteelStress2
recorder Element -eleRange 1 $numEle -time -file $dataDir/PrincipalAngle.dat
PrincipalAngle
```

```
set Rnode1 132
```

```
recorder Node -file $dataDir/FDH$Rnode1.dat -time -node $Rnode1 -dof 1 disp
recorder Node -file $dataDir/FDV$Rnode1.dat -time -node $Rnode1 -dof 3 disp
```

```
# Define Applying Loads
```

```
set N 640000;
set Ni [expr $N/10.0]
```

```
set Ni23 [expr (2.0/3.0)*$Ni]
set Ni13 [expr (1.0/3.0)*$Ni]
```

```

set Ni23 [expr (2.0/3.0)*$Ni]
set Ni13 [expr (1.0/3.0)*$Ni]

# Define Gravity Loads
pattern Plain 1 "Linear" {

    for {set i 0} {$i < $nTheta} {incr i} {
        if {[expr $i % 2] == 0} {
            load [expr ($nH-1)/2*(3*$nTheta/2)+$i+1] 0 0 -$Ni13 0 0 0
        } else {
            load [expr ($nH-1)/2*(3*$nTheta/2)+$i+1] 0 0 -$Ni23 0 0 0
        }
    }
}

# Define Analysis Parameter
system BandGeneral
constraints Plain
numberer Plain

# Define Create the Integration Scheme
test NormDispIncr 1.0e-3 100 5
integrator LoadControl 0.1

# Define Solution Algorithm
algorithm KrylovNewton
analysis Static

# Perform the Analysis
analyze 10

# Print out the state of nodes
puts "Finish Fist Analysis Step"
print node $Rnode1

# Solution 2: Applying horizontal load
loadConst -time 0.0

# Define Applying Loads

set P 1000;
set Pi [expr $P/10.0]

set Pi23 [expr (2.0/3.0)*$Pi]
set Pi13 [expr (1.0/3.0)*$Pi]

```

```

# Define Gravity Loads
pattern Plain 2 "Linear" {

    for {set i 0} {$i < $nTheta} {incr i} {
        if {[expr $i % 2] == 0} {
            load [expr ($nH-1)/2*(3*$nTheta/2)+$i+1] $Pi13 0 0 0 0 0
        } else {
            load [expr ($nH-1)/2*(3*$nTheta/2)+$i+1] $Pi23 0 0 0 0 0
        }
    }
}

}

# Define Analysis Parameter
system BandGeneral
constraints Plain
numberer Plain

# Define Create the Integration Scheme
test NormDispIncrVaryIter 0.5 17 3 numStep 56 112 140 168 197 226 282 338 394 450
563 676 788 900 1125 1350 735 numIter 150 150 150 150 150 150 150 150 150
150 150 150 150 150 150 150
integrator DisplacementPath $Rnode1 1 17 numStep 56 112 140 168 197 226 282 338
394 450 563 676 788 900 1125 1350 735 increment 0.1 -0.1 0.1 -0.1 0.1 -0.1 0.1 -0.1
0.1 -0.1 0.1 -0.1 0.1 -0.1 0.1 -0.1 0.1

# Define Solution Algorithm
algorithm KrylovNewton
analysis Static
initialize

# Perform the Analysis
set time1 [clock clicks -milliseconds]
analyze 4000
set time2 [clock clicks -milliseconds]

# Print out the state of nodes
puts "Finish Second Analysis Step"
puts "Elapsed time is [expr ($time2-$time1)/1000] seconds"
print node $Rnode1

```

The output file for load-displacement curve is presented as below

---

load (kN)	displacement (mm)
0	-0.00062
194.494	0.099376
394.854	0.199377
588.613	0.299377
785.159	0.399377
978.488	0.499377
1151.31	0.599377
1279.52	0.699377
1347.41	0.799377
1124.98	0.899377
1225.37	0.999377
1269.55	1.09938
1296.8	1.19938
1333.01	1.29938
1372.98	1.39938
1418.07	1.49938
1456.57	1.59938
1491.5	1.69938
1532.26	1.79938
1569.41	1.89938
1608.19	1.99938
1646.31	2.09938
1685.74	2.19938
1724.78	2.29938
1764.2	2.39938
1803.84	2.49938
1843.31	2.59938
1882.75	2.69938
1922.25	2.79938
1961.65	2.89938
2001.33	2.99938
2041.12	3.09938
2080.9	3.19938
2120.56	3.29938
2160.29	3.39938
2200.12	3.49938
2239.89	3.59938
2279.67	3.69938
2319.5	3.79938
.....	

# APPENDIX C

## INPUT FILE OF 2-STORY BUILDING SPECIMEN

The input file for the reserved cyclic analysis of the two-story unsymmetrical RC building specimen described in Chapter 6 is presented as below

---

```
# Input File for 2-story Building Specimen
# Unit: N, mm, sec, MPa
```

```
# Create ModelBuilder
  model BasicBuilder -ndm 3 -ndf 6
```

```
# Define Nodes
node 263 771 2941 4100
node 264 771 2941 4300
node 265 800 2883 2400
node 266 800 2883 2525
node 267 800 2883 2650
node 268 800 2883 2775
node 269 800 2883 2900
node 270 800 2883 3025
node 271 800 2883 3150
node 272 800 2883 3275
node 273 800 2883 3400
node 274 800 2883 3525
node 275 800 2883 3650
node 276 800 2883 3775
node 277 800 2883 3900
node 278 800 2883 4000
node 279 800 2883 4100
node 280 800 2883 4200
node 281 800 2883 4300
node 282 829 4215 2400
node 283 829 4215 4300
node 284 857 9202 0
node 285 857 9202 600
node 286 857 9202 1200
node 287 857 9202 1800
node 288 857 9202 2400
```

node	289	857	9202	2875
node	290	857	9202	3350
node	291	857	9202	3825
node	292	857	9202	4300
node	293	980	7274	2400
node	294	980	7274	4300
node	295	1017	2158	2400
node	296	1017	2158	4300
node	297	1103	5346	2400
node	298	1103	5346	4300
node	299	1254	8405	2400
node	1	-1828	7863	0
node	2	-1828	7863	600
node	3	-1828	7863	1200
node	4	-1828	7863	1800
node	5	-1828	7863	2400
node	6	-1828	7863	2875
node	7	-1828	7863	3350
node	8	-1828	7863	3825
node	9	-1828	7863	4300
node	10	-1431	7067	2400
node	11	-1431	7067	4300
node	12	-1157	8198	0
node	13	-1157	8198	1200
node	14	-1157	8198	2400
node	15	-1157	8198	3350
node	16	-1157	8198	4300
node	17	-1034	6270	2400
node	18	-1034	6270	4300
node	19	-760	7401	2400
node	20	-760	7401	4300
node	21	-637	5474	2400
node	22	-637	5474	4300
node	23	-486	8532	0
node	24	-486	8532	600
node	25	-486	8532	1200
node	26	-486	8532	1800
node	27	-486	8532	2400
node	28	-486	8532	2875
node	29	-486	8532	3350
node	30	-486	8532	3825
node	31	-486	8532	4300
node	32	-363	6605	2400
node	33	-363	6605	4300
node	34	-240	4677	2400
node	35	-240	4677	4300

node	36	-88 7736	2400
node	37	-88 7736	4300
node	38	35 5808	2400
node	39	35 5808	4300
node	40	158 3881	2400
node	41	158 3881	4300
node	42	186 8867	0
node	43	186 8867	1200
node	44	186 8867	2400
node	45	186 8867	3350
node	46	186 8867	4300
node	47	309 6939	2400
node	48	309 6939	4300
node	49	432 5012	2400
node	50	432 5012	4300
node	51	452 2999	2400
node	52	452 2999	2525
node	53	452 2999	2650
node	54	452 2999	2775
node	55	452 2999	2900
node	56	452 2999	3025
node	57	452 2999	3150
node	58	452 2999	3275
node	59	452 2999	3400
node	60	452 2999	3525
node	61	452 2999	3650
node	62	452 2999	3775
node	63	452 2999	3900
node	64	452 2999	4000
node	65	452 2999	4100
node	66	452 2999	4200
node	67	452 2999	4300
node	68	481 2941	2400
node	69	481 2941	2650
node	70	481 2941	2900
node	71	481 2941	3150
node	72	481 2941	3400
node	73	481 2941	3650
node	74	481 2941	3900
node	75	481 2941	4100
node	76	481 2941	4300
node	77	510 2883	2400
node	78	510 2883	2525
node	79	510 2883	2650
node	80	510 2883	2775
node	81	510 2883	2900

node	82	510 2883	3025
node	83	510 2883	3150
node	84	510 2883	3275
node	85	510 2883	3400
node	86	510 2883	3525
node	87	510 2883	3650
node	88	510 2883	3775
node	89	510 2883	3900
node	90	510 2883	4000
node	91	510 2883	4100
node	92	510 2883	4200
node	93	510 2883	4300
node	94	510 3028	2400
node	95	510 3028	2650
node	96	510 3028	2900
node	97	510 3028	3150
node	98	510 3028	3400
node	99	510 3028	3650
node	100	510 3028	3900
node	101	510 3028	4100
node	102	510 3028	4300
node	103	539 2825	2400
node	104	539 2825	2650
node	105	539 2825	2900
node	106	539 2825	3150
node	107	539 2825	3400
node	108	539 2825	3650
node	109	539 2825	3900
node	110	539 2825	4100
node	111	539 2825	4300
node	112	568 2767	2400
node	113	568 2767	2525
node	114	568 2767	2650
node	115	568 2767	2775
node	116	568 2767	2900
node	117	568 2767	3025
node	118	568 2767	3150
node	119	568 2767	3275
node	120	568 2767	3400
node	121	568 2767	3525
node	122	568 2767	3650
node	123	568 2767	3775
node	124	568 2767	3900
node	125	568 2767	4000
node	126	568 2767	4100
node	127	568 2767	4200

node	128	568	2767	4300
node	129	568	2912	2400
node	130	568	2912	3900
node	131	568	2912	4300
node	132	568	3057	2400
node	133	568	3057	2525
node	134	568	3057	2650
node	135	568	3057	2775
node	136	568	3057	2900
node	137	568	3057	3025
node	138	568	3057	3150
node	139	568	3057	3275
node	140	568	3057	3400
node	141	568	3057	3525
node	142	568	3057	3650
node	143	568	3057	3775
node	144	568	3057	3900
node	145	568	3057	4000
node	146	568	3057	4100
node	147	568	3057	4200
node	148	568	3057	4300
node	149	583	8071	2400
node	150	583	8071	4300
node	151	597	2999	2400
node	152	597	2999	3900
node	153	597	2999	4300
node	154	626	2796	2400
node	155	626	2796	2650
node	156	626	2796	2900
node	157	626	2796	3150
node	158	626	2796	3400
node	159	626	2796	3650
node	160	626	2796	3900
node	161	626	2796	4100
node	162	626	2796	4300
node	163	626	2941	0
node	164	626	2941	600
node	165	626	2941	1200
node	166	626	2941	1800
node	167	626	2941	2400
node	168	626	2941	3900
node	169	626	2941	4300
node	170	626	3086	2400
node	171	626	3086	2650
node	172	626	3086	2900
node	173	626	3086	3150

node	174	626	3086	3400
node	175	626	3086	3650
node	176	626	3086	3900
node	177	626	3086	4100
node	178	626	3086	4300
node	179	655	2883	2400
node	180	655	2883	3900
node	181	655	2883	4300
node	182	684	2825	2400
node	183	684	2825	2525
node	184	684	2825	2650
node	185	684	2825	2775
node	186	684	2825	2900
node	187	684	2825	3025
node	188	684	2825	3150
node	189	684	2825	3275
node	190	684	2825	3400
node	191	684	2825	3525
node	192	684	2825	3650
node	193	684	2825	3775
node	194	684	2825	3900
node	195	684	2825	4000
node	196	684	2825	4100
node	197	684	2825	4200
node	198	684	2825	4300
node	199	684	2970	2400
node	200	684	2970	3900
node	201	684	2970	4300
node	202	684	3115	2400
node	203	684	3115	2525
node	204	684	3115	2650
node	205	684	3115	2775
node	206	684	3115	2900
node	207	684	3115	3025
node	208	684	3115	3150
node	209	684	3115	3275
node	210	684	3115	3400
node	211	684	3115	3525
node	212	684	3115	3650
node	213	684	3115	3775
node	214	684	3115	3900
node	215	684	3115	4000
node	216	684	3115	4100
node	217	684	3115	4200
node	218	684	3115	4300
node	219	706	6143	2400

node	220	706	6143	4300
node	221	713	3057	2400
node	222	713	3057	2650
node	223	713	3057	2900
node	224	713	3057	3150
node	225	713	3057	3400
node	226	713	3057	3650
node	227	713	3057	3900
node	228	713	3057	4100
node	229	713	3057	4300
node	230	742	2854	2400
node	231	742	2854	2650
node	232	742	2854	2900
node	233	742	2854	3150
node	234	742	2854	3400
node	235	742	2854	3650
node	236	742	2854	3900
node	237	742	2854	4100
node	238	742	2854	4300
node	239	742	2999	2400
node	240	742	2999	2525
node	241	742	2999	2650
node	242	742	2999	2775
node	243	742	2999	2900
node	244	742	2999	3025
node	245	742	2999	3150
node	246	742	2999	3275
node	247	742	2999	3400
node	248	742	2999	3525
node	249	742	2999	3650
node	250	742	2999	3775
node	251	742	2999	3900
node	252	742	2999	4000
node	253	742	2999	4100
node	254	742	2999	4200
node	255	742	2999	4300
node	256	771	2941	2400
node	257	771	2941	2650
node	258	771	2941	2900
node	259	771	2941	3150
node	260	771	2941	3400
node	261	771	2941	3650
node	262	771	2941	3900
node	300	1254	8405	4300
node	301	1297	3276	2400
node	302	1297	3276	4300

node	303	1377	6478	2400
node	304	1377	6478	4300
node	305	1407	1375	2400
node	306	1407	1375	4300
node	307	1500	4550	2400
node	308	1500	4550	4300
node	309	1651	7609	2400
node	310	1651	7609	4300
node	311	1688	2493	2400
node	312	1688	2493	4300
node	313	1774	5681	2400
node	314	1774	5681	4300
node	315	1797	592	2400
node	316	1797	592	4300
node	317	1969	3610	2400
node	318	1969	3610	4300
node	319	2048	6812	2400
node	320	2048	6812	4300
node	321	2078	1710	2400
node	322	2078	1710	4300
node	323	2171	4885	2400
node	324	2171	4885	4300
node	325	2188	-191	0
node	326	2188	-191	600
node	327	2188	-191	1200
node	328	2188	-191	1800
node	329	2188	-191	2400
node	330	2188	-191	2875
node	331	2188	-191	3350
node	332	2188	-191	3825
node	333	2188	-191	4300
node	334	2359	2827	2400
node	335	2359	2827	4300
node	336	2445	6016	2400
node	337	2445	6016	4300
node	338	2469	926	2400
node	339	2469	926	4300
node	340	2640	3945	2400
node	341	2640	3945	4300
node	342	2749	2044	2400
node	343	2749	2044	4300
node	344	2842	5219	2400
node	345	2842	5219	4300
node	346	2859	143	2400
node	347	2859	143	4300
node	348	3030	3162	2400

node	349 3030	3162	4300
node	350 3140	1261	2400
node	351 3140	1261	4300
node	352 3311	4280	0
node	353 3311	4280	600
node	354 3311	4280	1200
node	355 3311	4280	1800
node	356 3311	4280	2400
node	357 3311	4280	2875
node	358 3311	4280	3350
node	359 3311	4280	3825
node	360 3311	4280	4300
node	361 3421	2379	2400
node	362 3421	2379	4300
node	363 3530	478	2400
node	364 3530	478	4300
node	365 3701	3497	0
node	366 3701	3497	1200
node	367 3701	3497	2400
node	368 3701	3497	3350
node	369 3701	3497	4300
node	370 3811	1596	2400
node	371 3811	1596	4300
node	372 4092	2713	0
node	373 4092	2713	600
node	374 4092	2713	1200
node	375 4092	2713	1800
node	376 4092	2713	2400
node	377 4092	2713	2875
node	378 4092	2713	3350
node	379 4092	2713	3825
node	380 4092	2713	4300
node	381 4201	813	2400
node	382 4201	813	4300
node	383 4482	1930	0
node	384 4482	1930	1200
node	385 4482	1930	2400
node	386 4482	1930	3350
node	387 4482	1930	4300
node	388 4873	1147	0
node	389 4873	1147	600
node	390 4873	1147	1200
node	391 4873	1147	1800
node	392 4873	1147	2400
node	393 4873	1147	2875
node	394 4873	1147	3350

```
node 395 4873 1147 3825
node 396 4873 1147 4300
```

```
# Define Constraints
```

```
fix 1 1 1 1 1 1 1
fix 12 1 1 1 1 1 1
fix 23 1 1 1 1 1 1
fix 42 1 1 1 1 1 1
fix 163 1 1 1 1 1 1
fix 284 1 1 1 1 1 1
fix 325 1 1 1 1 1 1
fix 352 1 1 1 1 1 1
fix 365 1 1 1 1 1 1
fix 372 1 1 1 1 1 1
fix 383 1 1 1 1 1 1
fix 388 1 1 1 1 1 1
```

```
# Define Column Elements
```

```
# Material
```

```
set fc 28.0
set Es 200000.0;
set fy 412;
set fyp [expr $fy]
set fup [expr 1.2*$fy]
set fdp [expr 0.2*$fy]
set eyp [expr $fy/$Es]
set eup [expr 0.1]
set edp [expr 0.15]
set fyn [expr $fy]
set fun [expr 1.2*$fy]
set fdn [expr 0.2*$fy]
set eyn [expr $fy/$Es]
set eun [expr 0.02]
set edn [expr 0.06]
```

```
uniaxialMaterial Concrete01 1 [expr -1.12*$fc] -0.003 [expr -0.24*$fc] -0.01
```

```
uniaxialMaterial Concrete01 2 -$fc -0.002 [expr -0.2*$fc] -0.005
```

```
# uniaxialMaterial Steel01 3 $fy $Es 0.005
```

```
# uniaxialMaterial Steel01 4 $fy $Es 0.005
```

```
uniaxialMaterial Hysteretic 3 $fyp $eyp $fup $eup $fdp $edp -$fyp -$eyp -$fup -$eup -
$fdp -$edp 0.0 0.0 0.0 0.0
```

```
uniaxialMaterial Hysteretic 4 $fyp $eyp $fup $eup $fdp $edp -$fyn -$eyn -$fun -$eun -
$fdn -$edn 0.0 0.0 0.0 0.0
```

```
set TorsionTag 70;
```

```

set Gt [expr 1e10];
uniaxialMaterial Elastic $TorsionTag $Gt;

# Cross-Section
set cover 25.0
set As4 126.0;
set As6 285.0;
set colWidth 400.0
set colDepth 400.0
set dd 110
set cy1 [expr $colDepth/2.0]
set cz1 [expr $colWidth/2.0]

set ColFiberTag1 1;
set ColFiberTag2 2;
set ColSecTag1 3;
set ColSecTag2 4;

section Fiber $ColFiberTag1 {
  patch rect 1 20 20 [expr -($cy1-$cover)] [expr -($cz1-$cover)] [expr $cy1-$cover]
[expr $cz1-$cover]
  patch rect 2 20 4 [expr -$cy1] [expr $cz1-$cover] [expr $cy1] [expr $cz1]
  patch rect 2 20 4 [expr -$cy1] [expr -$cz1] [expr $cy1] [expr -
$cz1+$cover]
  patch rect 2 4 20 [expr -$cy1] [expr -$cz1+$cover] [expr -$cy1+$cover] [expr
$cz1-$cover]
  patch rect 2 4 20 [expr $cy1-$cover] [expr -$cz1+$cover] [expr $cy1] [expr
$cz1-$cover]

  layer straight 3 4 $As6 [expr $cy1-$cover] [expr $cz1-$cover] [expr $cy1-$cover]
[expr -$cz1+$cover]
  layer straight 3 2 $As6 [expr $cy1-$cover-$dd] [expr $cz1-$cover] [expr $cy1-
$cover-$dd] [expr -$cz1+$cover]
  layer straight 3 4 $As6 [expr -$cy1+$cover] [expr $cz1-$cover] [expr -
$cy1+$cover] [expr -$cz1+$cover]
  layer straight 3 2 $As6 [expr -$cy1+$cover+$dd] [expr $cz1-$cover] [expr -
$cy1+$cover+$dd] [expr -$cz1+$cover]
}

section Fiber $ColFiberTag2 {
  patch rect 1 20 20 [expr -($cy1-$cover)] [expr -($cz1-$cover)] [expr $cy1-$cover]
[expr $cz1-$cover]
  patch rect 2 20 4 [expr -$cy1] [expr $cz1-$cover] [expr $cy1] [expr $cz1]
  patch rect 2 20 4 [expr -$cy1] [expr -$cz1] [expr $cy1] [expr -
$cz1+$cover]

```

```

    patch rect 2 4 20 [expr -$cy1]          [expr -$cz1+$cover] [expr -$cy1+$cover] [expr
$cz1-$cover]
    patch rect 2 4 20 [expr $cy1-$cover] [expr -$cz1+$cover] [expr $cy1]          [expr
$cz1-$cover]

    layer straight 4 4 $As6 [expr $cy1-$cover]    [expr $cz1-$cover] [expr $cy1-$cover]
[expr -$cz1+$cover]
    layer straight 4 2 $As6 [expr $cy1-$cover-$dd] [expr $cz1-$cover] [expr $cy1-
$cover-$dd] [expr -$cz1+$cover]
    layer straight 4 4 $As6 [expr -$cy1+$cover]          [expr $cz1-$cover] [expr -
$cy1+$cover] [expr -$cz1+$cover]
    layer straight 4 2 $As6 [expr -$cy1+$cover+$dd] [expr $cz1-$cover] [expr -
$cy1+$cover+$dd] [expr -$cz1+$cover]
}

section Aggregator $ColSecTag1 $TorsionTag T -section $ColFiberTag1;
section Aggregator $ColSecTag2 $TorsionTag T -section $ColFiberTag2;

# set PDelta "ON"
set PDelta "OFF"

# Geometric transformation for columns
set IDColTrans 1;

if {$PDelta == "ON"} {
#          tag vecxz
    geomTransf LinearWithPDelta $IDColTrans 1 0 0
} else {
    geomTransf Linear $IDColTrans 1 0 0
}

set np 4

# Type 1: Normal Column
element nonlinearBeamColumn 1 1 2 $np $ColSecTag1 $IDColTrans
element nonlinearBeamColumn 2 2 3 $np $ColSecTag1 $IDColTrans
element nonlinearBeamColumn 3 3 4 $np $ColSecTag1 $IDColTrans
element nonlinearBeamColumn 4 4 5 $np $ColSecTag1 $IDColTrans
element nonlinearBeamColumn 5 5 6 $np $ColSecTag1 $IDColTrans
element nonlinearBeamColumn 6 6 7 $np $ColSecTag1 $IDColTrans
element nonlinearBeamColumn 7 7 8 $np $ColSecTag1 $IDColTrans
element nonlinearBeamColumn 8 8 9 $np $ColSecTag1 $IDColTrans
element nonlinearBeamColumn 56 163 164 $np $ColSecTag1 $IDColTrans
element nonlinearBeamColumn 57 164 165 $np $ColSecTag1 $IDColTrans
element nonlinearBeamColumn 58 165 166 $np $ColSecTag1 $IDColTrans
element nonlinearBeamColumn 59 166 167 $np $ColSecTag1 $IDColTrans

```

```

element nonlinearBeamColumn 70 284 285 $np $ColSecTag1 $IDColTrans
element nonlinearBeamColumn 71 285 286 $np $ColSecTag1 $IDColTrans
element nonlinearBeamColumn 72 286 287 $np $ColSecTag1 $IDColTrans
element nonlinearBeamColumn 73 287 288 $np $ColSecTag1 $IDColTrans
element nonlinearBeamColumn 74 288 289 $np $ColSecTag1 $IDColTrans
element nonlinearBeamColumn 75 289 290 $np $ColSecTag1 $IDColTrans
element nonlinearBeamColumn 76 290 291 $np $ColSecTag1 $IDColTrans
element nonlinearBeamColumn 77 291 292 $np $ColSecTag1 $IDColTrans
element nonlinearBeamColumn 142 329 330 $np $ColSecTag1 $IDColTrans
element nonlinearBeamColumn 143 330 331 $np $ColSecTag1 $IDColTrans
element nonlinearBeamColumn 144 331 332 $np $ColSecTag1 $IDColTrans
element nonlinearBeamColumn 145 332 333 $np $ColSecTag1 $IDColTrans
element nonlinearBeamColumn 184 352 353 $np $ColSecTag1 $IDColTrans
element nonlinearBeamColumn 185 353 354 $np $ColSecTag1 $IDColTrans
element nonlinearBeamColumn 186 354 355 $np $ColSecTag1 $IDColTrans
element nonlinearBeamColumn 187 355 356 $np $ColSecTag1 $IDColTrans
element nonlinearBeamColumn 188 356 357 $np $ColSecTag1 $IDColTrans
element nonlinearBeamColumn 189 357 358 $np $ColSecTag1 $IDColTrans
element nonlinearBeamColumn 190 358 359 $np $ColSecTag1 $IDColTrans
element nonlinearBeamColumn 191 359 360 $np $ColSecTag1 $IDColTrans
element nonlinearBeamColumn 222 392 393 $np $ColSecTag1 $IDColTrans
element nonlinearBeamColumn 223 393 394 $np $ColSecTag1 $IDColTrans
element nonlinearBeamColumn 224 394 395 $np $ColSecTag1 $IDColTrans
element nonlinearBeamColumn 225 395 396 $np $ColSecTag1 $IDColTrans

```

# Type 1: Buckled Column

```

element nonlinearBeamColumn 138 325 326 $np $ColSecTag2 $IDColTrans
element nonlinearBeamColumn 139 326 327 $np $ColSecTag2 $IDColTrans
element nonlinearBeamColumn 140 327 328 $np $ColSecTag2 $IDColTrans
element nonlinearBeamColumn 141 328 329 $np $ColSecTag2 $IDColTrans
element nonlinearBeamColumn 218 388 389 $np $ColSecTag2 $IDColTrans
element nonlinearBeamColumn 219 389 390 $np $ColSecTag2 $IDColTrans
element nonlinearBeamColumn 220 390 391 $np $ColSecTag2 $IDColTrans
element nonlinearBeamColumn 221 391 392 $np $ColSecTag2 $IDColTrans

```

# Define Beam Elements

# Cross-Section

```

set beamWidth 300.0
set beamDepth 400.0
set cyl [expr $beamDepth/2.0]
set cz1 [expr $beamWidth/2.0]

```

```

set BeamFiberTag 5;
set BeamSecTag 6;

```

```

section Fiber $BeamFiberTag {
  patch rect 1 20 20 [expr -($cy1-$cover)] [expr -($cz1-$cover)] [expr $cy1-$cover]
[expr $cz1-$cover]
  patch rect 2 20 4 [expr -$cy1] [expr $cz1-$cover] [expr $cy1] [expr $cz1]
  patch rect 2 20 4 [expr -$cy1] [expr -$cz1] [expr $cy1] [expr -
$cz1+$cover]
  patch rect 2 4 20 [expr -$cy1] [expr -$cz1+$cover] [expr -$cy1+$cover] [expr
$cz1-$cover]
  patch rect 2 4 20 [expr $cy1-$cover] [expr -$cz1+$cover] [expr $cy1] [expr
$cz1-$cover]

```

```

# Create the reinforcing fibers (4 layers)
  layer straight 3 4 $As6 [expr $cy1-$cover] [expr $cz1-$cover] [expr $cy1-$cover]
[expr -$cz1+$cover]
  layer straight 3 4 $As6 [expr -$cy1+$cover] [expr $cz1-$cover] [expr -
$cy1+$cover] [expr -$cz1+$cover]
}

```

```

section Aggregator $BeamSecTag $TorsionTag T -section $BeamFiberTag;

```

```

set IDBeamTrans 2;
geomTransf Linear $IDBeamTrans 1 1 0;

```

```

set np 3

```

```

element nonlinearBeamColumn 9 10 5 $np $BeamSecTag $IDBeamTrans
element nonlinearBeamColumn 10 11 9 $np $BeamSecTag $IDBeamTrans
element nonlinearBeamColumn 11 9 16 $np $BeamSecTag $IDBeamTrans
element nonlinearBeamColumn 12 17 10 $np $BeamSecTag $IDBeamTrans
element nonlinearBeamColumn 13 18 11 $np $BeamSecTag $IDBeamTrans
element nonlinearBeamColumn 17 21 17 $np $BeamSecTag $IDBeamTrans
element nonlinearBeamColumn 18 22 18 $np $BeamSecTag $IDBeamTrans
element nonlinearBeamColumn 19 16 31 $np $BeamSecTag $IDBeamTrans
element nonlinearBeamColumn 24 34 21 $np $BeamSecTag $IDBeamTrans
element nonlinearBeamColumn 25 35 22 $np $BeamSecTag $IDBeamTrans
element nonlinearBeamColumn 33 31 46 $np $BeamSecTag $IDBeamTrans
element nonlinearBeamColumn 34 40 34 $np $BeamSecTag $IDBeamTrans
element nonlinearBeamColumn 35 41 35 $np $BeamSecTag $IDBeamTrans
element nonlinearBeamColumn 46 132 40 $np $BeamSecTag $IDBeamTrans
element nonlinearBeamColumn 47 148 41 $np $BeamSecTag $IDBeamTrans
element nonlinearBeamColumn 55 46 292 $np $BeamSecTag $IDBeamTrans
element nonlinearBeamColumn 68 295 182 $np $BeamSecTag $IDBeamTrans
element nonlinearBeamColumn 69 296 198 $np $BeamSecTag $IDBeamTrans
element nonlinearBeamColumn 82 239 301 $np $BeamSecTag $IDBeamTrans
element nonlinearBeamColumn 83 255 302 $np $BeamSecTag $IDBeamTrans
element nonlinearBeamColumn 86 299 288 $np $BeamSecTag $IDBeamTrans

```

element nonlinearBeamColumn	87	300	292	\$np	\$BeamSecTag	\$IDBeamTrans
element nonlinearBeamColumn	94	305	295	\$np	\$BeamSecTag	\$IDBeamTrans
element nonlinearBeamColumn	95	306	296	\$np	\$BeamSecTag	\$IDBeamTrans
element nonlinearBeamColumn	104	309	299	\$np	\$BeamSecTag	\$IDBeamTrans
element nonlinearBeamColumn	105	310	300	\$np	\$BeamSecTag	\$IDBeamTrans
element nonlinearBeamColumn	110	315	305	\$np	\$BeamSecTag	\$IDBeamTrans
element nonlinearBeamColumn	111	316	306	\$np	\$BeamSecTag	\$IDBeamTrans
element nonlinearBeamColumn	112	301	317	\$np	\$BeamSecTag	\$IDBeamTrans
element nonlinearBeamColumn	113	302	318	\$np	\$BeamSecTag	\$IDBeamTrans
element nonlinearBeamColumn	122	319	309	\$np	\$BeamSecTag	\$IDBeamTrans
element nonlinearBeamColumn	123	320	310	\$np	\$BeamSecTag	\$IDBeamTrans
element nonlinearBeamColumn	128	329	315	\$np	\$BeamSecTag	\$IDBeamTrans
element nonlinearBeamColumn	129	333	316	\$np	\$BeamSecTag	\$IDBeamTrans
element nonlinearBeamColumn	146	336	319	\$np	\$BeamSecTag	\$IDBeamTrans
element nonlinearBeamColumn	147	337	320	\$np	\$BeamSecTag	\$IDBeamTrans
element nonlinearBeamColumn	150	317	340	\$np	\$BeamSecTag	\$IDBeamTrans
element nonlinearBeamColumn	151	318	341	\$np	\$BeamSecTag	\$IDBeamTrans
element nonlinearBeamColumn	158	329	346	\$np	\$BeamSecTag	\$IDBeamTrans
element nonlinearBeamColumn	159	333	347	\$np	\$BeamSecTag	\$IDBeamTrans
element nonlinearBeamColumn	162	344	336	\$np	\$BeamSecTag	\$IDBeamTrans
element nonlinearBeamColumn	163	345	337	\$np	\$BeamSecTag	\$IDBeamTrans
element nonlinearBeamColumn	174	340	356	\$np	\$BeamSecTag	\$IDBeamTrans
element nonlinearBeamColumn	175	341	360	\$np	\$BeamSecTag	\$IDBeamTrans
element nonlinearBeamColumn	176	356	344	\$np	\$BeamSecTag	\$IDBeamTrans
element nonlinearBeamColumn	177	360	345	\$np	\$BeamSecTag	\$IDBeamTrans
element nonlinearBeamColumn	180	346	363	\$np	\$BeamSecTag	\$IDBeamTrans
element nonlinearBeamColumn	181	347	364	\$np	\$BeamSecTag	\$IDBeamTrans
element nonlinearBeamColumn	198	367	356	\$np	\$BeamSecTag	\$IDBeamTrans
element nonlinearBeamColumn	199	369	360	\$np	\$BeamSecTag	\$IDBeamTrans
element nonlinearBeamColumn	204	363	381	\$np	\$BeamSecTag	\$IDBeamTrans
element nonlinearBeamColumn	205	364	382	\$np	\$BeamSecTag	\$IDBeamTrans
element nonlinearBeamColumn	206	376	367	\$np	\$BeamSecTag	\$IDBeamTrans
element nonlinearBeamColumn	207	380	369	\$np	\$BeamSecTag	\$IDBeamTrans
element nonlinearBeamColumn	212	385	376	\$np	\$BeamSecTag	\$IDBeamTrans
element nonlinearBeamColumn	213	387	380	\$np	\$BeamSecTag	\$IDBeamTrans
element nonlinearBeamColumn	214	381	392	\$np	\$BeamSecTag	\$IDBeamTrans
element nonlinearBeamColumn	215	382	396	\$np	\$BeamSecTag	\$IDBeamTrans
element nonlinearBeamColumn	216	392	385	\$np	\$BeamSecTag	\$IDBeamTrans
element nonlinearBeamColumn	217	396	387	\$np	\$BeamSecTag	\$IDBeamTrans

# Define Slab Elements

# Cross-Section

```
set Hbs 200;
set Bbs 800;
set Abs [expr $Hbs*$Bbs];
```

```

set Ibsz [expr $Bbs*$Hbs*$Hbs*$Hbs/12.0];
set Ibsy [expr $Hbs*$Bbs*$Bbs*$Bbs/12.0];
set Jbs [expr $Ibsz+$Ibsy];
set Ebs [expr 0.35*4700.0*sqrt($fc)];
set GJbs [expr 1.e10];

```

```
set SlabSecTag 7
```

```
section Elastic $SlabSecTag $Ebs $Abs $Ibsz $Ibsy $GJbs $Jbs
```

```
set IDSlabTrans 3;
```

```
geomTransf Linear $IDSlabTrans 1 1 0;
```

element nonlinearBeamColumn	14	10	19	\$np	\$SlabSecTag	\$IDSlabTrans
element nonlinearBeamColumn	15	11	20	\$np	\$SlabSecTag	\$IDSlabTrans
element nonlinearBeamColumn	16	16	20	\$np	\$SlabSecTag	\$IDSlabTrans
element nonlinearBeamColumn	20	17	32	\$np	\$SlabSecTag	\$IDSlabTrans
element nonlinearBeamColumn	21	18	33	\$np	\$SlabSecTag	\$IDSlabTrans
element nonlinearBeamColumn	22	19	32	\$np	\$SlabSecTag	\$IDSlabTrans
element nonlinearBeamColumn	23	20	33	\$np	\$SlabSecTag	\$IDSlabTrans
element nonlinearBeamColumn	26	19	36	\$np	\$SlabSecTag	\$IDSlabTrans
element nonlinearBeamColumn	27	20	37	\$np	\$SlabSecTag	\$IDSlabTrans
element nonlinearBeamColumn	28	21	38	\$np	\$SlabSecTag	\$IDSlabTrans
element nonlinearBeamColumn	29	22	39	\$np	\$SlabSecTag	\$IDSlabTrans
element nonlinearBeamColumn	30	37	31	\$np	\$SlabSecTag	\$IDSlabTrans
element nonlinearBeamColumn	31	32	38	\$np	\$SlabSecTag	\$IDSlabTrans
element nonlinearBeamColumn	32	33	39	\$np	\$SlabSecTag	\$IDSlabTrans
element nonlinearBeamColumn	36	32	47	\$np	\$SlabSecTag	\$IDSlabTrans
element nonlinearBeamColumn	37	33	48	\$np	\$SlabSecTag	\$IDSlabTrans
element nonlinearBeamColumn	38	34	49	\$np	\$SlabSecTag	\$IDSlabTrans
element nonlinearBeamColumn	39	35	50	\$np	\$SlabSecTag	\$IDSlabTrans
element nonlinearBeamColumn	40	47	36	\$np	\$SlabSecTag	\$IDSlabTrans
element nonlinearBeamColumn	41	48	37	\$np	\$SlabSecTag	\$IDSlabTrans
element nonlinearBeamColumn	42	38	49	\$np	\$SlabSecTag	\$IDSlabTrans
element nonlinearBeamColumn	43	39	50	\$np	\$SlabSecTag	\$IDSlabTrans
element nonlinearBeamColumn	44	36	149	\$np	\$SlabSecTag	\$IDSlabTrans
element nonlinearBeamColumn	45	37	150	\$np	\$SlabSecTag	\$IDSlabTrans
element nonlinearBeamColumn	48	38	219	\$np	\$SlabSecTag	\$IDSlabTrans
element nonlinearBeamColumn	49	39	220	\$np	\$SlabSecTag	\$IDSlabTrans
element nonlinearBeamColumn	50	46	150	\$np	\$SlabSecTag	\$IDSlabTrans
element nonlinearBeamColumn	51	40	282	\$np	\$SlabSecTag	\$IDSlabTrans
element nonlinearBeamColumn	52	41	283	\$np	\$SlabSecTag	\$IDSlabTrans
element nonlinearBeamColumn	53	219	47	\$np	\$SlabSecTag	\$IDSlabTrans
element nonlinearBeamColumn	54	220	48	\$np	\$SlabSecTag	\$IDSlabTrans
element nonlinearBeamColumn	60	49	282	\$np	\$SlabSecTag	\$IDSlabTrans
element nonlinearBeamColumn	61	50	283	\$np	\$SlabSecTag	\$IDSlabTrans

element nonlinearBeamColumn	62	47	293	\$np	\$SlabSecTag	\$IDSlabTrans
element nonlinearBeamColumn	63	48	294	\$np	\$SlabSecTag	\$IDSlabTrans
element nonlinearBeamColumn	64	49	297	\$np	\$SlabSecTag	\$IDSlabTrans
element nonlinearBeamColumn	65	50	298	\$np	\$SlabSecTag	\$IDSlabTrans
element nonlinearBeamColumn	66	149	293	\$np	\$SlabSecTag	\$IDSlabTrans
element nonlinearBeamColumn	67	150	294	\$np	\$SlabSecTag	\$IDSlabTrans
element nonlinearBeamColumn	78	297	219	\$np	\$SlabSecTag	\$IDSlabTrans
element nonlinearBeamColumn	79	298	220	\$np	\$SlabSecTag	\$IDSlabTrans
element nonlinearBeamColumn	80	149	299	\$np	\$SlabSecTag	\$IDSlabTrans
element nonlinearBeamColumn	81	150	300	\$np	\$SlabSecTag	\$IDSlabTrans
element nonlinearBeamColumn	84	219	303	\$np	\$SlabSecTag	\$IDSlabTrans
element nonlinearBeamColumn	85	220	304	\$np	\$SlabSecTag	\$IDSlabTrans
element nonlinearBeamColumn	88	282	301	\$np	\$SlabSecTag	\$IDSlabTrans
element nonlinearBeamColumn	89	283	302	\$np	\$SlabSecTag	\$IDSlabTrans
element nonlinearBeamColumn	90	282	307	\$np	\$SlabSecTag	\$IDSlabTrans
element nonlinearBeamColumn	91	283	308	\$np	\$SlabSecTag	\$IDSlabTrans
element nonlinearBeamColumn	92	293	303	\$np	\$SlabSecTag	\$IDSlabTrans
element nonlinearBeamColumn	93	294	304	\$np	\$SlabSecTag	\$IDSlabTrans
element nonlinearBeamColumn	96	307	297	\$np	\$SlabSecTag	\$IDSlabTrans
element nonlinearBeamColumn	97	308	298	\$np	\$SlabSecTag	\$IDSlabTrans
element nonlinearBeamColumn	98	293	309	\$np	\$SlabSecTag	\$IDSlabTrans
element nonlinearBeamColumn	99	294	310	\$np	\$SlabSecTag	\$IDSlabTrans
element nonlinearBeamColumn	100	295	311	\$np	\$SlabSecTag	\$IDSlabTrans
element nonlinearBeamColumn	101	296	312	\$np	\$SlabSecTag	\$IDSlabTrans
element nonlinearBeamColumn	102	297	313	\$np	\$SlabSecTag	\$IDSlabTrans
element nonlinearBeamColumn	103	298	314	\$np	\$SlabSecTag	\$IDSlabTrans
element nonlinearBeamColumn	106	301	311	\$np	\$SlabSecTag	\$IDSlabTrans
element nonlinearBeamColumn	107	302	312	\$np	\$SlabSecTag	\$IDSlabTrans
element nonlinearBeamColumn	108	303	313	\$np	\$SlabSecTag	\$IDSlabTrans
element nonlinearBeamColumn	109	304	314	\$np	\$SlabSecTag	\$IDSlabTrans
element nonlinearBeamColumn	114	303	319	\$np	\$SlabSecTag	\$IDSlabTrans
element nonlinearBeamColumn	115	304	320	\$np	\$SlabSecTag	\$IDSlabTrans
element nonlinearBeamColumn	116	317	307	\$np	\$SlabSecTag	\$IDSlabTrans
element nonlinearBeamColumn	117	318	308	\$np	\$SlabSecTag	\$IDSlabTrans
element nonlinearBeamColumn	118	305	321	\$np	\$SlabSecTag	\$IDSlabTrans
element nonlinearBeamColumn	119	306	322	\$np	\$SlabSecTag	\$IDSlabTrans
element nonlinearBeamColumn	120	307	323	\$np	\$SlabSecTag	\$IDSlabTrans
element nonlinearBeamColumn	121	308	324	\$np	\$SlabSecTag	\$IDSlabTrans
element nonlinearBeamColumn	124	311	321	\$np	\$SlabSecTag	\$IDSlabTrans
element nonlinearBeamColumn	125	312	322	\$np	\$SlabSecTag	\$IDSlabTrans
element nonlinearBeamColumn	126	313	323	\$np	\$SlabSecTag	\$IDSlabTrans
element nonlinearBeamColumn	127	314	324	\$np	\$SlabSecTag	\$IDSlabTrans
element nonlinearBeamColumn	130	311	334	\$np	\$SlabSecTag	\$IDSlabTrans
element nonlinearBeamColumn	131	312	335	\$np	\$SlabSecTag	\$IDSlabTrans
element nonlinearBeamColumn	132	313	336	\$np	\$SlabSecTag	\$IDSlabTrans
element nonlinearBeamColumn	133	314	337	\$np	\$SlabSecTag	\$IDSlabTrans

element nonlinearBeamColumn	134 315 338	\$np	\$SlabSecTag	\$IDSlabTrans
element nonlinearBeamColumn	135 316 339	\$np	\$SlabSecTag	\$IDSlabTrans
element nonlinearBeamColumn	136 334 317	\$np	\$SlabSecTag	\$IDSlabTrans
element nonlinearBeamColumn	137 335 318	\$np	\$SlabSecTag	\$IDSlabTrans
element nonlinearBeamColumn	148 321 338	\$np	\$SlabSecTag	\$IDSlabTrans
element nonlinearBeamColumn	149 322 339	\$np	\$SlabSecTag	\$IDSlabTrans
element nonlinearBeamColumn	152 323 340	\$np	\$SlabSecTag	\$IDSlabTrans
element nonlinearBeamColumn	153 324 341	\$np	\$SlabSecTag	\$IDSlabTrans
element nonlinearBeamColumn	154 321 342	\$np	\$SlabSecTag	\$IDSlabTrans
element nonlinearBeamColumn	155 322 343	\$np	\$SlabSecTag	\$IDSlabTrans
element nonlinearBeamColumn	156 323 344	\$np	\$SlabSecTag	\$IDSlabTrans
element nonlinearBeamColumn	157 324 345	\$np	\$SlabSecTag	\$IDSlabTrans
element nonlinearBeamColumn	160 342 334	\$np	\$SlabSecTag	\$IDSlabTrans
element nonlinearBeamColumn	161 343 335	\$np	\$SlabSecTag	\$IDSlabTrans
element nonlinearBeamColumn	164 338 346	\$np	\$SlabSecTag	\$IDSlabTrans
element nonlinearBeamColumn	165 339 347	\$np	\$SlabSecTag	\$IDSlabTrans
element nonlinearBeamColumn	166 334 348	\$np	\$SlabSecTag	\$IDSlabTrans
element nonlinearBeamColumn	167 335 349	\$np	\$SlabSecTag	\$IDSlabTrans
element nonlinearBeamColumn	168 338 350	\$np	\$SlabSecTag	\$IDSlabTrans
element nonlinearBeamColumn	169 339 351	\$np	\$SlabSecTag	\$IDSlabTrans
element nonlinearBeamColumn	170 340 348	\$np	\$SlabSecTag	\$IDSlabTrans
element nonlinearBeamColumn	171 341 349	\$np	\$SlabSecTag	\$IDSlabTrans
element nonlinearBeamColumn	172 350 342	\$np	\$SlabSecTag	\$IDSlabTrans
element nonlinearBeamColumn	173 351 343	\$np	\$SlabSecTag	\$IDSlabTrans
element nonlinearBeamColumn	178 342 361	\$np	\$SlabSecTag	\$IDSlabTrans
element nonlinearBeamColumn	179 343 362	\$np	\$SlabSecTag	\$IDSlabTrans
element nonlinearBeamColumn	182 348 361	\$np	\$SlabSecTag	\$IDSlabTrans
element nonlinearBeamColumn	183 349 362	\$np	\$SlabSecTag	\$IDSlabTrans
element nonlinearBeamColumn	192 363 350	\$np	\$SlabSecTag	\$IDSlabTrans
element nonlinearBeamColumn	193 364 351	\$np	\$SlabSecTag	\$IDSlabTrans
element nonlinearBeamColumn	194 348 367	\$np	\$SlabSecTag	\$IDSlabTrans
element nonlinearBeamColumn	195 349 369	\$np	\$SlabSecTag	\$IDSlabTrans
element nonlinearBeamColumn	196 350 370	\$np	\$SlabSecTag	\$IDSlabTrans
element nonlinearBeamColumn	197 351 371	\$np	\$SlabSecTag	\$IDSlabTrans
element nonlinearBeamColumn	200 361 370	\$np	\$SlabSecTag	\$IDSlabTrans
element nonlinearBeamColumn	201 362 371	\$np	\$SlabSecTag	\$IDSlabTrans
element nonlinearBeamColumn	202 361 376	\$np	\$SlabSecTag	\$IDSlabTrans
element nonlinearBeamColumn	203 362 380	\$np	\$SlabSecTag	\$IDSlabTrans
element nonlinearBeamColumn	208 370 381	\$np	\$SlabSecTag	\$IDSlabTrans
element nonlinearBeamColumn	209 371 382	\$np	\$SlabSecTag	\$IDSlabTrans
element nonlinearBeamColumn	210 370 385	\$np	\$SlabSecTag	\$IDSlabTrans
element nonlinearBeamColumn	211 371 387	\$np	\$SlabSecTag	\$IDSlabTrans

# Define Shell Elements

# Set Prameters

```

set pi 3.141592654
set wfc 28.0
set ec0 0.003
set wfy 412.0
set wE 200000.0
set wGmin 5000
set wGmax 10000.0
set wGs [expr 3875.0*sqrt($wfc)/(2.4)]
set afa1 [expr 0.0*$pi]
set afa2 [expr 0.5*$pi]

```

# Wall A

```

set t1 100
set rou1 0.0036
set a1 40

```

```

uniaxialMaterial SteelZ01 11 $wfy $wE $wfc $rou1
uniaxialMaterial SteelZ01 12 $wfy $wE $wfc $rou1

```

```

uniaxialMaterial ConcreteZ01 13 [expr -$wfc] [expr -$ec0]
uniaxialMaterial ConcreteZ01 14 [expr -$wfc] [expr -$ec0]

```

```

nDMaterial CSMMLayer 15 0.0 11 12 13 14 $afa1 $afa2 $rou1 $rou1 $wfc $wfy
$wE $ec0 $wGs 1
nDMaterial CSMMLayer 16 0.0 11 12 13 14 $afa1 $afa2 $rou1 $rou1 $wfc $wfy
$wE $ec0 $wGs 0

```

```

set mata1 "15"
set mata2 "16"

```

```

set nlay 20

```

```

# shell Area Joint1 Joint2 Joint3 Joint4 Joint5 Joint6 Joint7 Joint8 Property
element CSMMShellS8 310 372 352 354 374 365 353 366 373 $nlay $t1 $a1 $mata1
$mata2
element CSMMShellS8 311 356 376 374 354 367 375 366 355 $nlay $t1 $a1 $mata1
$mata2
element CSMMShellS8 312 376 356 358 378 367 357 368 377 $nlay $t1 $a1 $mata1
$mata2
element CSMMShellS8 313 378 358 360 380 368 359 369 379 $nlay $t1 $a1 $mata1
$mata2
element CSMMShellS8 314 388 372 374 390 383 373 384 389 $nlay $t1 $a1 $mata1
$mata2
element CSMMShellS8 315 390 374 376 392 384 375 385 391 $nlay $t1 $a1 $mata1
$mata2

```

element CSMMShellS8 316 392 376 378 394 385 377 386 393 \$nlay \$t1 \$a1 \$mata1  
\$mata2

element CSMMShellS8 317 380 396 394 378 387 395 386 379 \$nlay \$t1 \$a1 \$mata1  
\$mata2

# Wall B

set t2 150  
set rou2 0.0048  
set a2 20

uniaxialMaterial SteelZ01 21 \$wfy \$wE \$wfc \$rou2  
uniaxialMaterial SteelZ01 22 \$wfy \$wE \$wfc \$rou2

uniaxialMaterial ConcreteZ01 23 [expr -\$wfc] [expr -\$ec0]  
uniaxialMaterial ConcreteZ01 24 [expr -\$wfc] [expr -\$ec0]

nDMaterial CSMMLayer 25 0.0 21 22 23 24 \$afa1 \$afa2 \$rou2 \$rou2 \$wfc \$wfy  
\$wE \$ec0 \$wGs 1

nDMaterial CSMMLayer 26 0.0 21 22 23 24 \$afa1 \$afa2 \$rou2 \$rou2 \$wfc \$wfy  
\$wE \$ec0 \$wGs 0

set matb1 "25"  
set matb2 "26"

set nlay 20

# shell Area Joint1 Joint2 Joint3 Joint4 Joint5 Joint6 Joint7 Joint8 Property  
element CSMMShellS8 226 3 25 23 1 13 24 12 2 \$nlay \$t2 \$a2 \$matb1  
\$matb2  
element CSMMShellS8 227 25 3 5 27 13 4 14 26 \$nlay \$t2 \$a2 \$matb1  
\$matb2  
element CSMMShellS8 228 27 5 7 29 14 6 15 28 \$nlay \$t2 \$a2 \$matb1  
\$matb2  
element CSMMShellS8 229 29 7 9 31 15 8 16 30 \$nlay \$t2 \$a2 \$matb1  
\$matb2  
element CSMMShellS8 230 284 23 25 286 42 24 43 285 \$nlay \$t2 \$a2 \$matb1  
\$matb2  
element CSMMShellS8 231 286 25 27 288 43 26 44 287 \$nlay \$t2 \$a2 \$matb1  
\$matb2  
element CSMMShellS8 232 29 290 288 27 45 289 44 28 \$nlay \$t2 \$a2 \$matb1  
\$matb2  
element CSMMShellS8 233 290 29 31 292 45 30 46 291 \$nlay \$t2 \$a2 \$matb1  
\$matb2

# Torsion Column

```

set t3 140
set rou3v 0.02
set rou3h 0.0018
set a3 60

```

```

uniaxialMaterial SteelZ01 31 $wfy $wE $wfc $rou3h
uniaxialMaterial SteelZ01 32 $wfy $wE $wfc $rou3v
# uniaxialMaterial Hysteretic 31 $fyp $eyp $fup $eup $fdp $edp -$fyp -$eyp -$fup -$eup
-$fdp -$edp 0.0 0.0 0.0 0.0
# uniaxialMaterial Hysteretic 32 $fyp $eyp $fup $eup $fdp $edp -$fyn -$eyn -$fun -$eun
-$fdn -$edn 0.0 0.0 0.0 0.0

```

```

uniaxialMaterial ConcreteZ01 33 [expr -$wfc] [expr -$ec0]
uniaxialMaterial ConcreteZ01 34 [expr -$wfc] [expr -$ec0]

```

```

nDMaterial CSMMLayer 35 0.0 21 22 23 24 $afa1 $afa2 $rou3h $rou3v $wfc $wfy
$wE $ec0 $wGs 1
nDMaterial CSMMLayer 36 0.0 21 22 23 24 $afa1 $afa2 $rou3h $rou3v $wfc $wfy
$wE $ec0 $wGs 0

```

```

set matc1 "35"
set matc2 "36"

```

```

set nlay 5

```

```

# shell Area Joint1 Joint2 Joint3 Joint4 Joint5 Joint6 Joint7 Joint8 Property
element CSMMSHELLS8 234 77 51 53 79 68 52 69 78 $nlay $t3 $a3 $matc1
$matc2
element CSMMSHELLS8 235 79 53 55 81 69 54 70 80 $nlay $t3 $a3 $matc1
$matc2
element CSMMSHELLS8 236 81 55 57 83 70 56 71 82 $nlay $t3 $a3 $matc1
$matc2
element CSMMSHELLS8 237 83 57 59 85 71 58 72 84 $nlay $t3 $a3 $matc1
$matc2
element CSMMSHELLS8 238 85 59 61 87 72 60 73 86 $nlay $t3 $a3 $matc1
$matc2
element CSMMSHELLS8 239 87 61 63 89 73 62 74 88 $nlay $t3 $a3 $matc1
$matc2
element CSMMSHELLS8 242 134 53 51 132 95 52 94 133 $nlay $t3 $a3 $matc1
$matc2
element CSMMSHELLS8 243 53 134 136 55 95 135 96 54 $nlay $t3 $a3 $matc1
$matc2
element CSMMSHELLS8 244 55 136 138 57 96 137 97 56 $nlay $t3 $a3 $matc1
$matc2

```

element CSMMShellS8	245	57	138	140	59	97	139	98	58	\$nlay	\$t3	\$a3	\$matc1
\$matc2													
element CSMMShellS8	246	59	140	142	61	98	141	99	60	\$nlay	\$t3	\$a3	\$matc1
\$matc2													
element CSMMShellS8	247	61	142	144	63	99	143	100	62	\$nlay	\$t3	\$a3	\$matc1
\$matc2													
element CSMMShellS8	250	112	77	79	114	103	78	104	113	\$nlay	\$t3	\$a3	\$matc1
\$matc2													
element CSMMShellS8	251	114	79	81	116	104	80	105	115	\$nlay	\$t3	\$a3	\$matc1
\$matc2													
element CSMMShellS8	252	116	81	83	118	105	82	106	117	\$nlay	\$t3	\$a3	\$matc1
\$matc2													
element CSMMShellS8	253	118	83	85	120	106	84	107	119	\$nlay	\$t3	\$a3	\$matc1
\$matc2													
element CSMMShellS8	254	120	85	87	122	107	86	108	121	\$nlay	\$t3	\$a3	\$matc1
\$matc2													
element CSMMShellS8	255	89	124	122	87	109	123	108	88	\$nlay	\$t3	\$a3	\$matc1
\$matc2													
element CSMMShellS8	264	112	182	184	114	154	183	155	113	\$nlay	\$t3	\$a3	\$matc1
\$matc2													
element CSMMShellS8	265	186	116	114	184	156	115	155	185	\$nlay	\$t3	\$a3	\$matc1
\$matc2													
element CSMMShellS8	266	116	186	188	118	156	187	157	117	\$nlay	\$t3	\$a3	\$matc1
\$matc2													
element CSMMShellS8	267	118	188	190	120	157	189	158	119	\$nlay	\$t3	\$a3	\$matc1
\$matc2													
element CSMMShellS8	268	120	190	192	122	158	191	159	121	\$nlay	\$t3	\$a3	\$matc1
\$matc2													
element CSMMShellS8	269	122	192	194	124	159	193	160	123	\$nlay	\$t3	\$a3	\$matc1
\$matc2													
element CSMMShellS8	272	204	134	132	202	171	133	170	203	\$nlay	\$t3	\$a3	\$matc1
\$matc2													
element CSMMShellS8	273	134	204	206	136	171	205	172	135	\$nlay	\$t3	\$a3	\$matc1
\$matc2													
element CSMMShellS8	274	136	206	208	138	172	207	173	137	\$nlay	\$t3	\$a3	\$matc1
\$matc2													
element CSMMShellS8	275	138	208	210	140	173	209	174	139	\$nlay	\$t3	\$a3	\$matc1
\$matc2													
element CSMMShellS8	276	140	210	212	142	174	211	175	141	\$nlay	\$t3	\$a3	\$matc1
\$matc2													
element CSMMShellS8	277	142	212	214	144	175	213	176	143	\$nlay	\$t3	\$a3	\$matc1
\$matc2													
element CSMMShellS8	286	239	202	204	241	221	203	222	240	\$nlay	\$t3	\$a3	\$matc1
\$matc2													
element CSMMShellS8	287	241	204	206	243	222	205	223	242	\$nlay	\$t3	\$a3	\$matc1
\$matc2													

```

element CSMMSHELLS8 288 208 245 243 206 224 244 223 207 $nlay $t3 $a3 $matc1
$matc2
element CSMMSHELLS8 289 245 208 210 247 224 209 225 246 $nlay $t3 $a3 $matc1
$matc2
element CSMMSHELLS8 290 247 210 212 249 225 211 226 248 $nlay $t3 $a3 $matc1
$matc2
element CSMMSHELLS8 291 249 212 214 251 226 213 227 250 $nlay $t3 $a3 $matc1
$matc2
element CSMMSHELLS8 294 267 184 182 265 231 183 230 266 $nlay $t3 $a3 $matc1
$matc2
element CSMMSHELLS8 295 269 186 184 267 232 185 231 268 $nlay $t3 $a3 $matc1
$matc2
element CSMMSHELLS8 296 186 269 271 188 232 270 233 187 $nlay $t3 $a3 $matc1
$matc2
element CSMMSHELLS8 297 188 271 273 190 233 272 234 189 $nlay $t3 $a3 $matc1
$matc2
element CSMMSHELLS8 298 190 273 275 192 234 274 235 191 $nlay $t3 $a3 $matc1
$matc2
element CSMMSHELLS8 299 192 275 277 194 235 276 236 193 $nlay $t3 $a3 $matc1
$matc2
element CSMMSHELLS8 302 265 239 241 267 256 240 257 266 $nlay $t3 $a3 $matc1
$matc2
element CSMMSHELLS8 303 267 241 243 269 257 242 258 268 $nlay $t3 $a3 $matc1
$matc2
element CSMMSHELLS8 304 269 243 245 271 258 244 259 270 $nlay $t3 $a3 $matc1
$matc2
element CSMMSHELLS8 305 271 245 247 273 259 246 260 272 $nlay $t3 $a3 $matc1
$matc2
element CSMMSHELLS8 306 273 247 249 275 260 248 261 274 $nlay $t3 $a3 $matc1
$matc2
element CSMMSHELLS8 307 275 249 251 277 261 250 262 276 $nlay $t3 $a3 $matc1
$matc2

```

```
# Define Shell Elements 2
```

```
# Set Parameters
```

```
set E 9.e10
```

```
set v 0.2
```

```
set rho 1
```

```
set to 200.0
```

```
nDMaterial LinearFiber 40 $E $v $rho
```

```
set matd "40"
```

```
# shell Area Joint1 Joint2 Joint3 Joint4 Joint5 Joint6 Joint7 Joint8 Property
```

```

element ElasticShellS8 240 89 63 65 91 74 64 75 90 $to $matd
element ElasticShellS8 241 91 65 67 93 75 66 76 92 $to $matd
element ElasticShellS8 248 146 65 63 144 101 64 100 145 $to $matd
element ElasticShellS8 249 148 67 65 146 102 66 101 147 $to $matd
element ElasticShellS8 256 124 89 91 126 109 90 110 125 $to $matd
element ElasticShellS8 257 126 91 93 128 110 92 111 127 $to $matd
element ElasticShellS8 258 77 167 132 51 129 151 94 68 $to $matd
element ElasticShellS8 259 89 168 144 63 130 152 100 74 $to $matd
element ElasticShellS8 260 93 169 148 67 131 153 102 76 $to $matd
element ElasticShellS8 261 112 182 167 77 154 179 129 103 $to $matd
element ElasticShellS8 262 124 194 168 89 160 180 130 109 $to $matd
element ElasticShellS8 263 128 198 169 93 162 181 131 111 $to $matd
element ElasticShellS8 270 124 194 196 126 160 195 161 125 $to $matd
element ElasticShellS8 271 126 196 198 128 161 197 162 127 $to $matd
element ElasticShellS8 278 216 146 144 214 177 145 176 215 $to $matd
element ElasticShellS8 279 146 216 218 148 177 217 178 147 $to $matd
element ElasticShellS8 280 167 239 202 132 199 221 170 151 $to $matd
element ElasticShellS8 281 168 251 214 144 200 227 176 152 $to $matd
element ElasticShellS8 282 169 255 218 148 201 229 178 153 $to $matd
element ElasticShellS8 283 182 265 239 167 230 256 199 179 $to $matd
element ElasticShellS8 284 194 277 251 168 236 262 200 180 $to $matd
element ElasticShellS8 285 198 281 255 169 238 264 201 181 $to $matd
element ElasticShellS8 292 251 214 216 253 227 215 228 252 $to $matd
element ElasticShellS8 293 253 216 218 255 228 217 229 254 $to $matd
element ElasticShellS8 300 194 277 279 196 236 278 237 195 $to $matd
element ElasticShellS8 301 281 198 196 279 238 197 237 280 $to $matd
element ElasticShellS8 308 277 251 253 279 262 252 263 278 $to $matd
element ElasticShellS8 309 279 253 255 281 263 254 264 280 $to $matd

```

```
# Define Applying Loads
```

```
set N 850000;
```

```
# Define gravity loads
```

```
pattern Plain 1 "Linear" {
```

```
load 333 0 0 -$N 0 0 0
```

```
}
```

```
# Define Output
```

```
set dataDir Analyze1
```

```
file mkdir $dataDir/
```

```
ExportVTK NodeAll $dataDir/kennode.dat
```

```
ExportVTK Element2 $dataDir/keneleF.dat
```

```

ExportVTK Element8 $dataDir/keneleS.dat
ExportVTK Recorderdisp $dataDir/Recorderdisp.tcl $dataDir/nodedisp.dat
source "$dataDir/Recorderdisp.tcl"

set Rnode2 308
set Rnode1 307

# Define Analysis Parameter
system BandGeneral
constraints Plain
numberer Plain

# Define Create the Integration Scheme
test NormDispIncr 1.0e-3 100 5
integrator LoadControl 0.1

# Define Solution Algorithm
algorithm KrylovNewton
analysis Static

# Perform the Analysis
analyze 10

# Print out the state of nodes
print node $Rnode1 $Rnode2

# Analyze2Cyclic.tcl

# Sourcing the Previous File
source Analyze1.tcl

# Redefine time
loadConst -time 0.0

# Define Loading

set P 1000.0;
set P1 [expr (1/2.83)*$P]
set P2 [expr (1.83/2.83)*$P]

# Define lateral loads
pattern Plain 2 "Linear" {
  load $Rnode1 $P1 0 0 0 0
  load $Rnode2 $P2 0 0 0 0

```

```

}

# Define Output

set dataDir1 Analyze2Cyclic2
file mkdir $dataDir1/

recorder Node -file $dataDir1/FD$Rnode2.dat -time -node $Rnode2 -dof 1 disp

# Define Analysis Parameter
system BandGeneral
constraints Plain
numberer Plain

# Define Create the Integration Scheme
test NormDispIncrVaryIter 0.5 61 5 numStep 8 16 16 16 16 16 20 24 24 24 24 24
30 36 36 36 36 36 45 54 54 54 54 54 64 74 74 74 74 74 93 112 112 112 112
112 132 152 152 152 152 152 192 232 232 232 232 232 273 314 314 314 314 314 397
480 480 480 480 480 218 \
    numIter 150 150 150 150 150 150 150 150 150 150 150 150 150 150 150
150 150 150 150 150 150 150 150 150 150 150 150 150 150 150 150 150 150 150
150 150 150 150 150 150 150 150 150 150 150 150 150 150 150 150 150 150 150
150 150 150 150 150 150 150 150

integrator DisplacementPath $Rnode2 1 61 numStep 8 16 16 16 16 16 20 24 24
24 24 24 30 36 36 36 36 36 45 54 54 54 54 54 64 74 74 74 74 74 93 112
112 112 112 112 132 152 152 152 152 152 192 232 232 232 232 232 273 314 314 314
314 314 397 480 480 480 480 480 218 \
    increment 0.5 -0.5 0.5 -0.5 0.5 -0.5 0.5 -0.5 0.5 -0.5 0.5 -0.5
0.5 -0.5 0.5 -0.5 0.5 -0.5 0.5 -0.5 0.5 -0.5 0.5 -0.5 0.5 -0.5 0.5 -0.5
0.5 -0.5 0.5 -0.5 0.5 -0.5 0.5 -0.5 0.5 -0.5 0.5 -0.5 0.5 -0.5 0.5 -0.5
0.5 -0.5 0.5 -0.5 0.5 -0.5 0.5 -0.5 0.5 -0.5 0.5 -0.5 0.5 -0.5 0.5 -0.5

# Define Solution Algorithm
algorithm KrylovNewton
analysis Static
initialize

# Perform the Analysis
set time1 [clock clicks -milliseconds]
analyze 8942
set time2 [clock clicks -milliseconds]
puts "Elapsed time is [expr ($time2-$time1)/1000] seconds"

```

```
# Print out the state of nodes
print node $Rnode1 $Rnode2
```

The output file for load-displacement curve is presented as below

---

load (kN)	displacement (mm)
0	-0.170281
62.4417	0.329719
119.123	0.829719
176.024	1.32972
231.822	1.82972
285.823	2.32972
338.041	2.82972
388.651	3.32972
437.694	3.82972
385.481	3.32972
332.627	2.82972
278.89	2.32972
223.939	1.82972
167.506	1.32972
110.501	0.829719
54.02	0.329719
-6.30247	-0.170281
-64.1995	-0.670281
-121.126	-1.17028
-176.893	-1.67028
-231.264	-2.17028
-284.468	-2.67028
-336.486	-3.17028
-387.271	-3.67028
-436.754	-4.17028
-383.466	-3.67028
-329.917	-3.17028
-275.816	-2.67028
-221.015	-2.17028
-165.733	-1.67028
-109.411	-1.17028
-53.7609	-0.670281
3.24312	-0.170281
61.3389	0.329719
117.053	0.829719
172.971	1.32972
227.992	1.82972
281.877	2.32972
334.797	2.82972
.....	

